PL-TR-97-2069
Environmental Research Papers, No. 1206

PROCEEDINGS OF THE 19TH ANNUAL CONFERENCE ON ATMOSPHERIC TRANSMISSION MODELS, 4-6 JUNE 1996

Editors:

Gail P. Anderson
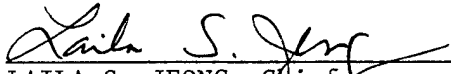Richard H. Picard
James H. Chetwynd
Laurence S. Rothman

22 May 1997

PHILLIPS LABORATORY
Directorate of Geophysics
AIR FORCE MATERIEL COMMAND
HANSCOM AFB, MA 01731-3010

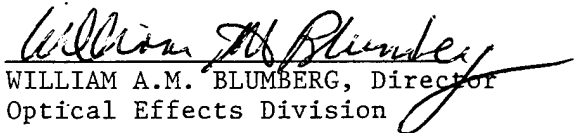19970808 020

"This technical report has been reviewed and is approved for publication"

LAILA S. JEONG, Chief
Background Clutter Mitigation Branch

WILLIAM A.M. BLUMBERG, Director
Optical Effects Division

Qualified requestors may obtain additional copies from the Defense Technical Information Center (DTIC).

If your address has changed, if you wish to be removed from the mailing list, or if the addressee is not longer employed by your organization, please notify PL/IM, 29 Randolph Road, Hanscom AFB, MA 01731-3010. This will assist us in maintaining a current mailing list.

Do not return copies of this report unless contractual obligations or notices on a specific document requires that it be returned.

REPORT DOCUMENTATION PAGE

Form Approved
OMB No. 0704-0188

1. AGENCY USE ONLY (Leave blank)	2. REPORT DATE 22 May 1997	3. REPORT TYPE AND DATES COVERED Scientific

4. TITLE AND SUBTITLE
PROCEEDINGS OF THE 19th ANNUAL CONFERENCE ON ATMOSPHERIC TRANSMISSION MODELS, 4-6 June 1996

5. FUNDING NUMBERS
PE: 62101F
PR: 3054
TA: GD
WU: 01

6. AUTHOR(S)
Editors: GAIL P. ANDERSON   LAURENCE S. ROTHMAN
RICHARD H. PICARD
JAMES H. CHETWYND

7. PERFORMING ORGANIZATION NAME(S) AND ADDRESS(ES)
Phillips Laboratory/GPOS
29 Randolph Road
Hanscom AFB, MA   01731-3010

8. PERFORMING ORGANIZATION REPORT NUMBER
PL-TR-97-2069
ERP, No. 1206

9. SPONSORING/MONITORING AGENCY NAME(S) AND ADDRESS(ES)

10. SPONSORING/MONITORING AGENCY REPORT NUMBER

11. SUPPLEMENTARY NOTES

12a. DISTRIBUTION/AVAILABILITY STATEMENT
Approved for public Release; Distribution Unlimited

12b. DISTRIBUTION CODE

13. ABSTRACT (Maximum 200 words)
CONTAINS THE VIEWGRAPHS AND OTHER MATERIALS FOR THE 57 PAPERS PRESENTED AT THE 19th ANNUAL REVIEW CONFERENCE ON ATMOSPHERIC TRANSMISSION MODELS HELD AT THE GEOPHYSICS DIRECTORATE, PHILLIPS LABORATORY (AFMC), HANSCOM AFB, ON: 4-6 JUNE 1996.

14. SUBJECT TERMS
Atmospheric transmittance   Clouds   Lasers
Aerosols   Radiative transfer   Lidar
Atmospheric propagation   Optical turbulence

15. NUMBER OF PAGES 300

16. PRICE CODE

17. SECURITY CLASSIFICATION OF REPORT	18. SECURITY CLASSIFICATION OF THIS PAGE	19. SECURITY CLASSIFICATION OF ABSTRACT	20. LIMITATION OF ABSTRACT
Unclassified	Unclassified	Unclassified	SAR

TABLE OF CONTENTS

REAL INSTRUMENTS - REAL TECHNIQUES

HIGH RESOLUTION MODELING AND RADIATIVE TRANSFER

CLOUDS AND AEROSOLS

MODERATE RESOLUTION RT AND CODE ARCHITECTURE

HIGH ALTITUDE MODELS/STRUCTURE

LASER/LIDAR

POSTER SESSION

HITRAN: MOLECULAR PARAMETERS

PREFACE

The Nineteenth DoD Tri-Service Review Conference on
Atmospheric Transmission Models was held at the Geophysics
Directorate of the USAF Phillips Laborarory at Hanscom AFB,
Massachusetts on 4-6 June 1996.

A total of 57 papers and posters was given by and to
an international audience of participants. Topics addressed
included advances in codes such as PLEXUS, FASCOD, MODTRAN,
MOSART, SHARC, etc., including the applications of codes to
various atmospheric problems such as radiative transfer,
structure, and chemical reactions. Laser and lidar techniques
were given their own session as were clouds and aerosols.
Spectroscopic additions and corrections to data bases were
dealt with in the HITRAN sessions.

This volume contains the abstracts of the papers,
grouped together at the front, in the order of
presentation, and texts and hardcopy provided by
the authors. An Author Index is also given.

The Editors thank the authors and audience for
making the meeting such a success by their attendance and
participation.

Gail P. Anderson
Background Clutter Mitigation Branch
Optical Effects Division

SPECTROSCOPIC DEVELOPMENT FOR THE ANALYSIS OF MEASUREMENTS FROM THE GLOBAL OZONE MONITORING EXPERIMENT

Kelly Chance

Harvard-Smithsonian Center for Astrophysics
60 Garden Street
Cambridge, MA

The European Space Agency's Global Ozone Monitoring Experiment (GOME) was launched on the European Remote Sensing 2 satellite on April 20, 1995. It has currently operated for more than one year, obtaining nadir atmospheric spectra from 240-790 nm. The spectral resolution is 0.2 nm in the ultraviolet and 0.4 nm in the visible. The objectives of the GOME project include enhanced mapping of ozone, with emphasis on the global distribution of tropospheric ozone. This talk presents results of GOME measurements and details of several of the developments in quantitative molecular spectroscopy and radiative transfer that support the analysis of the spectra.

The major spectroscopic feature that permits tropospheric O_3 to be distinguished from stratospheric O_3 in nadir viewing is the nonlinear, structured temperature dependence of absorption in the ultraviolet Huggins bands. Details of the Huggins band absorption as they affect retrieval of height-resolved O_3 determinations are presented. Accurate analysis of GOME spectra to retrieve concentrations of O_3 and other atmospheric species must account for the inelastic scattering of light from the Fraunhoffer irradiance spectrum, including corrections for atmospheric absorptions (the "Ring effect"). An improved characterization and parameterization of the microscopic molecular physics for Ring effect scattering due to the rotational Raman effect is presented. GOME uses the visible O_2A band for cloud correction in the O_3 retrieval process. The determination of an improved molecular spectroscopic database for O_2A band absorption is presented and correction for pressure- and temperature-dependent formation of the O_2-O_2 collisional complex is discussed

SESSION 1: 9:15

ESTIMATION OF BIOMASS FIRE TEMPERATURE AND AREAL EXTENT FROM INVERSION OF A MODTRAN-BASED MODEL AND CALIBRATED AVIRIS SPECTRA

Robert O. Green, Thomas G. Chrien

Jet Propulsion Laboratory
California Institute of Technology
Pasadena, CA 91109
and
University California
Santa Barbara, CA 93106

Biomass burning is an important process on the Earth at the local, regional and global scale. To investigate issue related to biomass during, a range of remotely acquired data were measured as part of the NASA Smoke Cloud Aerosol and Radiation experiment in Brazil, 1995. As part of this experiment, images of calibrated spectral radiance from 400 to 2500 nm at 10 nm intervals were acquired by AVIRIS.

To investigate the expression of biomass fires in AVIRIS spectra, a MODTRAN-based model of the upwelling radiance from a burning fire was developed. This spectral model accounts for four components in the 20 by 20 m AVIRIS spatial resolution element. These are: (1) the atmospheric path radiance, (2) the solar reflected radiance from unburnt vegetation and soil, (3) the apparent temperature and area of a primary fire, and (4) the apparent temperature and area of a secondary fire. A nonlinear least squares spectral fitting algorithms was developed to invert this model for the AVIRIS spectra. The derived biomass burning parameters from this algorithm are presented for AVIRIS spectral images acquired over Cuiaba, Brazil on the 25th of August 1995.

SESSION 1: 9:45

2

CALCULATION OF COOLING RATES FOR ASHOE USING MODTRAN3

S.C. Lee, H.E. Revercomb, R.O. Knuteson, W.L. Smith

University of Wisconsin-Madison CIMSS
1225 W. Dayton Street
Madison, WI 53706

During the Airborne Southern Hemisphere Ozone Experiment (ASHOE), the High-resolution Interferometer Sounder (HIS) measured upwelling spectral radiances from the NASA ER2 flying at 20km. The retrieved temperature and water vapor profiles and a Sub-Arctic Winter model ozone profile have been used in MODTRAN3 to calculate atmospheric fluxes and derive cooling rates. The cooling rates are of interest for their impact on the dynamics of trace gas transport from the poles to lower latitudes. Cooling rates have been calculated for April 13, August 8, August 10, and October 3, 1994. Calculated cooling rates for October 3 using HIS retrieved profiles compare well with results from Clough's Rapid Radiative Transfer Model. Differences between HIS derived cooling rates and those calculated using temperature and water vapor profiles from the NCEP, ECMWF, GASP, and UKMO forecast models will be discussed. Sensitivity studies of the cooling rate to the upper level water vapor profile are described.

SESSION 1: 10:20

COMPARISON OF MEASURED AND CALCULATED TROPICAL ATMOSPHERIC EMISSION

Yong Han, Joseph A. Shaw, James H. Churnside

NOAA Environmental Technology Lab.
325 Broadway
Boulder, CO 80303

and

Shepard A. Clough
AER. Inc.
840 Memorial Drive
Cambridge, MA 02139

The water vapor continuum model used in the current Air Force transmission codes includes a correction based on Infrared spectral radiances measured in Papua New Guinea with an FTIR spectroradiometer. Because that data set included only a small number of clear-sky measurements under questionably clear conditions, further model validation is necessary. New measurements from an FTIR deployed on the NOAA Research Vessel Discoverer in the tropical Pacific provide that opportunity. These measurements agree more closely with the codes having the modified continuum than they do with the old codes. This demonstrates that the modified continuum model is significantly improved, but still requires modification.

SESSION 1: 10:40

EXTRACTION OF SURFACE CHARACTERISTICS FROM LANDSAT TM IMAGERY USING LOWTRAN-7 RADIATION CODE

Kwang-Sun Ryu

Department of Physics
Korea Advanced Institute of Science and Technology
373-1 Yousung Gu
Gusung Dong 400
Taejon, South Korea

Tae-Yong Kwon

Division of Global Environment Information
Systems Engineering Research Institute
P.O. Box 1
Yousung Gu 305-600
Taejon, South Korea

Consideration of the atmospheric propagation of electromagnetic waves is essential in extracting the surface characteristics from satellite-sensed data. The optical properties of the atmosphere can be represented by the transmittance and the path radiance. These radiative variables, which are usually obtained from surface radiation measurements and satellite imagery itself, have been used for estimating the physical quantities of the surface from satellite radiance. In recent, attempts are being made to correct the atmospheric effects using detailed radiative transfer calculations. This study presents a method to estimate the surface albedo and temperature from Landsat TM imagery using the Lowtran-7 radiation model. Among the atmospheric profile data necessary for running the radiation model, temperature, pressure, water vapor amount and ozone concentration are taken from measurements of radiosonde and Dobson spectrometer within the study area, and the concentrations of the other minor gases are from the U.S. Standard Atmosphere. The Landsat TM radiance was simulated with varying the value of input parameters (surface reflectance and surface

temperature) in Lowtran-7. It was shown that there is a strong linearity between the simulated radiance and the value of input parameters. This linear relationship was applies to calculating the surface reflectance and temperature from the radiance measured by Landsat TM sensor instead of using the radiative variables (transmittance and path radiance). Compared with iterating the radiation code to simulate the radiance of each pixel in the image, this method can save much of computing time and efforts. The preliminary results of this method, surface albedo, was compared with those obtained from the conventional methods and with those from the direct measurements by Kotoda (1986). This study was performed as a preliminary study for applying the radiation code to extracting surface characteristics from remotely-sensed imagery. The further validation of these algorithms should be made by preparing the more detailed atmospheric profile data and comparing with the ground truth measurements in the future.

SESSION 1: 11:00

RADIATIVE TRANSFER SIMULATIONS FOR DEVELOPMENT OF EOS MODIS LAND-SURFACE TEMPERATURE ALGORITHMS AND PRODUCTS

Zhengming Wan

ICESS
University of California
Santa Barbara, CA 93106-3060

Based on atmospheric radiative transfer simulations we have developed EOS/MODIS land-surface temperature (LST) algorithms. The molecular band absorption database in the MODTRAN code has been used to build up exponential-sum fitting tables. These tables then are incorporated into an adding/doubling method based multiscattering radiative transfer model for computational efficient simulations in a series of surface temperature and emissivity conditions. A new day/night LST algorithm retrieves simultaneously surface band-averaged emissivities and temperature from day/night data in 7 MODIS TIR bands. These LST algorithms are being validated by in-situ measurements, satellite and aircraft data. The uncertainty in water vapor continuum absorption is of much concern

SESSION 1: 11:20

IMPLICATIONS FOR ATMOSPHERIC STATE SPECIFICATION FROM THE ANALYSIS OF A QUALITY MEASUREMENT EXPERIMENT AS PART OF THE ATMOSPHERIC RADIATION MEASUREMENT PROGRAM

P.D. Brown, S.A. Clough

Atmospheric and Environmental Research, Inc.
840 Memorial Drive
Cambridge, MA 02139

J.C. Liljegren, T.R. Shippert, D.D. Turner

Pacific Northwest Laboratory
Battelle Boulevard
P.O. Box 989
Richland, WA 99352

A Quality Measurement Experiment (QME), which analyzes the spectral residuals between the downwelling longwave radiance measured by the University of Wisconsin Atmospheric Emitted Radiance Interferometer (AERI) and spectral radiance calculated by the Line By Line Radiative Transfer Model (LBLRTM), is ongoing as part of the DoE Atmospheric Radiation Measurement Program (ARM). This experiment is used to assess three critical components: the quality of AERI measurements, the accuracy of LBLRTM calculations, and the ability to define the radiating atmospheric column. Clear sky analyses over the period of April, 1994 through the present have elucidated the challenges in specifying atmospheric state, particularly with respect to water vapor. Comparison between the line by line model and measurements from both the prototype AERI00 as well as the current operational AERI01 show negative residuals in the transparent regions between lines, suggesting limitations in the current ability to characterize water vapor in the atmospheric column. Disagreement among radiosonde, Surface Meteorological Observation Stations (SMOS) and Microwave Radiometer (MWR) measurements also indicate uncertainties in

the definition of the atmospheric state. Further water vapor information regarding line intensities, the water vapor continuum, and abundances are obtained in the study of single water vapor lines in the microwave region. The results of a new QME comparing the MWR measurement of brightness temperature at 23.8 Ghz and 31.4 Ghz with line by line calculations using LBLRTM are also shown.

SESSION 1: 11:40

OBSERVATIONS OF POLAR STRATOSPHERE CLOUDS WITH POAM II

M.D. Fromm
Computational Physics Inc.
2750 Prosperity Avenue
Fairfax, VA 22031

E.P. Shettle, J.S. Hornstein, J.D. Lumpel, R.M. Bevilacqua, K.W. Hoppel

Remote Sensing Division
Code 7227
NRL
Washington, DC 20375-5351

S. Massie
NCAR
Boulder, CO 80307

Observations of Polar Stratospheric Clouds (PSCs) with Polar Ozone and Aerosol Measurement (POAM II) solar occultation instrument will be described. POAM II has been measuring the vertical distribution of aerosols, clouds, ozone, as well as several other atmospheric species since October 1993. The cloud detection algorithm used to identify PSCs from the POAM II measurements will be described along with a presentation of some of the first two years of measurements, focusing on results from the southern hemisphere. The frequency of PSC occurrence builds up during the Antarctic winter reaching a peak of about 3/4 of all POAM II measurements during September include a PSC. There is a strong longitudinal variation in the cloud frequency, with a broad minimum centered near the international dateline (180°) and a broad maximum centered about (320°) W, where the PSC frequency is about twice that near the minimum.

SESSION 1: 12:00

FASCODE FOR THE ENVIRONMENT (FASE)

H.E. Snell

Atmospheric and Environmental Research, Inc.
840 Memorial Dr.
Cambridge, MA 02139

G.P. Anderson, J.H. Chetwynd, S. Miller

Geophysics Directorate
Phillips Laboratory
Hanscom AFB, MA 01731-3010

The Optical Physics Division of the Phillips Laboratory with support from the DoE Atmospheric Radiation Measurement (ARM) Program is developing a state-of-the-art line-by-line atmospheric radiative transfer model as the successor to FASCODE. The goal of this project is to create a computationally efficient model which contains the most up-to-date physics. The new model, known as FASCODE for the Environment, or "FASE", combines the best features of FASCODE and LBLRTM, the DoE's standard radiative transfer model. Upgrades to FASE include improvement of the cloud and aerosol descriptors, based on changes made to MODTRAN, and the capability of incorporating the new heavy molecule absorption cross-section data found on HITRAN96, which is of slightly different format from the previous HITRAN cross-section data. This paper addresses changes which have been made to FASCODE and LBLRTM to create FASE, and gives an overview of the new capabilities and recent model validations.

SESSION 2: 13:30

RRTM AND ITS VALIDATION

Eli J. Mlawer, Shepard A. Clough

Atmospheric and Environmental Research, Inc.
840 Memorial Drive
Cambridge, MA 02139

RRTM is a rapid and accurate radiative transfer model that has been developed as part of the DOE Atmospheric Radiation Measurement (ARM) Program. The model, which uses the correlated-k method, calculates thermal clear sky fluxes and cooling rates for an arbitrary atmosphere and is currently being extended to the solar spectral regime. RRTM has been extensively validated against the line-by-line model LBLRTM and has an accuracy over the spectral range 10-3000 cm-1 of 1.0 W/m2 in net flux at all altitudes, 0.05 K/day for cooling rates in the lower atmosphere, and 0.75 K/day for cooling rates in the upper atmosphere. In addition, RRTM has been successfully validated in each of its component spectral bands in the thermal and solar regions. It is essential in evaluating the accuracy of a model to consider the sensitivity of its calculated fluxes to variations in all important physical quantities. Many of these incremental validations have been performed on RRTM and results will be presented for the doubling of CO_2 from current levels and for the addition of key CFC's to a standard atmospheric profile.

SESSION 2: 13:50

HIGH SPECTRAL RESOLUTION SOLAR RADIATIVE TRANSFER: AN APPROXIMATE METHOD FOR ABSORBING AND SCATTERING ATMOSPHERES

P. Dubuisson

Laboratoire d'Optique Atmospherique
Universite du Littoral
Station Marine de Wimereux
62930 Wimereux
France

J.C. Buriez, Y. Fouquart

Laboratoire d'Optique Atmospherique
Universite des Sciences et Technologies de Lille
59655 Villeneuve d'Ascq Cedex
France

We have developed a fast, accurate method for approximating high spectral resolution satellite radiances, in the shortwave region. The method applies to atmospheres including clouds and aerosols. In this method, interactions between molecular absorption and multiple scattering are treated using an extension of the Scaling Approximation. The method is first tested in the simple case of an isolated absorption line and then in the case of real spectra including numerous absorption lines. The atmospheric models used in the simulation correspond to conditions including clouds and aerosols. Both cases of absorption by water vapor and oxygen have been tested. The maximum error in the monochromatic radiances is less than 10% of the radiance without absorption. The maximum error decreases to 1% for a simulated resolution of 1 cm^{-1} and 0.1% for 5 cm^{-1}.

SESSION 2: 14:10

RETRIEVAL ALGORITHM TO DEAL WITH A NON-LINEAR TERM

Shinji Kadokura, Hirokazu Kobayashi, Akiro Shimota

Central Research Institute of the Electric Power Industry
Iwadokita, Komea, Tokyo, Japan

Since High-Resolution infrared spectroscopy is an effective method for probing atmospheric parameters, such as temperature and/or greenhouse gas concentrations, it is applied to IMG, the Interferometric Monitor for Greenhouse gases carried on an Earth observing satellite. The atmospheric parameters are retrieved by inverse analysis of the remote sensing data. The inversion algorithm previously developed has been improved to reduce the error which originates from non-linear effects. First, the non-linear term is added to a noise matrix so that the channels strongly influenced by non-linear errors have less effect on the retrieved values. Second, the channel selection algorithm, developed to reduce the calculation time for the forward analysis has been improved. These improvements have been applied to the simulation of IMG data analysis and achieved good results

ABSOLUTE CALIBRATION OF INFRARED STELLER FLUXES

R.A. Bell, K. Scaldeferri

Department of Astronomy
University of Maryland
College Park, MD 20742

The extinction of starlight is non-linear with airmass in the infrared, owing to strong water vapour lines in the spectrum of the earth's atmosphere. Such lines occur in the pass bands which have been used to determine the absolute fluxes of Vega, found by comparing the star to a standard furnace. The difference between these fluxes and the values obtained from model stellar photospheres and the angular diameter of the star may be due to inadequate treatment of the extinction. The HITRAN 92 database and the SAAG3 program (Stevenson 1994) have been used to study this problem.

SESSION 2: 14:50

INTERCOMPARISON OF INFRARED OPTICAL CONSTANTS OF VARIOUS AEROSOL SUBSTANCES

W.G. Egan, J. Joseph Jr.

Natural Sciences Department
York College/City University of New York
Jamaica, NY 11451

The absorption and refractive portions of the infrared complex index of refraction of various aerosol sands and soils were determined in the wavelength range 2.5 to 50 μm.   Measurements of the reflection and transmission of KBr pellet samples were analyzed using the Kubelka-Munk radiative transfer theory to separate the scattering from the absorption. Samples consisted of aerosol particles, Sahara and Sinai Desert sands, coral and silica sands, and farm soil. The data are presented graphically for easy comparison. The variations between the indices of the samples influence atmospheric radiative transfer processes in different regions of the globe.

SESSION 3: 15:30

ESTIMATION OF AIRBORNE PARTICULATES SIZE DISTRIBUTION ACCORDING TO WEATHER CONDITIONS AND IINFLUENCE ON IMAGING SYSTEMS

I. Dror, N.S. Kopeika

Department of Electrical and Computer Engineering
Ben Gurion University of the Negev
P.O. Box 653
Beer Sheva 84105
Israel

In this study the aerosol particulate size distribution curve is estimated according to simple meteorological parameters. The statistical models presented here show very strong relationships between current weather conditions and quantity and size distribution of aerosols. The model is based on 3 years of extensive aerosol size distribution measurements using a particulate optical counter. Comparisons between measurements of the atmospheric extinction coefficient and those calculated by the MODTRAN software show large deviation between the computerized models and our measurements. The MODTRAN atmospheric models give excellent results regarding the influence of the molecular particulates on the scattering and absorption properties of the atmosphere, satisfactory results for the fine dust particulates, but poor results regarding the influence of large dust aerosols, particularly in desert environment. This research presents also comparison between the MODTRAN aerosols models and measurements of the aerosol extinction coefficient in semi-arid, rural, and maritime environments. The comparison shows that MODTRAN models have problems in the prediction of the atmospheric extinction especially when the coarse mode of the particulate size distribution is dominant. Unlike MODTRAN, the new model presented here yields excellent results for predictions coarse mode aerosol size distribution.

SESSION 3: 15:50

NUMERICAL AND ANALYTICAL SOLUTIONS OF THE SMALL PARTICLE AMPLITUDE IN THE NAVY AEROSOL MODEL

Terry E. Battalino

Geophysics Branch, Code 521420E
Naval Air Warfare Center Weapons Division
Point Mugu, CA 93042-5001

The Navy Aerosol Model (NAM) statistically models maritime aerosol particle size distributions as the sum of three independent log-normal functions, each of which are characterized by amplitudes that depend upon meteorological input parameters. The first NAM amplitude (A_1) adjusts the magnitude of the particle number density about a modal radius of 0.03 μm, and is determined by the input of an air mass parameter that can be selected from three methods: (1) radon gas concentration, (2) air trajectory, and (3) subjective estimate. A new methodology utilizing measurements of condensation nuclei is introduced in this paper. The technique is mathematically formulated by integrating over the NAM spectrum and solving for the A_1 term as a function of the CN count and meteorological input parameters. Numerical solutions for the CN count and A_1 amplitude are provided for the possible range of meteorological input variables. CN threshold levels are identified for equivalent radon input parameters, and an analytical expression involving error functions is derived for the A_1 term.

SESSION 3: 16:10

THERMAL RADIATIVE EXCHANGE AT STRATUS CLOUD TOPS

James W. Telford

Atmospheric Concepts Inc.
1975 Fallen Leaf Court
Reno, NV 89500-3559

The continued growth and dissipation of long lived marine stratus clouds is thought to be strongly influenced by thermal radiation transfer. However the actual interactions are more complex than at first conjectured and have the effect of mixing dry overlying air into the clouds rather than adding moisture from the sea. The moisture is added from below by a moisture driven convective process involving latent heat but no permanent clouds.

Detailed calculations using analytic integration across layers, and algebraic expressions to eliminate the canceling terms between layers, allows the vertical resolution to be small enough to follow the heat transfer at wavelengths where the 1/e absorption distance is less than a centimeter or so. For actual inversions at cloud top, often of 10 C over 10 m or so, this transfer cools the warm clear air above and heats the cloud top enough to dominate the heat loss up through the radiative atmospheric window. Satellite observations confirm that the clouds do not spread to fill clear patches at night, and do not enlarge them after dawn.

SESSION 3: 16:30

A METHOD FOR RAPID GENERATION OF CLOUD PROPERTIES

Eric Schmidt, Mark Raffensberger

TASC
55 Walkers Brook Dr.
Reading, MA 01867

Thomas Caudill

USAF Phillips Laboratory
Hanscom AFB, MA 01731

We have developed a first-generation method to rapidly generate radiometrically accurate visible and infrared properties of water clouds. The heart of the Fast-Map approach is the construction of a set of 2-D tables relating water content to particle size, optical properties, radiative properties, and graphical quantities, such as transparency, absorptivity, and diffusivity. The conversion process is highly flexible, computationally efficient and fast. The Fast-Map method includes: (1) a spatially variable particle size distribution, $N9R,Z)$, where r is the particle radius and z is the height above the cloud base, (2) a translation from water content and $n(r,z)$ values into wavelength dependent optical properties, such as extinction optical depth (σ) and single-scatter albedo (ω_0), (3) tables of radiative properties constructed using a radiative transfer model code and/or parameterizations, and (4) a mapping between radiative properties and graphical quantities. Cumuliform and stratiform cloud properties are presented.

SESSION 3: 16:50

BISTATIC LIDAR MEASUREMENTS OF LOWER TROPOSPHERIC PARTICLE SIZE DISTRIBUTION AND OPTICAL EXTINCTION

T.D. Stevens, C.R. Philbrick

The Pennsylvania State University
PSU/ARL Lidar Laboratory
University Park, PA 16802

A study has been conducted to investigate the application of a unique bistatic lidar receiver to remotely determine properties of lower tropospheric aerosols, particularly optical extinction, median radius and size distribution width. The bistatic remote receiver uses a linear photodiode array to image the radiation scattered from any high power CW or pulsed laser system. By observing the angular scattering along a horizontal path, additional information contained in the scattering angle phase function can be obtained.

The first studies using the bistatic lidar were conducted in a marine environment during the Wallops CASE I (Coastal Aerosol Scattering Experiment) program. The measurements were made under sufficiently high relative humidities that it is reasonable to use a spherical model to describe the scatterers. A trimodal lognormal distribution of aerosols was observed on September 14, 1995 to increase in size during a period of several hours when the relative humidity remained constant at 92% and the temperature decreased from 23 to 22 deg. C.

SESSION 3: 17:10

"ENVIRONMENTAL REPRESENTATIONS AND EFFECTS AND AN UPDATE ON THE MOSART CODE"

William M. Cornette

Technical Advisor for Defense Modeling and Simulation
Terrain Modeling Project Office
Defense Mapping Agency (ATSS/Stop A-13)
8613 Lee Highway
Fairfax, VA 22031-2137

Under Secretary of Defense for Acquisition and Techniology (USD(A&T)) has designated three modeling and simulation (M&S) executive agents (EAs) for simulated environments (i.e., terrain, ocean, and aerospace), which are directed by the Defense Modeling and Simulation Office (DMSO) for the Director Defense Research and Engineering (DDR&E) and USD(A&T). A brief overview of each M&S Environmental EA will be provided with a discussion of the various programs (i.e., Requirements, Standards,and Research & Development). Also, an update on the MOSART code will be provided regarding its current status, availability, and potential future growth (e.g., upgrades in the terrain temperature module, the terrain data bases, 3D atmospheres). Some information on future terrain material representations will be given.

SESSION 4: 8:30

IMPROVING MODTRAN'S MOLECULAR TRANSMITTANCE ALGORITHM

Steven Adler-Golden, Prabhat Acharya, Alexander Berk,
Lawrence Bernstein

Spectral Sciences, Inc
99 S. Bedford #7
Burlington, MA 01803

Gail Anderson, James Chetwynd

Air Force Phillips Laboratory
29 Randolph Road
Hanscom AFB, MA 01731

Improved accuracy in transmittance and radiance spectra calculated by MODTRAN is desired for remote sensing of atmospheric species and temperatures. In this study, errors associated with the various molecular transmittance approximations in MODTRAN were characterized. Issues addressed include (1) the treatment of the line tails, (2) line position correlation, and (3) the line strength distribution and its effect on the curve of growth, focusing on ozone. Several improvements to the transmittance algorithm were developed and incorporated in beta test code. Comparisons were made between MODTRAN3, the test code, and FASCODE for representative remote-sensing cases. The test code provides noticeable improvements over MODTRAN3, although with both codes the agreement with FASCODE is generally very good (within several percent in transmittance).

SESSION 4: 9:00

MODTRAN3.5

A. Berk, L. S. Bernstein, P. K. Acharya, D. C. Robertson

Spectral Sciences, Inc.,
99 S. Bedford #7
Burlington, MA 01803

G. P. Anderson ,J. H. Chetwynd

Geophysics Directorate,
Phillips Laboratory, Hanscom AFB, MA 01731

J. J. Vail
Mei Technology Corp.,
1050 Waltham Street
Lexington, MA 02173

MODTRAN3.5 is now available from the Phillips Laboratory ftp site. The current model is still officially a beta-test version and should be run in parallel with the latest version of MODTRAN3. MODTRAN3.5 affords the users many new options and features. These include more flexible cloud inputs with an option to model mixed phase clouds, HITRAN96 based band model parameters at an expanded temperature grid, calculation of multiple scattering vertical fluxes at H2 (the path final altitude), a finer default altitude grid including the option to input negative altitudes, and a new plot (x vs y) output file. Upgrades will be described, and validation calculations presented.

SESSION 4: 9:20

ADDITION OF A CORRELATED-K CAPABILITY TO MODTRAN

L.S. Bernstein, A. Berk, D.C. Robertson, P.K. Acharya

Spectral Sciences, Inc.
99 S. Bedford Street #7
Burlington, MA 01803-5269

G.P. Anderson, J.H. Chetwynd

Geophysics Directorate
Phillips Laboratory
29 Randolph Road
Hanscom AFB, MA 01731-3010

This presentation describes the addition of a Correlated-k (CK) capability to the MODTRAN atmospheric transmission/radiance computer code. Addition of a CK capability to MODTRAN provides an accurate and fast means for evaluation of the effects of clouds and heavy aerosol loading on retrievals (both surface properties and species concentration profiles) and on atmospheric radiative heating/cooling calculation. These radiative transfer computations require coupling the effects of gaseous molecular absorption due primarily to water vapor, carbon dioxide, and ozone, with particulate multiple scattering due to volcanic aerosols, ice crystals, and water droplets. The molecular absorption band model used in MODTRAN is not suitable for interfacing with standard multiple scattering algorithms. This is because the scattering models require a <u>monochromatic</u> representation of the molecular transmission (i.e., Beer's law), whereas molecular band models which represent the transmission for a <u>finite spectral interval</u> do not follow Beer's law. In order to adapt a band model approach for use in scattering calculations it is necessary to express the band model transmission function in terms of a weighted sum of Beer's law exponential terms. Thus, one of the fundamental problems addressed in this work was the development of a method for determining the weighting factors and monochromatic absorption coefficients corresponding to the MODTRAN band model.

The k-distribution g(K) is determined using a Monte-Carlo line-by-line simulation which is constrained by the same physical assumptions (i.e., uncorrelated equal-strength lines) used to derive the band model parameters. A compact database representation of the g(K)'s for the atmospheric molecules is developed and incorporated into MODTRAN for real-time access during a radiative transfer calculation. Sample calculations are presented which demonstrate the importance of using the CK approach for multiple scattering calculations. Comparisons are made to recent down looking near-infrared measurements of solar scattering off an opaque cumulus cloud.

SESSION 4: 9:40

ATMOSPHERIC EFFECTS INTERPOLATION ALGORITHM

Glenn J. Higgins, P. Daniel Hestand

TASC
55 Walkers Brook Drive
Reading, MA 01867

An interpolation algorithm has been developed to efficiently estimate atmospheric path transmission and radiance to support infrared scene visualization activities at PL/GPAA. The method uses MODTRAN to compute atmospheric path transmission and radiance for user-selected scenario parameters and for a limited number of geometries, dependent on the scenario parameters. Scaling laws and interpolation provide estimates of these quantities for other desired geometries corresponding to the locations of scene elements, yielding a significant time savings relative to executing MODTRAN for every desired geometry. Estimates of interpolation error for quantities as well as for apparent temperature are provided.

SESSION 4: 10:00

TERRESTRIAL REFRACTION MODEL

Michael E. Thomas, Richard I. Joseph

Applied Physics Laboratory/Johns Hopkins University
Laurel, MD 20723

A model for the atmospheric ray path is constructed from a geometrical optics solution of the eikonal equation. The optical ray path is developed in the earth coordinate system for the lower atmosphere. An exact solution is obtained for a vertical refractive index profile that is quadratic in the altitude. From this development formulae for the location of the optical horizon are obtained. A general solution is also obtained for any vertical refractive index profile.

SESSION 4: 10:40

THIS PAGE BLANK

AN EXPERIMENT IN COMPUTING VIA THE WEB

Dave Sowle

Mission Research Corporation
P.O. Box 719
Santa Barbara, CA 93102

Under the auspices of the ARM-UAV program, MRC is making available climate research community standard algorithms for use over the Web. The idea is that the user brings up our Web page at: http://arm.mrcsb.com and chooses from available algorithms. Using a GUI, the user can submit a calculation and get results, all via the Web. Advantages are hardware independence and no knowledge of code details required for operation. The only algorithms now available are the SBDART code (Stamnes' DISORT transfer code plus LOWTRAN added by UCSB), and a Nakajima/King cloud properties algorithm. Suggestions for other algorithms are sought.

SESSION 4: 11:20

THE STATUS OF PLEXUS:
PHILLIPS LABORATORY EXPERT UNIFIED SOFTWARE

Dale Sinclair

Geophysics Directorate,
Phillips Laboratory,USAF
29 Randolph Road
Hanscom AFB, MA 01731

PLEXUS is an ambitious project to provide both interactive and non-interactive interfaces to a suite of Geophysics models covering all spatial regimes (ground to space), spectral regimes (ultraviolet to radio frequency), and spectral resolutions (broad-band to laser). The PLEXUS core is an Expert System guaranteeing accuracy and ease of access, and permitting a range of user expertise from pre-phase zero conceptual design, through engineering optimization, field limits, and war gaming. PLEXUS addresses variability issues with modern default atmospheric vertical profiles which provide geographical, seasonal, and time dependency. We will list present status, how to obtain PLEXUS, and future deliverables and design goals.

SESSION 4: 11:40

A COMPUTER CODING ARCHITECTURE

Dr. Frank O. Clark

Geophysics Directorate,
Phillips Laboratory, USAF
29 Randolph Road
Hanscom AFB, MA 01731

We are currently designing a new machine independent, distributed, multithreaded, modular computer software architecture for our PLEXUS suite of codes. The design goals address Department of Defense user requirements in several arenas. These design goals will be useful in many Department of Defense software projects.

SESSION 4: 12:00

WHY DO DRAMATIC LOCALIZED (RADIATING) HEATING EVENTS OCCUR IN THE MESOSPHERE?

E.M. Dewan, R.H. Picard

Geophysics Directorate,
Phillips Laboratory, USAF
29 Randolph Road
Hanscom AFB, MA 01731

T.F. Tuan, T.Y. Huang

Physics Department
University of Cincinnati
Cincinnati, OH 45221

Forecasting radiance structure with sharp gradients in the mesosphere is of great importance to the Air Force. These structures can be caused by the sharp increases in temperature (e.g. 40°K) over a small height region (2-3km) of the type observed by lidar observations during the ALOHA 93 Campaign. The purpose of this presentation is to give a physical explanation for such events, raising the possibility of forecasting them. The mechanism involves gravity waves depositing their horizontal momentum in a narrow "critical layer". This, when continued over time, can accelerate a small portion of the mean wind to the point where critical shear is exceeded. It will be shown that the resulting turbulence can cause the observed heating in the very narrow layer. The resulting radiative effects will be presented in another paper at this meeting.

SESSION 5: 13:30

NON-LTE INFRARED RADIANCE FROM
LOCALIZED STRUCTURES

R.H. Picard, J.R. Winick, E.M. Dewan

Phillips Laboratory
Geophysics Directorate (GPOS)
29 Randolp Road
Hanscom AFB, MA 01731

P.P. Wintersteiner

ARCON Corporation
Waltham, MA 02154

U.B. Makhlouf

Stewart Radiance Laboratory
Bedford, MA 01730

Extremes of non-LTE radiance and radiance gradients well above average values are often associated with spatially localized structures. Consequently, these structures can be among the most stressing background features for surveillance systems. Examples of such localized structures include inversion layers (vertically localized and fronts (horizontally localized). We give examples of such structures seen in the upper atmosphere during the ALOHA-93 Campaign and show that they are associated with visible radiance extremes. We also calculate the infrared radiance seen in the earthlimb resulting from upper-atmospheric temperature inversion layers and show that large changes of infrared radiance and gradients are possible, especially at 4.3 μm.

SESSION 5: 13:50

"SIG: THE SHARC IMAGE GENERATOR - OVERVIEW OF A NEW NON-STATIONARY STOCHASTIC SCENE GENERATOR FOR SHARC"

James H. Brown

Phillips Laboratory/GPOS
29 Randolph Road
Hanscom AFB, MA 01731

Neil Grossbard

Boston College
Institute for Space Research
Chestnut Hill, MA 02167

A new integrated user-friendly code will soon be available that provides sensor specific IR synthetic images. The non-stationary methods use SHARC 4 output information and can generate scenes for limb, nadir, and cloud-free off-nadir viewing geometries. A brief description of the various 3-D and 2-D methods will be presented. The user interface will be described and the product will be illustrated with several false color structure synthetic images.

SESSION 5: 14:10

15 MICRON NON-LTE COOLING RATES FROM CIRRIS-1A

P.P. Wintersteiner

ARCON Corporation
Waltham, MA 02154

J.O. Wise, R.H. Picard, J.R. Winick

Phillips Laboratory/GPOS
29 Randolph Road
Hanscom AFB, MA 01731

R.G. Roble

National Center for Atmospheric Research
Box 3000
Boulder, CO 80302

Using the ARC non-LTE radiation code, the NCAR TIME-GCM general circulation model, and the CIRRIS-1A earthlimb data, we are able to explore the variability of 15 μm cooling rates in the mesosphere and lower thermosphere. Starting with the atmospheric conditions predicted by the NCAR TIME-GCM, we calculate the long-wave infrared radiance and the associated atmospheric cooling using the ARC line-by-line radiative transfer codes. By comparing the modeled limb radiance with the CIRRIS radiometer and interferometer data for different conditions, we show that the peak cooling rates in the lower thermosphere vary by more than a factor of two and in some cases may exceed 200 K/day. We also compare the derived cooling rates with those used in the TIME-GCM.

SESSION 5: 14:30

QUASICLASSICAL TRAJECTORY STUDY OF THE N(^{4}S)+NO(X^{2}Π)→N$_2$(X^{1}Σ^+_g)+O(^{3}P) REACTION RATE CONSTANT: IMPLICATIONS FOR THERMOSPHERIC NO FORMATION

J.W. Duff
Spectral Sciences, Inc.
99 S. Bedford Street
Burlington, MA

R.D. Sharma
Phillips Laboratory/Geophysics Directorate
Optical Environment Division (GPOS)
29 Randolph Road
Hanscom AFB, MA 01731-3010

A. Dalgarno
Harvard-Smithsonian Center for Astrophysics
Cambridge, MA

J.L. Fox
Institute for Terrestrial and Planetary Atmospheres
and Marine Sciences Research Center
State University of New York
Stony Brook, NY

The reaction of N atoms with NO is probably the most important loss process for odd nitrogen in the Terrestrial and Martian thermospheres. Recent analyses of NO density [Fox, 1994; Siskind and Rusch, 1992] suggest a temperature dependence for this rate coefficient in the temperature range $100 \leq T \leq 1000$ K to reconcile model predictions with rocket observations, contrary to the JPL-recommended temperature independent rate constant. The present quasiclassical trajectory study extends previous calculations [Gilibert et al., 1992) of the rate constant down to 100 K. In the absence of a detailed treatment of spin-orbit coupling, the QCT results are in excellent agreement with the experiments of Lee et al. [1978], Michael and Lim [1992] and JPL recommended rate

constant, indicating only a slight temperature dependence over the temperature range of 100 to 1000 K. A consideration of the uncertainty in the rate constant introduced by the neglect of spin-orbit coupling (a factor of 2-4) may yield a rate constant within a factor of 5 of the value suggested by Fox at 100 K. Furthermore, more elaborate calculations to help understand the correlation of the $N+NO^3A$" ground state potential energy surfaces with the NO $\Omega=1/2$ and $\Omega=3/2$ spin-orbit states may elucidate the possible role of N+NO in the NO spin-orbit distributions, such as those observed by CIRRIS 1A [Lipson et al.,1994;Sharma et al.,1996]. Finally, the present study does not support the temperature dependent rate constant derived by Siskind and Rusch for T > 700 K and thus the inconsistency between NO observations and current NO models in the middle and upper thermosphere remains unresolved.

SESSION 5: 15:10

SENSITIVITY TRADE OF VARIOUS LASER WAVELENGTHS TO A MARTIME ENVIRONMENT

Larrene K. Harada

W.J. Schafer Associates
1901 N. Fort Myere Drive
Suite 800
Arlington, VA 22209

A high energy laser device to be mounted on a ship for point defense is under consideration. A sensitivity trade of various laser wavelengths has been performed to study the range of meteorological conditions found in the maritime environment and their effect on propagation. The trade is to determine the laser wavelength with the most favorable propagation under all conditions of interest. Since a FEL is one of the devices being considered, we have also done a search around the atmospheric windows. FASCODE calculations were performed to determine the regions of lowest absorption. Shown is also a comparison of the relative transmissions calculated using LOWTRAN, MODTRAN and FASCODE in the regions of 1.06 microns, 1.315, 1.6, 2.2, and MIRACL wavelengths.

SESSION 6: 15:50

LARC (Laser Radar Code) ATMOSPHERIC TRANSMISSION LOOK-UP TABLE

Dima Seliverstov, M.J. Yoder

MITRE Corporation
202 Burlington Road
Bedford, MA 01730

In this paper we describe a simple method for coupling FASCODE3P results to other practical applied codes. This enables these applied codes to run faster and use less powerful computers. In particular our application is the MITRE Laser Radar Code (LARC). LARC calculates the probability of detection for arbitrary sensor locations and target trajectories and includes the relevant physical effects. The laser radar range equation is solved for a real curved-earth geometry and includes free air induced turbulent beam spreading effects. LARC includes target fading and atmospheric scintillation. LARC computes the detection statistics for both pulsed and Continuous Wave (CW) laser systems.

The LARC Code is decoupled from the FASCODE3P program by use of an atmospheric extinction coefficient lookup table. This method uses FASCODE3P to compute the extinction coefficients as a function of laser wavelength, altitude and atmospheric model. Using the extinction coefficients, a curved earth ray tracing routine computes the corresponding atmospheric transmission much faster then using the directly coupled FASCODE3P code. This paper describes the calculations involved and compares the results to directly calculated FASCODE3P transmission.

SESSION 6: 16:10

LIDAR MEASUREMENTS TO DESCRIBE THE ELECTRO-OPTICAL ENVIRONMENT AND ATMOSPHERIC PROPERTIES

C. Russel Philbrick, Franz Balsiger, Tim D. Stevens

The Pennsylvania State University
PSU/ARL Remote Sensing Department
P.O. Box 30
State College, PA 16804

Scattering of visible, ultraviolet and infrared radiation by atmospheric particles has a major impact on commercial air traffic and on many military systems. It has become critically important, with many modern systems, that the electro-optical environment be properly characterized.

Most of the past applications of lidar to describe the electro-optical environment have failed to provide satisfactory results because the techniques have generally focused on measurement of the backscattered radiation at the transmitted wavelength. We have shown that molecular scattering from rotational and vibrational Raman backscatter can be used to directly determine the extinction profile through optical scattering regions containing aerosols and cloud layers.

SESSION 6: 16:30

THIS PAGE BLANK

ANALYSIS OF LONG TERM TEMPERATURE TRENDS AT THE SOUTH POLE USING MODTRAN3

W.G. Egan

Natural Sciences Department
York College
City University of New York
Jamaica, NY 11451

A.W. Hogan

U.S. Army Cold Regions Research and Engineeriing Laboratory
Hanover, NH 03755-1290

In published long term mean surface temperature trends at the south Pole 1958-1983, there is no annual variation; however, the Austral summer shows a temperature increase and the winter shows a decrease up to 1976. The variations are analyzed in terms of effects resulting from annual changes in water vapor, carbon dioxide, methane and ozone using selected input atmospheric profiles available in MODTRAN3. The question of a possible increase in water vapor cuased by the attachment to carbon dioxide is examined. It has been hypoethesized that the frequent storms in the northern portion of the eastern hemisphere are caused by increased atmospheric water vapor caused by increasing carbon dioxide.

SESSION 6: 17:10

(HAWKS96) THE HITRAN ATMOSPHERIC WORKSTATION

L. S. Rothman and G. Anderson, AF Geophysics Directorate, Hanscom AFB, MA
J. Schroeder and A. McCann, Ontar Corp, North Andover, MA
R.R. Gamache, U. Mass Lowell, Lowell, MA
R.B. Wattson, Stewart Radiance Lab, Utah State U., Bedford, MA
J.-M. Flaud, A. Perrin, V. Dana, and J.-Y. Mandin, U. P.et M. Curie, Paris, FRANCE
A. Goldman, U. Denver, Denver, CO
P. Varanasi, SUNY Stony Brook, NY
K. Yoshino, Harvard-Smithsonian Center for Astrophysics, Cambridge, MA

A new edition of the HITRAN molecular spectroscopic database has been released this year. It is included in a compilation called HAWKS (HITRAN Atmospheric Workstation). HAWKS represents more fully a "matter" database. Besides an updated HITRAN high-resolution molecular database of about one million transitions, there are files of aerosol indices of refraction, UV line-by-line and cross-section parameters, supplemental files of gases such as ionic species and ozone parameters suitable for atmospheric non-local thermodynamic equilibrium conditions, extensive IR cross-sections now at different pressures and temperatures, and molecular parameters suitable for modeling high-temperature radiance. In addition there is a moderate-resolution band-model code, MODTRAN3.

There is also vastly improved software handling of the data in both WINDOWS and UNIX platforms, such as more sophisticated selection filters, plotting capabilities, pointers to significant references, and documentation. HAWKS is being made available on CD-ROM. This presentation will discuss some of the interesting features that are present on the compilation as well as give some interesting examples of new capabilities.

SESSION 7: 8:30

OZONE, NITROGEN DIOXIDE, AND NITRIC ACID FOR THE HITRAN DATABASE

Jean-Marie Flaud

Laboratoire de Physique Moléculaire et Applications

Université Pierre et Marie Curie

Paris

FRANCE

Since the previous issue of the HITRAN database, a number of studies have been devoted to the improvement of the spectral parameters of molecules of atmospheric interest. This presentation is an overview of the recent results concerning the ozone, the nitrogen dioxide, and the nitric acid molecules with estimates given regarding their accuracy. Also tentative recommendations for related future efforts will be made.

SESSION 7: 9:00

THE HOT BANDS OF METHANE BETWEEN 5 AND 10 μm

O. Ouardi, J. C. Hilico, M. Loete
Laboratoire de Physique de l'Université de Bourgogne, France

L. R. Brown
Jet Propulsion Laboratory, California Institute of Technology
4800 Oak Grove Drive, Pasadena, CA 91109, USA

Experimental line intensities of 1727 transitions arising from nine hot bands between 900 and 2000 cm^{-1} have been measured using the Fourier transform spectrometer at Kitt Peak. The observed hot bands that arise between levels of the five-band pentad near 3.3 μm and the ν_4 and ν_2 dyad are: $\nu_3 - \nu_2$, $\nu_1 - \nu_2$, $\nu_3 - \nu_4$, $\nu_1 - \nu_4$, $2\nu_4 - \nu_4$, $2\nu_4 - \nu_2$, $2\nu_2 - \nu_4$, $\nu_2 + \nu_4 - \nu_4$ and $\nu_2 + \nu_4 - \nu_2$. These data have been combined with 1206 previously-analyzed intensities of the dyad (Brown et al., *J. Mol. Spectrosc.* **133**, 272 (1989)) and fitted to first and second order using the effective dipole moment expansion in the polyad scheme. In second order, the dyad lines are fitted with an rms of 3% and the hot band lines with an rms of 6.5%.

The dyad parameters are essentially the same as the 1996 database, but the new hot band calculation greatly improves the 1996 values.

SESSION 7: 9:30

SPECTROSCOPIC DATABASE FOR REMOTE SENSING OF CFCs

Prasad Varanasi
Institute for Terrestrial and Planetary Atmospheres
The University at Stony Brook
Stony Brook, NY

Remote sensing of and global warming by the chlorofluorocarbons and their alternates in the atmosphere will be discussed. The recent revisions in the HITRAN database reflecting the growing interest in the infrared cross-sections of these human-made molecules will be reviewed along with a presentation of the laboratory and semi-empirical techniques. The application of the spectroscopic database in ADEOS and other atmospheric remote-sensing projects will be emphasized.

SESSION 7: 9:40

HIGH RESOLUTION CROSS SECTION MEASUREMENTS OF NO_2

W.H. Parkinson, J.R. Esmond, and K. Yoshino
Harvard-Smithsonian Center for Astrophysics
60 Garden Street
Cambridge, MA 02138

Cross section measurements of NO_2 at 295K have been obtained in the wavelength region 360 nm to 470 nm. We used the 6.65-m vacuum spectrometer with a 1200 l/mm grating, which gives 1.24 Å/mm dispersion. A tungsten lamp, operating at 12 V ac, was used as the background source. Data were taken every 0.118 sec for every 15 mÅ (0.074 cm-1). In each scan range, we ran an Fe hollow cathode spectrum for wavelength calibration. The accuracy of wavelenth position was 0.02 Å. The pressures of NO_2 were selected as 0.5, 1.0, 1.5, 2.0, 2.5, and 3.0 Torr. The cross section measurements at the beginning wavelengths show a slight but definite negative pressure dependency, because of dimer formation. As a result, we could estimate the range of dimer density of 0.5% at 0.5 Torr to 2.5% at 3 Torr. After the column density of NO_2 was calibrated, we obtained cross sections of NO_2 for all runs at all pressures. We will present the cross section values of NO_2, and compare them with previous results.

SESSION 7: 10:20

RADIATIVE FORCING CALCULATIONS FOR CH_3Cl AND CH_3Br

Allen S. Grossman, Keith E. Grant
Global Climate Research Division, L-262
Lawrence Livermore National Laboratory, P.O. Box 808
Livermore, CA 94551

William E. Blass
Department of Physics and Astronomy
University of Tennessee
Knoxville, TN 37996-1200

Donald J. Wuebbles
Department of Atmospheric Sciences
University of Illinois
Urbana, IL 61801

Methyl chloride, CH_3Cl, and methyl bromide, CH_3Br, are particularly important in the global atmosphere as major natural sources of chlorine and bromine to the stratosphere. We will estimate the radiative forcing and Global Warming Potentials (GWPs) of CH_3Cl and CH_3Br. Our calculations use an infrared radiative transfer model based on the correlated k-distribution algorithm. Radiative forcing values of 0.0046 W/m^2 per ppbv for CH_3Cl in the troposphere and 0.0049 W/m^2 per ppbv for CH_3Br in thre troposphere were obtained. The radiative forcing values are about 2 percent of the forcing of CFC-11 and about 270 times the forcing of CO_2, on a per molecule basis. The Global Warming Potentials of CH_3Cl and CH_3Br were determined giving GWPs of about 8 for CH_3Cl and about 4 for CH_3Br for a time integration of 100 years ($CO_2 = 1$). The results indicate that while CH_3Cl and CH_3Br have direct GWPs similar to that of CH_4, the current emission rates are too low to meaningfully contribute to atmospheric greenhouse heating effects.

SESSION 7: 10:40

SIMPLE MODELING OF THE TEMPERATURE DEPENDENCE OF THE FIRST-ORDER LINE-MIXING COEFFICIENTS $Y_\ell(T)$

R.Rodrigues and J.-M. Hartmann
Laboratoire de Physique Moléculaire et Applications, CNRS UPR136 unité
associé aux universités de P. et M. Curie et Paris-Sud, Université de Paris-Sud
(Bât 350), 91405 Orsay Cedex, FRANCE

A simple approach is proposed in order to model the temperature dependence of the first-order line-mixing coefficients Y_ℓ (T). It respects a sum rule whose breakdown leads to large errors in atmospheric spectral computations. Furthermore, only two parameters, which can be represented with no more than three significant figures, are required (for air-broadening) for each line. Contrary to previous ones, our model is thus particularly suitable for storage of line-mixing parameters in databases. Tests in the case of two CO_2 Q-branches near 14 μm and of O_2 absorption in the centimeter wave region under various pressure and temperature conditions show the accuracy of our approach.

SESSION 7: 11:00

LINE COUPLING IN PERTURBATION THEORY:
A CAUTIONARY NOTE

Michael Hoke

Phillips Laboratory

Geophysics Directorate

Hanscom AFB, MA 01731

The general description of line coupling requires inverting the line shape operator matrix at each pressure and temperature required for the calculation. Consequently, in atmospheric radiative transfer codes, line coupling is usually accommodated in first order perturbation theory, which works well if the line coupling coefficient is small. Failure in perturbation theory can be benign or lead to significant differences between the calculations and measurement. Examples in fifteen micrometer carbon dioxide Q-branches will be presented to illustrate the point.

SESSION 7: 11:30

IMPROVED SPECTRAL PARAMETERS FOR THE THREE MOST ABUNDANT ISOTOPOMERS OF THE OXYGEN MOLECULE

Robert R. Gamache
Center for Atmospheric Research
University of Massachusetts Lowell
450 Aiken Street
Lowell, MA 01854

Aaron Goldman
Department of Physics
University of Denver
Denver, CO 80208

Laurence S. Rothman
AF Geophysics Directorate
PL/GPOS
Hanscom AFB, MA 01731

The spectral parameters for the three most abundant isotopomers of molecular oxygen in the terrestrial atmosphere, $^{16}O_2$, $^{16}O^{18}O$, and $^{16}O^{17}O$, have been re-calculated. These parameters include the line positions, the line intensities and strengths, the lower state energies, and the air-broadened halfwidths. Magnetic dipole and elecltric quadrupole transitions in and among the three lowest lying electronic states, $X^3\Sigma_g^- \leftarrow X^3\Sigma_g^-$, $a^1\Delta_g \leftarrow X^3\Sigma_g^-$, and $bX^1\Sigma_g^+ \leftarrow X^3\Sigma_g^-$, are considered resulting in transitions from the microwave to the visible. The expression for the line intensity in terms of the Einstein A coefficient is developed and the confusion concerning the 1.27 μm band intensities is addressed. The final data file contains 9292 transitions belonging to 18 bands. These data are now contained in the 1996 HITRAN database.

SESSION 8: 13:30-16:00

IMPROVEMENTS OF NITROGEN DIOXIDE FOR UPDATING HITRAN

V. Dana, J.-Y. Mandin, A. Perrin
Laboratoire de Physique Moléculaire et Applications
CNRS, Université Pierre et Marie Curie, Case Courier 76
Tour 13, 4, place Jussieu, 75252 Paris Cedex 05
FRANCE

L. Regalia and A. Barbe
Groupe de Spectroscopie Moléculaire et Atmosphérique
Faculté des Sciences, 51062 Reims Cedex
FRANCE

Nitrogen dioxide is a minor constituent in the stratosphere and in the upper troposphere. It is also present in the lower troposphere as a pollutant. The $v_1 + v_3$ band, located around 3.4 μm, is well suited to study NO_2 in atmospheric spectra from the ground, since several NO_2 peaks of this band appear well isolated and free of other tropospheric absorptions.

The current HITRAN version contains line positions and intensities which need to be improved, and a single value of the air-broadening coefficient has been quoted for all the lines. In this work, we have determined accurate line positions and intensities from Fourier transform spectra recorded at GSMA (Reims). In addition, a consistent set of self- and nitrogen-broadening coefficients has been obtained for a wide domain of N and K_a rotational quantum number values.

The method set up to retrieve line parameters from the spectra is presented. The determination of collisional line widths was particularly difficult because the spectrum is very crowded, and because the spin-rotation doubling has to be known very accurately from a reliable theoretical calculation.

The results are presented and discussed within the context of atmospheric applications.

SESSION 8: 13:30-16:00

UPDATED LINE PARAMETERS FOR OH X²Π ← X ²Π (v',v")

A. Goldman, W.G. Schoenfeld
University of Denver
Denver, CO 80208, U.S.A

D. Goorvitch
Space Science Division
NASA Ames Research Center
Moffett Field, CA 94035, U.S.A

C. Chackerian, Jr.
Earth System Science Division
NASA Ames Research Center
Moffett Field, CA 94035, U.S.A

H. Dothe
Mei Technologies
1050 Waltham St, Lexington, MA 02173, U.S.A.

F. Melen
Institut d'Astrophysique
Université de Liège
5 Avenue de Cointe
B-4000, Liège, Belgium

M.C. Abrams
SAIC- Aerosol Research Branch
Atmospheric Sciences Division
NASA Langley Research Center
Hampton, VA 23681, U.S.A

New spectral line parameters have been generated for the OH X²Π ← X ²Π pure rotation and vibration-rotation transitions for v = 0,...,6, v = 0,...,10 for HITRAN and HITEMP. Line parameters sets have been prepared with J_{max} = 49.5 and are provided at 296K and 6000K. Thus, 56 separate bands were calculated; 11 pure rotation bands and 45 vibration-rotation bands. Recent advances in the calculations of line intensities from wavefunctions and electric dipole moment function, and in line positions from term analysis of modern field

and laboratory spectra, allow significant improvement in the line parameters.

SESSION 8: 13:30-16:00

INDICES OF REFRACTION IN THE HITRAN COMPILATION

S. T. Massie
NCAR
Boulder, CO

A. Goldman
University of Denver
Denver, CO 80208

A review of the indices of refraction, which are included in the HITRAN compilation, is presented. The need for additional laboratory work is also discussed. Application of the indices, to obtain area and volume densities, for both volcanic areosol and Polar Stratospheric Cloud particles, is illustrated using infrared aerosol extinction observed by experiments on the Upper Atmosphere Research Satellite (UARS).

SESSION 8: 13:30-16:00

THE JET PROPULSION LABORATORY SUBMILLIMETER, MILLIMETER, AND MICROWAVE SPECTRAL LINE CATALOG

H.M. Pickett, R.L. Poynter, E.A. Cohen,
M.L. Delitsky, J.C. Pearson, H.S.P. Müller
Jet Propulsion Laboratory, California Institute of Technology
Pasadena, California 91109

This report describes a computer-accessible catalog of submillimeter, millimeter, and microwave spectral lines in the frequency range between 0 and 10,000 GHz. The catalog can be used as a planning guide or as an aid in the identification and analysis of observed spectral lines. The information listed for each spectral line includes the frequency and its estimated error, the intensity, the lower state energy, and the quantum number assignment. This edition of the catalog has information on 298 atomic and molecular species and includes a total of 1,448,153 lines.

The catalog has been constructed by using theoretical least squares fits of published spectral lines to accepted molecular models. The associated predictions and their estimated errors are based upon the resultant fitted parameters and their covariances. Future versions of this catalog will add more atoms and molecules and update the present listings as new data appear.

The catalog is available on-line via anonymous ftp at spec.jpl.nasa.gov and on the world wide web at http://spec.jpl.nasa.gov.

SESSION 8: 13:30-16:00

THE GEISA DATABASE IN THE FRAME OF THE IASI MISSION OF THE EUMETSAT POLAR SYSTEM:GEISA/IASI

N.Jacquinet-Husson, N.A.Scott, A.Chedin, B.Bonnet LMD Palaiseau (France)

A.Barbe and Vl.G.Tyuterev, LSMA,Reims (France)

J.P.Champion, LPUB, Dijon (France)

M.Winnewisser, JLU, Giessen (Germany)

L.R.Brown, JPL, Pasadena(USA)

R.Gamache, CAR, Lowell(USA)

V.Golovko and A.Chursin, Tomsk(Russia)

IASI (Infrared Atmospheric Sounding Interferometer), part of the future EUMETSAT Polar System(EPS), will be the first space-borne operational instrument which is expected to meet the requirements of the World Meteorological Organisation (i.e; temperature with an average error of 1K; humidity with an average error of 10%; vertical resolution of 1km, at least in the lower troposphere), for operational numerical weather prediction and climate research.

For many years, the GEISA system, a spectroscopic line compilation (more than 730,000 entries between 0 and 22,656 cm^{-1}, corresponding to 40 molecules and 86 isotopic species) and its associated software, have been widely used for monitoring the forward atmospheric transfer modeling with the maximum reliability, tractability, and efficiency. The GEISA/IASI project, issued from GEISA and intended to produce the best possible Spectroscopic Database for IASI, will be presented.

SESSION 8: 13:30-16:00

EXTENDED LINE PARAMETERS OF AMMONIA
FROM 2200 TO 5300 cm^{-1}

L. R. Brown, J. S. Margolis, J. A. Crisp, D. Crisp
Jet Propulsion Laboratory, California Institute of Technology, 4800 Oak Grove
Drive, Pasadena, CA 91109, USA

I. Kleiner, G. Tarrago
Laboratoire de Physique Moleculaire Applications, CNRS, Universit9 Pierre et
Marie Curie, Bte 76, 4 Place Jussieu, 75252 Paris Cedex 05, France,

Š. Urban and P. Pracna
Czech Academy of Sciences
Heyrovský Institute
Prague, Czech Republic

Line parameters of ammonia from 2200 to 5300 cm^{-1} been added to the
HITRAN database for the first time. The parameters for the 4 μm region are
calculated from results of Kleiner et al. (*J. Mol. Spectrosc.* **173**, 120 (1995)) in
which both line positions and intensities were modeled for $3\nu_2$ and $\nu_2 + \nu_4$. The
3μm and 2.3 μm regions are calculations based on the analyses of line positions by
Guelachvili et al. (*J. Mol. Spectrosc.* **133**, 345 (1989)) and Urban et al. (*J. Mol.
Spectrosc.* **133**, 312 (1989)) with relative intensities normalized using limited data.
The 2μm region is based on empirical measurements of positions, intensities and
lower state energies with known assignments matched to the observed features.

SESSION 8: 13:30-16:00

ANALYSIS OF THE FIRST [$2v_2$, v_1 and v_3] AND SECOND [$3v_2$, $v_1 + v_2$ and $v_2 + v_3$] TRIADS OF H_2S

L. R. Brown, J. A. Crisp, D. Crisp
Jet Propulsion Laboratory, California Institute of Technology
4800 Oak Grove Drive, Pasadena, CA 91109, USA

A. Perrin
Laboratoire de Physique Moléculaire Applications, CNRS, Université Pierre et
Marie Curie, Bte 76, 4 Place Jussieu, 75252 Paris Cedex 05, France

O. V. Naumenko, M. A. Smirnov, and L. N. Sinitsa
Institute of Atmospheric Optics, SB, Russian Academy of Science
634055 Tomsk, Russia

The two triad systems of hydrogen sulfide [$2v_2$, v_1 and v_3 near 4 μm and $3v_2$, $v_1 + v_2$ and $v_2 + v_3$ near 2.7 μm] were analyzed using fourteen spectra recorded at 0.0056 and 0.011 cm^{-1} resolution with the McMath Fourier transform spectrometer located at Kitt Peak National Observatory. Experimental upper state levels of $H_2{}^{32}S$, $H_2{}^{34}S$ and $H_2{}^{33}S$ were obtained from assigned positions (as high as J = 20 and K_a = 15 for the main isotope). These were fitted to the A-reduced Watson Hamiltonian to determine precise sets of rotational constants through J^{10} and up to nine Fermi and Coriolis coupling parameters. Intensities of the two $H_2{}^{32}S$ triads were modeled with rms values of 2.5%, using the transformed transition moment expansion with 19 terms for 558 intensities of the first triad and 11 terms for the 526 intensities of the second triad. The combination band strengths were found to be greater than the two fundamental band strengths. The coefficients of the transformed moment expansion were obtained, corresponding to band strengths in cm^{-2}/atm at 296 K of: 0.3312 for $2v_2$, 0.4519 for v_1 and 0.1197 for v_3, 0.0303 for $3v_2$, 1.820 for $v_1 + v_3$ and 2.870 for $v_2 + v_3$. In addition, the transitions of six hot band were identified. Finally, a composite database of hydrogen sulfide line parameters was predicted for the 5 to 2.5 μm region; this catalog should be used in place of the calculation at 4 μm appearing in the 1996 version of HITRAN.

SESSION 8: 13:30-16:00

CHARACTERISTICS OF INFRARED DATA NEEDS FOR FUTURE MARTIAN AND COMETARY OBSERVATIONS

C. Muller, D. Moreau
Belgian Institute for Space Aeronomy
Brussels, BELGIUM

A.V. Rodin
Space Research Institute
Moscow, RUSSIA

Since the 1986 encounter of comet Halley and the 1989 PHOBOS Martian observations, the list of possible molecules in the atmospheres of Mars and comets has been extended to the new observed molecules (formaldehyde and methane) and still non observed chemically related constituents. The chemistry involved differs essentially from terrestrial processes by the absence of rainout and of U-V.filtering and has commonalities with the earth photochemical smog compositions.

The list of molecules will be presented together with a priority rating. Both Mars and cometary research stress also the importance of spectra of condensed phases and aerosols, as well as molecular complexes. A list of targets accessible by existing or proposed instruments is shown together with simulations using the 1992 HITRAN database with Martian and cometary models.

SESSION 8: 13:30-16:00

EXTRAPOLATION OF CARBON DIOXIDE LINE POSITIONS FOR HITEMP

Robert L. Hawkins, Laurence S. Rothman
Simulation Branch, Geophysics Directorate
PL/GPOS,
Hanscom AFB, MA 01731-3010

Richard B. Wattson
Stewart Radiance Laboratory
Utah State University
Bedford, MA

Simulation of carbon dioxide spectra at temperatures up to 1500K requires higher vibrational levels, and line positions to much higher angular momentum quantum number J, than have been observed. Direct Numerical Diagonalization (DND)[1] allows extrapolation to such high vibrational levels and high J, but does not reproduce observed lower-J line positions to within experimental accuracy.

For the HITEMP line parameter compilation, we chose to fit spectroscopic constants $G_v, B_v, D_v, H_v, L_v,$ and P_v to the observed line positions, and to high-J DND-calculated line positions, simultaneously. This allows smooth extrapolation while preserving a good fit to the observed positions. Examples of bands fitted in this way, and the quality of fit to be expected in HITEMP, will be presented.

---

1. R.B. Wattson and L.S. Rothman, *J. Mol. Spectrosc.* **119**, 83 (1986).

SESSION 8: 13:30-16:00

HITEMP VALIDATION AND ISSUES

J.E.A. Selby, Northrup-Grumman, Bethpage, NY
L.S. Rothman, AF Geophysics Directorate, Hanscom AFB, MA
R.B. Wattson, Utah State University, Bedford, MA
C. Camy-Peyret, J-M. Flaud, Université Pierre et Marie Curie, Paris, FRANCE
R.R. Gamache, University of Mass. Lowell, Lowell, MA
R.H. Tipping, University of Alabama, Tuscaloosa, AL
A.Goldman, University of Denver, Denver, CO

A description of a high-temperature molecular database and its development will be given together with validation examples.

Currently the HITEMP database has focussed on the generation of molecular line parameters for H_2O, CO_2, CO, and OH which are suitable for the calculation of transmittance and radiance spectra by these molecules at elevated temperatures (approaching 2000K) over the 2 to 20 micrometer region. (To date the base temperature of the calculated HITEMP line strengths and positions has been 1500K, but will be extended to 3000K in the future.)

The CO_2 and H_2O line parameters in HITEMP are based on the DND approach, while those for CO and OH use the classical approach. Two earlier versions of a high-temperature database assembled in 1992 and 1995 have incorporated the other atmospheric species contained in HITRAN92 over the restricted wavelength range (2 to 20 µm), in order to simulate the attenuation of hot gaseous emission over atmospheric paths by correctly accounting for the hot/cool line-correlation effects.

We have attempted to use laboratory hot cell and flame measurements to validate the theoretically developed HITEMP line parameter database. Some of the current problems and issues concerning the accuracy and limitations of the HITEMP database will be discussed as well as suggestions for future improvements.

SESSION 8: 13:30-16:00

Cooling Rate Calculations for the Airborne Southern Hemisphere Ozone Experiment (ASHOE) using MODTRAN3

Szu-Chia Lee, H. Revercomb, R. Knuteson, and W. Smith
Space Science and Engineering Center
University of Wisconsin-Madison

Overview

1. Motivation

2. Method

3. MODTRAN3 vs. Other Models

4. Sensitivity Study

5. ASHOE

6. Summary and Future Goals

1. Motivation: Why do cooling rates for ASHOE?

• To understand how the ozone depleted air is transported to populated regions outside the polar vortex.

• Vertical motions and transport of air around the South Pole are related to atmospheric cooling rates.

• To validate cooling rates in dynamical models for the polar vortex using observed data and more accurate radiative transfer models.

2. Method: How do we get cooling rates?

Monochromatic thermal radiation for clear sky at a given level

μ = zenith direction cosine, ϕ = azimuthal angle

Upwelling flux

$$F_v^+ = \int_0^{2\pi} \int_0^1 I_v(\mu)\,\mu\,d\mu\,d\phi$$

Downwelling flux

$$F_v^- = \int_0^{2\pi} \int_{-1}^0 I_v(\mu)\,\mu\,d\mu\,d\phi$$

Azimuthally integrated flux

$$F_v^\pm = \pm 2\pi \int_0^{\pm 1} I_v(\mu)\,\mu\,d\mu$$

Three-point Gaussian Quadrature angles: 77.74°, 53.80°, 24.29°

Net flux

$$F_v = F_v^+ - F_v^-$$

Monochromatic cooling rate

$$Q_v = \Delta F_v$$

In terms of potential temperature change in a layer

$$\left.\frac{\partial \theta}{\partial t}\right|_{v;l,l-1} = \frac{g}{C_p} \frac{F_{v;l} - F_{v;l-1}}{P_l - P_{l-1}}$$

3. MODTRAN3 vs. Other Models

- FASCODE (High Spectral Resolution but SLOW)

- MODTRAN3 (Low Spectral Resolution but FAST)

- Rapid Radiative Transfer Model (RRTM)

    (Integrated and VERY FAST)

Cooling Rate Comparison with FLAT-earth Approximation Using Same Pressure Level Boundaries
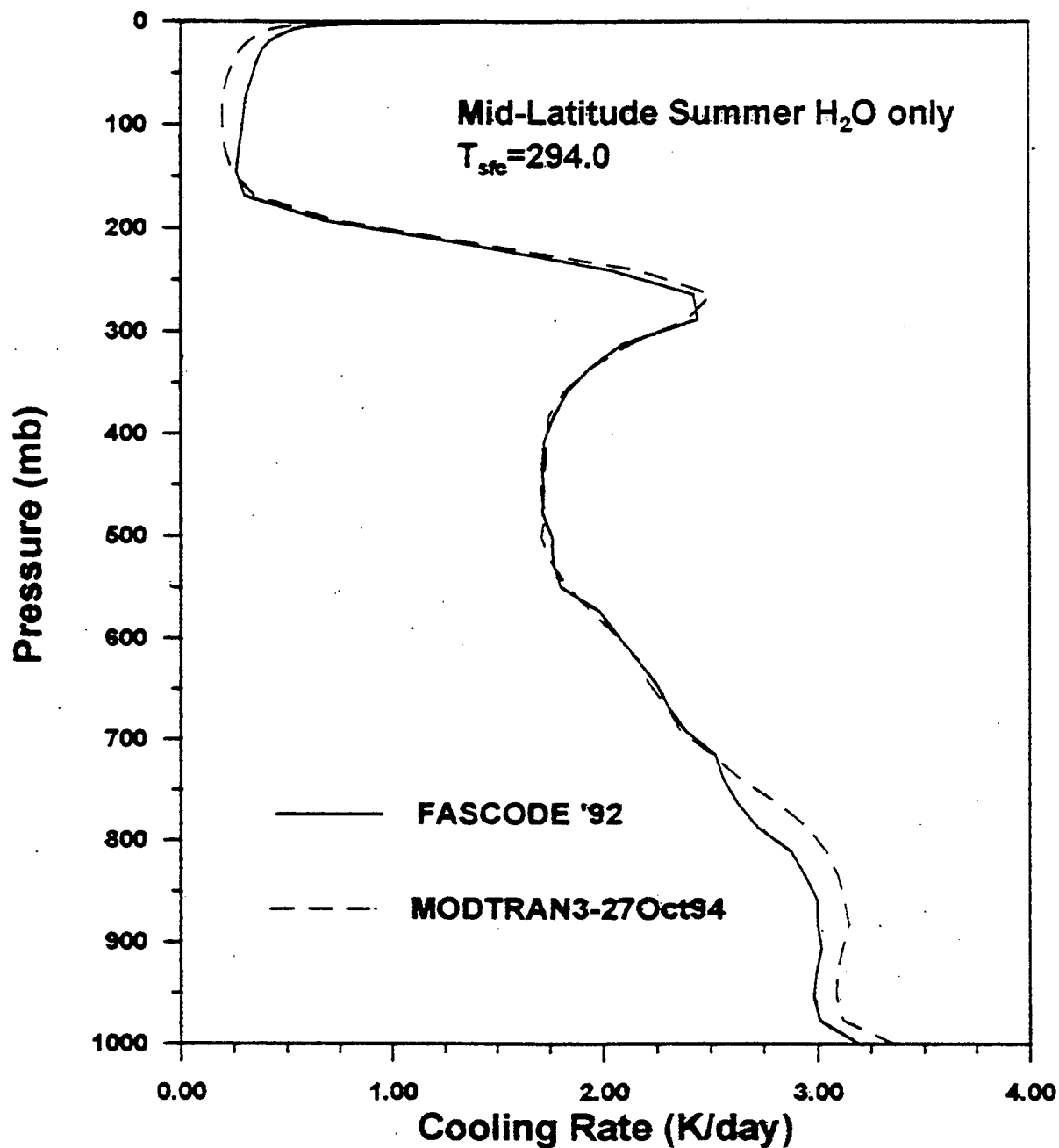
Cooling Rate Comparison between Two Models
for ASHOE - 3/4 October 68S
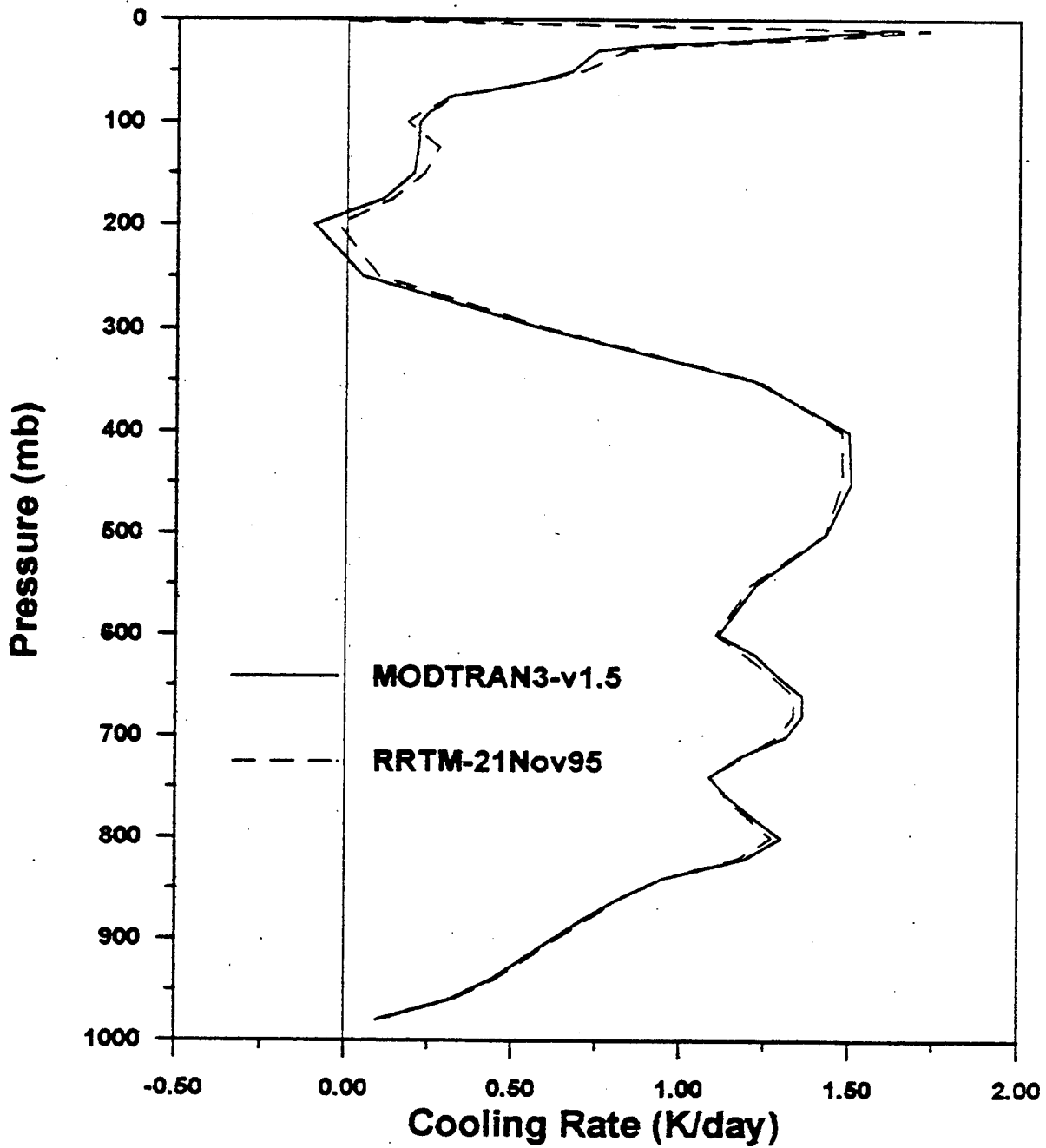
4. SENSITIVITY STUDY

Comparison of Water Vapor Profiles for
ASHOE - 13 April 1994 68S
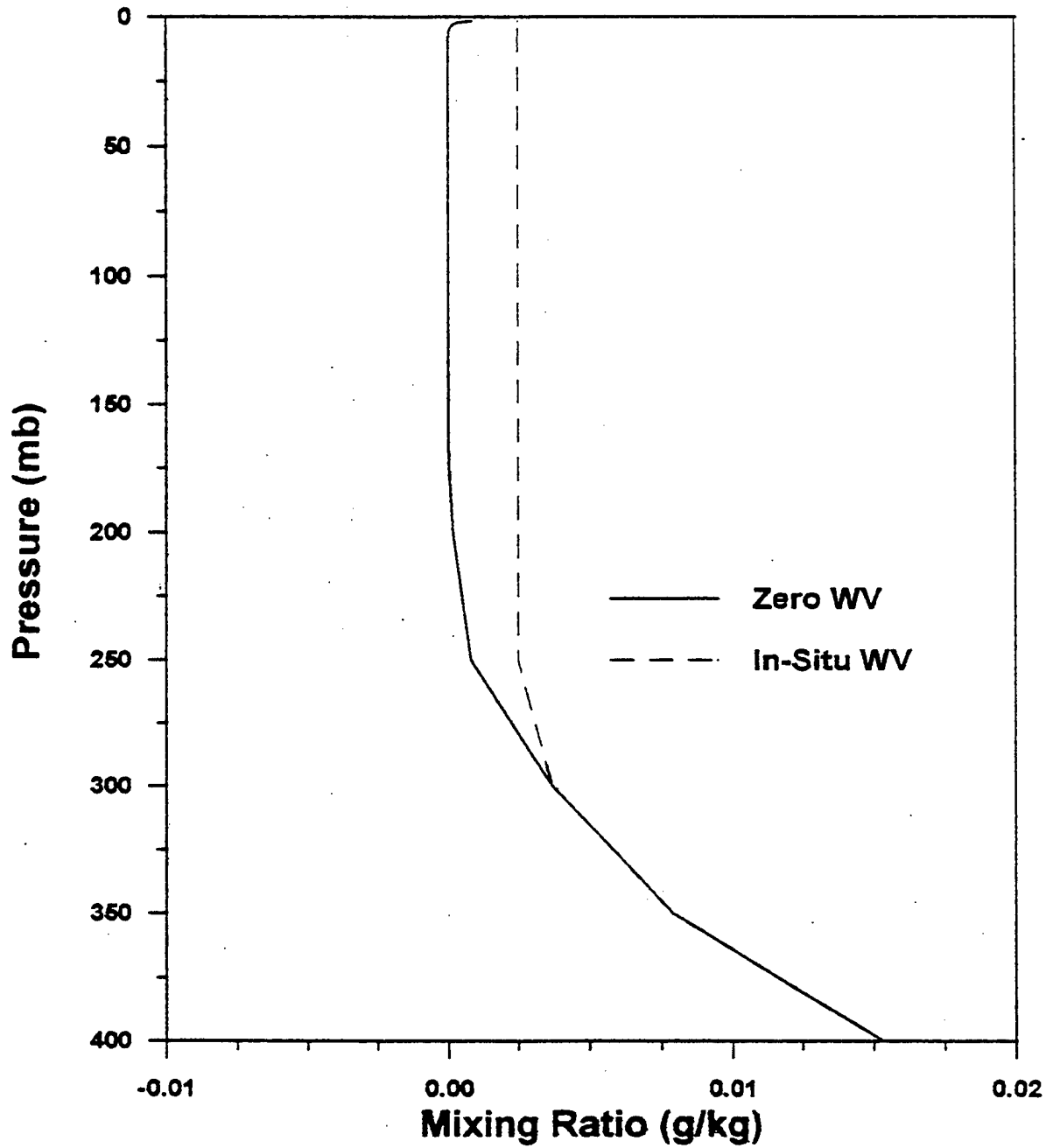
Comparison of Cooling Rates Calculated with Different Water Vapor Profiles for ASHOE - 13 April 1994 68S
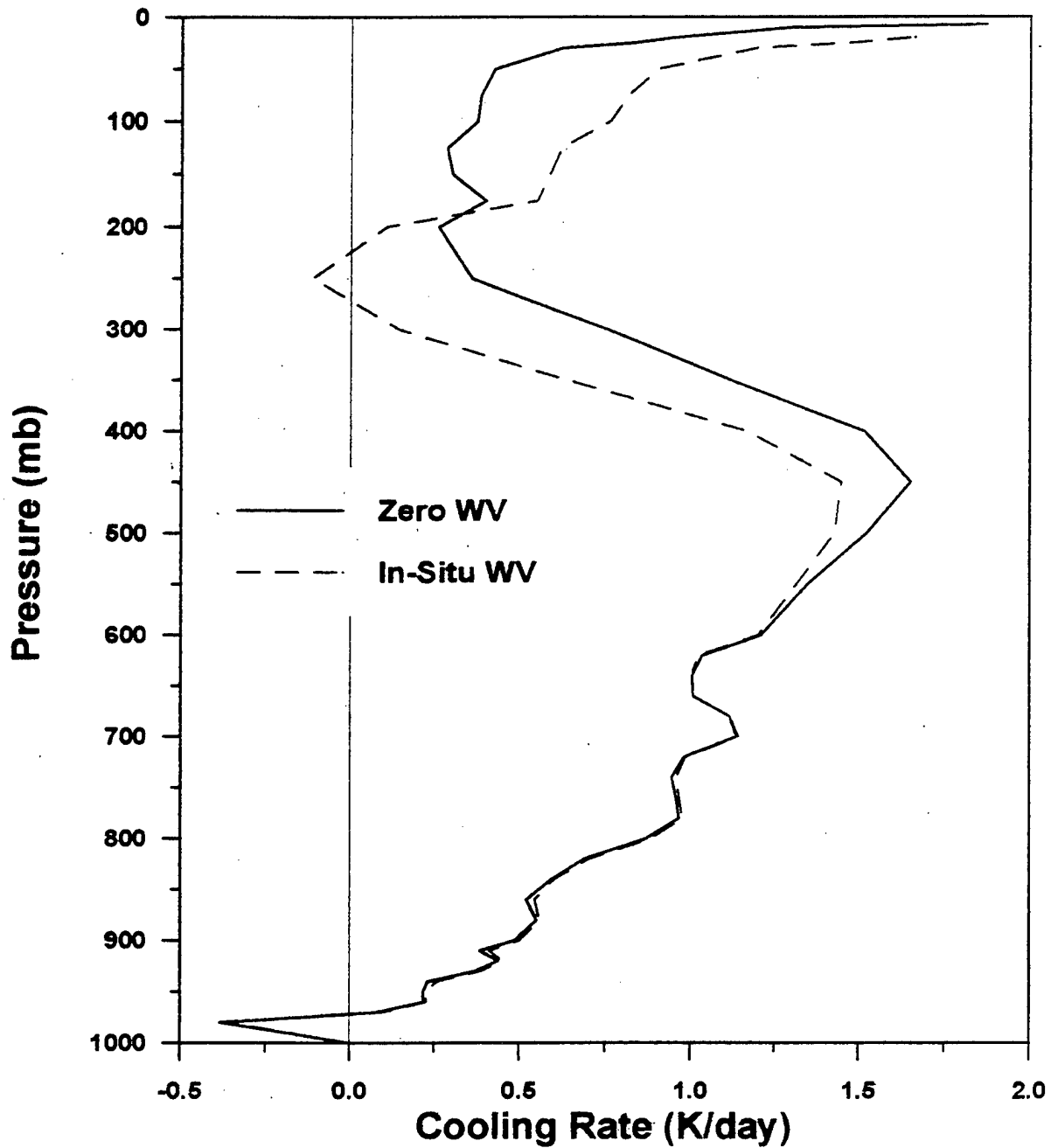
5. ASHOE: Airborne Southern Hemisphere Ozone Experiment

- Objectives

- ER2 Flight Payload

- Flight track

- HIS Observations of T_b for 8 August 1994

- MODTRAN3 Cooling Rates: HIS vs. Global Models

- Contributions of O_3, H_2O, and CO_2 to Cooling Rates

- Spectral Cooling Rates

- **Objectives of ASHOE:**

To examine the causes of ozone loss in the Southern

Hemisphere lower stratosphere and to investigate how the

loss is related to polar, mid-latitude, and tropical

processes, including radiative transfer.

NASA Ames Research Center

Dynamics & Radiation
PAYLOAD CONFIGURATION

Nose
- MMS (Chan)
- Ballast

Q-Bay
- Water Vapor (Kelly)
- NOAA Ozone (Proffitt)
- Meteorological Measurement System (MMS)

Right Cheek
- MTP (Gary)

Left SpearPod
- CO_2 (Boering)
- CNC (Wilson)
- Ballast

Right SpearPod
- ALIAS (Webster)
- ATLAS (Loewenstein)
- FCAS II (Wilson)
- MASP (Dye / Baumgardner)

- APS (Pueschel)

- HIS (Smith)

- CPFM (UV-VIS) (McElroy)

Ballast

NASA 709

Earth Science Projects Office

75
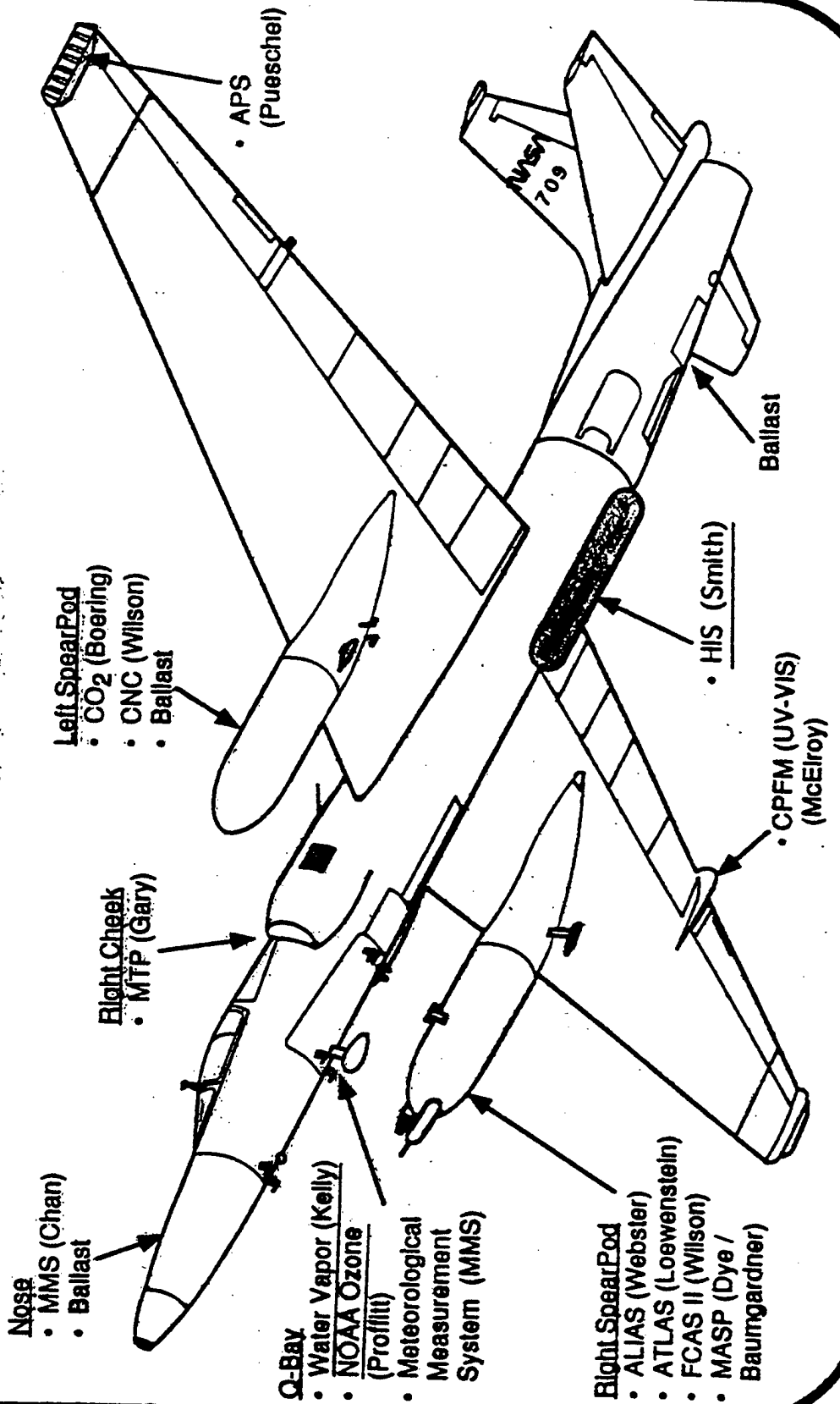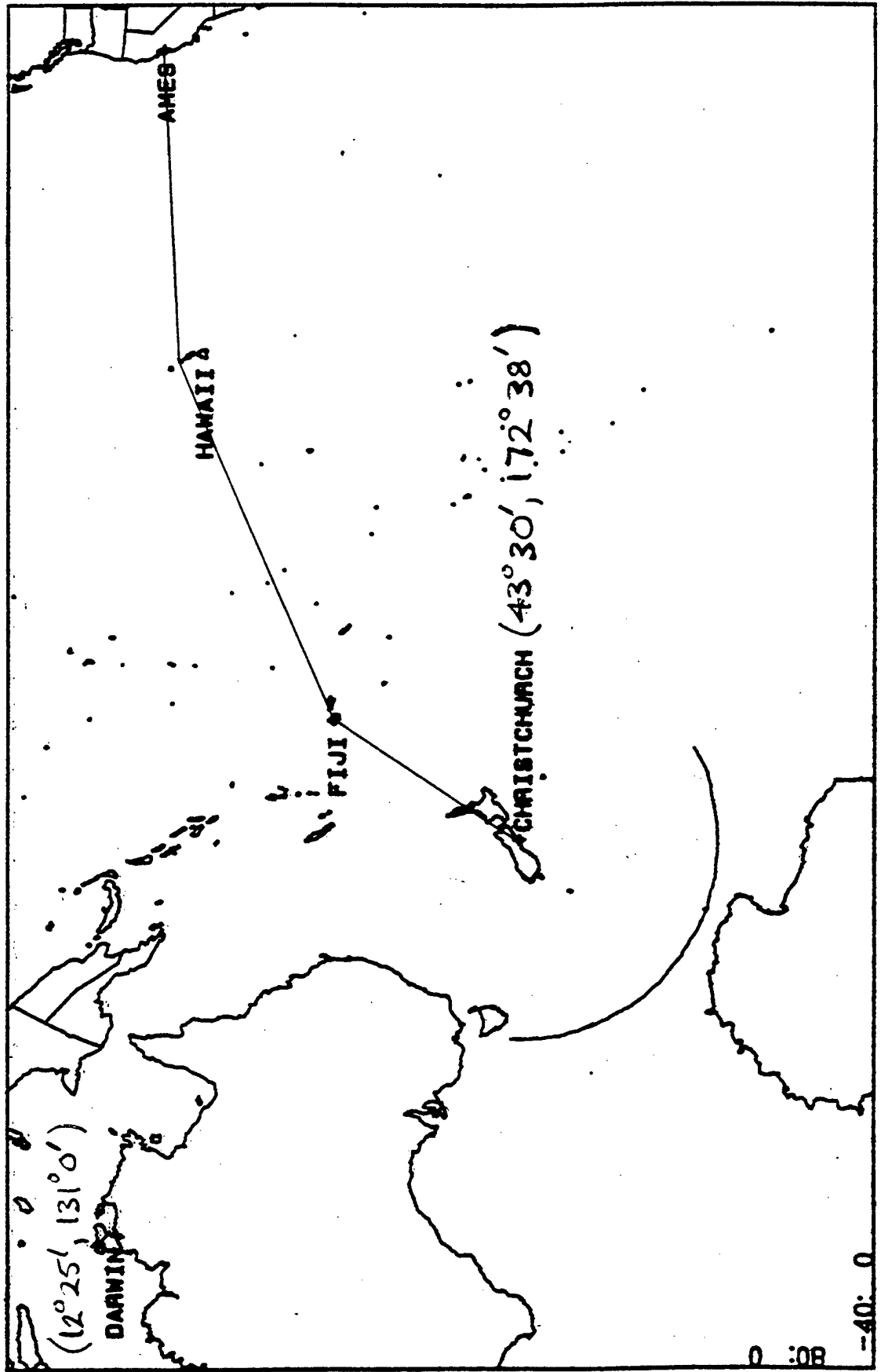
ASHOE/MAESA AREA OF OPERATION

SCALE = 1:7.50E+07

4 October 1994

MIT/CRC Contour Advection

460K surface   94100400   GSFC winds
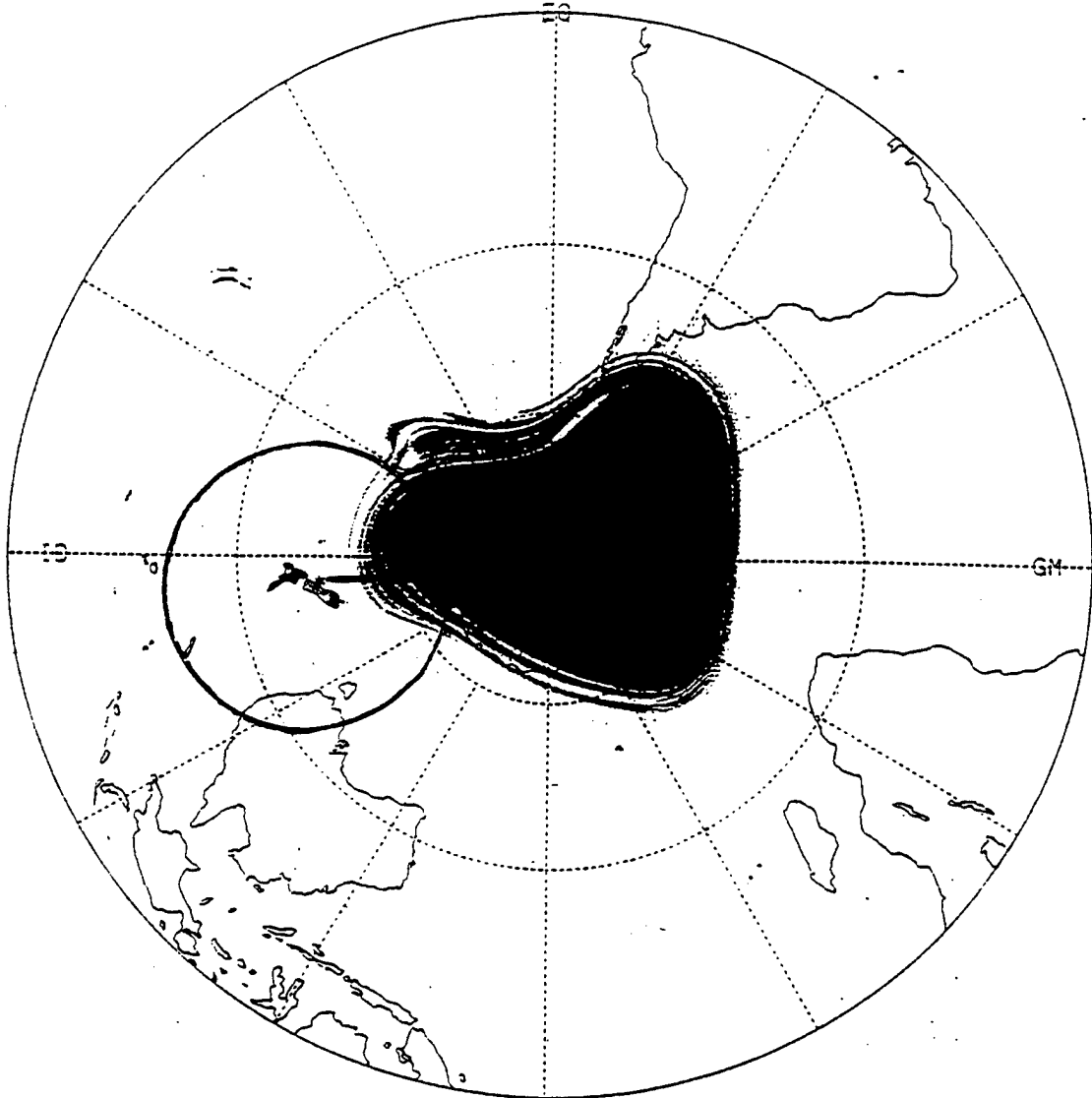
start=94092412, anals until 94100512
NMC PV=-{2.0.2.5...5.0}e-5, 460K, 940924

ASHOE: Airborne Southern Hemisphere Ozone Experiment

From Bill.

HIS Brightness Temperature Spectra
ASHOE, 8 August, 1994
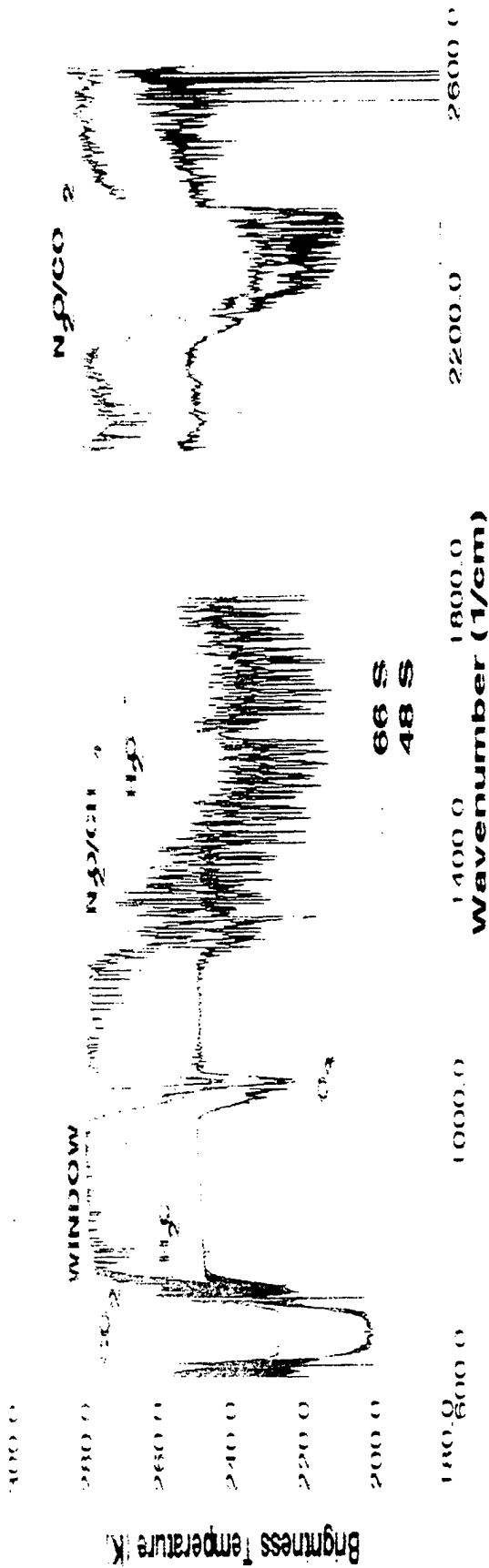
A/C HIS Sounding System — Temperature

ASHOE 220 JD 1994
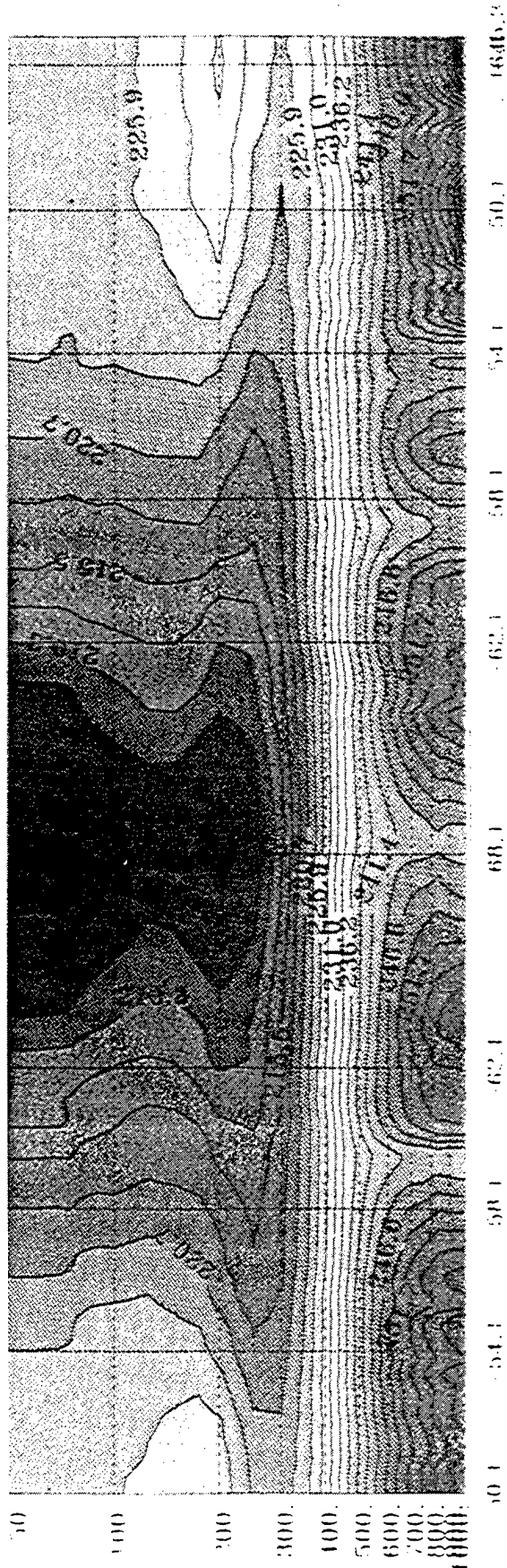
Cooling Rate Comparison

ASHOE - October 3/4 1994 68S
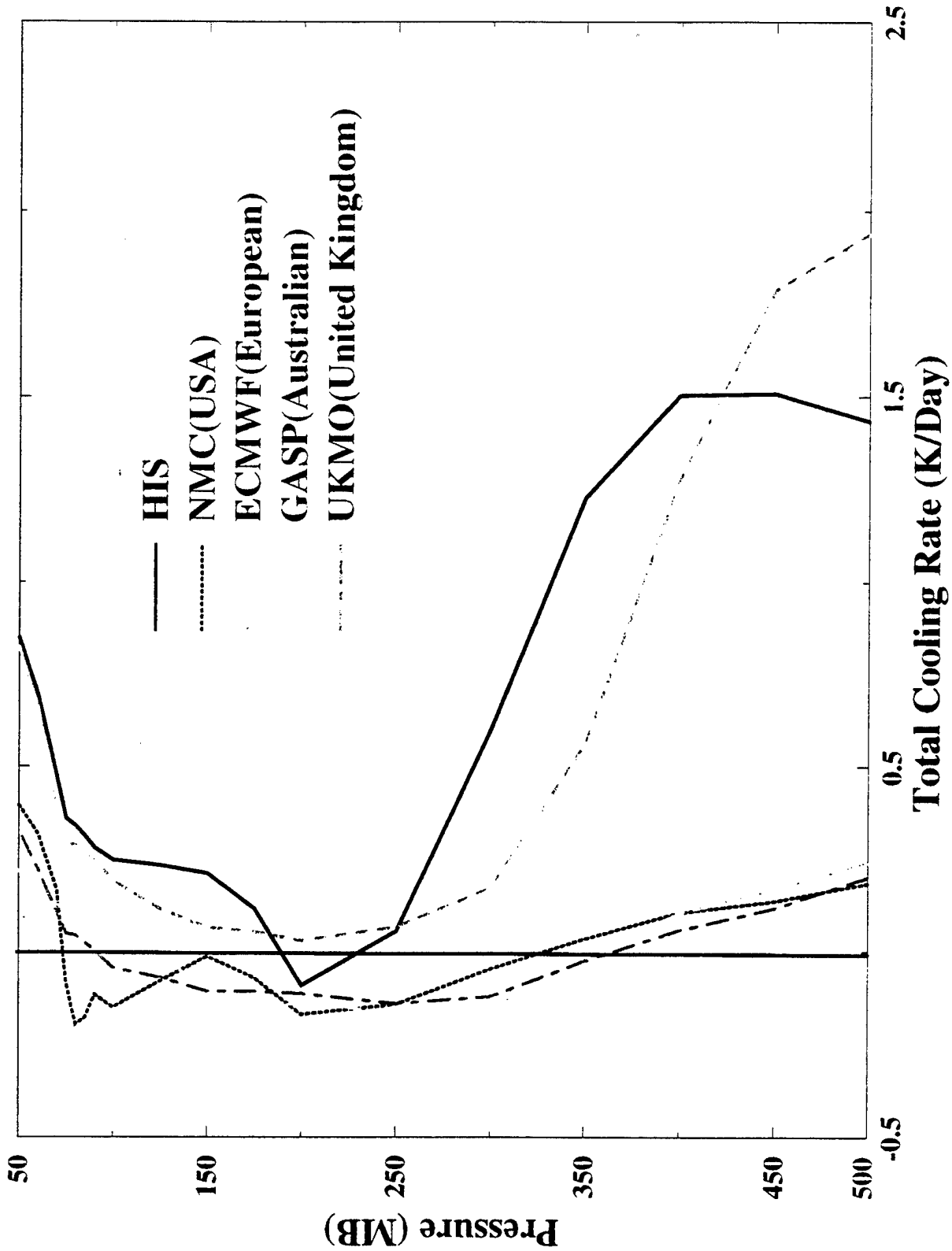
CIMSS/UW

From Bill

HIS Reg Water Vapor (g/kg) 276 JD 1994

Oct 3   Oct 4
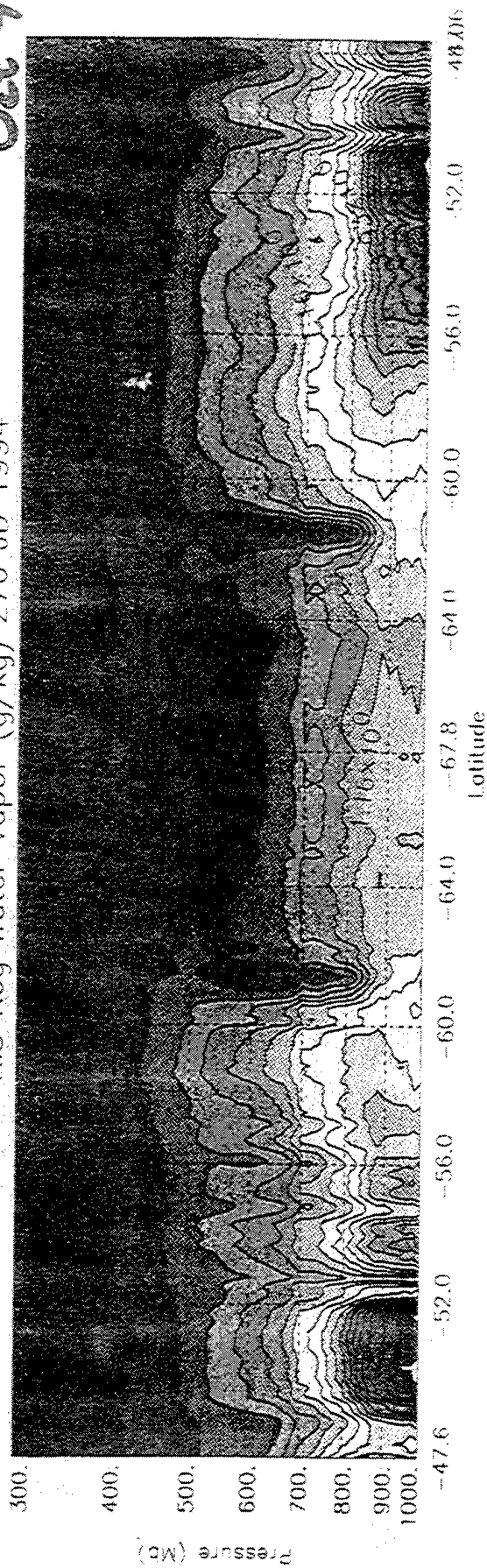
ECMWF Water Vapor (g/kg) 277 JD 1994

HIS Cooling Rate (K/Day) 226 JD 1994 (Aug 8/9)

HIS Cooling Rate (K/Day) 276 JD 1994 (Oct 3/4)

HIS Cooling Rate (K/Day) 103 JD 1994 (Apr 13/14)

HIS Cooling Rate (K/Day) 222 JD 1994 (Aug 10/11)

81
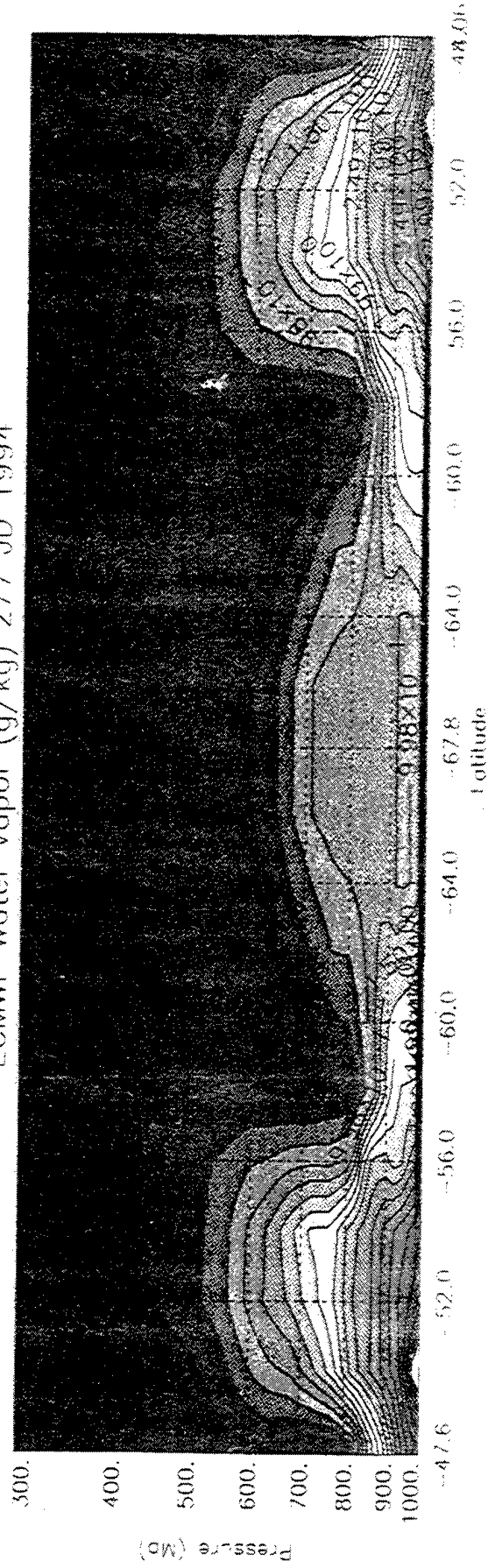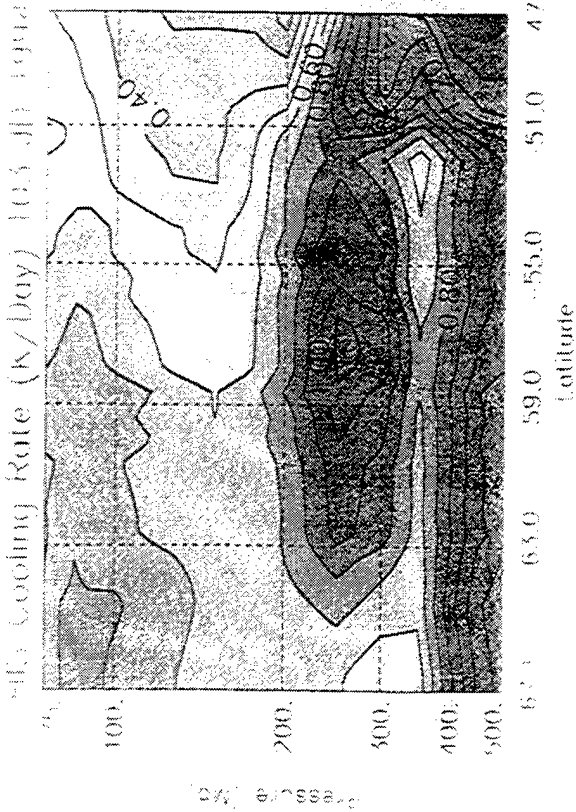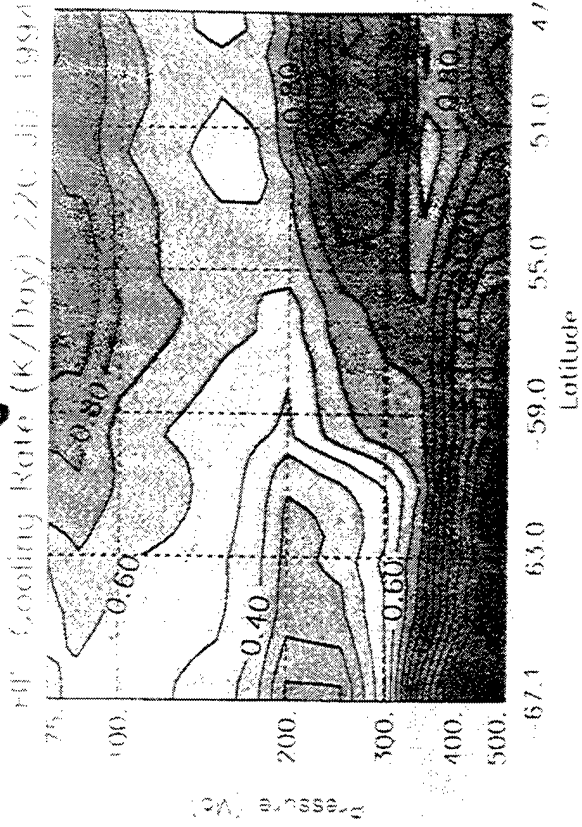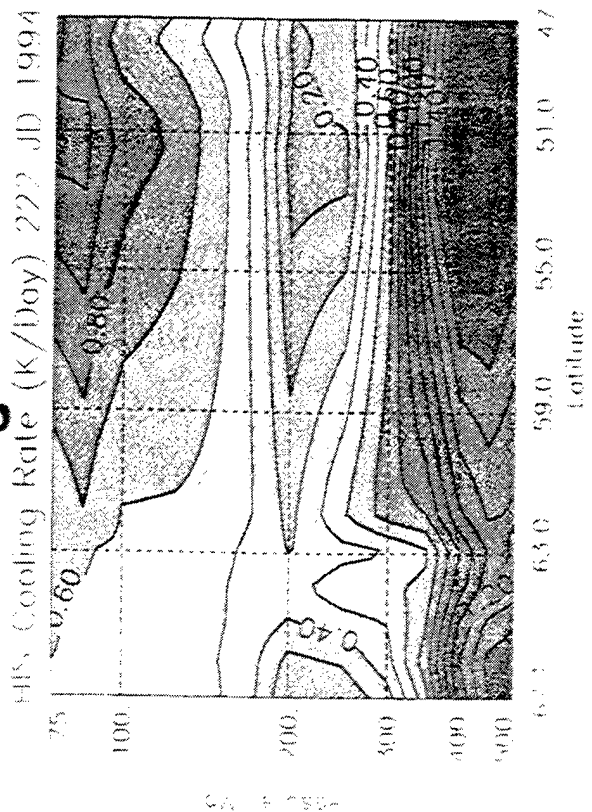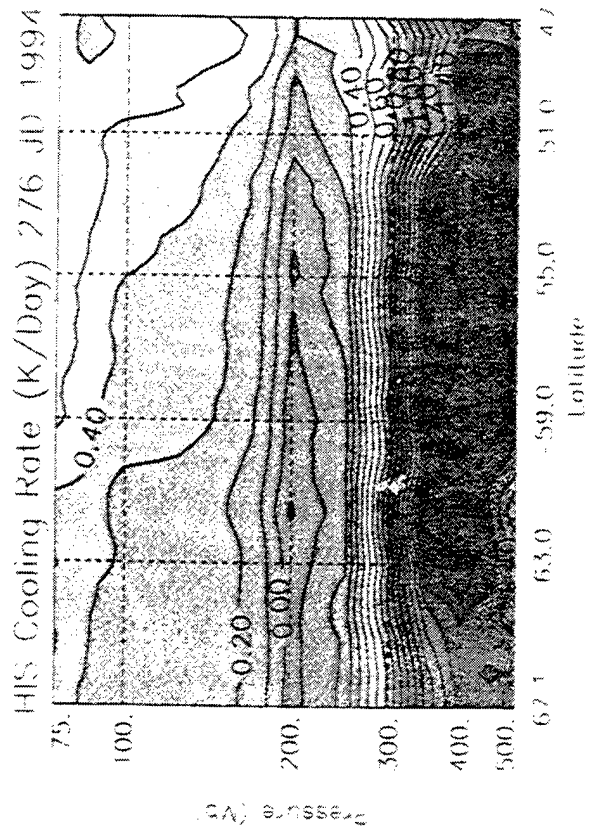
Layer Mean Cooling Rates
Polar Vortex (-67 deg), 3/4 October 1994

82
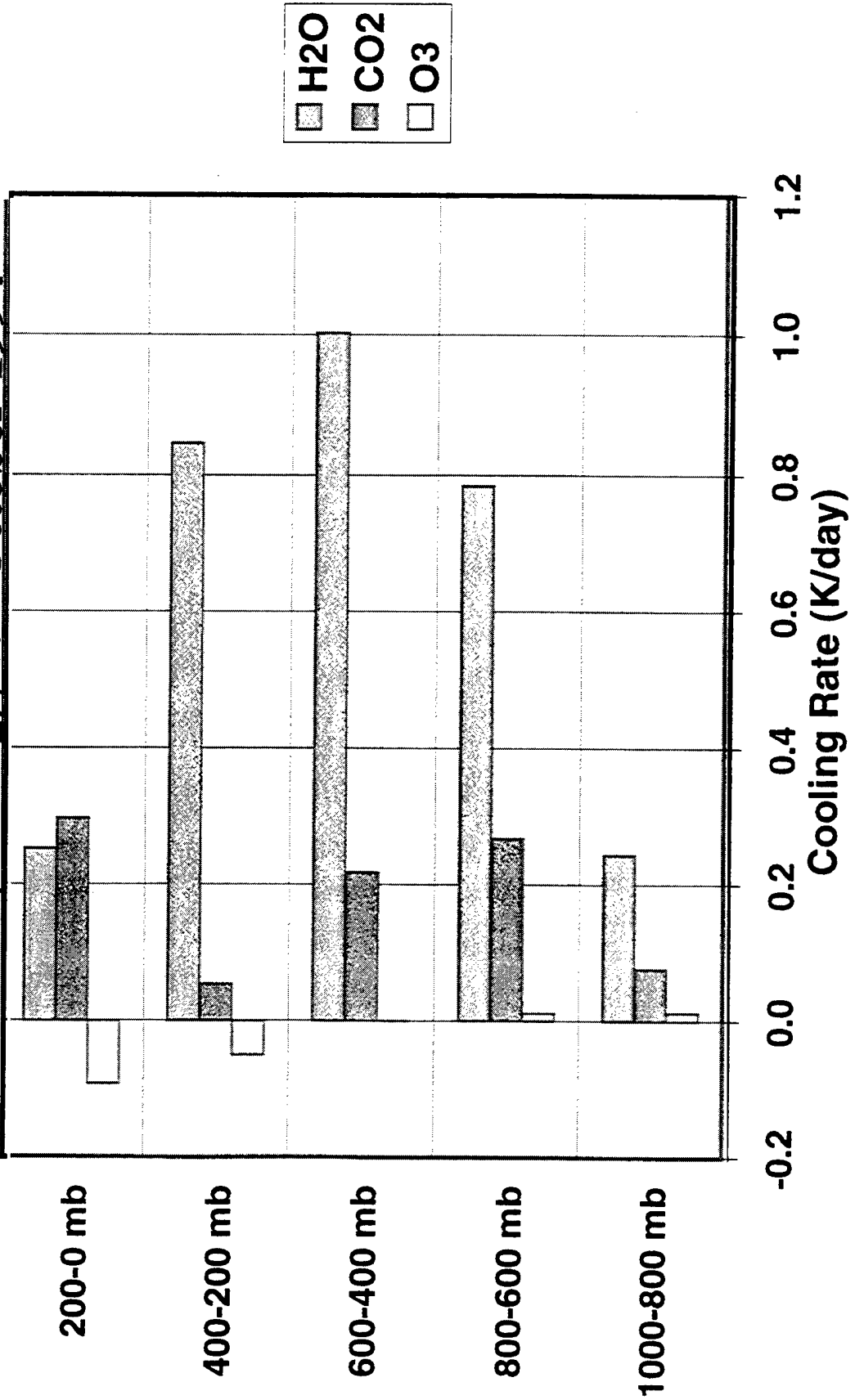
ASHOE Cooling Rate for ac941004 Rec.40 (-67.7,172.2)

Cooling Rate (x10⁵ K.d⁻¹.(cm⁻¹)⁻¹)
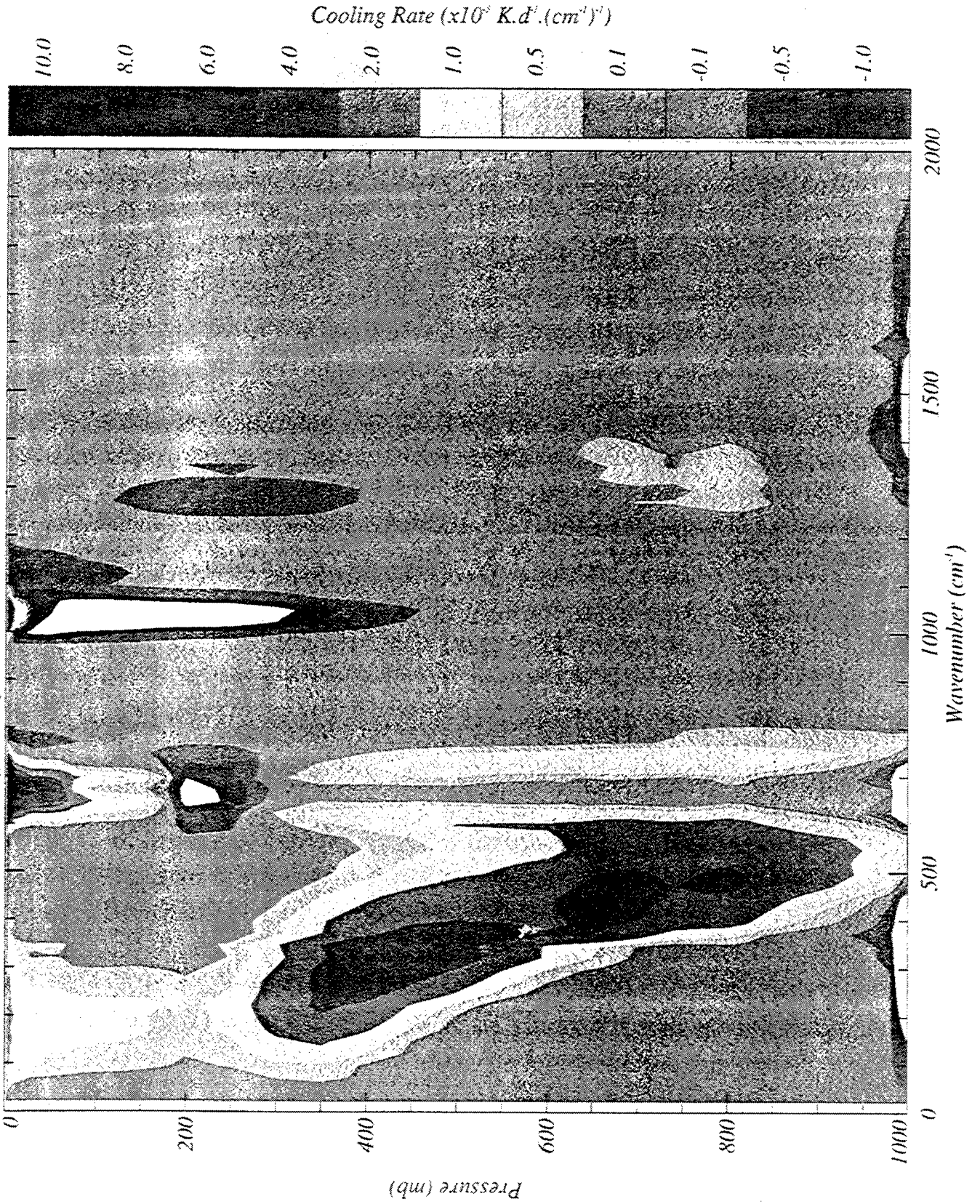
6.

• Summary

- If model has no water vapor above 200 mb then model is

  making a 0.2 K/day error in the cooling rate

- Cooling rate is not dominated by carbon dioxide but by water

  vapor in the upper troposphere

• Future Goals

- Combining the longwave cooling and shortwave heating

- Cooling/heating rates in the presence of clouds

RADIATIVE TRANSFER SIMULATIONS FOR DEVELOPMENT OF EOS MODIS LAND-SURFACE TEMPERATURE ALGORITHMS AND PRODUCTS

Zhengming Wan

Institute for Computational Earth System Science
University of California, Santa Barbara, CA 93106-3060, USA

- EOS MODIS LST

- Theoretical background

- Description of the algorithm

- Atmospheric radiative transfer simulations

- Major concerns

1. Brief introduction of LST and its applications

- Land-Surface Temperature (LST) will be retrieved from EOS/MODIS data starting in 1998. "Land-Surface" here means the target surface on the ground observed by MODIS. It could be vegetation canopy, bare soil, inland water bodies, snow, ice, rock, sands, and their mixture.

— Daily daytime and nighttime LSTs at 1km resolution level-2 and 5km level-3 for the at-launch product. Derivative level-3 LST products: 8-day 1km equal area grid, daily, 8-day and monthly 0.5 degree equal angle grid.

— Goal of the LST accuracy: 1 °K, goal of the LSE accuracy: 0.02 for bands 29, 31 & 32; 0.05 for bands 20, 22 & 23.

- major applications:
  — as input to other MODIS land products: land-cover, NPP.
  — as input to 17 EOS IDS studies.
  — synergism with GCM to provide LST in all sky conditions.
  — long-term record of LST will provide a direct answer to questions on global change and greenhouse effect.
  — LST very close to surface air temperature in polar region.
  — nighttime LST close to surface air temperature, small angular dependence.
  — MODIS LST from AM & PM platforms will find more applications due to its diurnal information.

2. Theoretical background

- Theoretical background

— The radiance measured in MODIS band j can be expressed as

$$L(j) = t_1(j) \, \varepsilon(j) \, B_j(T_s) + L_a(j) + L_s(j) +$$

$$\frac{1 - \varepsilon(j)}{\pi} \, [t_2(j) \, \alpha_r \, \mu_0 E_0(j) + t_3(j) \, E_d(j) + t_4(j) \, E_t(j)]$$

where $\varepsilon(j)$ the band-averaged emissivity, $B_j(T_s)$ band-averaged Planck function for LST T_s, L_a atmospheric thermal path radiance, L_s scattered solar radiation path radiance, E_d the solar irradiance at surface, E_t the atmospheric downward thermal irradiance, $t_i(j)$, $i = 1, \dots 4$, are band effective transmission coefficients. E_0 is the solar irradiance incident on TOA (normal to the beam), μ_0 the cosine of the solar zenith angle,

and α_r, the BRDF anisotropy factor for the incident solar beam at MODIS view angle, is defined by

$$\alpha_r = \frac{\pi \, f_r(\mu; \mu_0, \phi)}{1 - \varepsilon(j)} \, .$$

— Accurate atmospheric radiative transfer simulation is the only practical way for LST algorithm development. It is too expensive and too difficult to develop LST algorithm measurements concurrent with satellite observations like for SST.

• Heritage

— split-window SST algorithm -> generalized split-window LST algorithm.

— AVHRR day/night LST method using 3 bands -> MODIS day/night LST method using 7 bands.

3. Description of the MODIS LST algorithms

- Generalized split-window LST algorithm (Wan & Dozier)

$$T_s = (A_1 + A_2 \frac{1-\varepsilon}{\varepsilon} + A_3 \frac{\Delta\varepsilon}{\varepsilon^2}) \frac{T_{31}+T_{32}}{2} +$$

$$(B_1 + B_2 \frac{1-\varepsilon}{\varepsilon} + B_3 \frac{\Delta\varepsilon}{\varepsilon^2})(T_{31} - T_{32}) + C ,$$

where $\varepsilon = 0.5 (\varepsilon_{31} + \varepsilon_{32})$ and $\Delta\varepsilon = \varepsilon_{31} - \varepsilon_{32}$.

— Objective - for land covers with stable known emissivities.

— New features for improving accuracy

— view-angle dependent,

— coefficients depend on ranges of T_a, cwv, T_s & ε

— use of knowledge base of band-emissivities,

— use MODIS products: cloud mask, atmospheric temperature & water vapor profiles, snow, land-cover, NDVI.

- Physics-based day/night algorithm (Wan & Li)
  - 7 day and 7 night observations in MODIS bands 20, 22, 23, 29, 31, 32 & 33
  - to retrieve 14 variables: day & night LST, 7 ε_i, BRDF anisotropy factor, day & night T_{air} and column water vapor,
  - Heritage - 3-band knowledge-based AVHRR day/night LST method (Li & Becker)
  - Two approaches: statistical regression & χ^2 fitting.
  - New features:
    — solar radiation as TIR source in the 3.5-4.2 μm range,
    — atmospheric downward radiation as source in the 3.5-14 μm range,
    — radiative transfer simulations made to establish LUT,
    — suitable for general surface conditions.

4. Atmospheric radiative transfer simulations

- ATRAD

— deals with accurate multiple scattering based on the interaction principle and adding/doubling method.

— uses an exponential-sum for each atmospheric molecular's transmission function. All cross terms in the product of exponential-sums for H_2O, $CO_2 +$ and O_3 are included in radiative transfer calculations.

- T & P dependences of water vapor band absorption

— step 1, separate exponential-sum tables are obtained for different temperature and pressure values (T, P) in the wide ranges of 200 to 300 °K and 1 to 1013.25 mb by using the "exponential-sum-fitting" method (Wiscombe and Evans, 1977) on data of MODTRAN transmission functions over a wide range of absorber amount W.

— step 2, the exponential-sum table at pressure $P_0 = 1013.25$ mb and temperature $T_0 = 296 °K$ is used as a base table to find the averaged ratio $R_i(T,P)$ for various W over each wave number interval of each exponential-sum table at given (T, P).

— step 3, to make quadratic regression analysis of $\ln[R_i(T,P)]$ against variables T/T_0, P/P_0, $\ln(T/T_0)$, and $\ln(P/P_0)$ to find generalized temperature and pressure scaling factors as coefficients of the regression equation.

• ATRAD + T & P dependence of band absorption

— advantage: giving reasonable band effective transmission coefficients, i.e., $t_1 \neq t_3 \neq t_4$.

— disadvantage: taking too much CPU time.

5. *Major concerns*

- The temperature range for band absorption coefficients needs to expand.

- Accuracy of water vapor continuum absorption and its temperature dependence.

- Computational efficiency.

- How to get the best accuracy-versus-speed tradeoff?

Observations of Polar Stratosphere Clouds with POAM II

M.D. Fromm[1], E.P. Shettle[2], J.S. Hornstein[2], J.D. Lumpe[1], R.M. Bevilacqua[2], S.Massie[3],
K.W. Hoppel[2]

1 - Computational Physics Inc., 2750 Prosperity Ave., Fairfax, VA 22031

2 - Remote Sensing Division, Code 7227, NRL, Washington, DC 20375-5351

3 - NCAR, Boulder, CO, 80307

Abstract

Observations of Polar Stratospheric Clouds [PSCs] with the Polar Ozone and
Aerosol Measurement [POAM II] solar occultation instrument will be described. POAM
II has been measuring the vertical distribution of aerosols, clouds, ozone, as well as
several other atmospheric species since October 1993. The cloud detection algorithm
used to identify PSCs from the POAM II measurements will be described along with a
presentation of some of the first two years of measurements, focusing on results from the
southern hemisphere. The frequency of PSC occurrence builds up during the during the
Antarctic winter reaching a peak of about 3/4 of all POAM II measurements during
September including a PSC. There is a strong longitudinal variation in the cloud
frequency, with a broad minimum centered near the international dateline [180°] and a
broad maximum centered about 320° W, where the PSC frequency is about twice that
near the minimum. In May the PSCs are observed as high as 28 km, with the altitudes
moving downward as the coldest air descends within the polar vortex, and by the end of
October nearly all are below 20 km.

POAM II - (Polar Ozone & Aerosol Measurement)

9 Channel Solar Occultation Instrument launched on the SPOT 3 Satellite

- Designed to measure long-term trends in ozone abundances at polar latitudes, and examine the morphology of spring-time ozone depletions in the polar regions.

- Measure stratospheric aerosol extinction profiles and obtain a climatology of Polar Stratospheric Clouds (PSC's).

- Make zonal average measurements of H_2O and NO_2 in the stratosphere.

- Make observations of the frequency of occurrence and optical thickness of high cirrus clouds.

SOLAR OCCULTATION MEASUREMENT GEOMETRY
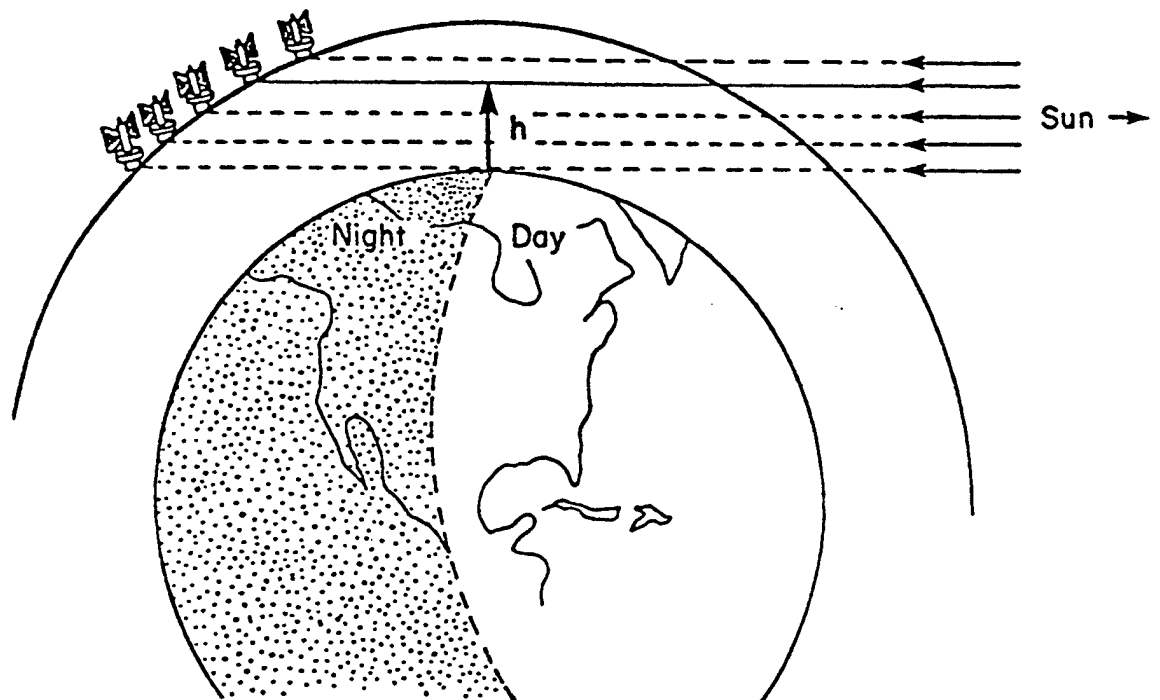
POLAR OZONE AND AEROSOL MEASUREMENTS (POAM II)

9 Solar Occultation Channels

Wavelength (nm)	Width (nm)	Primary Purpose
353.0	5	Aerosols
442.0	2	NO_2 Off
448.3	2	NO_2 On
600.0	15	Ozone
760.8	2	O_2 On
780.0	15	O_2 Off
920.0	2	H_2O Off
935.5	2	H_2O On
1059.0	10	Aerosols

POAM II Measurement Capabilities:

PARAMETER	HEIGHT RANGE (km)
Aerosols	10 - 40
O_3	10 - 60
H_2O	15 - 40
NO_2	20 - 40
Temperature	10 - 60

Vertical Resolution: 1 km

Atmospheric Extinction at 20 km

Channel	Purpose
353.0	rayleigh
442.0	NO_2 off
448.3	NO_2 on
600.0	O_3
760.8	O_2 on
780.0	O_2 off
920.0	H_2O off
935.5	H_2O on
1059.0	aerosol

POAM II

NRL/CPI
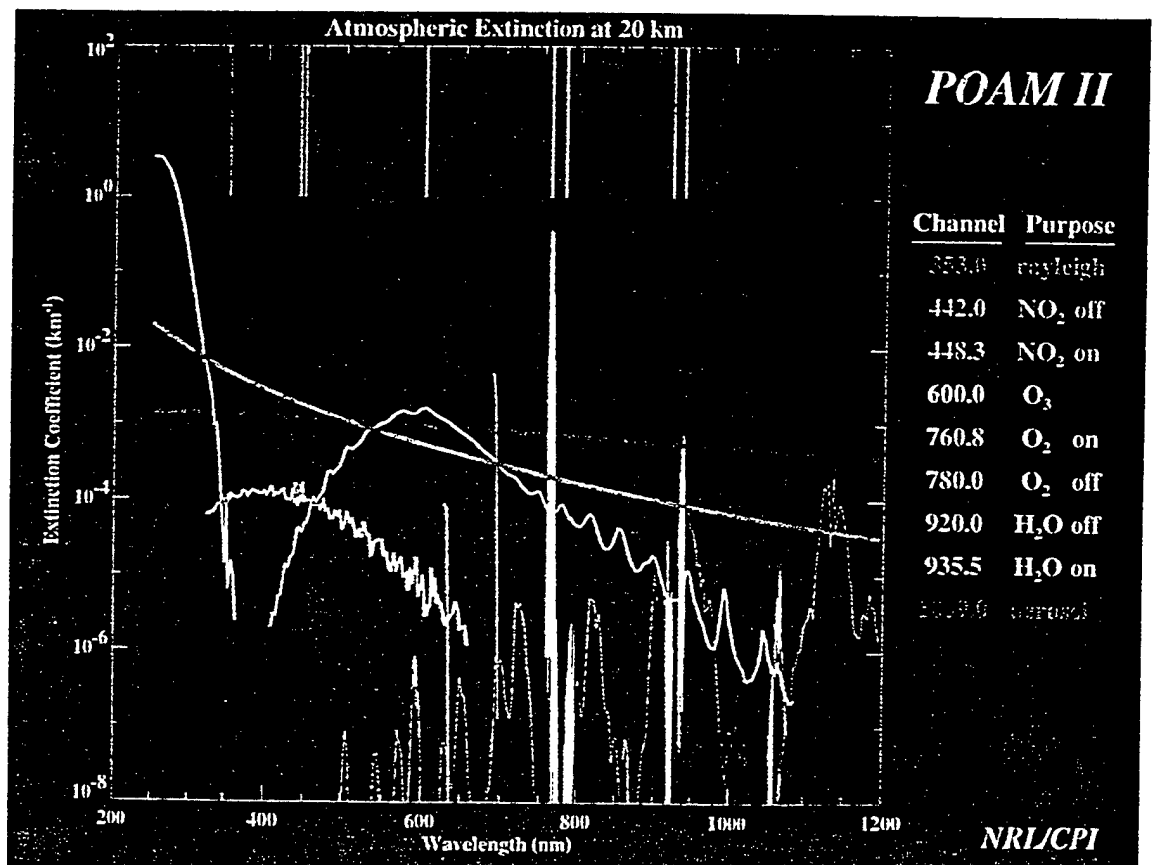
POAM II Polar Stratospheric Cloud [PSC] Detection Algorithm

* PSCs are manifested in two distinct profile signatures

1. Layer of high aerosol amount

 * Aerosol extinction is compared with a "clear air" profile value.
 * "Clear air" profile is computed monthly
 * PSC is detected if extinction exceeds 4 sigma of "clear-air" value between 13 - 30 km.
 * PSC altitude is that of the maximum normalized deviation.

2. High-altitude loss or start of sun track

 * Optically thick PSCs cause POAM sun tracker to delay onset of tracking until above PSC altitude.
 * PSC is detected when profile minimum altitude is at or above 17 km.
 * Upper limit of PSC height is the altitude where POAM sun tracker threshold is exceeded.

POAM II PSC DETECTION

- Aerosol Extinction Profile - 1059 nm channel

- Region of focus: 13 - 30 km

- "Clear Air " Screening is Based on Raw Signal Count Profiles

    - Raw Signals provide highest resolution of vertical structure & greatest distinction from aerosol extinction used in cloud screening

    - Use the 3 longest wavelength aerosol channels [780, 936, & 1060 nm]

    - Calculated for each month

    - Eliminate all profiles for which signal goes to 0 at above average altitude

    - Limit to profiles with monotonic signal decrease with decreasing altitude In all of the 3 long wavelength aerosol channels

Signal Counts for Clear, Layer, and High Zmin Example
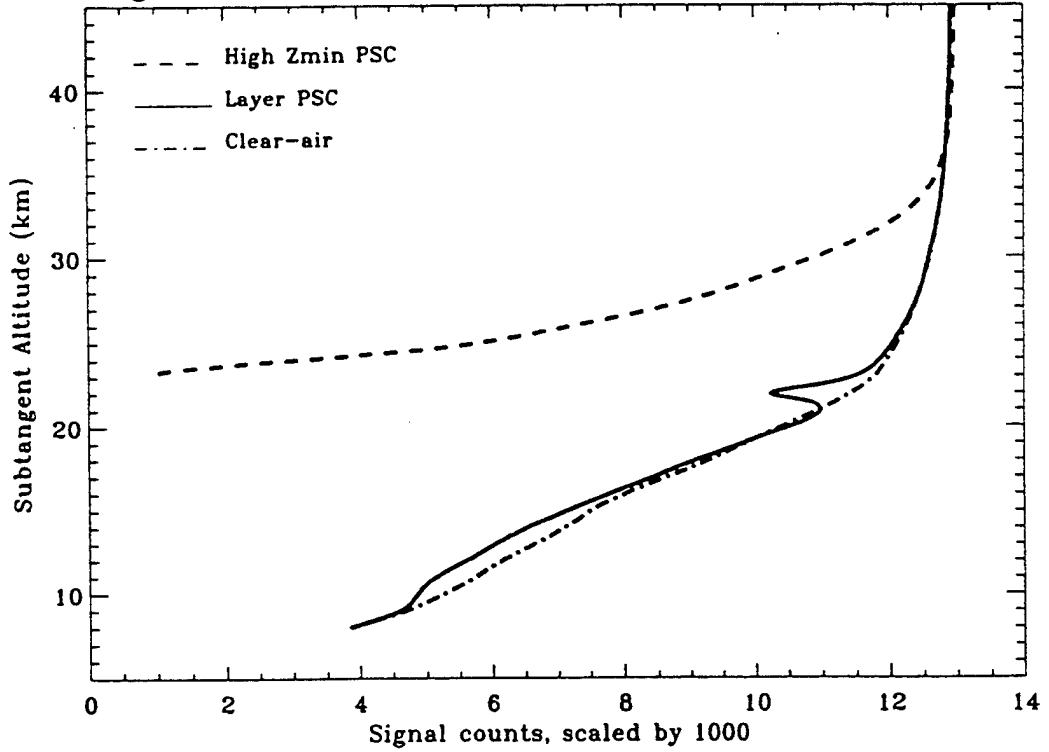
POAM II 1059nm Aerosol Exctinction, Northern Hemisphere January 1995

99
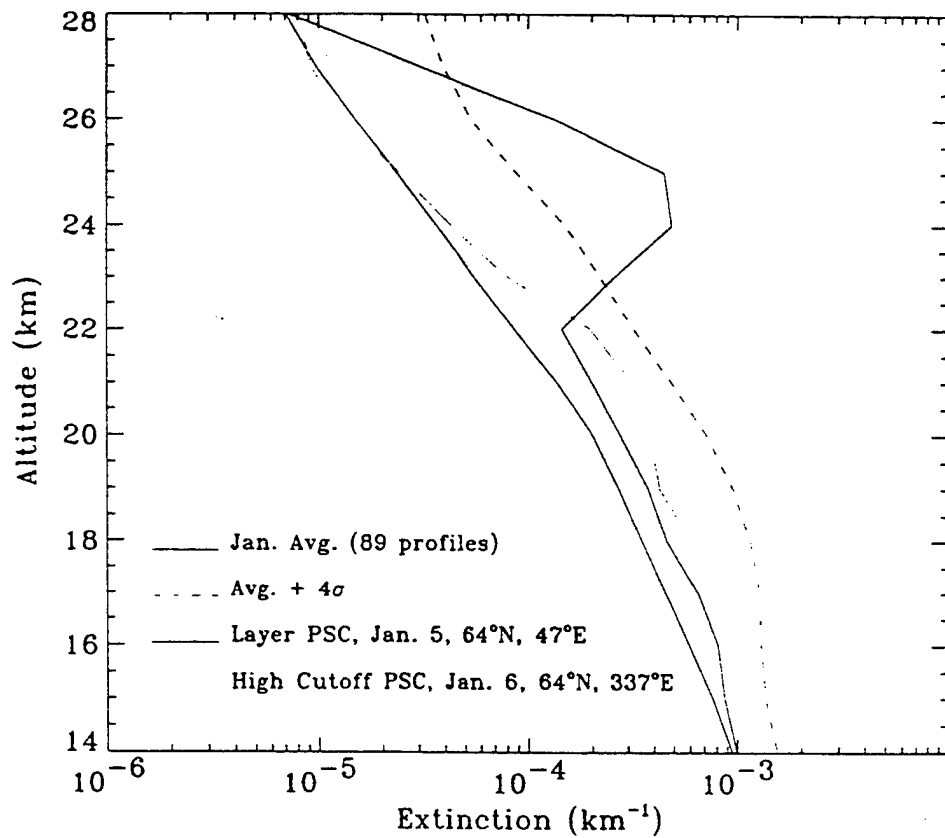
Avg. (solid) & 1σ (dashed) Extinction, Nov 93, Outside the Vortex (θ=450 K)
SAM II (red), POAM II (blue)
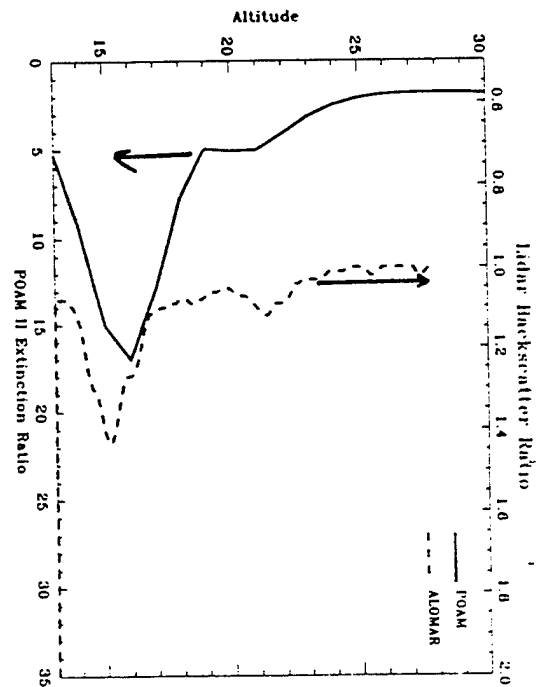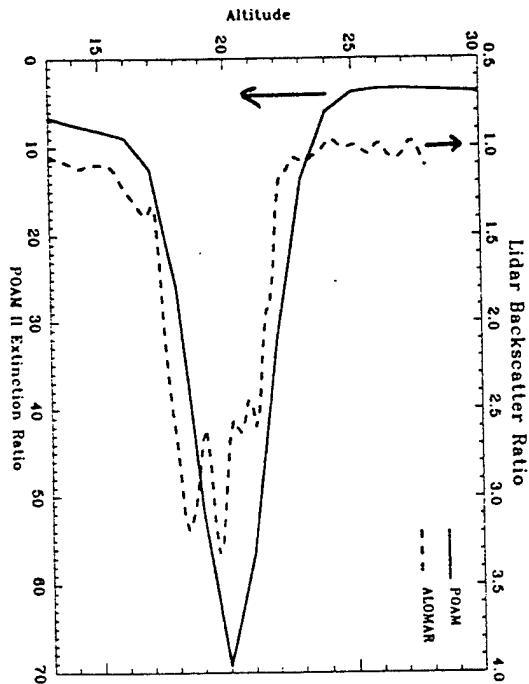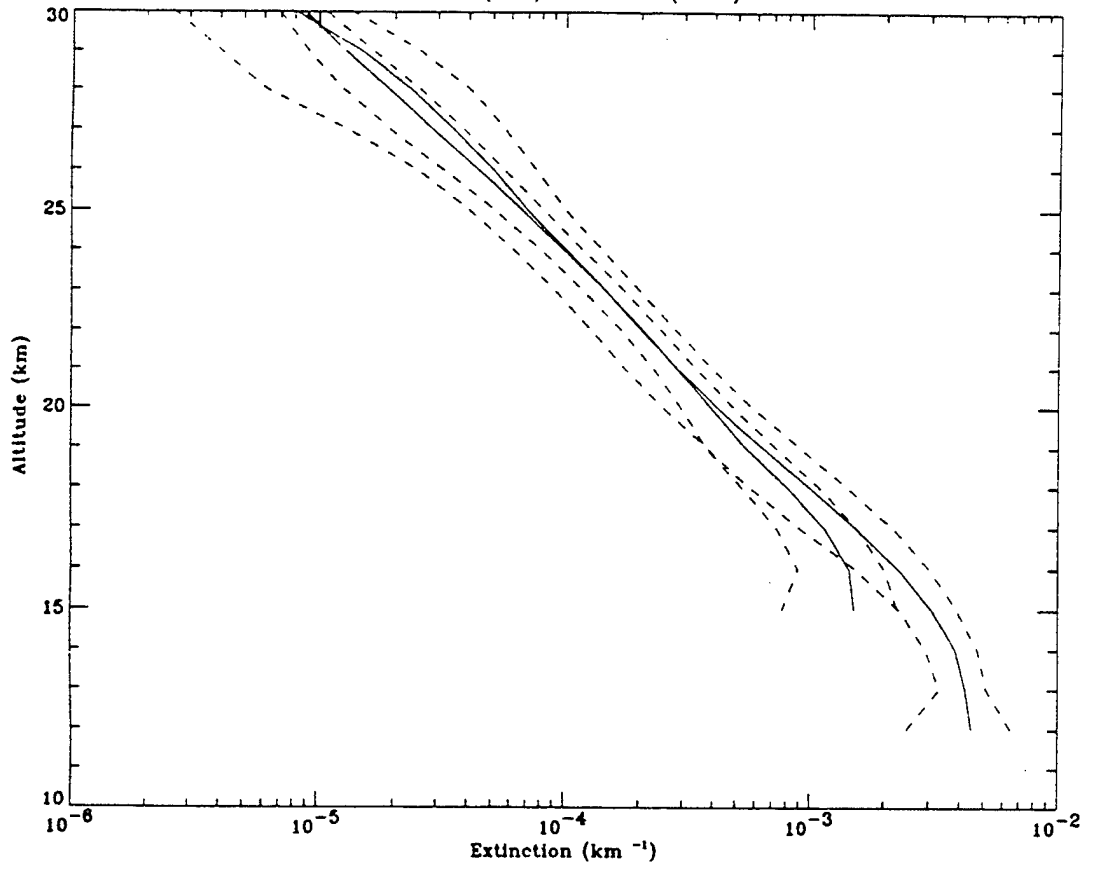
Polar Stratospheric Clouds Detected By POAM II (v44)

270

1 May through 30 Nov, 1995

180 .... 0 E

+ No PSC

● PSC

Polar Stratospheric Clouds Detected By POAM II (v44)

270
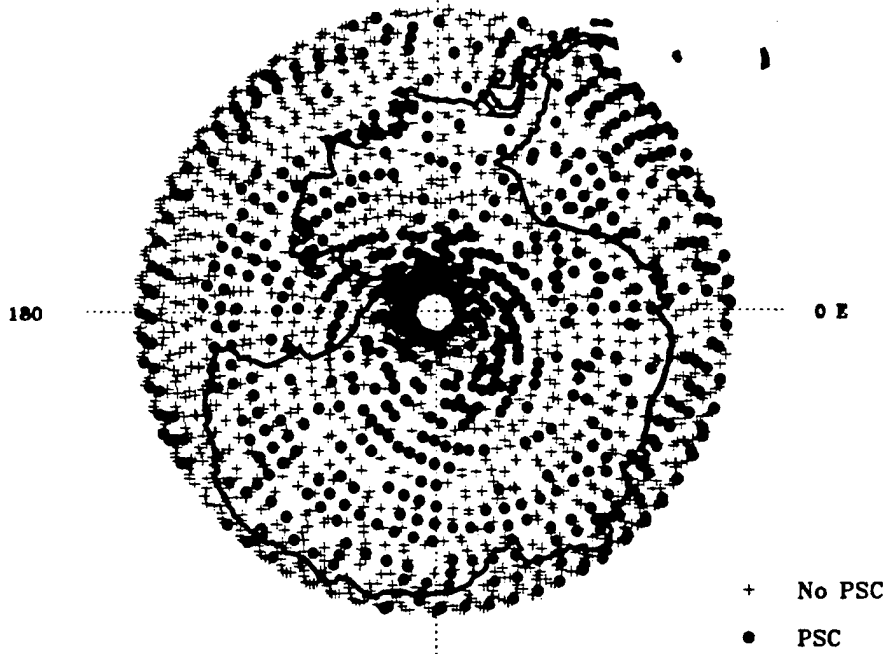
1 May through 30 Nov, 1994

180 .... 0 E

+ No PSC

● PSC

90

101
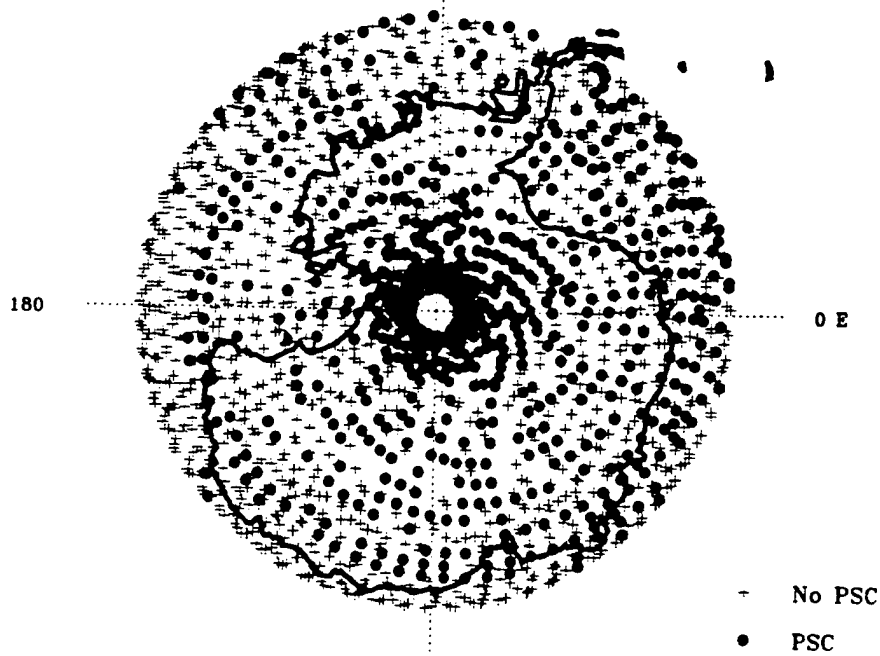
PSC Frequency, S. Hemi
1994(black), 1995(grey), SAM II(lined)

Percent of Total Events

80

60

40

20

0

M   J   J   A   S   O   N

May through November, 1994/1995
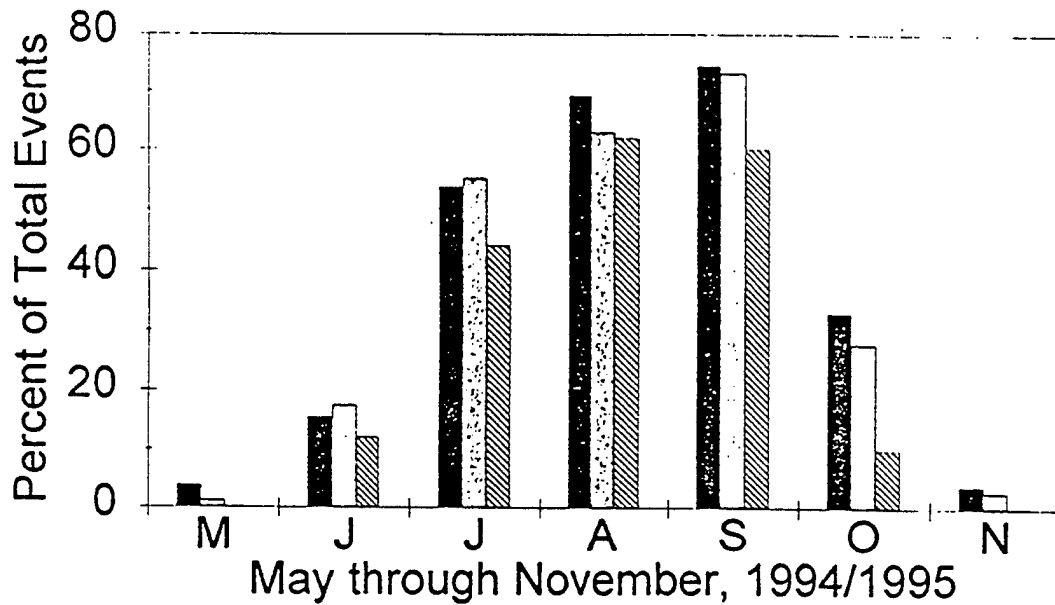
POAM II PSCs by Longitude
1994(blue) & 1995(green)

Frequency (%)

60

50

40

30

20

10

0

15   75   135   195   255   315

Longitude (30-degree bins)
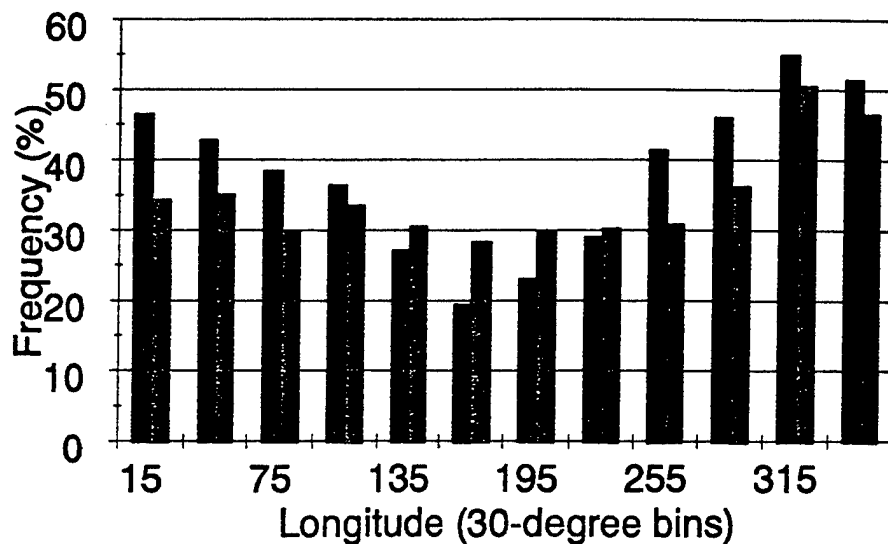
POAM II PSC Frequency
& Avg. 20-km Temperature

July 1994

July 1995

August 1994

August 1995
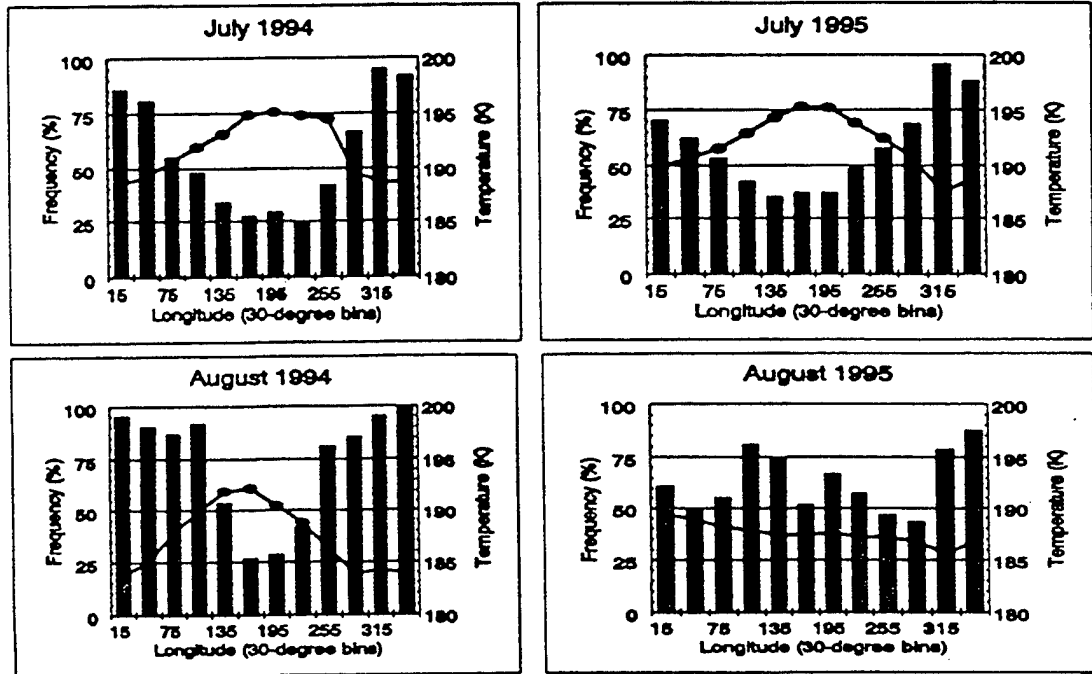
SH Weekly Avg. Temp. & Layer (diamond) + HiZmin (star) PSC Altitude, 1995
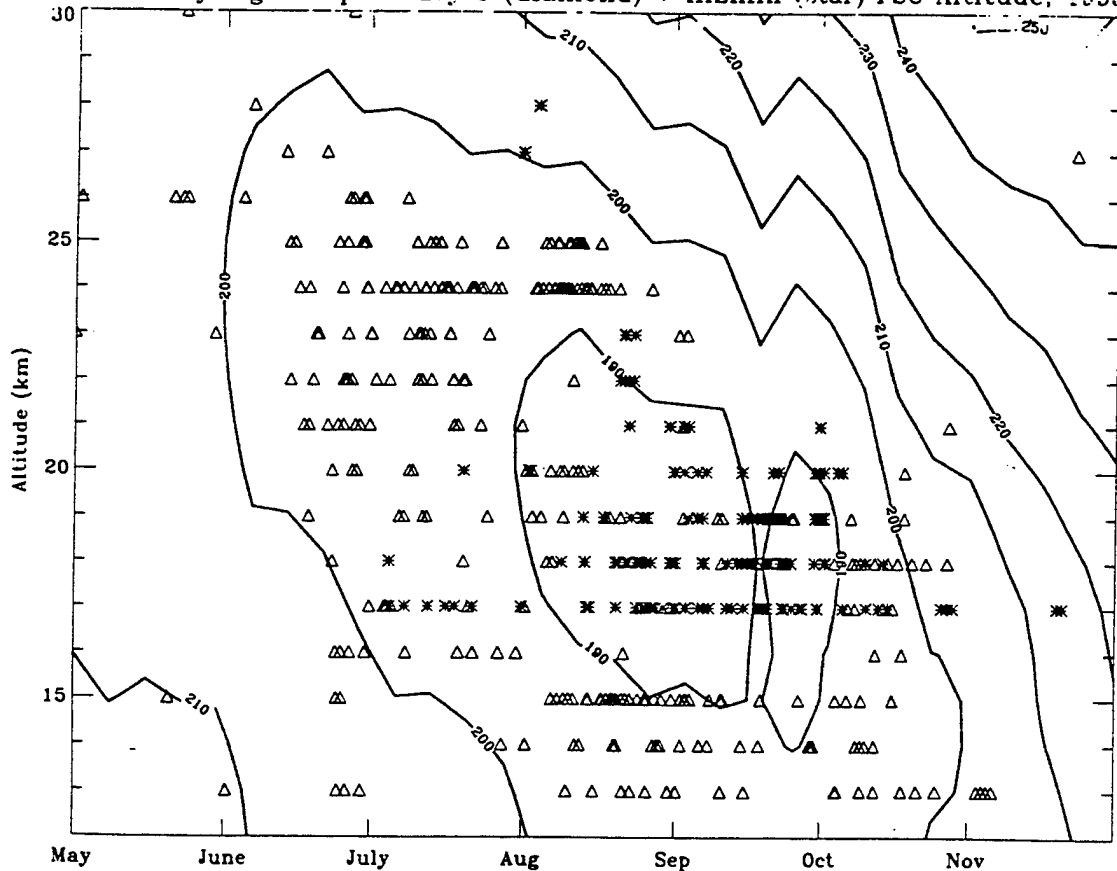
PSC Altitude, 1 May to 9 November 1994
POAM Detection Method

Background shade:
Temp < 195 K

Altitude (km)

May   Jun   Jul   Aug   Sep   Oct   Nov

Antarctic Fall/Winter/Spring, 1994

NMC Temperature (K)

POAM
NMC
Clear-Air Surrogate.

Altitude (km)

Extinction (km^{-1})
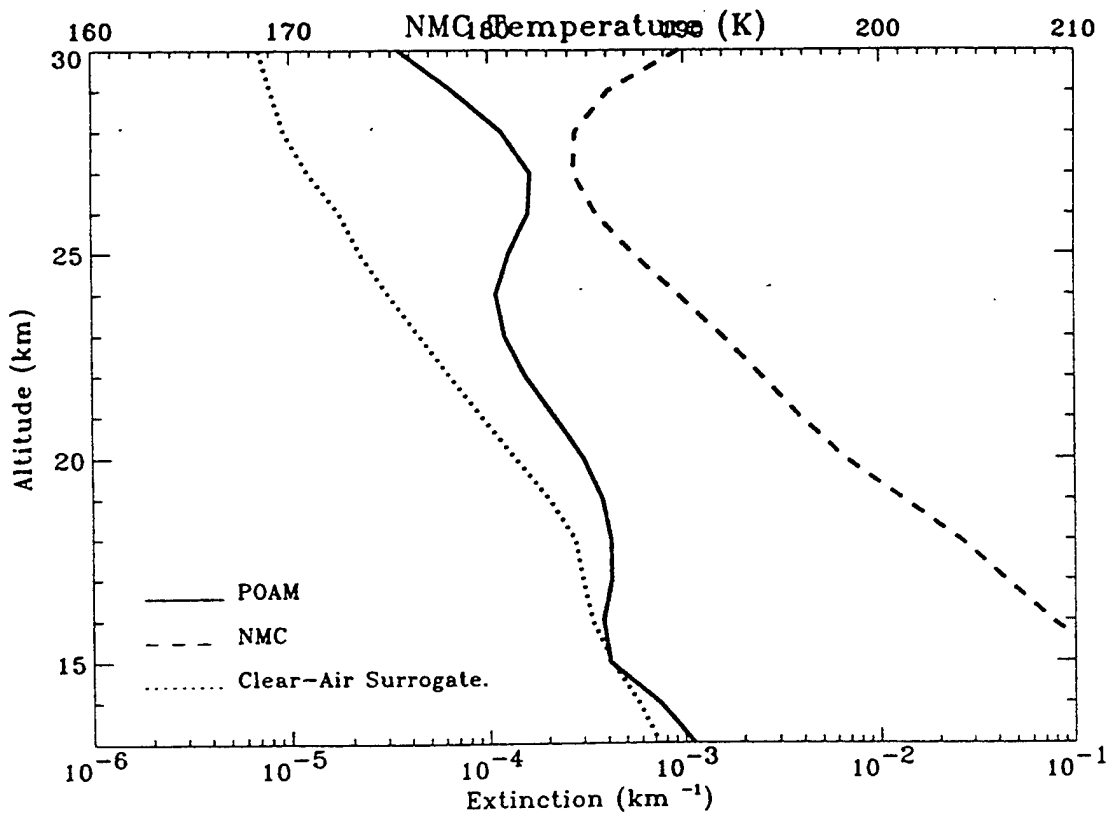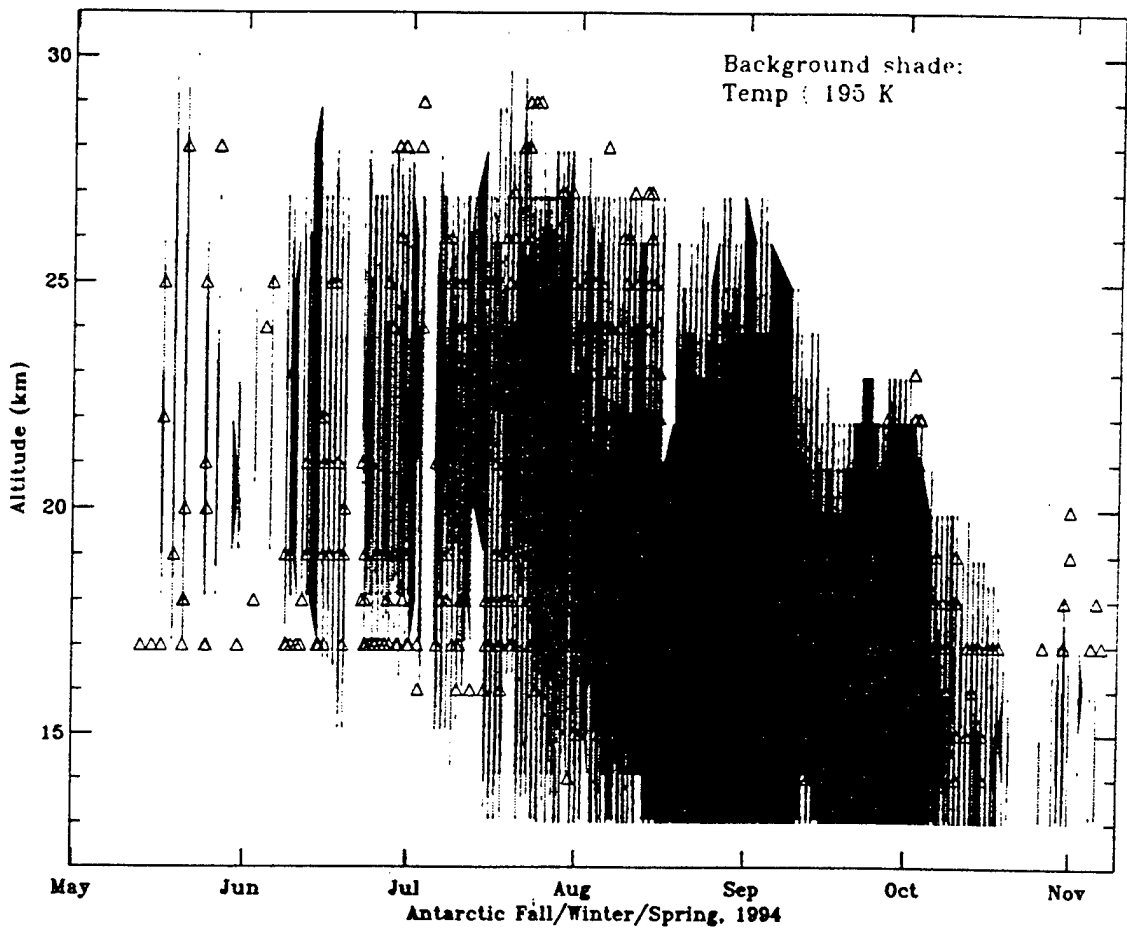
FUTURE WORK

- ● Study temperature dependence of PSC occurrence
  - Compare with lab studies of various combinations of H_2O / H_2SO_4 / HNO_3 at low temperatures

- ● Utilize wavelength dependence of POAM measurements
  - To infer particle size
  - As an additional test to separate PSCs from aerosols
  - Investigate feasibility of distinguishing Type I and Type II PSCs

- ● Look at PSC correlation with ozone depletion and dehydration
  - Trajectory analysis to follow individual air parcels (& changes in their chemistry) over time and with exposure to sunlight

References

"First results from POAM II: The Dissipation of the 1993 Antarctic Ozone Hole", R.M. Bevilacqua et al. (1995), *Geophys. Res. Letters.*, **21**, 909-912.

"Preliminary Results from POAM II: Stratospheric Ozone Densities at Northern Latitudes", C.E.Randall, et al., (1995), *Geophys. Res. Letters.*, **21**, 2733-2336.

"Observations of Clouds in the Polar Stratosphere and Polar Mesosphere from POAM II", Shettle, E.P., et al., page 138-145 in *Passive Infrared Remote Sensing of Clouds and the Atmosphere III*, Proceedings of SPIE Conference No. 2578, Ed. by D. Lynch & E.P.Shettle, 1995.

"Measurements of Antarctic Ozone by POAM II", Shettle, E.P., et al., page 306-312 in *Atmospheric Sensing and Modeling II*, Proceedings of SPIE Conference No. 2582, Ed. by R.Santer., 1995

"The Polar Ozone and Aerosol Measurement (POAM II) Instrument", W.Glaccum, et al., accepted for publication in *J. Geophys. Res.*, **101**, 1996.

"POAM II: Early Results and Comparisons with the COSPAR International Reference Atmosphere Models", E.P.Shettle, et al., accepted for publication in *Advances in Space Res.*, **18**, 1996.

"Preliminary Analysis of Southern Hemisphere POAM II Observations of Polar Mesospheric Clouds", D.J.Debrestian, et al., to be published in *J. Geophys. Res.*, 1996.

HIGH SPECTRAL RESOLUTION SOLAR RADIATIVE TRANFER: AN APPROXIMATE METHOD FOR ABSORBING AND SCATTERING ATMOSPHERES.

P. DUBUISSON,† J.C. BURIEZ,§ and Y. FOUQUART§

† Laboratoire d'Optique Atmosphérique
Université du Littoral, Station marine de Wimereux, 62930 Wimereux, France
§ Laboratoire d'Optique Atmosphérique
Université des Sciences et Technologies de Lille, 59655 Villeneuve d'Ascq Cedex, France

1   Introduction

Most of satellite instruments of the new generation have a very high spectral resolution. Interpreting the observations collected by satellite instruments often requires sophisticated software tools that can simulate the observed signal at a resolution similar to the satellite instrument. It is therefore necessary to develop high resolution radiative transfer codes capable of simulating instrument signals that correspond to radiation emitted and reflected from heterogeneous atmospheres with realistic absorbing and scattering properties.

From a theoretical point of view, calculating the exact outgoing radiances at high spectral resolution is not problematic. It requires designing an algorithm in which gaseous absorption is computed with a line by line model and scattering by clouds and aerosols is calculated by accurately solving the Radiative Transfer Equation (RTE).

While the scattering properties of clouds or aerosols vary slowly as a function of frequency, this is not the case for absorption. When the absorption-scattering interactions become non-negligible, employing a complex multiple scattering model for each frequency makes the computation time extremely long and, consequently, approximate methods become necessary. We have then developed a fast, accurate method for calculating radiative transfer in the shortwave spectral region. The method enables one to simulate the monochromatic radiances, similar to those observed by satellite instruments, for an atmosphere separated into plane and homogeneous layers.

2   Approximate method

2.1   Scaling approximation applied to far line wings

In the method interactions between molecular absorption and scattering are treated using a Scaling Approximation (Goody, 1964) that can be applied when the absorption coefficient $k_\nu(z)$, which varies as a function of the frequency ν and the altitude z, can be decomposed such that $k_\nu(z) = h(z)k_\nu(z_o)$. This decomposition, however, is only accurate for the far line wings. In this case and for a given atmosphere, the exact radiance is calculated for the profile $h(z)$, which represents the vertical variation of the absorption profile for the line wings and for some

106

absorption coefficients $k_\nu(z_o)$ distributed in the interval $[0, +\infty[$. Due to the slow spectral variation of atmospheric scattering parameters, these calculations can be considered constant for large spectral bands. In the line wings the monochromatic radiances can then be obtained accurately through interpolation.

2.2 Generalization to the entire line (Modified Scaling Approximation)

This approximation is then extended to the entire line. However, in the more general case where the line has the full Lorentz shape, the dependence of the absorption coefficient with frequency, on the one hand, and with the pressure and temperature, on the other, are fully coupled. An additional complication derives from the fact that, at high altitudes, the Voigt line shape applies and the absorption coefficient has not a simple analytical form. In this case, the absorption coefficient can not be decomposed into the product of a term independent of the frequency and a term independent of the altitude. The Scaling Approximation is then modified in order to compensate for errors it introduces to the line centers and the intermediate absorbing regimes: $k_\nu(z) = h(z)k_\nu^*(z_o)$, thus giving a Modified Scaling Approximation (MSA). The modified absorption coefficient $k_\nu^*(z_o)$ is calculated in two steps:

(1) For reference, consider the case of a non-scattering atmosphere with reflection occurring at altitude Z_s. Then, in any regime of the line, a modified absorption coefficient $k_\nu^*(z_o)$ can be defined formally if we suppose that the absorption must be the same for the exact vertical absorption profile and for the line wing absorption profile $h(z)$:

$$k_\nu^*(z_o) \int_{Z_s}^{Z^{toa}} h(z)\rho(z)dz = \int_{Z_s}^{Z^{toa}} k_\nu(z)\rho(z)dz. \tag{1}$$

where Z^{toa} is the top of the atmosphere altitude. In the case of a non-scattering atmosphere Z_s is the ground altitude. $\rho(z)$ is the absorbing gas density.

(2) In scattering atmospheres, reflections may occur at any level depending on the scattering events. There exists, however, an atmospheric region where photons originate preferentially. Photon penetration in the atmosphere depends both on the scattering and absorbing characteristics of the atmosphere. Let us then call Z_ν^* the equivalent reflecting level at frequency ν. Then,

$$k_\nu^*(z_o) = \frac{\int_{Z_\nu^*}^{Z^{toa}} k_\nu(z)\rho(z)dz}{\int_{Z_\nu^*}^{Z^{toa}} h(z)\rho(z)dz}. \tag{2}$$

For a given atmosphere, equivalent reflecting levels are calculated by accurately solving the RTE, for some values of absorption coefficient, for which there is no vertical dependence. Monochromatic reflecting levels are interpolated according to absorption coefficients computed with the line by line model.

Approximate radiances are then interpolated from exact radiances, according to the modified absorption coefficient, which is directly performed from the line by line model.

3 Application to realistic absorption spectra

3.1 Study characteristics

Validating the approximations requires comparing the derived results with exact results obtained for a variety of conditions. We considered water vapor and oxygen absorption, whose concentrations are variable and constant, respectively, as a function of altitude. The atmospheric model employed is the Mac Clatchey et al. (1972) tropical atmosphere. The spectroscopic data for these two gases are derived from the GEISA database (Gestion et Etude des Informations Spectroscopiques Atmosphériques) from the Laboratoire de Météorologie Dynamique (LMD) of Paris (Husson et al., 1991). Using these data we employed the LMD STRANSAC line by line model (Scott, 1974) to obtain the monochromatic absorption coefficients $k_\nu(z)$ for each atmospheric layer. Figure 1 displays the atmospheric transmissions calculated using the STRANSAC model in the spectral intervals selected. The STRANSAC model, originally developped in the longwave region, was extended to the shortwave in collaboration with the LMD. Figure 2 shows comparisons between STRANSAC model and ICRCCM data or MODTRAN results.

The RTE resolution in a horizontally homogeneous scattering atmosphere can be achieved, in the plane-parallel approximation, using the discrete ordinates method (DOM) (Stamnes et al., 1988). Two atmospheric models were considered : (1) a tropical atmosphere with a cirrus cloud ($\tau = 2$) and (2) a cirrus cloud overshadowing low clouds ($\tau = 8$). We have also included molecular and aerosol scattering. We have considered a lambertian reflectance for the surface.

3.2 Results and conclusions

We tested the MSA method by comparing the approximate results with those derived from 'exact' calculations. Using the line by line model resolution ($\simeq 0.01\ cm^{-1}$), we calculated the radiances and plotted the deviations with respect to the radiance without absorption I_c:

$$\frac{\Delta I_\nu}{I_c} = \frac{(I_\nu^{app} - I_\nu)}{I_c} \tag{3}$$

where I_ν^{app} and I_ν represent the approximate and exact monochromatic radiances, respectively. The results are presented in figure 3. For all the cases considered, the maximum deviations remain generally less than 3% and usually less than 1%. The maximum errors occur at the line centers, where the approximations are the crudest.

When using resolutions commonly employed in experiments, integrating the results calculated at the nominal line by line resolution provides a favorable compensation in errors (figure 4); in the general case, the accuracy is better than 1% for resolutions between 0.5 and 5 cm^{-1} and better than 0.1% for a resolution $\simeq 10\ cm^{-1}$.

One can note, however, larger errors reaching 6% in the monochromatic case when one considers the specific case of oxygen absorption during conditions of high clouds and low solar zenith and satellite viewing angles. Indeed, under these conditions the absorption-scattering interactions take place primarily above the high clouds where the absorption profile is principally Voigt shape, and for which our approximations are less verified. The MSA method is consequently much more accurate when the absorption-scattering interactions take place in the lower atmospheric layers.

The simple approximations used in the MSA method can be conveniently applied to a line by line model to provide fast, accurate results and a considerable decrease in computation time of about 200 compared to the exact method. The main applications of such a code are primarily theoretical, for developing and validating simpler, low spectral resolution models, or more directly for studies needing high accuracy and high spectral resolution. Comparisons with satellite observations are of course also possible. As instrument resolutions continue to increase, employing our code will become more useful as it can simulate satellite-observed radiances at the same resolution. Although the MSA method is well adapted to simulate radiances for satellite instrument observations, it does not allow one to estimate radiances at the surface, where the equivalent reflection level has no physical meaning.

REFERENCES

- R. M. Goody, *Quart. J. Roy. Meteor. Soc.* **78**, 165 (1952).
- N. Husson, B. Bonnet, N. A. Scott, and A. Chédin, Management and study of spectroscopic information: the GEISA program, *J. Quant. Spectrosc. Radiat. Transfer*, vol 48, No 5/6, pp. 509-518, 1992.
- R. A. McClatchey, R. W. Fenn, J. E. A. Selby. F. E. Volz, and J. S. Garing, *Optical properties of the atmosphere*, p. 98, Rep. AFCRL-72-0497, Hanscom Air Force Base, Bedford, Mass. (1972).
- N. A. Scott, *JQSRT*,**14**, 691 (1974).
- K. Stamnes, S.C. Tsay, W. Wiscombe, and K. Jayaweera, *Appl. Opt.* **27**, 2502 (1988).
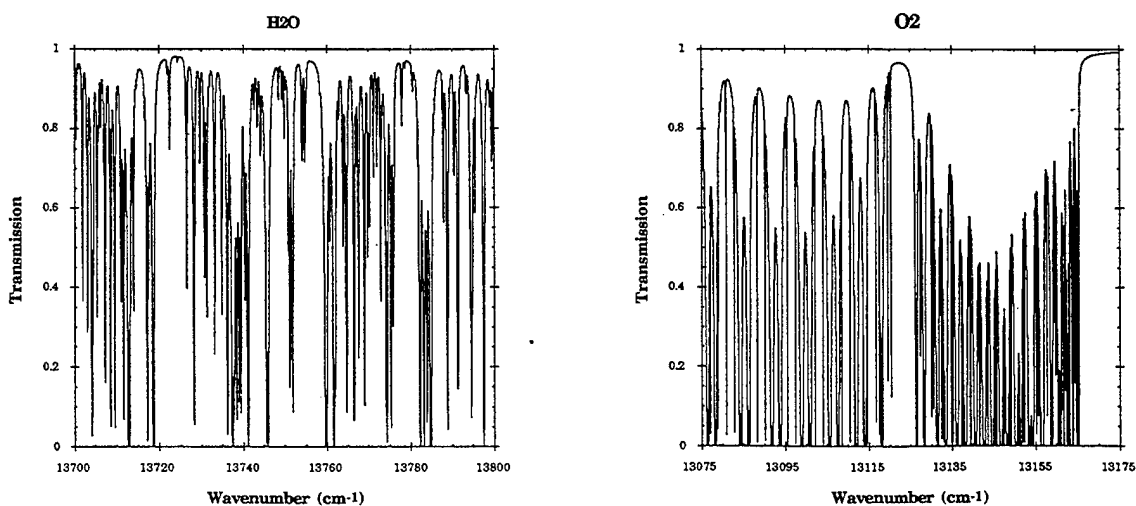
Figure 1: Transmittance spectra through a tropical atmosphere in the water vapor and oxygen spectral intervals used for the comparisons.

ATMOSPHERIC TRANSMISSION

Purely absorbing cases: surface albedo 0.2			
Case	Gases	Atmosphere	Zenith angle, deg
1	H_2O line absorption only	mid-latitude summer	30
2	H_2O line absorption only	mid-latitude summer	75
3	H_2O line absorption only	tropical	30
4	H_2O line absorption only	tropical	75
5	H_2O line absorption only	sub-Artic winter	30
6	H_2O line absorption only	sub-Artic winter	75
7	H_2O, O_2, CO_2 (300 ppmv)	mid-latitude summer	30
8	H_2O, O_2, CO_2 (300 ppmv)	mid-latitude summer	75
9	H_2O, O_2, CO_2 (300 ppmv)	tropical	30
10	H_2O, O_2, CO_2 (300 ppmv)	tropical	75
11	H_2O, O_2, CO_2 (300 ppmv)	sub-Artic winter	30
12	H_2O, O_2, CO_2 (300 ppmv)	sub-Artic winter	75

Downward flux at the surface (W/m^2)			
Case	LBL1	LBL2	STRANSAC
1	1014.2	1009.7	1013.1
2	286.2	283.9	284.1
3	999.3	993.1	996.0
4	281.0	277.9	277.9
5	1089.5	1085.0	1090.9
6	313.7	312.0	313.8
7	1006.5		1004.8
8	282.7		280.2
9	991.8		988.0
10	277.6		274.1
11	1080.9		1081.7
12	309.7		309.3

LBL1 and LBL2 refer to ICRCCM line-by-line calculations.
LBL refers to the STRANSAC line-by-line model.
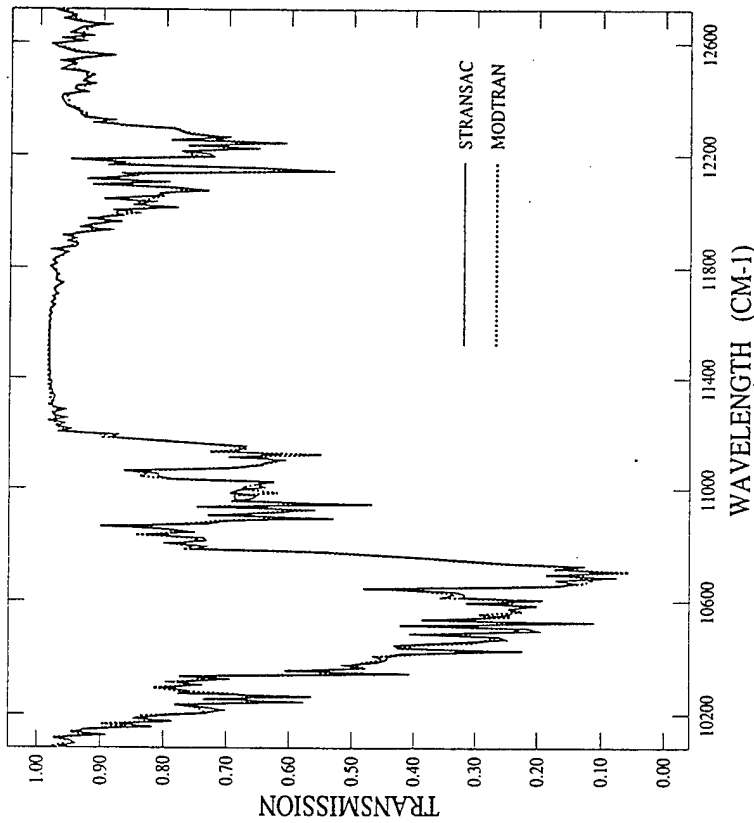
Figure 2: Comparisons between STRANSAC line-by-line model and ICRCCM data (Fluxes are integrated over the total solar spectrum) or MODTRAN transmissions (with a spectral resolution of 10 cm-1)
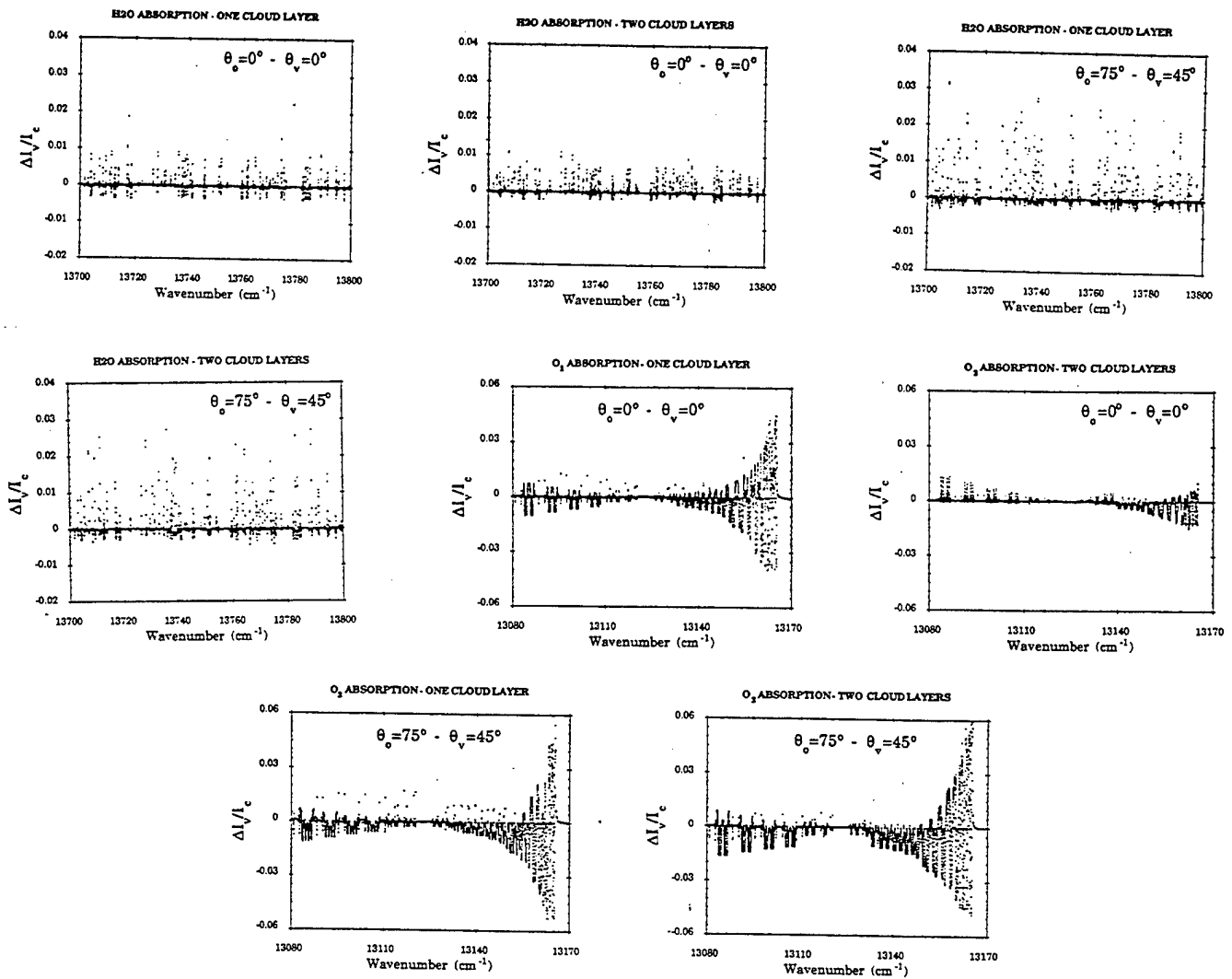
Figure 3: Deviations between exact and approximate line profiles I_ν/I_c, due to the water vapor and oxygen absorption. The deviations are shown with the line-by-line model resolution.
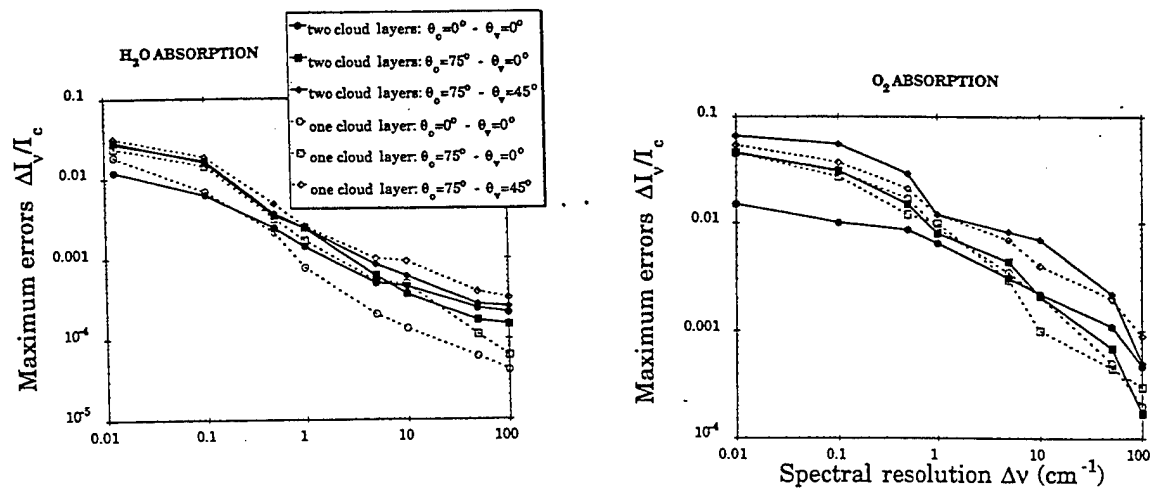
Figure 4: Maximum errors $\Delta I_\nu/I_c$ in the approximate profiles I_ν/I_c as a function of the spectral resolution $\Delta\nu$.

Intercomparison of Infrared Optical Constants of Various Aerosol Substances

W. G. Egan and J. Jr. Joseph, Natural Sciences Department,

York College/City University of New York

Jamaica, NY 11451

E-Mail: EGAN@YCVAX.YORK.CUNY.EDU

ABSTRACT

The absorption and refractive portions of the infrared complex index of refraction of various aerosol sands and soils were determined in the wavelength range 2.5 to 50 μm. Measurements of the reflection and transmission of KBr pellet samples were analyzed using the Kubelka-Munk radiative transfer theory to separate the scattering from the absorption. Samples consisted of aerosol particles, Sahara and Sinai Desert sands, coral and silica sands, and farm soil. The data are presented graphically for easy comparison. The variations between the indices of the samples influence atmospheric radiative transfer processes in different regions of the globe.

INTRODUCTION

An essential component in the LOWTRAN and MODTRAN atmospheric models is the optical properties of aerosols; these have been determined in the infrared spectral region using samples and powders in compressed KBr pellets (Ref. 1). It has been pointed out by Steyer et al (Ref. 2) that the KBr pellet technique was unreliable to determine quantitative absorption values. In this report we examine quantitatively the reliability of determining

112

absorption using standard glass filter powders in the ultraviolet to the near infrared; we then apply scattering theories (the Kubelka-Munk {K-M} and the Modified-Kubelka-Munk {M-K-M}) (Ref. 3) to drastically enhance by orders of magnitude the accuracy of determination of the absorption portion of the refracive index of powders and other scatterers using transmission and reflection measurements of KBr pellets. In an extension of these measurements from the near infrared to the far infrared, an intercomparison is then made of various powders of the absorption indices using the K-M theory. Further, we examine the reliability of Brewester angle determination of the refractive portion of the index of refraction of compressed powders.

RESULTS

Figure 1 shows the results of Brewster angle measurements of the refractive indes of compressed powders of Al_2O_3 with sizes 0.05, 0.3, 1.0, and 3 μm. The sizes were carefully quality controlled because the powders are used as polishing media. It is seen that there is a significant variation between particle sizes at different wavelengths (Ref. 4); the n_d=1.773. Thus, for accurate measurements of the refractive index, sub-micron sized are desirable. The explanation of these effecs is in the effective medium theory (Ref. 4). We reported the optical constants Of Sahara sand, volcanic ash, and water soluble aerosols which showed 1 to 2 orders of magnitude less "absorption" than the Volz measurements (Ref. 1). The differences are the result of scattering not included in the Volz analysis (Ref. 1). To illustrate the point, we used a standard Corning CS1-64 glass (Table 1) both as a sintered powder

(bubble glass) and as a powder contained beteen microscope cover glasses. The transmission and reflection of both of these samples was measured; from the transmission , the bulk absorption was determined. A comparison with the bulk glass vlues (α_{calc}), and the α was also determined using the K-M and M-K-M theories; the discrepancy betweem α_{calc} and the bulk values show up to one order of magnitude difference for the bubble glass and up to two orders of magnitude for the powder.Further, in Table 2, comparisons of the mass absorption coefficients of KBr pellets with a layered glass posder coating with uniformly distributed powder,with diffuse transmission measurements made on an integrating sphere and by point by point measurements show instances over two orders of magnitude differences. The use of the K-M or M-K-M theories drastically reduce the dicrepanies.Figure 2 shows the relative transmissions of two Sahara sand samples on which the calculation of absorption is made using the K-M theory;the two sands are different. Figure 3 shows the refractive indices of a variety of samples based on the use of the K-M scattering theory on aerosol particles, Sinai and Sahara Desert sands, Coral and silica sands,and a Long Island Farm soil.The data are presented graphically for easy comparison.

REFERENCES

1. F. E. Volz, "Infrared Optical Constants of Ammonium Sulfate, Sahara Dust, Volcanic Pumice, and Flyash", Applied Optics, 12, 564-568 (1973)

2. T. R. Steyer, K. L. Day, & D. R. Huffman, "Infrared Absorption by Small Amorphous Quartz Spheres", Applied Optics, 13,

1586-1590 (1974)

3.W. G. Egan and T. W. Hilgeman,"Optical Properties of Inhomogeneous Materials", Academic Press,New York, 235pp, (1974)

4.W. G. Egan & D. E. Aspnes, "Finite-wavelength effects in composite media", Physical Review, B, 26, 5313-5320 (1982)

5.W. G. Egan & J. Jr.Joseph, "Infrared Optical Constants of Sahara Sand, Volcanic Ash, and Water Soluble Aerosols", Proceedings of 18th Annual Review of Atmospheric Transmission Models, Air Force Phillips Laboratories, Lexington, Massachusetts, 6-8 June 1995

Comparison of Absorption and Scattering Coefficients for Standard Glass Samples (Contained in KBr Pellets)[a]

Table 1

λ	Method[b]	Sample[c]	n_D[d]	α (cm^{-1})	s (cm^{-1})	α_{bulk} (cm^{-1})	$\alpha_{MKM}/\alpha_{bulk}$	α_{bulk}/s ($\times 10^4$)	α_{calc} (cm^{-1})
		CS1-64							
0.400	S	L	1.477	8.00	913	0.16	50.0	1.75	160
	P	L		3.64	868		22.1	1.84	
	S	U		11.76	429		73.5	3.73	
	P	U		7.79	301		48.8	5.32	
0.600	S	L		12.94	644	9.2	1.41	143	146
	P	L		8.83	657		0.96	141	
	S	U		22.29	287		2.42	320	
	P	U		15.71	222		1.71	417	
0.633		CS5-61							
	S	L	1.54	21.85	799	14.7	1.5	184	136
	P	L		24.94	878		1.7	168	
	S	U		22.70	191		1.6	770	
	P	U		29.43	185		2.0	795	
		CS4-77							
	S	L	1.558	59.76	531	37.0	1.6	697	178
	P	L		55.95	452		1.5	818	
	S	U		74.76	106		2.0	3490	
	P	U		76.80	70		2.1	5280	

Modified KM theory (α, s, α_{bulk} columns)

[b] S, Integrating sphere; P, point-by-point angular measurement.
[c] L, Layered sample; U, uniformly distributed sample.
[d] Sodium D-line index, n_D

Corning CS1-64 Glass Data Analysis

Table 2

Sintered bubble glass						Powder				
KM		Modified KM				Bulk	KM		Modified KM	
α (cm^{-1})	s (cm^{-1})	α (cm^{-1})	s (cm^{-1})	α_{calc} (cm^{-1})	$\lambda_{\mu m}$	α (cm^{-1})	α[b] (cm^{-1})	s (cm^{-1})	α[b] (cm^{-1})	s (cm^{-1})	α_{calc} (cm^{-1})
1.6	9.5	0.72	23	19.0	0.400	0.16	7.8	161	2.8	442	342
8.3	2.2	13.8	5.0	37.7	0.600	9.2	27.1	152	11.6	377	568
1.7	3.8	1.09	9.1	12.9	0.907	0.21	2.8	188	1.15	477	26.9
2.9	3.1	2.3	8.3	16.8	1.5	0.52	8.2	135	3.2	340	21.9

115
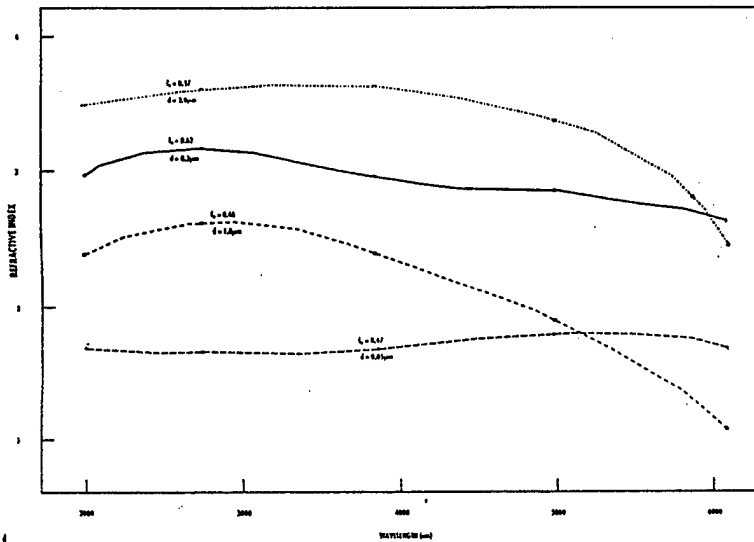
Fig. 1 Refractive Index of Compressed Pellets of Al_2O_3 determined
by Brewster Angle Tecnique
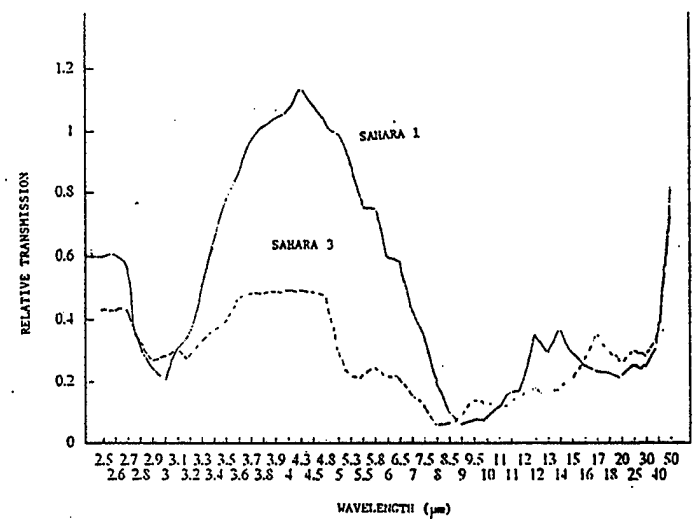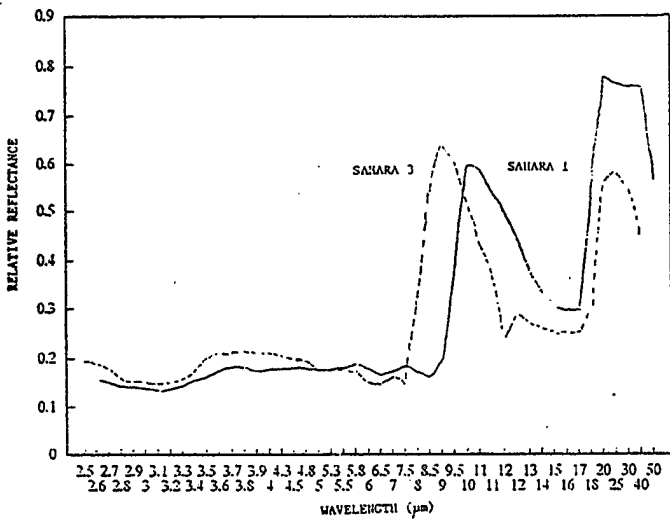
Fig. 2 Relative transmission and reflection of two types of Sahara
sands determined on a Perkin-Elmer recording spectrophotometer
(#1:Azelik flood plain; #3: Amakon dune sand from Tenere Desert)
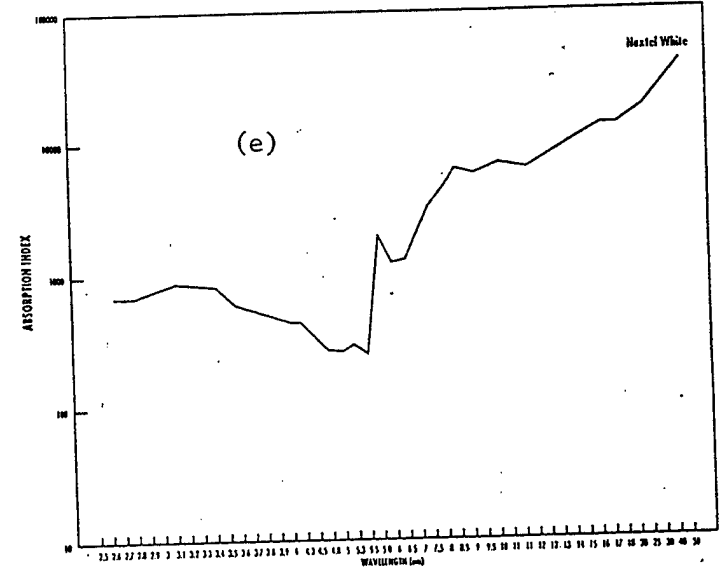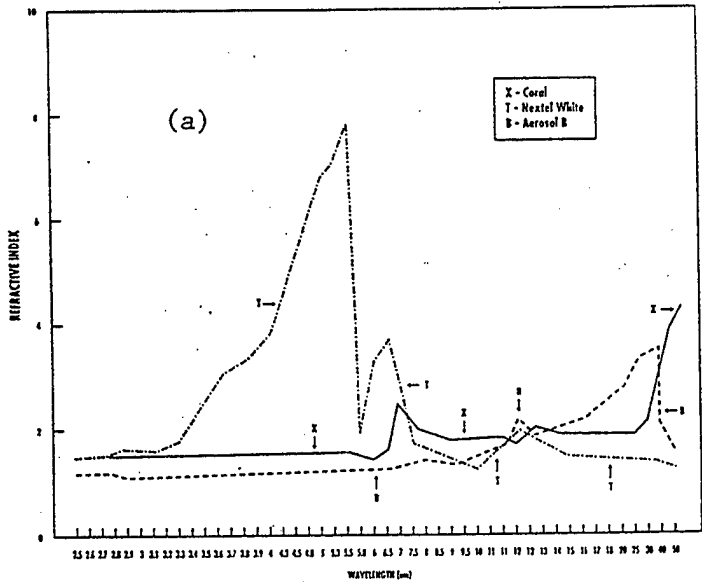
Fig. 3 Figs. a-d: Refractive index of various substances on a compressed KBr pellet
Figs. e-h Absorption index (multiplied by 10^4)of various substances on a
compressed KBr pellet   116

Fig. 3 Figs. a-d: Refractive index of various substances on a compressed KBr pellet
Figs. e-h Absorption index (multiplied by 10^4)of various substances on a
compressed KBr pellet

117
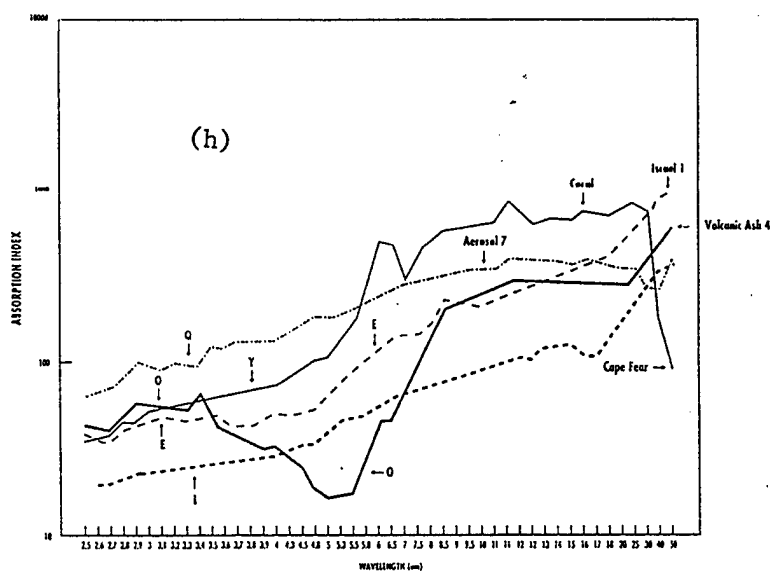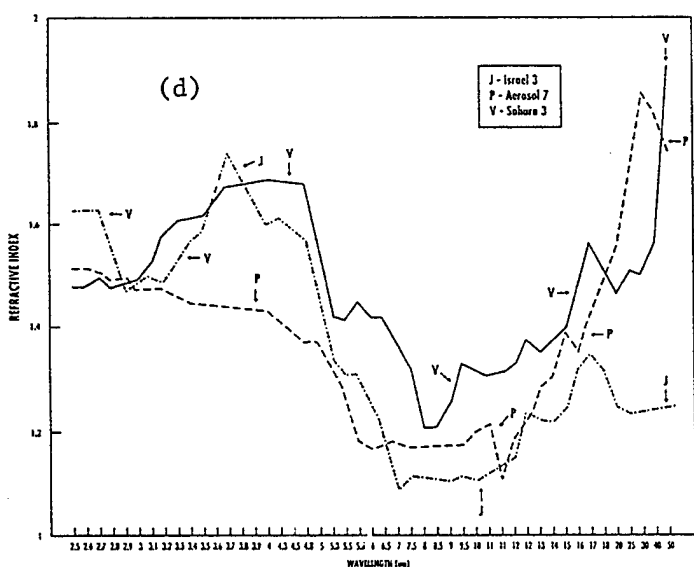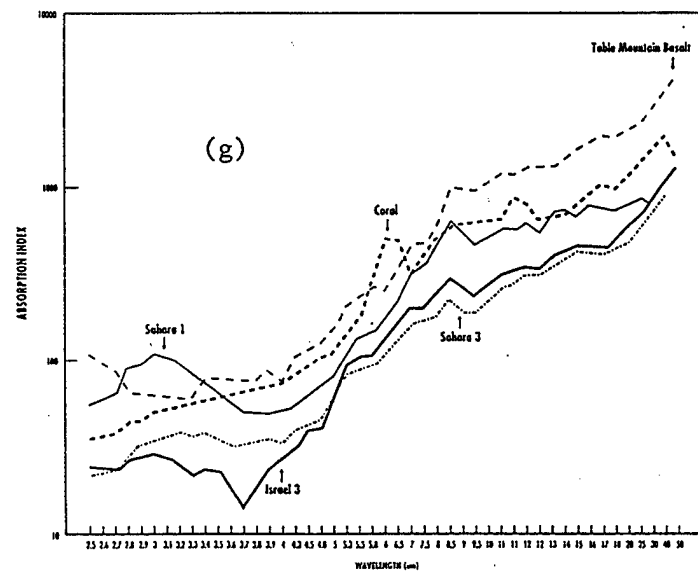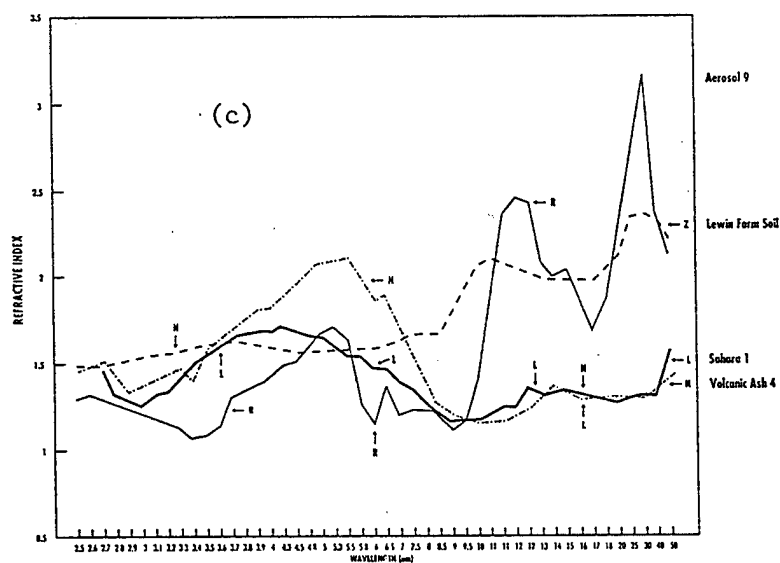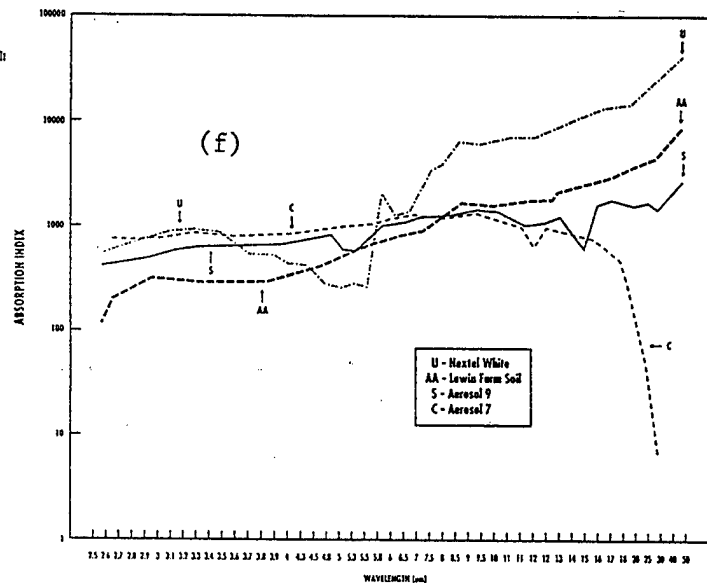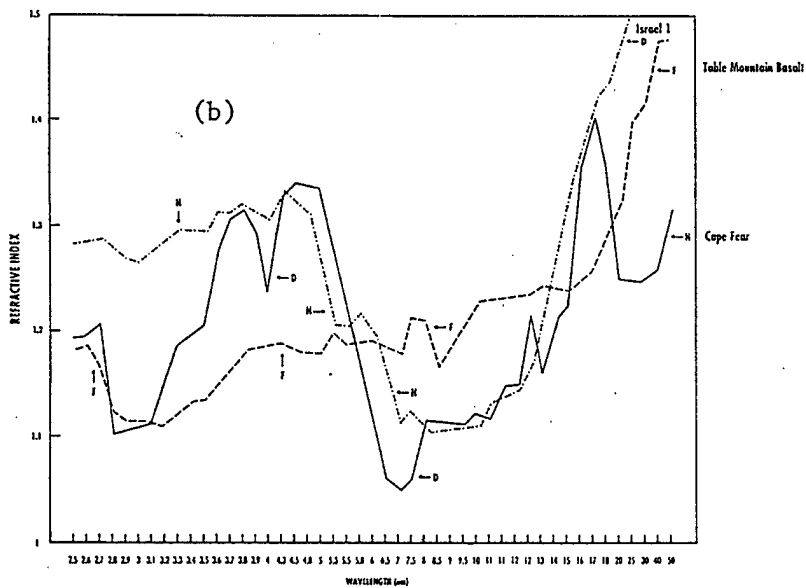
Estimation of airborne particulates size distribution according to weather conditions and influence on imaging systems

I. Dror and N. S. Kopeika

Ben Gurion University of the Negev
Department of Electrical and Computer Engineering
Beer Sheva, Israel 84105

Abstract

In this study the aerosol particulate size distribution curve is estimated according to simple meteorological parameters. The statistical models presented here show very strong relationships between current weather conditions and quantity and size distribution of aerosols. The model is based on 3 years of extensive aerosol size distribution measurements using a particulate optical counter. Comparisons between measurements of the atmospheric extinction coefficient and those calculated by the MODTRAN software show large deviation between the computerized models and our measurements. The MODTRAN atmospheric models give excellent results regarding the influence of the molecular particulates on the scattering and absorption properties of the atmosphere, satisfactory results for the fine dust particulates, but poor results regarding the influence of large dust aerosols, particularly in desert environment. This research presents also comparison between the MODTRAN aerosols models and measurements of the aerosol extinction coefficient in semi-arid, rural, and maritime environments. The comparison shows that MODTRAN models have problems in the prediction of the atmospheric extinction especially when the coarse mode of the particulate size distribution is dominant. Unlike MODTRAN, the new model presented here yields excellent results for predicting coarse mode aerosol size distribution.

keywords: aerosols, size distribution, prediction, MODTRAN, weather, MTF, imaging.

1. Introduction

The aerosols that are suspended in the atmosphere are a major factor that influence the quality of images that are propagating through the atmosphere. Scattering and absorption of light rays by the suspended aerosols contribute to the loss of contrast of the received image, forward light scattering in the direction of the image propagation also reduce the atmospheric modulation transfer function (MTF) and cause to image blur.

Prediction of the aerosol size distribution can lead to the prediction of the scattering and absorption coefficients and also the scattering phase function of the atmospheric propagating medium. These properties characterize the extinction coefficient of the atmosphere as well as the MTF of the atmosphere

2. Experiment

The particulate size distribution of the atmosphere was measured over the radius range of 0.16 to 10 μm using a PMS CSASP-100 optical particles counter. The optical counter was located at a height of 25 m above ground. Integration time of half an hour was chosen and every half an hour the average particulate size distribution was recorded. Meteorological parameters were also measured close to the PMS location and the half hour average of the temperature, relative humidity, wind speed, wind direction and solar flux were also recorded. The measurements were taken at the Ben-Gurion University of the Negev in Beer-Sheva, Israel. Data was collected form June 1991. Both PMS counter and Campbell Scientific meteorological station were connected to a personal computer.

Since this research is trying to relate the aerosol particulate size distribution parameters to simple weather parameters, the integration time selected for counting and classifying particles according to their size was to be shorter than the meteorological time constants. On the other hand, a short integration time leads to a particulate size distribution curve with insufficient data which is hard to fit to a known size distribution model. In our measurements an integration time of half an hour was chosen as a compromise between the need for a smooth size distribution curve and the need to measure the aerosol statistics under stationary meteorological conditions.

3. Data analysis

The deviations in the aerosol size distribution are large. The aerosols in the area of our measurements consist of a large variety of aerosol sources. Aerosol chemistry and area meteorology are described in detail in ref. 2. The aerosol sources are urban and rural, marine, haze, industrial and desert dust aerosols that are transferred from the Sahara desert and from the Arabian desert[4] during dust storms,

Fig. 1. describes two extreme aerosol size distributions that were measured during the year 1992. The differences between the two extreme cases is about two orders of magnitude. The lower curve is not continuous because particles at several radii were not counted during an integration period of half an hour. Fig. 2. shows the normalized standard deviation of the measured aerosol at each radius. The standard deviation ranges from 0.5 at radius of 0.16 µm to 12 at radius of 10 µm. The aerosol size distribution consists of several distributions that can be modeled by superposition of lognormal distributions.[5] The standard deviation of the particle count is smaller for small radii than for high radii since the low, or fine mode of the aerosol distribution consists mainly of local aerosols while the large aerosol population contains also particles that are transported from remote areas. The local aerosols are less affected by changes in the weather parameters while the larger particles are very sensitive to the wind speed and to the wind direction which, in some cases, yields information concerning the source of the remote aerosols.

A simple size distribution that can characterize the coarse aerosol size distribution is the Junge power law distribution.[6] The size distribution is defined by only two parameters A and α:

$$\frac{dn}{dr} = Ar^{-\alpha} \tag{1}$$

r is the particle radius and n is the particulate number concentration.

The advantage of this size distribution is that a measured size distribution can be fitted to this model by a simple one variable linear regression.

In our analysis the measured size distributions were fitted to Junge power law models. The data were separated into two major groups. One consists of the measured data during the summer season from May to October. This corresponds to arid and semi-arid regions. The second group consisted of data that was measured during the winter season, starting from November until April. This corresponds to wet, non-arid regions.

The climate in our region is such that there are two major seasons. Summer is the hot and dry season with no precipitation at all. Winter is the colder season. All precipitation is during this season.

3.1 A model for the summer season

Fig. 3. describe the average particulate size distribution and the power law fit. All 6000 measurements of the aerosol size distribution from May 1992 to October 1992 were fitted to the power law distribution and the values of α and A were extracted. The average square of the correlation coefficient R^2 was 0.95.

The power law size distribution parameters A and α were related to the weather parameters that were measured nearby the particulate counter using multiple linear regression analysis. The summer model obtained for A is given by:

$$A = a_0 + a_1 rh + a_2 rh^2 + a_3 rh^3 + a_4 rh^4 \tag{2}$$

were rh is the relative humidity. The coefficient of the model are given in table 1.

Table 1. Summer model for the prediction of the parameter A.

a_0	a_1	a_2	a_3	a_4
1.917	-0.128	$4.61 \cdot 10^{-3}$	$6.85 \cdot 10^{-5}$	$3.73 \cdot 10^{-7}$

The model obtained for α was the following:

$$\alpha = b_0 + b_1 rh + b_2 rh + b_3 ws \tag{3}$$

were ws is the average wind speed in m/s. The coefficients for the prediction of α are given in table 2.

Table 2. Summer model for the prediction of the parameter α.

b_0	b_1	b_2	b_3
2.68	$2.3 \cdot 10^{-3}$	$8.16 \cdot 10^{-5}$	$-2.65 \cdot 10^{-2}$

119

The A parameter in this model depends only on the relative humidity. Other dependencies were weak and insignificant. The parameter α depends also on the average wind speed. Fig. 4 describes in an ascending order the measured α and the modeled α. From this figure it is shown that there is a good agreement between the measured parameter and the modeled parameter except for extreme weather conditions. Fig. 5. shows the measured parameter A in ascending order and the modeled parameter. The model gives good correlation here too except for extreme weather conditions.

Figs. 6. show typical measured particulate aerosol distributions (solid lines) and predicted size distribution according to the measured weather parameters (dashed lines). The curves shows that there is a very good agreement between the measured data and the model for the parameters α and A under a variety of weather conditions.
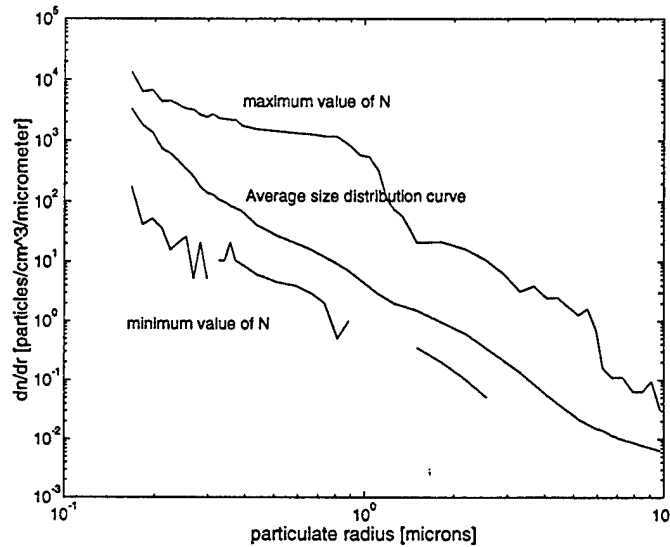
Fig. 1. Average aerosol size distribution curve and size distributions with the property of minimum and maximum number of particles that were measured.
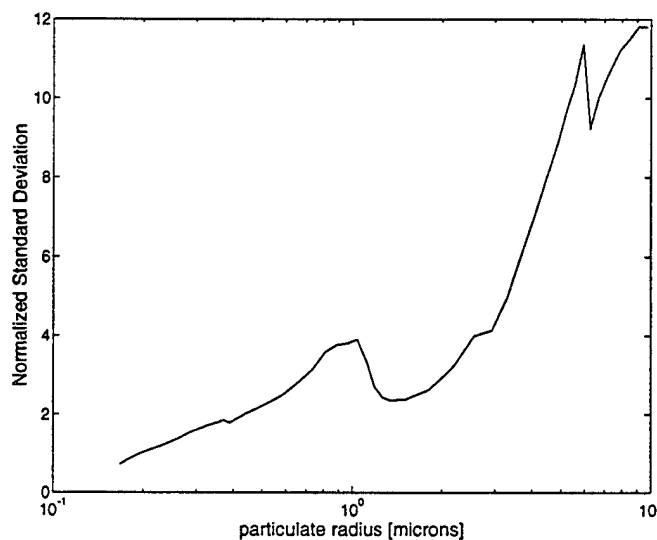
Fig. 2. Normalized standard deviation of the aerosol size distribution.
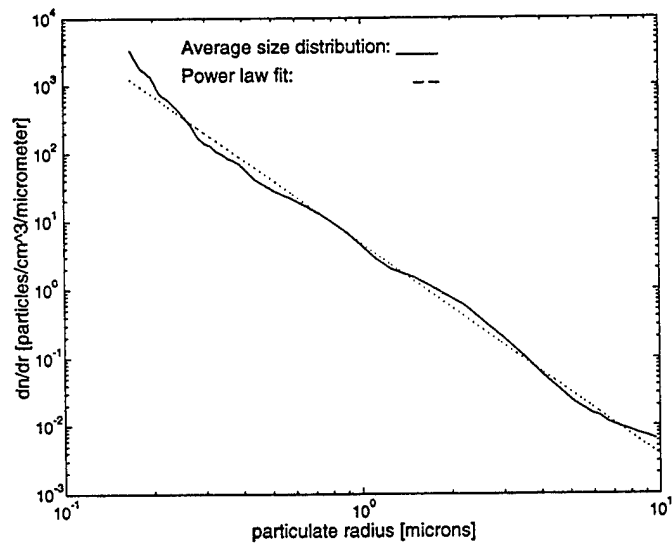
Fig. 3. The measured average particulate size distribution and its power law fit.
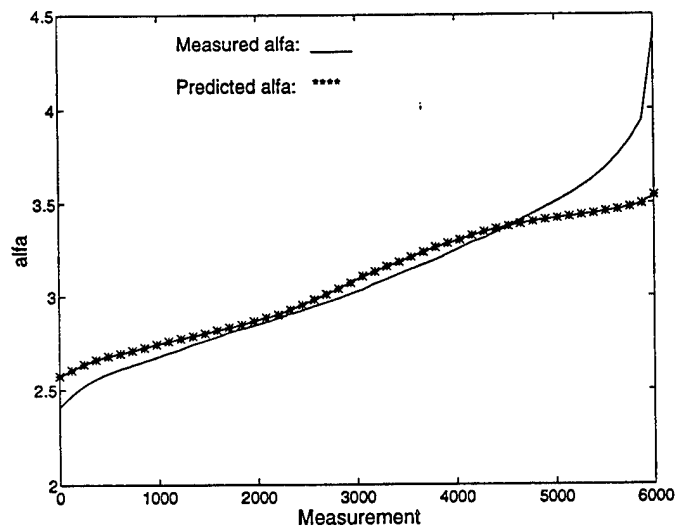
Fig. 4. Measured α parameter and predicted α.
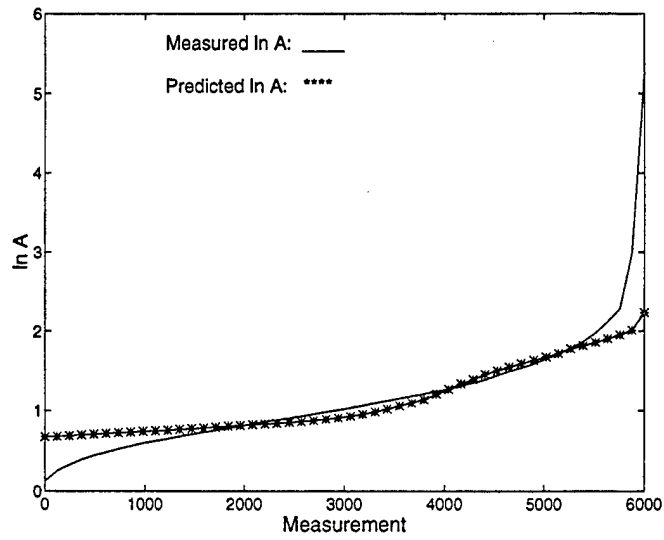
Fig. 5. Measured A parameter and predicted A.
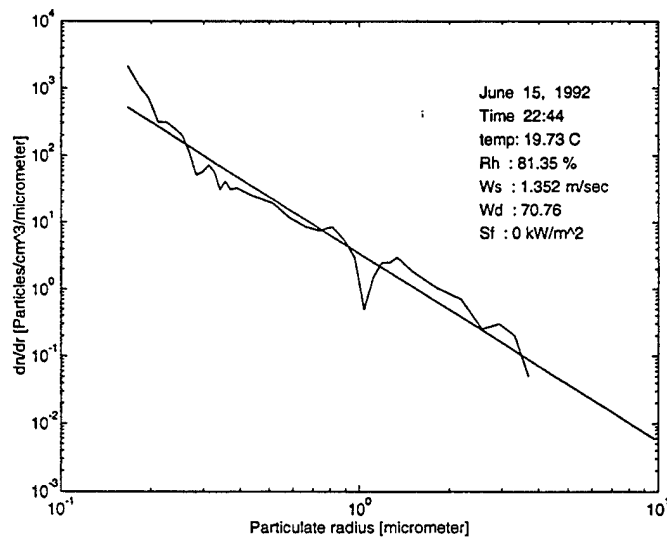
Fig. 6a. Measured particulate size distribution and the modeled size distribution.
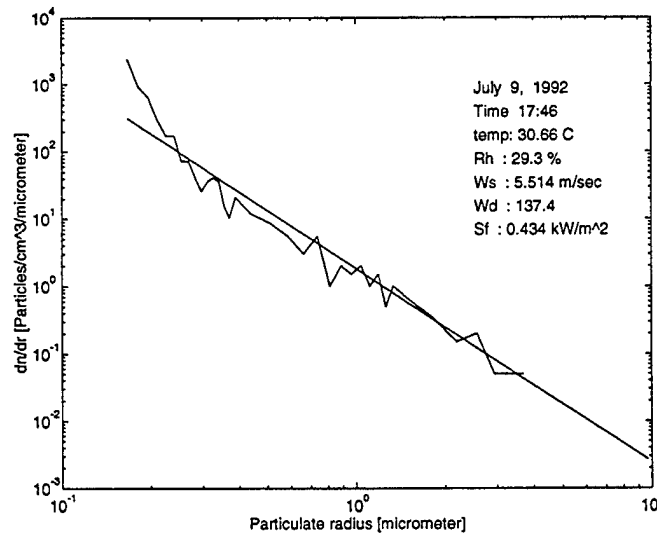
Fig. 6b. Measured particulate size distribution and the modeled size distribution.
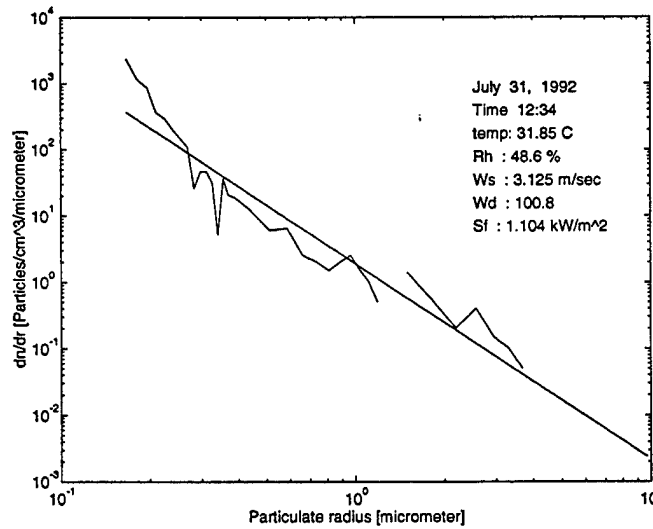
Fig. 6c. Measured particulate size distribution and the modeled size distribution.

4.2 A model for the winter season

A similar approach for modeling the aerosol size distribution for the winter season which is the wet and rainy season in our area was used. The two parameters of the power law model for the aerosol size distribution were related to weather parameters. The major difference between the two seasonal models is that for the winter season, not only were the measured weather parameters necessary but also the history of some of them. The model here is based on about 5000 different measurements of the aerosol size distribution during winter seasons.

The model for ln A is the following:

$$\ln A = a_0 + a_1\, rh + a_2\, \overline{rh}_{24} + a_3\, (\overline{rh}_{24})^2 + a_4\, ws + a_5\, \overline{ws}_{24} + a_6\, (\overline{ws}_{24})^2 + a_7\, tm + a_8\, sf \qquad (4)$$

123

where rh is relative humidity, $\overline{rh}_{24}$ is the last 24 hour average of the relative humidity, ws is the wind speed in m·s^{-1} $\overline{ws}_{24}$ is the 24 average of the wind speed, tm is the temperature in ° C, and sf is the solar flux in kwatt·m^{-2}. The following model was obtained for α:

$$\alpha = b_0 + b_1\, rh + b_2\, \overline{rh}_{24} + b_3\, (\overline{rh}_{24})^2 + b_4\, ws + b_5\, \overline{ws}_{24} + b_6\, (\overline{ws}_{24})^2 + b_7\, tm + b_8\, sf \qquad (5)$$

Fig. 7 show an example of the measured aerosol size distribution and the modeled size distribution according to the weather parameters and the 24 hour averages of the wind speed and the relative humidity.
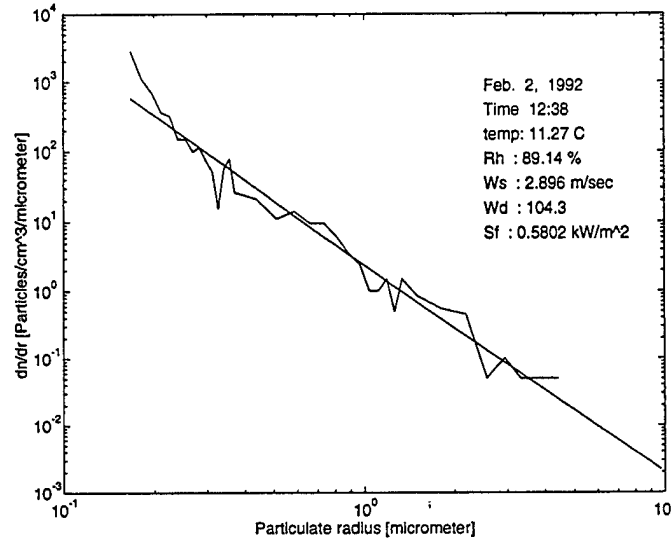
Fig. 7. Measured particulate size distribution and the modeled size distribution for the winter season.

5. Conclusions

The major conclusion of this research is that the coarse aerosol size distribution parameters can be predicted according to simple meteorological parameters. A strong statistical relation exists between the aerosol size distribution curve and the local weather. Although the Junge power law distribution is not accurate since it does not model the size distribution at radii that are smaller than 0.1 μm and the fine details of the curve are lost, it can model roughly the aerosol size distribution and it is very easy to extract its two parameters A and α even if the aerosol histogram is composed of relatively low counts of particles. The strong statistical dependence of the power law distribution on local weather parameters show us that in most cases the statistics of the aerosols are influenced by the local weather. There are few exceptions, mainly when the aerosol size distribution consists of particles such as desert dust particles or marine particles that are transported from other areas.

Introducing the history of the meteorological parameters such as the previous 24 hours average of the wind speed and that of the relative humidity was very significant to the winter model and contributed significantly to the correlation of the model with measurement.

6. References

1. I. Dror and N. S. Kopeika, "Aerosol and Turbulence MTFs: Comparison Measurements in the Open Atmosphere," *Optics Letters* **17**, 1532-1534, 1992.
2. J. Gottlieb, B. Fogel, I. Dror, Z. Y. Offer, and N. S. Kopeika, "Prediction of airborne particle statistics according to weather forecast: concentration and scattering area," to be published in *Opt. Eng.*
3. I. Dror and N. S. Kopeika, "Prediction of aerosol distribution parameters according to weather forecast," in *Atmospheric Propagation and Remote Sensing*, A. Kohnle and W. Miller, eds., Proc SPIE, vol. 1688, 123-131, 1992.

4. E. Ganor, H. A. Foner, S. Brenner, E. Neeman, and H. Lavi, "The chemical composition of aerosols settling in Israel following dust storms," Atmosph Environment, 25A, No. 12, 2665-2670, 1991.

5. E. P. Shettle and R. W. Fenn, "Models for the aerosols of the lower atmosphere and the effects of humidity variations on their optical properties," AFGL-TR-79-0214, 1979.

6. M. M. R. Williams and S. K. Loyalka, *Aerosol Science*, Chap. 1, Pergamon Press, 1991.

COOLING of MARINE STRATUS CLOUD TOPS

by James W. Telford

Atmospheric Concepts Inc.

THE 19th ANNUAL REVIEW CONFERENCE on ATMOSPHERIC RADIATION MODELS

PHILLIPS LAB, 4 June 1996

The continued growth and dissipation of long lived marine stratus clouds is thought to be strongly influenced by thermal radiation transfer. However the actual interactions are more complex than at first conjectured and have the effect of mixing dry overlying air into the clouds rather than adding moisture from the sea. The moisture is added from below by a moisture driven convective process involving latent heat but this local condensation does not form permanent clouds.

Previous observations show that the absolute potential temperature of the top cloudy layer is usually just a little bit warmer than the cloud under it so it is not cooling. Also the need for this conjectured cooling to drive downward convection to the surface to bring up more moisture is now known to be unnecessary. Observations show that the transport of moisture up from the sea to cloud base continues even when the sea is cooler than the air. Isolated patches of air become saturated at the sea surface and on moving upwards release latent heat and so can move further upwards, without forming permanent cloud, This process occurs whenever the stability is less than that of the wet adiabatic lapse rate.

Recent observations at dawn show the same higher temperature at cloud tops under conditions where the solar heating is negligible. Thus thermal radiative cooling has no effect, if it is actually occurring.

The area of marine stratus cloud can be seen on the GOES satellite photographs, and on the occasion shown in Fig.1 the cloud free regions are seen to gradually diminish from 1 AM local time, through dawn at 7 AM, on until 9 AM, and then through mid-day until 1 PM. These clouds are located by the more northern black patches in the figure, west of the northern Baja Peninsular. The area to the north and west is uniformly covered by marine stratus clouds. There is certainly no tendency for these open patches, shown as black, to increase in area after sunrise. In fact the sea in Baja Gulf clouds over after the sun rises.

In contrast, the region just to the south of these clouds, south of an east-west line where higher level clouds are moving in from the west, have open cloud patches in the marine stratus which behave in the opposite way. The cloud free area greatly increases in size after sunrise. The change in the composition of the overlying air seems certainly to be the influence which controls the contrasting difference in cloud growth. This strongly suggesting that radiative transfer is not the controlling influence, but that the overlying air does exert a significant influence. Fig. 2 shows a typical view of these clouds from above.

The resolution of this problem wherein the theoretical cloud top cooling does not adequately represent the facts, seems to be essential if the feedback effects of the albedo changes on global thermal balance are to be accurately modeled.
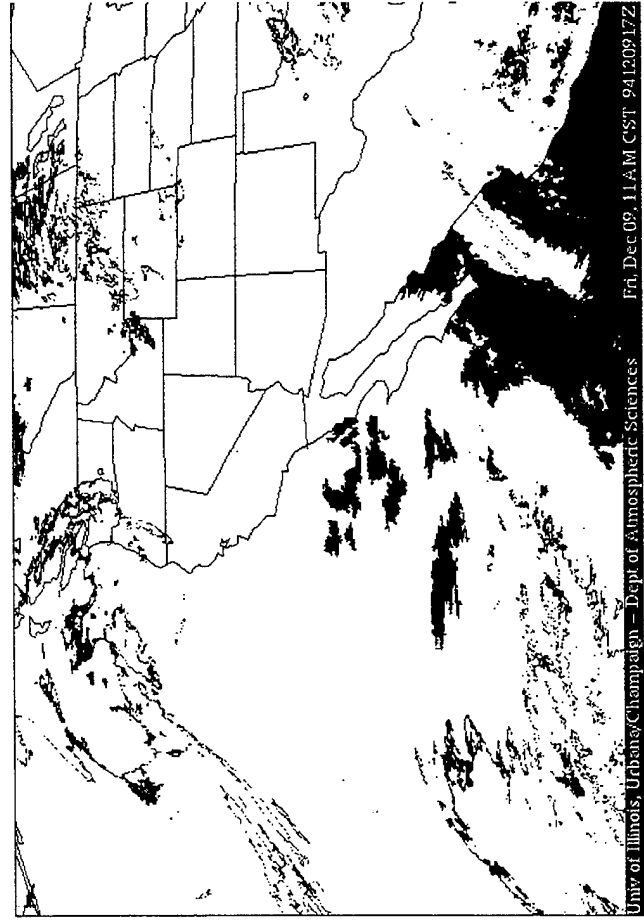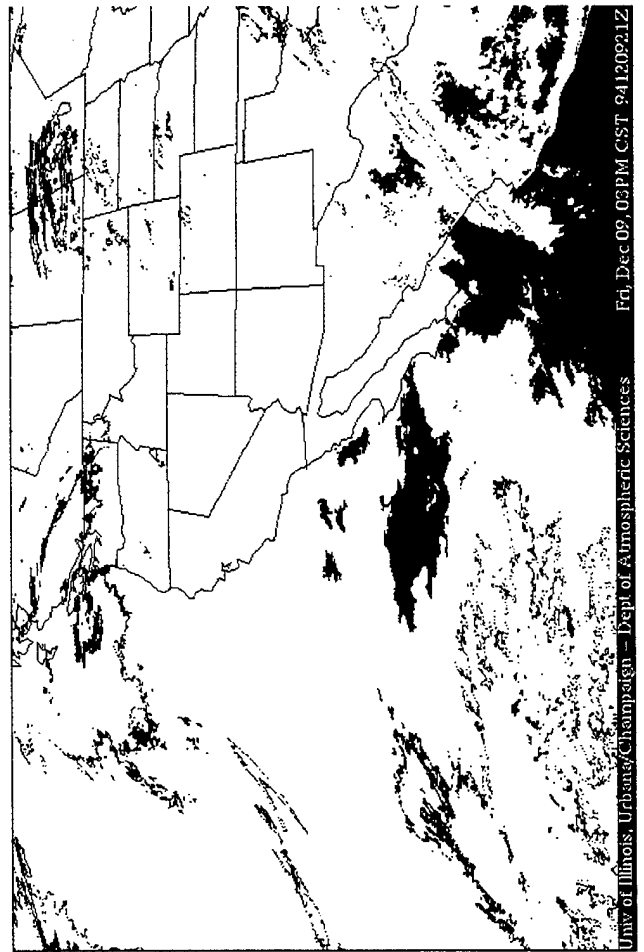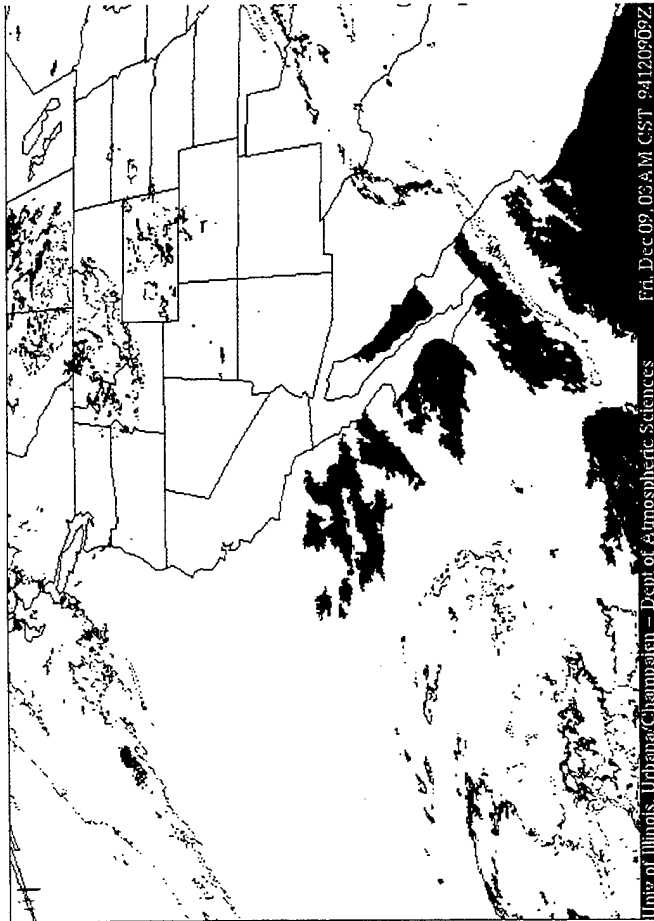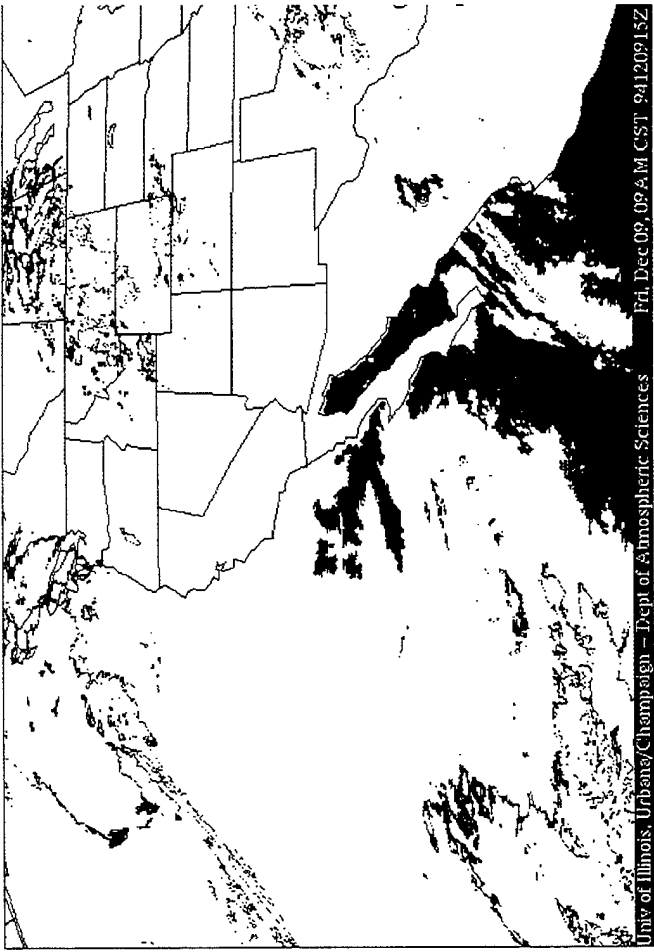
126

FIGURE 1

Univ of Illinois, Urbana/Champaign – Dept of Atmospheric Sciences   Fri, Dec 09, 09 AM CST 941209 1512

Univ of Illinois, Urbana/Champaign – Dept of Atmospheric Sciences   Fri, Dec 09, 03 PM CST 941209 2112

Univ of Illinois, Urbana/Champaign – Dept of Atmospheric Sciences   Fri, Dec 09, 03 AM CST 941209 0912

Univ of Illinois, Urbana/Champaign – Dept of Atmospheric Sciences   Fri, Dec 09, 11 AM CST 941209 1712

127

FIGURE 2

128

Detailed calculations using analytic integration across layers, and algebraic expressions to eliminate the canceling terms between layers, allows the vertical resolution to be small enough to follow the heat transfer at wavelengths where the 1/e absorption distance is less than a centimeter or so. For actual inversions at cloud top, often of 10°C over 10 m or so, this transfer cools the warm clear air above and heats the cloud top enough to dominate the heat loss up through the radiative atmospheric window. Satellite observations confirm that the clouds do not spread to fill clear patches at night, and do not enlarge them after dawn.

Such calculations show that the cooling effect is less then that usually described. Some calculations have been based on the specific heat of the cloud, and including latent heat about halves the rate of change of temperature. Another significant effect relates to the transfer of heat by the most absorbing lines in CO_2 and water vapor. Some of these lines reduce their photon path by e^{-1} in a few centimeters and when the temperature changes by 10°C in 10 m or so, as is observed to usually occur at the tops of these clouds, a significant heat transfer occurs between the warm inversion air and the cloud top. This effect again reduces cloud top cooling by another factor of two. However the cloud top still seems to be cooling by radiation, in conflict with the observations.

This cloud top transfer has the important effect of cooling the cloud free air just above cloud, which produces a very distinct layer against the top of the cloud with a lower wet bulb temperature and this air us unstable to mixing with the cloud air, and hence promotes the addition of subsaturated air to the cloud which dries it out. Thus this effect of the radiative transfer tends to dissipate the cloud rather than to promote its formation as originally thought.

Thus there remains the question of why the cloud tops are observed to be warmer than the cloud below when the theory suggests that they are cooling appreciably by thermal radiative transfer. Another interesting point is that the cooling of the cloud top increases the cloud drop diameters so that even though the cloud becomes cooler, in theory, in cools at an increasing rate.

Some results of these calculations are given in the following figures. Fig. 3 shows the effect of suppressing the most absorbing thermal radiation lines from the calculation. The cooling just above cloud in the clear air is significantly reduced but the cooling of the cloud top itself is not greatly reduced. Fig. 4 shows the effect of reducing the cloud drop concentration linearly from 25 m in the cloud to 1/10 of the drop concentration right at the top surface. The cooling rate 50 m below cloud top is not much reduced, although the cooling is spread a few meters deeper into the cloud. The temperature reduction after 15 minutes, and 30 minutes, is shown. The actual cooling rate is increased in the cooler cloud top, contrary to any expected reduction in cooling rate due to the lower temperature, because the cooling has reduced the water vapor in the top cloud layers and condensed water onto the cloud drops and made them bigger so they cool faster.

Atmospheric Radiation with highest absorption suppressed

A:: Absorption more than 0.1 kg/squ.m removed
B::: Absorption more than 0.01 kg/squ.m removed
C::: No Absorption removed.

CLOUD TOP

Radiative Flux Down (W/Squ.M)
Radiative Flux Net (W/Squ.M)
Radiative Flux Up (W/Squ.M)

HEATING RATES (Deg.C/Day)
(Deg.C x 100)
Temperature

CLOUD TOP
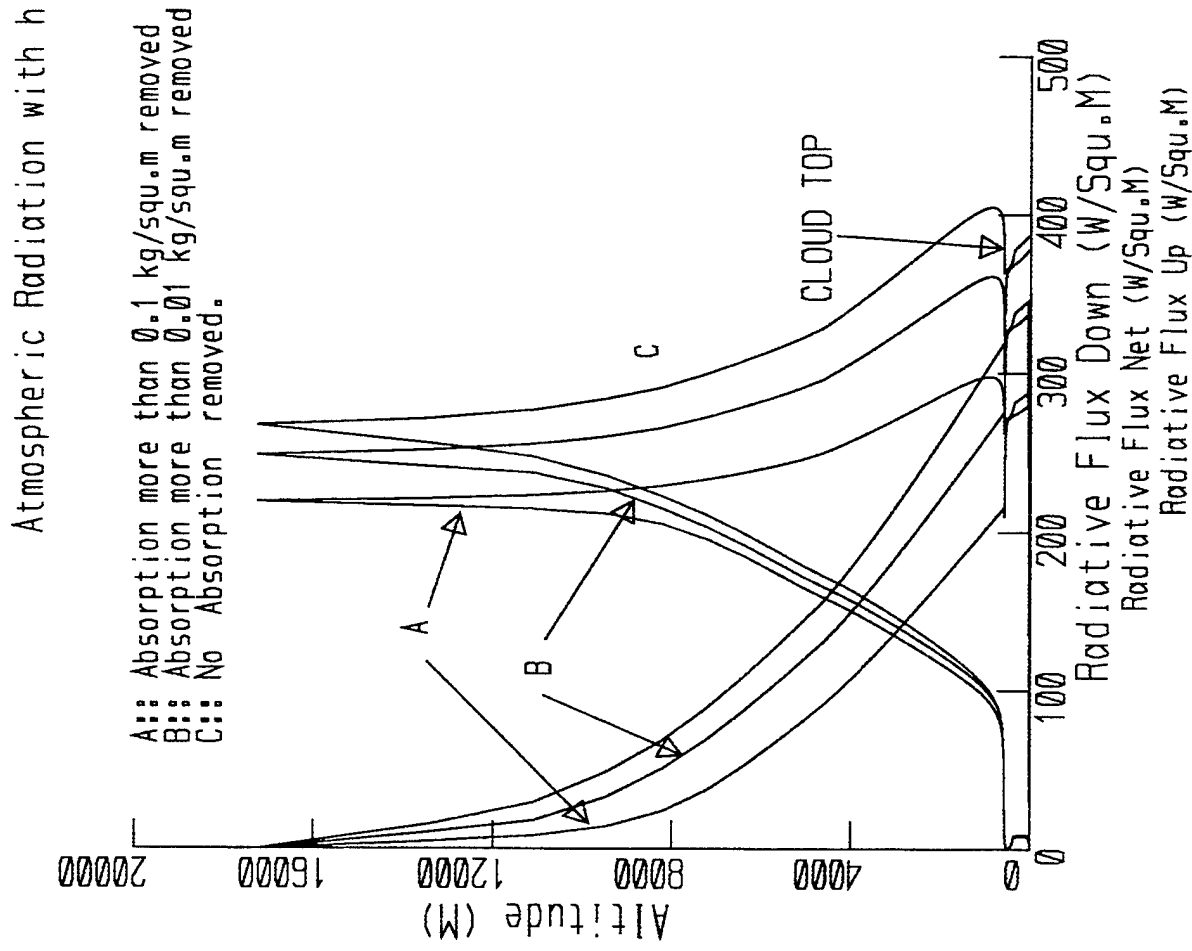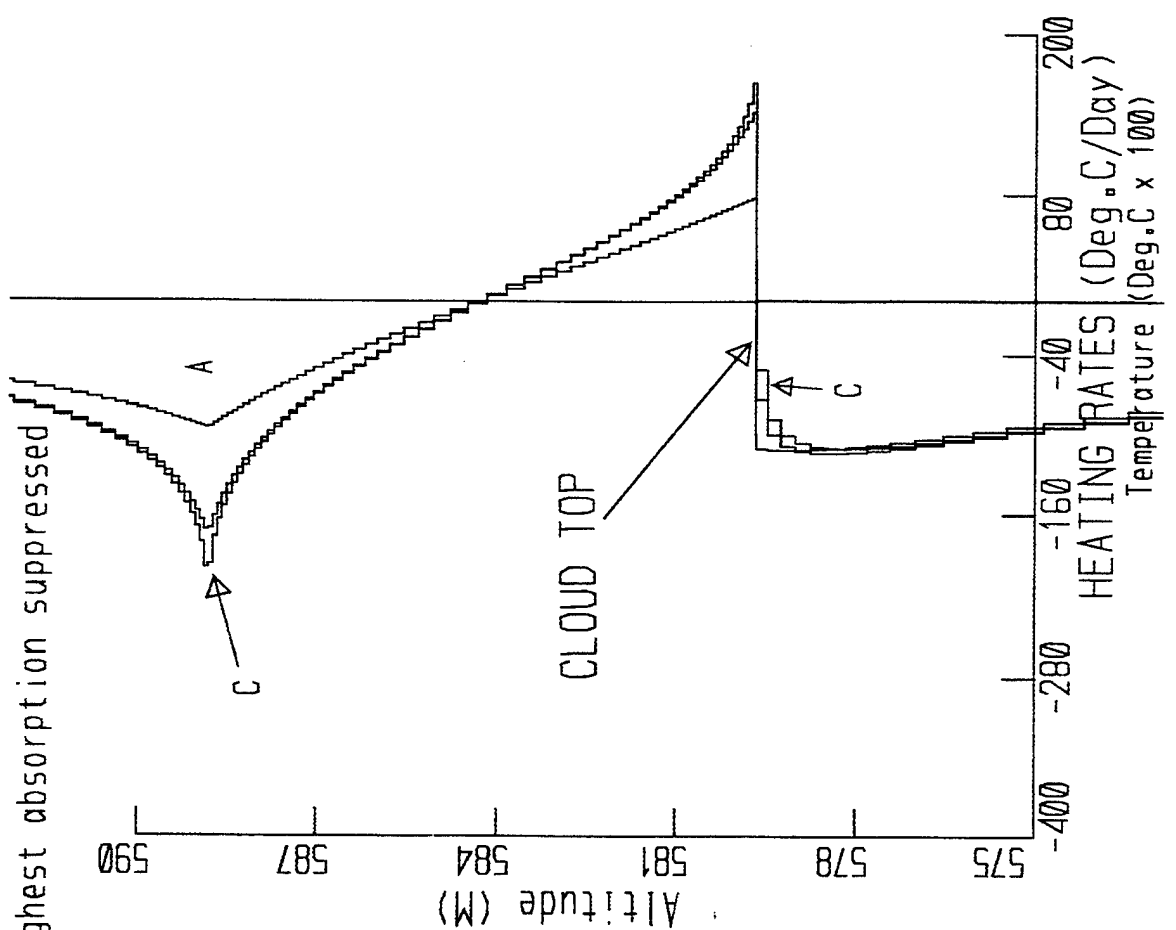
DATA RAD FILE NAME: arda.dat

FIGURE 3

130

RADIATION at CLOUD TOPS

TRANSITION OVER 25 M at CLOUD TOP

from 10% to 100% of Drop Concentration

TEMPERATURE

CLOUD LAYER

after 1/2 hour for cooling

HEATING RATES (Deg.C/Day)
Temperature (Deg.C x 100)

Altitude (M)

Radiative Flux Down (W/Squ.M)
Radiative Flux Net (W/Squ.M)
Radiative Flux Up (W/Squ.M)
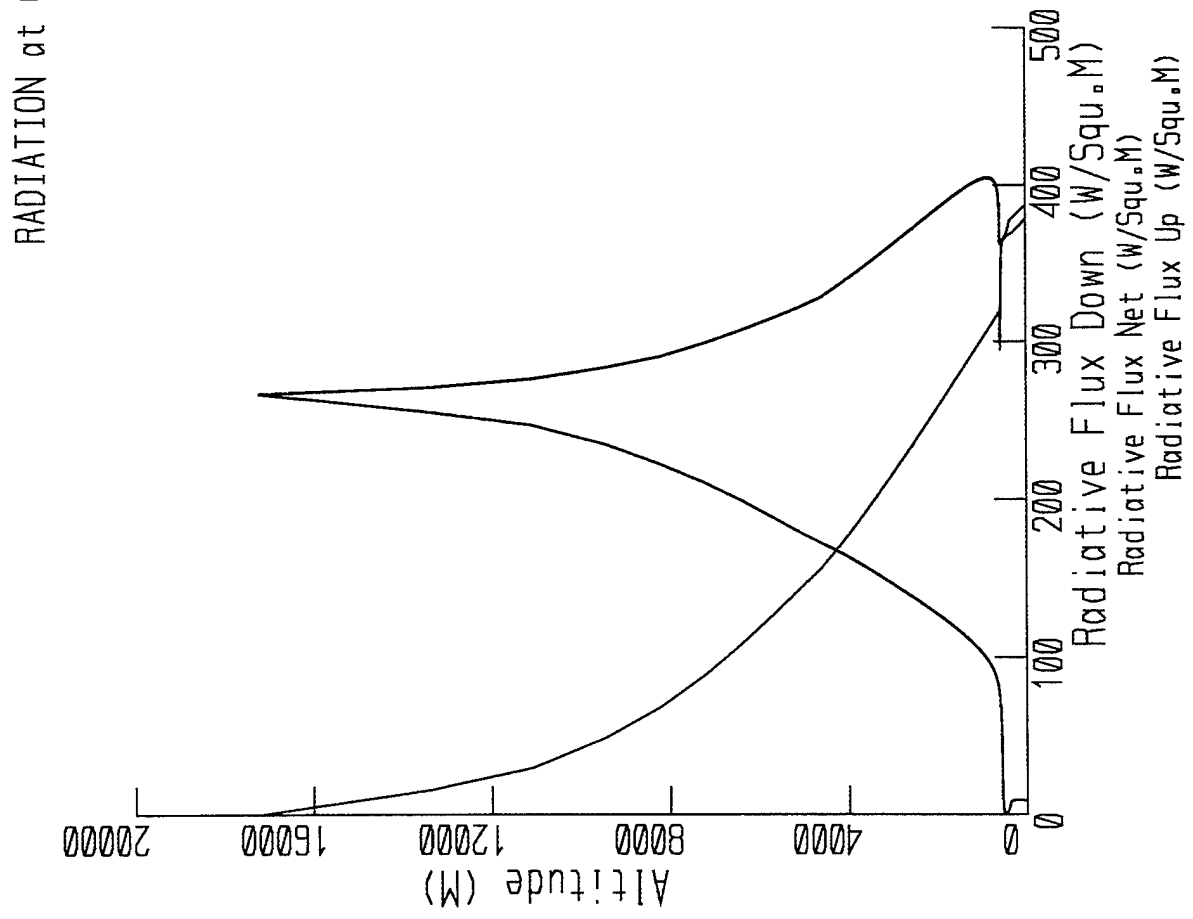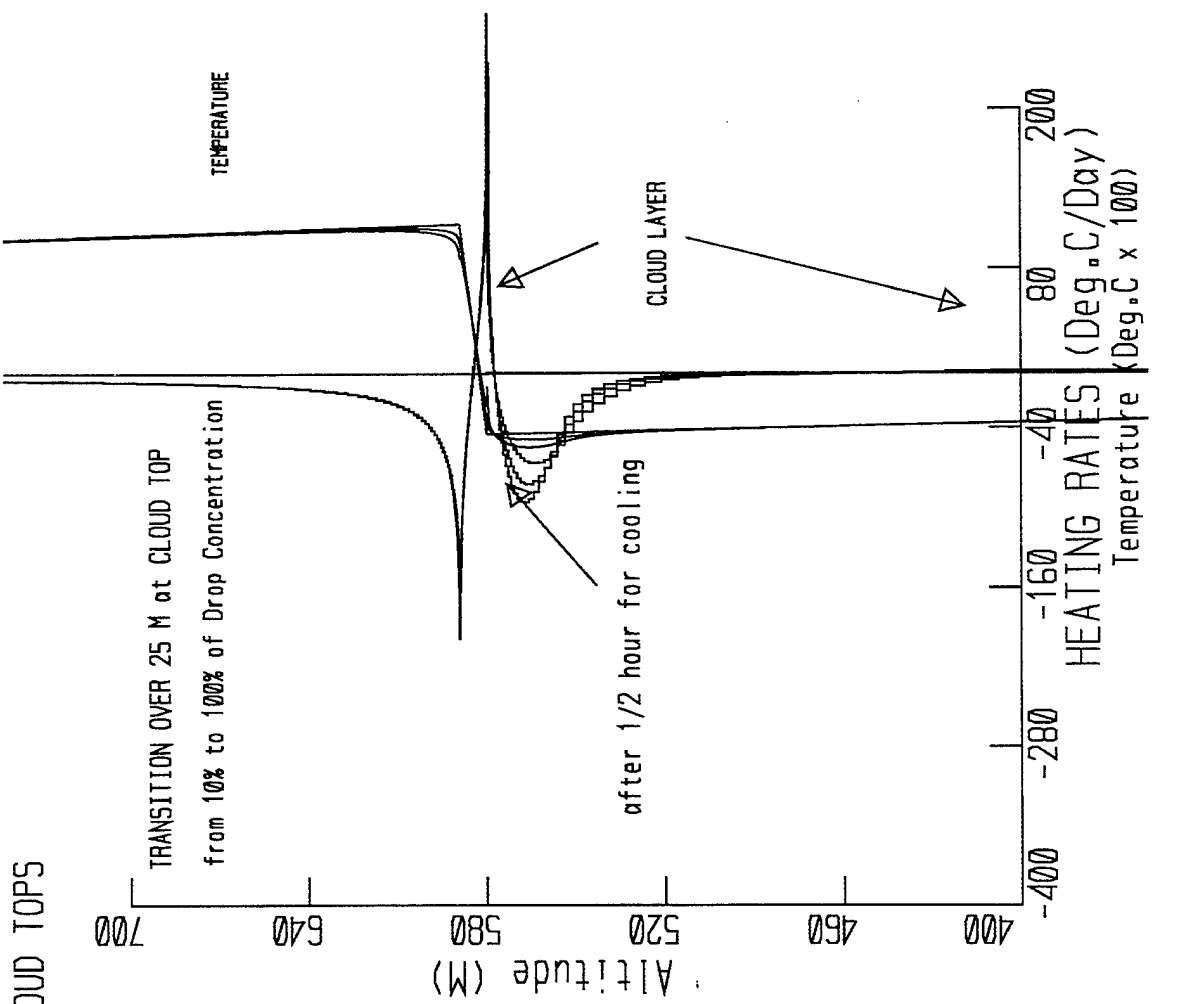
DATA RAD FILE NAME: FIG11.GRA

FIGURE 4

131

A Method for Rapid Generation of Cloud Properties

Eric Schmidt and Mark Raffensberger
TASC, Reading, MA

ABSTRACT

We have developed a first–generation method to rapidly generate radiometrically accurate visible and infrared properties of water clouds. The basis for the Fast-Map approach is the construction of a set of 2-D tables relating water content to particle size, optical properties, radiative properties, and graphical quantities. The conversion process is highly flexible, computationally efficient and fast. Fast-Map includes: (1) a spatially variable particle size distribution, $n(r,z)$, where r is the particle radius and z is the height above the cloud base, (2) a translation from water content and $n(r,z)$ values into wavelength dependent optical properties, such as extinction optical depth (δ) and single-scatter albedo (ω_o), (3) tables of radiative properties constructed using a radiative transfer model code and/or parameterizations, and (4) a mapping between radiative properties and graphical quantities.

1.   INTRODUCTION

This paper describes the science behind the Fast-Map processor developed by TASC for the Geophysics Directorate of the USAF Phillips Laboratory. The "Fast-Map" processor is a software tool developed to speed the creation of visible and infrared (IR) images of 3-D water clouds, such as stratus and cumulus, by providing physics-based optical, radiative and graphical quantities for rendering. The approach is based on the conversion of water content output from the Cloud Scene Simulation Model (CSSM)[1] into graphical quantities through a series of modular analytic processes. However, Fast-Map can be used to generate cloud properties for water content fields from any model or observations, provided they are written into a simple input file format.

The heart of the Fast-Map approach is the construction of a database of 2-D tables relating cloud water content to cloud type, particle size, optical properties, radiative properties and graphical quantities. Look-up tables are utilized to reduce the computation time and allow flexibility, as the tables can be generated independently. Fast-Map is designed to speed scene generation or rendering by producing a 3-D grid of graphical quantities based on the physics of clouds, removing the computational burden from computer image generator (CIG) software. The Fast-Map approach is shown schematically in Figure 1.
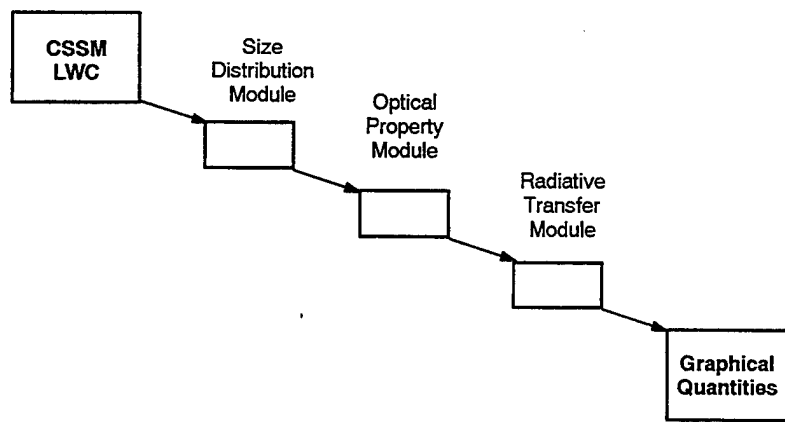
Figure 1   Schematic Representation of Data Flow through Fast-Map Driver

The analytical processes shown as modules in Figure 1 are: (1) develop a spatially variable particle size distribution, n(r,x,y,z), where r is the particle radius and (x,y,z) is the location inside the cloud, (2) use n(r,x,y,z) to calculate extinction optical depth (δ) and single-scatter albedo (ω_o), including wavelength dependence, (3) construct tables of radiative properties using a radiative transfer model to map (δ,ω_0) to radiative properties, and (4) develop the wavelength-dependent mapping between radiative properties and graphical quantities.

The approach defined by these steps is independent of cloud type; the implementation is not. The spatial variation of a typical particle size distribution must be developed for cumuliform and stratiform water clouds. Translation of water content and n(r,x,y,z) into (δ,ω_o) is performed for IR and visible wavelengths and water clouds only. Radiative transfer parameterizations exist for broadband wavelengths for water clouds. For those cases where parameterizations are not available, they must be developed or else a scheme developed (look-up tables in this case) to minimize the number of computations.

2.   **THEORETICAL DISCUSSION**

Size Distribution. Any particle size distribution can be broken into discrete size bins, as the example in Figure 2 indicates. The conversion of number density into optical properties and the derivation of radiative properties are simplified by selecting a number of narrow size bins to form a discrete representation.

The typical function used to describe particle size distributions is the modified gamma distribution[2]. Nominal values for the parameters are determined from statistical values reported in the scientific literature[3]. The particle number density for a specific size bin is determined once the form of the analytic function is specified (or a set of observations provided). Single- and multi-modal distributions are supported by the discrete sampling method.

Spatial Variability. The spatial variation of particle size is important to accurately model the behavior of clouds in terms of physical, optical, and radiative properties. Variation of particle size with height (z) is the first-order approach we have chosen. We assume that n(r,z) = n(r)G(z) is true, i.e., that the variation of the number density of the cloud particles with particle size is independent from the variation with height. This assumption is not generally true: particle size and spatial location are related. However, a reasonable first-generation approach is to ignore these effects.

Particle Size Distribution
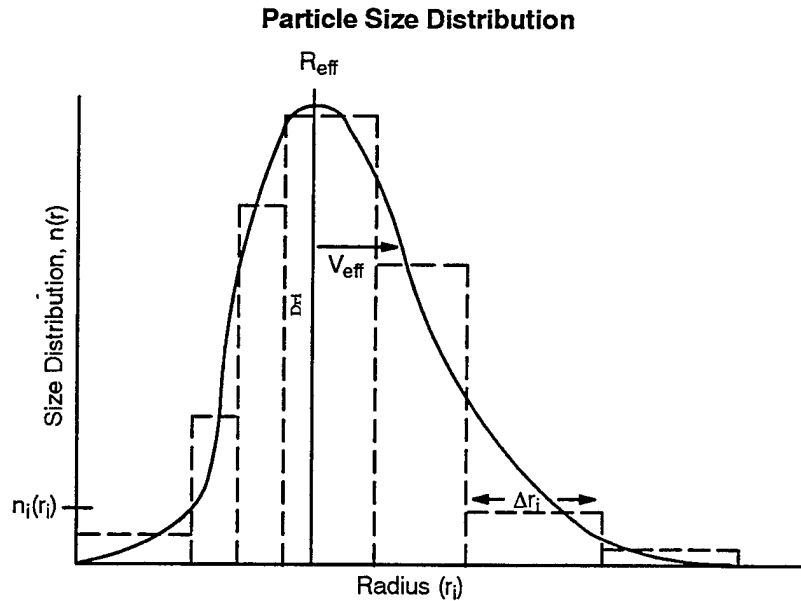
Figure 2   Typical Modified Gamma Particle Size Distribution Broken into Discrete Size Bins

The first-generation software adjusts the modified gamma size distribution linearly with height above cloud base. We assume that z is an arbitrary height above cloud base and Δz_c is the cloud thickness. Next, we assume that the number density at the cloud top $n(z_t)$ is a linear function of the number density at cloud base, $n(z_b)$, or $n(z_t) = \varepsilon n(z_b)$. Since $n(r,z) = n(r)G(z)$ was assumed and $n(r,0) = n(z_b)$, the expression for $G(z)$ is $G(z) = 1 + (\varepsilon-1)(z-z_b/\Delta z_c)$.

LWC Versus Number Density Relation. The particle size information is represented by statistical averages derived from observations and analysis for individual cloud types[3]. We assume that the relationship between local average number density and liquid water content is identical to that between the average number density and liquid water content for the cloud mass.

Figure 3 indicates the result of the conversion process: a table of number densities for discrete particle size bins. We only store the minimum and maximum values for each size bin, reducing a large number of grid points to fewer than 50 values. Later sections discuss the retrieval of accurate optical and radiative properties when the 3-D grids are reconstructed.

Optical Properties. Computing extinction optical depth for each particle size is a straightforward process, particularly if the partigths from 0.25-14 μm. These look up tables were computed using a Mie code[4]. Using the cles are uniform in size and spherical. We have used a set of tables computed for wavelenMie code and the actual variation of particle number density provides a more accurate estimate of the extinction coefficients. The single-scatter albedo (ω_0) and asymmetry factor (g) are independent of the number density (n_i) for any specific size bin. Figure 4 indicates the conversion of microphysical properties to optical, radiative and graphical properties.
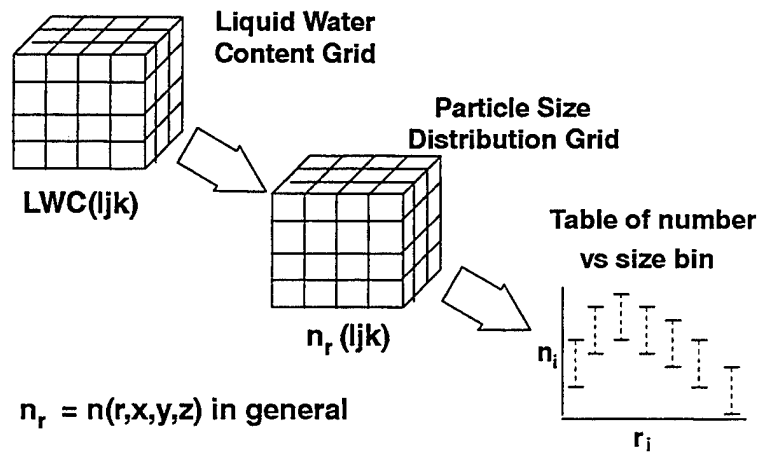
Figure 3 Translation of the 3-D Cloud Water Content Grid into a 2-D Table of Number Densities for Discrete Size Bins

Radiative Properties. The purpose of the radiative transfer module is to transform optical properties ($\omega_{0i}, g_i, \delta_i$) into radiative properties: transmittance (τ_i), emittance (ε_i), reflectance (ρ_i) and absorptance (α_i). For the purposes of the first-generation Fast-Map software, we treat hemispheric reflectance. Later versions will provide parameterizations based on scattering angles. Several simplifying assumptions were made to minimize pre-computation, yet still provide a reasonable degree of accuracy. The first assumption was that Kirchoff's relation is valid for the infrared (11 μm) wavelengths and that the visible (0.55 μm) emittance was zero. Second, we decided that the calculations would be monochromatic. Look up tables were generated for a range of optical properties, using (ω_0, δ) to index transmittance, reflectance, absorptance and emittance. Once 2-D tables of radiative properties are obtained, translation of (ω_{0i}, δ_i) into ($\tau_i, \varepsilon_i, \rho_i, \alpha_i$) for each size bin.
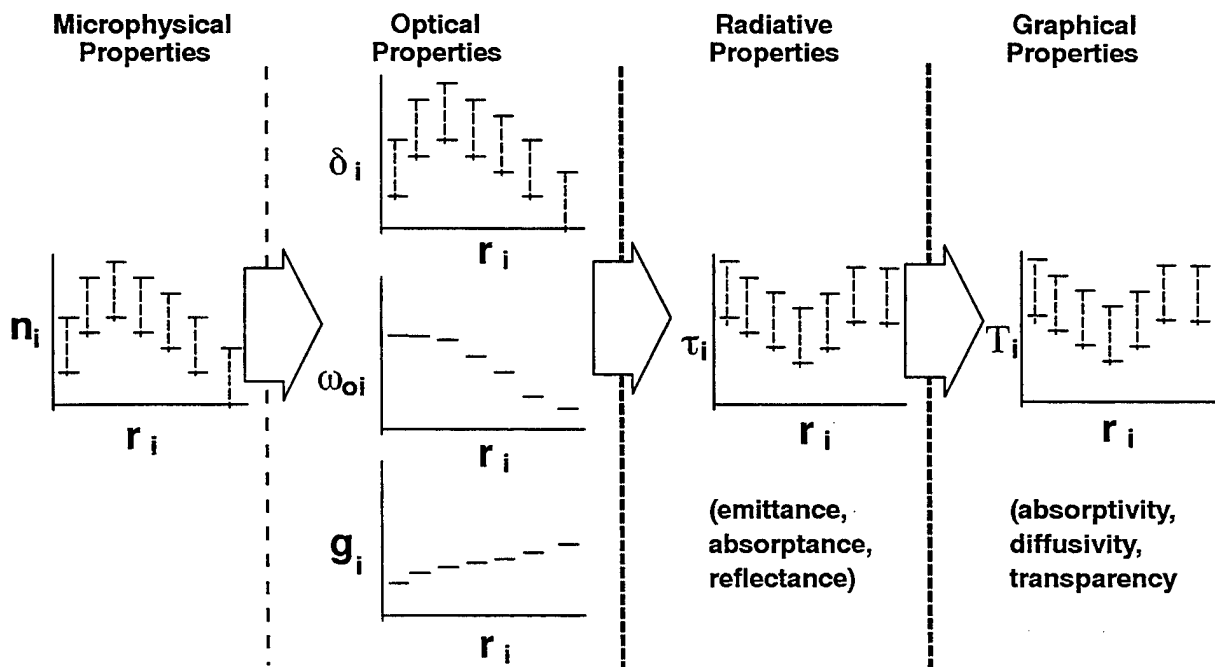
Figure 4 Transformtaion of 2-D Table of Microphysical Properties into Tables of Optical, Radiative, and Graphical Properties.

135

τ_i

r_i

$\tau(ljk)$

Transmittance Table

Transmittance Grid
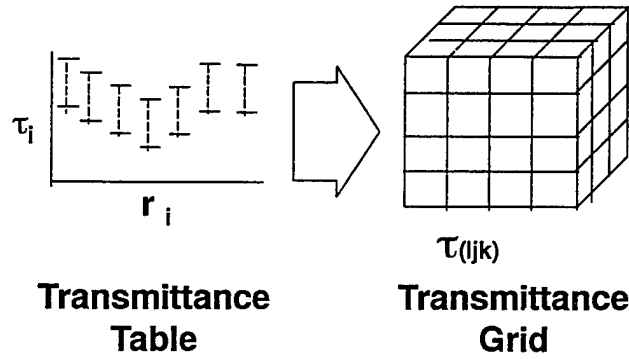
Figure 5   3-D Grid Reconstruction from 2-D Table

Figure 5 illustrates the 3-D grid reconstruction process for transmittance only. Several steps must be followed to produce weighted output quantities: (1) compute transmittance, $\tau(l,j,k)$ = $\Pi\,\tau_i(l,j,k)$; (2) derive hemispheric reflectance and absorptance, where $\rho(l,j,k) = 1-\Pi\,[1-\rho_i(l,j,k)]$ for the visible and $\alpha(l,j,k) = 1-\Pi\,[1-\alpha_i(l,j,k)]$ for the infrared, and (3) emittance is given by $\varepsilon = \alpha$ (Kirchoff's relation for the IR). All of these values are optional products of the Fast-Map software, selected by the user.

Graphical Quantities. Translation or mapping of radiative properties to graphical quantities is the final step in the Fast-Map process. The normal graphical quantities used by CIGs expresses the properties of pixels in terms of three quantities. One set of these properties is transparency (T), absorptivity (A) and diffusivity (D). The most significant part of the problem is how one maps four radiative properties into three graphical quantities. The translation of $(\tau_i,\varepsilon_i,\rho_i,\alpha_i)$ to (T_i,A_i,D_i) also has a complex wavelength dependence. However, once the mapping is computed for a given set of wavelengths, it can be applied repetitively without further computational overhead. We have utilized the visible and infrared mapping in the first-generation Fast-Map software.

For the purposes of the first-generation software, we have mapped 2-D tables of radiative properties into 2-D tables of graphical quantities with values between 0-1. The final step is the reconstruction of the 3-D grid of graphical quantities as output products. We map the atomic radiative properties to their equivalent atomic graphical quantities, then we weight the graphical quantities in a similar manner to the radiative property weighting to reconstruct the 3-D grids of (T,A,D).

3.   SUMMARY

Generation of radiometric images occurs by means of a computer image generator or scene generation tool. These applications position illumination sources and background objects, then interpolate 3-D grids of optical or radiative properties to derive graphical quantities, e.g. (T,A,D). Ray-tracing through the volume from back to front is the final step in this process. These steps are typically slow due to the use of software, not hardware, to perform the integration. Short-cuts are often used to speed up the time required to render scenes, particularly for real-time applications that operate with ten or more image per second. However, these short-cuts usually require one to disregard some of the physical relationships.

136

Fast-Map speeds scene generation or rendering processes by producing a 3-D grid of graphical quantities (T,A,D) based on the physics of clouds, reducing the computational burden of the software used by a rendering engine. By using the graphical information, the computer image generator will only have to perform ray-tracing or node summation. These processes are fast, so the time required to render the scene should dramatically decrease. We hope that with further development and improvement in the hardware and software, the Fast-Map application will prove to add significant value to the visualization of atmospheric scenes, particularly those that contain clouds.

ACKNOWLEDGEMENTS

REFERENCES

1. Cianciolo, M.E., M.E. Raffensberger, E.O. Schmidt, and J.R. Stearns, Atmospheric Scene Simulation Modeling and Visualization, Final Technical Report, April 1996

2. Hansen, J.E. and L.D. Travis, Light Scattering in Planetary Atmospheres, Space Sci. Rev., 16, 527–610, 1974

3. Shettle, E.P., Models of Aerosols, Clouds and Precipitation for Atmospheric Propagation Studies, Proc. AGARD 45th Sym. Electromag Wave Prop Panel, Copenhagen, Denmark, 9–13 Oct, 1989

4. Wiscombe, W.J., Mie Scattering Calculations: Advances in technique and fast, vector-speed computer codes, NCAR/TN-140 + STR, National Center for Atmospheric Research, Boulder, CO, 1979

Environmental Representations and Effects

William M. Cornette
Technical Advisor for Defense Modeling and Simulation
Terrain Modeling Project Office
Defense Mapping Agency (+)
4600 Sangamore Road, MS D-33
Bethesda, MD 20816-5003
CornetteW@nima.mil

Abstract

Under Secretary of Defense for Acquisition and Techniology (USD(A&T)) has designated three modeling and simulation executive agents for synthetic environments (i.e., terrain, ocean, and aerospace), which are directed through the Defense Modeling and Simulation Office (DMSO) to Director Defense Research and Engineering (DDR&E) and USD(A&T). The Executive Agent (EA) for Terrain is the Director of the Defense Mapping Agency, whose operational arm of the EA for Terrain is the Terrain Modeling Project Office (TMPO).

A brief overview of the M&S EA's will be provided with a discussion of the TMPO programs (i.e., Requirements, Standards, and Research & Development).

Introduction

This paper outlines the general procedures by which the Department of Defense (DoD) Modeling and Simulation (M&S) Executive Agent (MSEA) for authoritative representation of the Terrain environment conducts operations. The Under Secretary of Defense for Acquisition & Technology (USD(A&T)) designated the Defense Mapping Agency (as of 1 October 1996, the National Imagery and Mapping Agency) as the DoD MSEA for authoritative representation of the Terrain environment. In fulfilling responsibilities under DoD Directive (DoDD) 5000.59, DoD Modeling and Simulation Management, the MSEA must coordinate with other EAs, DoD Components, Federal Agencies, and various commercial sources.

DoDD 5000.59 defines an MSEA as a DoD Component to whom the USD(A&T) assigns management responsibility and delegates authority for the development and maintenance of a specific area of M&S application, including relevant standards and databases, used by or common to many models and simulations. In fulfilling its responsibilities the MSEA must:

a. Foster interoperability and reuse as critical elements in establishing cost-effective capabilities to build and use simulated and/or synthetic environments.

b. Facilitate the establishment and operation of a process by which M&S developers and users have a responsive means to acquire source data from a range of data producers.

c. Serve the M&S community as a center of excellence for the specific area of M&S application, to include related dynamic processes.

(+) Effective 1 October 1996, the Defense Mapping Agency is incorporated into the National Imagery and Mapping Agency

In the execution of these responsibilities, the MSEA shall be accountable through the Defense Modeling and Simulation Office (DMSO) to the Director, Defense Research and Engineering (DDR&E).

Terrain

To ensure a clear and common understanding of what is meant by the term "terrain", the following definition is used:

"Terrain is the configuration, composition, and representation of the surface of the earth, including its relief, natural features, permanent or semi-permanent manmade features, and the terrain modification effects of dynamic processes."

The terrain "surface" includes:

a. Inland waters, and the seafloor bottom to the 10 meter depth curve at lowest astronomical tide. Responsibility for representation of coastal bathymetry is shared and coordinated with the MSEA for Oceans.

b. The mutual interaction of dynamic phenomena and the terrain. Identification of the terrain data (features and attributes) required as input to specific models, such as mobility, weapons effects, etc., and the resulting collateral effects on the terrain will be closely coordinated with the appropriate functional expert and other EAs as required.

Excluded from the terrain "surface" are:

a. Oceans (responsibility of the Ocean EA).

b. Atmospheric phenomenology and non-terrain related effects (responsibility of the Air & Space Natural Environment EA).

c. Manmade objects which may move across the terrain, and their representations.

Terrain Representations

There are four major problems encountered in terrain representations within the M&S community today:

a. Standards for terrain data which fully support M&S community needs are not fully defined and accepted. Additionally, the associated certification and accreditation procedures are not fully established and known to the community. The result is the wasteful consumption of resources to generate system-specific databases which cannot be shared/reused, thereby limiting interoperability.

b. Although improving, the lack of an effective rapid terrain data production capability limits support to planning and rehearsal for crisis/contingency operations.

c. There continues to be a significant number, although to a large extent reduced since the creation of the MSEA for Terrain, of users and developers with limited

knowledge of terrain representation. This results in wasted resources, duplication, and unfulfilled needs.

d. The lack of sufficient means to represent dynamic terrain effects (weather, weapons effects, etc.) limits realism and operational capability.

Of the four problems areas, standardization is the more difficult to solve, but the unknowledgeable user is by far the more dangerous.

The M&S market place continues to generate a wide variety of workstations, peripherals, application software, and data. The resulting simulation systems are characterized by variations in media, format, and access software. In virtual simulations a growing variety of computational and graphics display hardware and software is used. There are no widely accepted interchange formats with supporting application program interfaces to facilitate the interchange of terrain (and other environmental) data.

The increasingly blurred distinction between simulation, mission planning, and crisis/mission rehearsal has resulted in a theoretical increase in the overall terrain representation requirement, while also offering potential savings by utilizing common data sources. However, the potential of the broad and diverse production base has not been fully exploited. The required data specifications, which fully support M&S needs, have not been established, thereby limiting authoritative data sources.

There is no widely available catalog of all available source terrain data (DTED, ITD, etc.) and/or enhanced databases. There is also not yet a comprehensive repository system to deliver simulated environment databases for evaluation and further development. Thus, users lack the knowledge to effectively locate and utilize terrain data appropriately. The inappropriate use of data can result in inaccurate analysis, negative training, and unsafe operational conditions.

A growing capability for terrain data generation from commercial sources remains largely untapped. New, untested sources of terrain data often present unacceptable risk to developers and users. With no set data certification procedures in place to qualify producers, industry response has not been well-focused.

Value-adding (feature/attribute additions and deletions) remains a major expense in database development. This leads to:

a. Extensive consumption of resources and unwarranted duplication.

b. Undocumented transformations of data. There are no established procedures for documenting what has occurred in the modification process. Thus data producers remain largely unaware of opportunities to yield large benefits to the users by making small changes in data production processes. Therefore, what might only require small changes in source data production, with large yield to the user, often go unreported.

c. Little reuse of the (often) expensive, high-value data additions/modifications. The lack of defined procedures and VV&A/C processes limits data producer and other simulation reuse of changes that can't be locally checked.

Underlying all of the issues identified above is the full understanding of terrain data and representation requirements. This limits support to standards development and results in ineffective terrain data production, and increased value-adding and data throw away. This leads to:

a. Lengthened terrain data production timelines.

b. Little data reuse.

c. Limited interoperability.

d. Wasted resources.

Terrain EA Objectives:

The primary objective of the procedures and projects of the Terrain EA is to ensure that authoritative representations of the terrain are defined and accessible to the DoD M&S analysis, acquisition, and training communities. These common representations tailored to individual system capabilities, supporting software tools, and algorithms must be:

a. Reusable to the largest extent possible to promote interoperability and cost savings.

b. Accessible to simulation developers and simulation users in a timely and efficient manner through a resource repository system in standard data and metadata formats, retrievable through common interchange format.

c. Based on broadly accepted standards that can be used by a range of government and/or commercial producers to meet area coverage and production timeline requirements.

d. Appropriately verified, validated and certified/accredited.

The MSEA role in the standardization and development process is generally that of facilitator in the project startup phase, catalyst during development, and certifier in the capability delivery phase.

EA Business Model:

The following process will be used to guide execution program development, project selection, oversight, and evaluation.

a. M&S community CUSTOMERS must be identified through an aggressive outreach program.

b. Customer REQUIREMENTS are gathered through hands-on participation with M&S system developers and users.

c. Requirements analysis identifies broadly-applicable ISSUES with potentially high payoff.

d. A STRATEGY is developed that addresses these issues, leveraging other projects/funding sources where appropriate.

e. Specific TASKS are defined to execute the strategy and achieve the required capabilities.

f. Each task must be FUNDED at a level that delivers timely results.

g. The funded projects produce DELIVERABLES that provide customer defined capabilities while achieving the previously stated objectives.

This business model demands continuous dialogue with, and feedback to, the customer. The process is not complete until a migration plan for each deliverable is established. This migration plan must address not only the delivery of a capability to a customer. It must also address the process by which a data set definition, standard, or procedure is coordinated with and adopted by the larger M&S community, including its production base. Throughout this process, maximum effort is made to use established international, national, commercial, or DoD standards and procedures.

The MSEA will execute its responsibilities and achieve its objectives by working with the M&S community, along with other government or industry organizations.

Business Model
M&S EA Business Model
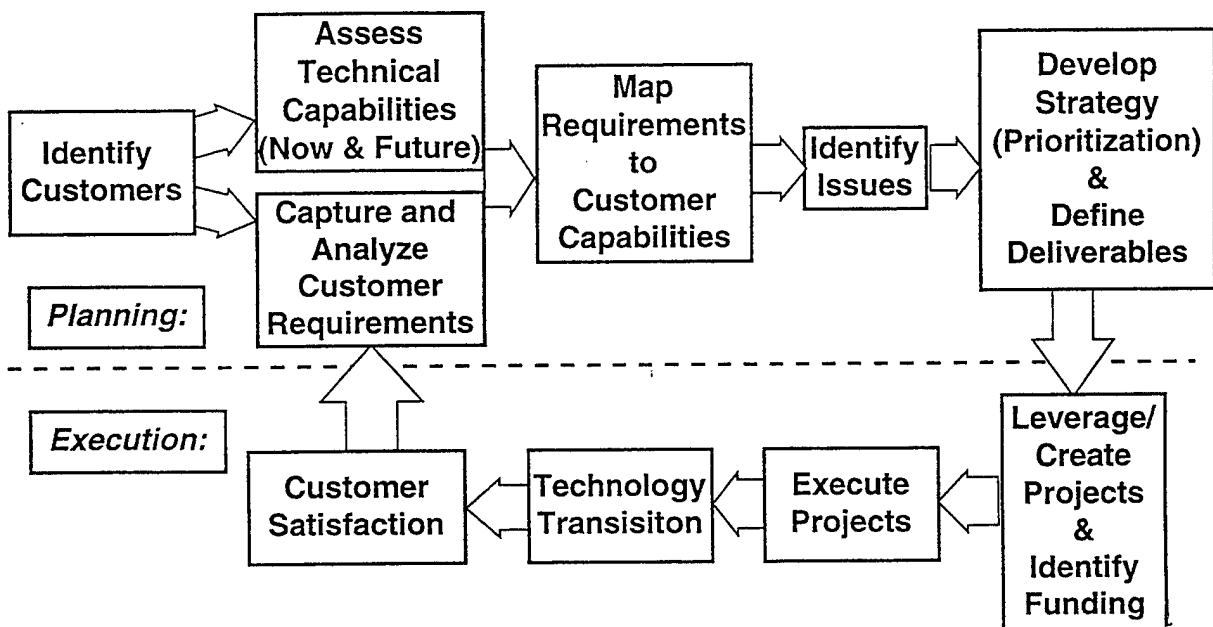
In general, prototyping is a central element of MSEA strategy. Prototyping activities fall into the following areas:

    a. To test existing data sets in new applications.

    b. To define content and design of new data sets.

    c. To study transformation processes to show producers where process or data set redesign can eliminate user modification, promote expanded reuse, and improve consistency.

    d. To study database generation techniques to seek out critical areas where promoting investment will improve database generation time and quality.

    e. To evaluate verification, validation, data certification, and software accreditation procedures and tools.

Terrain MSEA Execution Plan

The Terrain Execution Plan conforms to the general guidance obtained from the issues and actions contained in the DoD M&S Master Plan (MSMP) (DoD 5000.59-P) Sub-objective 2-1. They define M&S community wide activity areas which the MSEA will be required to report on periodically to the M&S Working Group and the Executive Council on M&S. In the event of a contradiction between this document and the DoD MSMP, the MSMP shall take precedence.

Some of the issues being addressed by the Terrain Modeling Project Office are:

a. Define user community requirements in terms of required feature data content, levels of resolution, accuracy, and fidelity for terrain representation.

b. Develop standard, correlated terrain representations at multiple levels of detail.

c. Determine availability of source data (e.g., imagery from overhead systems).

d. Coordinate terrain representation production to reduce costs and improve data consistency and quality.

e. Develop a cost-effective capability to produce standardized terrain data rapidly to meet Component needs, including the requirements of the Joint Commands to support short-notice operational planning and mission rehearsal.

f. Develop standard representations of terrain processes (e.g., thermodynamic and hydrologic models, soil strength, slump) and seasonal changes (e.g., foliage, ground cover, and reflectance).

g. Develop capabilities to represent terrain changes dynamically (e.g., weapons and/or collateral effects, craters, earth moving, damage to structures) and diurnal changes (e.g., illumination, shadows, temperature, and reflectance).

h. Develop standard methods to link models and simulations that use terrain data of differing resolution.

I. Produce geo-typical, vice geo-specific, terrain representations for training exercises.

j. Enhance the accessibility and reuse of three-dimensional models of typical cultural features (e.g., buildings, bridges).

Some of the on-going actions in the Terrain Modeling Project Office are:

a. Develop authoritative terrain prototype data sets to support M&S activities.

(1) Specify the data resolution levels, fidelity, and accuracy required to support major M&S functional areas.

(2) Develop data dictionaries in FY 96 for the feature content and attribution requirements of each M&S resolution level.

(3) Define in FY 96 the data structure, coding and attribution scheme, symbology, and metadata requirements.

b. Make all terrain representations available to the M&S community through the resource repository system.

c. Demonstrate rapid terrain data generation capability for all specified M&S resolution levels from controlled national imagery and intelligence sources.

(1) Demonstrate computer-assisted feature extraction from multiple-source imagery, with data generalization techniques applied to generate multiple database resolution levels from single pass extraction in FY 96.

(2) Demonstrate an initial capability in FY 96 to produce, within 1 week, standard terrain data to meet M&S functional area requirements contained within a nominal 2500 km^2 area.

(3) Demonstrate in FY 97 the capability to produce standard terrain data to meet M&S functional area requirements contained within a nominal 2500 km^2 area (with three-dimensional terrain, including three-dimensional man-made features, reasonably attributed), within 72 hours.

d. Nominate data exchange standards to Assistant Secretary of Defense, Command, Control, Communications, and Intelligence, as required.

e. Demonstrate the capability to generate and/or receive and apply data updates to standard terrain representations, and document the configuration control process in FY 96.

f. Develop authoritative terrain process representations, to include the interface with atmospheric and oceanographic effects (e.g., littoral regions), for selected M&S functional areas.

(1) Document terrain process representations in existing weapons effects and vehicle mobility models to establish the base line for subsequent specification of standard terrain process representation in FY 96.

(2) Establish standard process representations of soil mechanics for weapons effects, engineering earthworks, and ground mobility in FY 96.

(3) Establish an enhanced set of standard terrain process representations (e.g., thermodynamic and hydrologic models) in FY 97.

g. Develop capabilities for dynamic terrain.

(1) Establish standard capabilities for multi-state objects (e.g., damaged structures, changes in vegetation) in FY 96.

(2) Establish initial capabilities for dynamic terrain in FY 97.

(3) Develop standard process representations for dynamic terrain in FY 98.

(4) In FY 97, develop a standard methodology for interconnecting simulations (live, virtual and constructive) that use terrain models of differing resolution.

MSEA Office Organizational Structure:

The Terrain Modeling Project Office (TMPO) was created by the Director, Defense Mapping Agency to execute the activities of the DoD MSEA for Terrain. TMPO will execute the MSEA mission through independent, yet interleaved, projects and initiatives organized into three program areas:

     a. Requirements, Analysis, and Outreach

     b. Standards, Interoperability and Design

     c. Research and Development Initiatives

Each area is equally important to the success of the overall mission.

TMPO is designed as a high performance teaming environment, with no individual project executed in isolation. The Director, DMA has staffed TMPO as follows:

     a. Currently there are 11 full-time staff assigned.

     b. A full-time DMA liaison officer resides at DMSO and works directly for the Chief, TMPO.

     c. Other DoD community resource personnel are drawn in as needed to meet TMPO related project demands or provide technical expertise on an as-needed basis to support M&S related development efforts and working groups (e.g., the High Level Architecture (HLA) Architecture Management Group (AMG), Modeling and Simulation Working Group (MSWG), Environmental Representation Technical Working Group (ERTWG), and other related M&S community subgroups).

References

1. DoD Directive 5000.59, DoD Modeling and Simulation (M&S) Management, 4 January 1994.

2. DoD Modeling and Simulation Master Plan, DoD 5000.59-P, 17 October 1995.

3. Under Secretary of Defense (Acquisition and Technology) MEMORANDUM, Designation as DoD Modeling and Simulation (M&S) Executive Agent (MSEA) for Terrain, 5 April 1995.

4. Memorandum of Understanding for the Assignment of a Defense Mapping Agency Liaison to the Office of the Secretary of Defense, Director for Defense Research and Engineering, Defense Modeling and Simulation Office, 28 December 1994.

5. Defense Mapping Agency Strategic Plan, 1996 Through 2005.

6. Report of the Defense Science Board Task Force on Defense Mapping for Future Operations, Office of the Under Secretary of Defense for Acquisition and Technology, September 1995.

7. Modeling and Simulation Terrain Execution Plan (Version 96-4.1), Terrain Modeling Project Office, Defense Mapping Agency, March 21, 1996

MOSART Update

William M. Cornette
Technical Advisor for Defense Modeling and Simulation
Terrain Modeling Project Office
Defense Mapping Agency (+)
4600 Sangamore Road, MS D-33
Bethesda, MD 20816-5003
CornetteW@nima.mil

Abstract

A review and a brief summary of the status of the MOSART code is provided.

Introduction

This paper summarizes the status of the Moderate Spectral Atmospheric Radiance and Transmittance (MOSART) code. MOSART is a U.S. Government standard code with the ability to support scene and signature simulations. It grew out of a merging of the MODTRAN and APART (Refs. 1-5) codes with some additional capabilities added.

Code Description

Except for DISORT, MOSART contains all MODTRAN 3.0 capabilities and has been compared against it for a number of conditions by Spectral Sciences, Inc. It is being upgraded to MODTRAN 3.5 in the near future.

The version of the DISORT code in MODTRAN 3.5 is still under beta testing and further work is on-going at Spectral Sciences, Inc. (SSI) and at Phillips Laboratory, Hanscom AFB, MA. As soon as it is approved by Phillips Laboratory, it will be incorporated into MOSART.

As with MODTRAN, MOSART uses a 1 cm^-1 resolution set of band parameters derived from the 1995 HITRAN line atlas (N.B.: This will be upgraded to the 1996 HITRAN line atlas in the near future). Based on comparisons with degraded spectral created by the line-by-line code FASCODE, the actual resolution of both MODTRAN and MOSART are slight greater than 1 cm^-1 and are usually advertised as 2 cm^-1. In the UV/ Visible region, additional molecular absorption bands are included at a coarser resolution, and the Multiple Scatter Model uses a iterative three-stream model that is quite different from that used in MODTRAN. Further details are available in the MOSART Technical Reference Manual (Ref. 8).

The observer-source-background geometries include all MODTRAN 3.0 geometries, plus some new geometries, including Observer-Source, Observer-Background, Observer-Source-Background, Earthlimb, Horizontal, At-Source (i.e., Observer & Source are co-located). The geometry can be specified by various subsets of a number of different parameters (e.g., observer altitude, source altitude, and range; observer altitude/latitude/longitude and tangent point latitude/longitude -- or tangent altitude), so the user is able to specify any desired geometry.

An X-Windows/Motif Input GUI is available, as is a simple scrolling input file builder. However, once the user becomes familiar with the self-documenting input file structure (i.e., it contains full text descriptions of each input), an editor like vi or emacs is quite adequate.

(+) Effective 1 October 1996, the Defense Mapping Agency is incorporated into the National Imagery and Mapping Agency

Software Description

The MOSART code consists of approximately 185,000 lines of ANSI FORTRAN X3.9-1978 (FORTRAN 77) code, and in addition to the main code includes the following utilities:

<u>Installation Utilities</u>
>
> FPTEST (Floating Point/Configuration Testing Code)
> INSTDB (Data Base Installation Code)

<u>File Utilities</u>
>
> ASCBIN (ASCII-Binary Conversion Utility)
> CRFILE (File Creation Utility)
> MRFLTR (MOSART Filter Integrator)
> PLTGEN (NCAR Plotting Utility Code)

<u>UNIX Utilities</u>
>
> Makefiles
> Directory Set Up
> X-Windows/Motif Input Builder GUI
> C++ Driver

<u>Ancillary Codes</u>
>
> BBTEMP (Equivalent Blackbody Temperature Code)
> FACET (Flat/Cylindrical/Spherical Facet Signature Code)
> FANTOM (Filter Optimization Code)
> SCNGEN (Statistical Scene Generator)
> TERTEM (Terrain Material Temperature Code)
> VISUAL (Human Visual Response Code)

<u>Test Cases (11)</u>

<u>Data Bases</u>
>
> MODTRAN Molecular
> MOSART Molecular
> SAG/NRL Atmospheres
> Global Terrain/Ecosystem
> Global Climatology

Hardware Requirements

Recommended platforms for the MOSART code are moderate-to-high end workstations (e.g., SGI, Sun, HP, DEC Alpha), although it will run on a high end PC (e.g., 100 MHz, 32/64 Mb RAM, 50-75 Mb of free disk space). It has been thoroughly tested on machines that use the IEEE floating point Standard 754 (e.g., SGI, Sun, HP). On machines that use other numerical representations (e.g., VAX/VMS), there may be some minor numerical problems. For example, a numerical problem was encountered with the hard underflow on the VAX; once the problem was isolated, the fix was quite simple and was purely numerical.

Documentation

The MOSART code is accompanied by four (4) manuals:

> Installation Reference Manual (Ref. 6),
> User's Reference Manual (Ref. 7),
> Technical Reference Manual (Ref. 8), and
> Software Reference Manual (Ref. 9).

The Installation Reference Manual (Ref. 6) provides sufficient discussion to allow a user familiar with their system (i.e., hardware, operating system, and compilers) to determine the configuration requirements (e.g., record lengths for direct access files, numerical constraints), configure the code, install the code, and run a test case.

The User's Reference Manual (Ref. 7) describes the main input file and auxiliary input files in detail. It also summarizes the data bases, and the various output files available to the user. It provides all details required for treating the MOSART code as a "black box."

The Technical Reference Manual (Ref. 8) provides the user with many of the technical details used in developing the MOSART code and its data bases. It is not meant to be a comprehensive description of all the theory within the code, but it does present most of the major features.

The Software Reference Manual (Ref. 9) is designed to assist the user who wishes to analyze the internal source code. It contains flow diagrams, calling trees, module descriptions, and variable definitions for all global variables (i.e., variable in COMMON blocks and routine arguments).

Status

Version 1.41 of the MOSART code was formally released on 2 September 1995. Any copy of the code with an earlier version number should be considered an "alpha" test version and should be replaced with Version 1.41 immediately. An errata document is available from the author (see address below). The errata document contains corrections to the manuals (e.g., typographical errors), clarifications based upon user questions, and modifications to the code. The modifications are either corrections or upgrades (e.g., incorporating MODTRAN 3.5 features).

To assist in some interactive scene generation and modeling, a copy of MOSART labeled Version 1.95 was created. It contains "alpha" test versions of some the upgrade capabilities. However, it is not fully tested and should be considered a preliminary code, and Version 1.41 is recommended instead.

Potential Upgrades

There are a number of potential upgrades to the MOSART code, some of which have been installed in a "sandbox" version under development by the author. Some of these potential upgrades include:

<u>Atmosphere</u>
(++)   3-D Atmosphere Characterization (Version 1.41 is 2-D)
(++)   Broken Cloud Fields
(++)   Global Humidity Data Base
        Diffuse Transmission Through Clouds
        DISORT Integration
        New Exponential Sum Fit Algorithm
        Improved Radiative Transfer Algorithm
(++)   Microwave/Millimeter Wave Capability

Polarization

<u>Terrain</u>
(++)   Global Snow Cover & Sea Ice Data Bases
(++)   Higher Resolution Reflectivity Data Base
         Interface with FACC Standard
(++)   Microwave/Millimeter Wave Capability
         Polarization

<u>Miscellaneous</u>
(++)   Allow Multiple, Overlapping Sensor Response Curves
         Allow Insertion of User-Defined Elements (e.g., Clouds, Smoke)
         Interface with Weather Data Bases

(++) Currently in the "sandbox" version of the code.

Availability

At this time, the Ballistic Missile Defense Office (BMDO) and Air Force Public
Affairs have cleared the MOSART source code, data bases, and documentation for public
release. The Geophysics Directorate of the Phillips Laboratory still considers Version
1.41 of MOSART a "beta" release, and is controlling the distribution until further testing
has occurred. Requests for the code should be submitted to:

Dr. Laila Jeong (PL/GPOS)
Geophysics Directorate
Phillips Laboratory
29 Randolph Road
Hanscom AFB, MA 01731-3010
(617) 377-3671
jeong@plh.af.mil

Technical questions about MOSART should be directed to the author at:

Dr. William M. Cornette
National Imagery and Mapping Agency (SA)
4600 Sangamore Road, MS D-33
Bethesda, MD 20816-5003
(301) 227-3492
cornettew@nima.mil

or to:

Dr. Prabhat K. Acharya
Spectral Sciences, Inc.
99 So. Bedford Street, #7
Burlington, MA 01803-5169
(617) 273-4770
prab@spectral.com

References

1. Cornette, W.M., Atmospheric Propagation and Radiative Transfer (APART) Computer Code (Version 7.00), Volume I: Installation Reference Manual. Photon Research Associates, Inc. PRA R-024-90 (1990)

2. Cornette, W.M., Atmospheric Propagation and Radiative Transfer (APART) Computer Code (Version 7.00), Volume II: User Reference Manual. Photon Research Associates, Inc. PRA R-062-90 (1990)

3. Cornette, W.M., Atmospheric Propagation and Radiative Transfer (APART) Computer Code (Version 7.00), Volume III: Technical Reference Manual. Photon Research Associates, Inc. PRA R-077-90 (1990)

4. Cornette, W.M., Atmospheric Propagation and Radiative Transfer (APART) Computer Code (Version 7.00), Volume IV: Software Reference Manual. Photon Research Associates, Inc. PRA R-075-90 (1990)

5. Cornette, W.M., Atmospheric Propagation and Radiative Transfer (APART) Computer Code (Version 7.00), Volume V: Source Code Listing. Photon Research Associates, Inc. PRA R-070-90 (1990)

6. Cornette, W.M., P. Acharya, D. Robertson, and G.P. Anderson, Moderate Spectral Atmospheric Radiance and Transmittance Code (MOSART). Volume I: Installation Reference Manual. PL-TR-94-2244(I). 7 November 1995. ADA304038

7. Cornette, W.M., P. Acharya, D. Robertson, and G.P. Anderson, Moderate Spectral Atmospheric Radiance and Transmittance Code (MOSART). Volume II: User's Reference Manual. PL-TR-94-2244(II). 7 November 1995. ADA304180

8. Cornette, W.M., P. Acharya, D. Robertson, and G.P. Anderson, Moderate Spectral Atmospheric Radiance and Transmittance Code (MOSART). Volume III: Technical Reference Manual. PL-TR-94-2244(III). 7 November 1995. ADA304072

9. Cornette, W.M., P. Acharya, D. Robertson, and G.P. Anderson, Moderate Spectral Atmospheric Radiance and Transmittance Code (MOSART). Volume IV: Software Reference Manual. PL-TR-94-2244(IV). 7 November 1995. ADA304073

IMPROVING MODTRAN'S MOLECULAR TRANSMITTANCE ALGORITHM

S. Adler-Golden, P. Acharya, A. Berk, and L. Bernstein
Spectral Sciences, Inc.
Burlington, MA 01803

G. Anderson and J. Chetwynd
Air Force Phillips Laboratory
Hanscom AFB, MA 01731

19th Annual Review of Atmospheric Transmission Models

4-6 June 1996

MOTIVATION

- Track down problems in data-model comparisons for water vapor sounding

- Characterize MODTRAN accuracy for typical remote-sensing scenarios

- Improve MODTRAN accuracy

  High accuracy and speed needed for climatology, retrievals

  Focus on molecular transmittance algorithm

HOW GOOD IS MODTRAN?

- Errors Depend on Species, Altitude, Path, Resolution
- Typical RMS Errors at 5 cm^{-1} Resolution:
  1% Transmittance, 5% Optical Depth
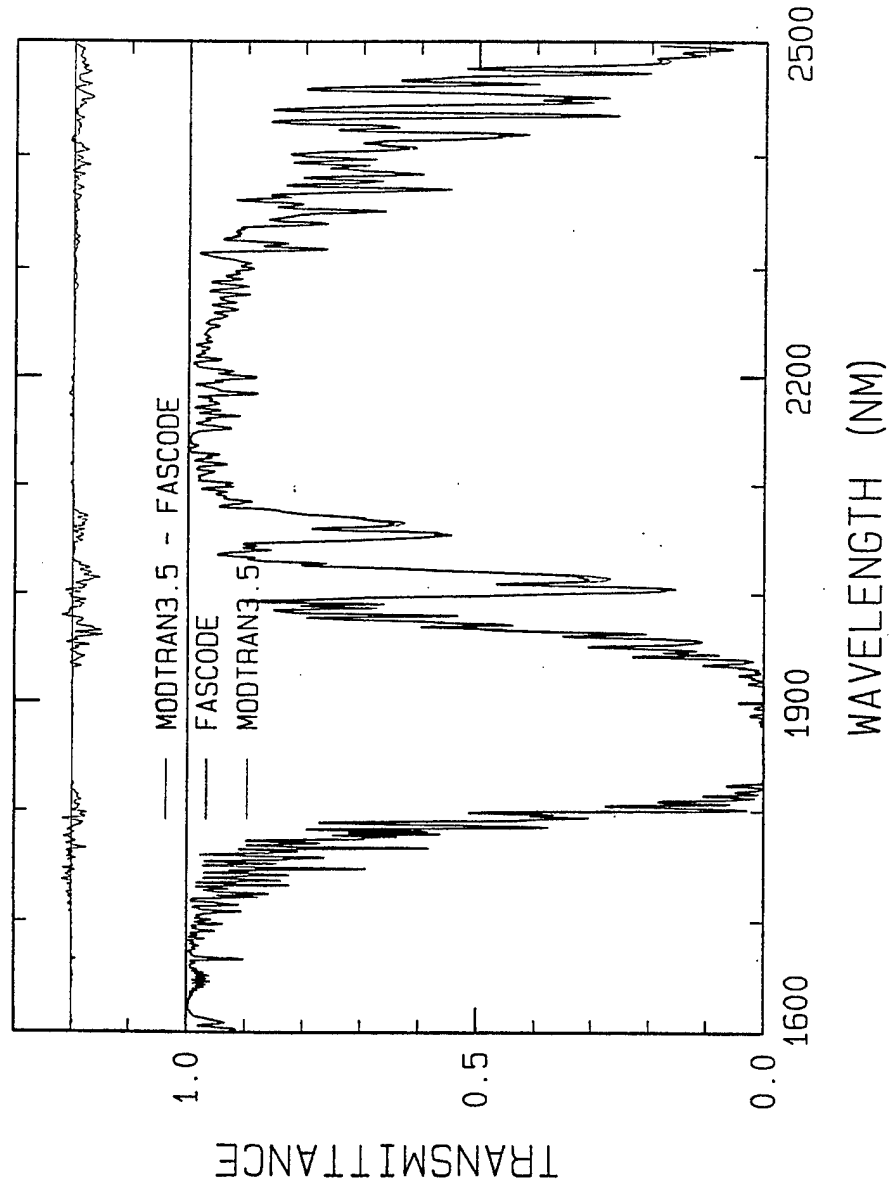
MOLECULAR TRANSMITTANCE ASSUMPTIONS

- Narrow-band model, 1 cm^{-1} bins

- Randomly located, equal-strength lines in bin for each species (Goody band model)

  Bin transmittances are product of separate transmittances for each line and species

- Formulas for equivalent width (W) used to calculate single-line transmittance (1-W)

  Rogers-Williams formula for Voigt W

  Approximate corrections for line tail leakage: reduce W, add line tail continuum

RESULTS OF INVESTIGATION

- Improved line tail treatment

  Incorporated in MODTRAN3.5

- Developed correction for non-random (correlated)
  line positions

- Developed new 2-line-group model to account for
  line strength distribution

PROCEDURE

- Isolate sources of error in transmittance algorithm

  Separately test approximations vs. exact solution

- Develop computationally efficient improvements that are compatible with current code structure

- Compare MODTRAN and FASCODE spectra, assess differences

LINE TAIL TREATMENT

- Basic idea

  Calculate in-bin W for "standard" line location
  Add tails to neighboring bins as continuum
    Continuum scales with pressure

- MODTRAN3.5 upgrade

  Adjust continuum for actual line locations

  Results:
    Errors reduced up to 40% (3 cm^{-1} res.) at 1 atm
    Very little effect at 10 cm^{-1} res., low pressure
    No effect on execution time, code structure

ZENITH VIEW FROM GROUND

MODTRAN3.5 ——
FASCODE - - - -

Error: MODTRAN3

Error: New tails (MODTRAN3.5)

Radiance (W/cm2/sr/cm-1)

Wavenumber (cm-1)

159
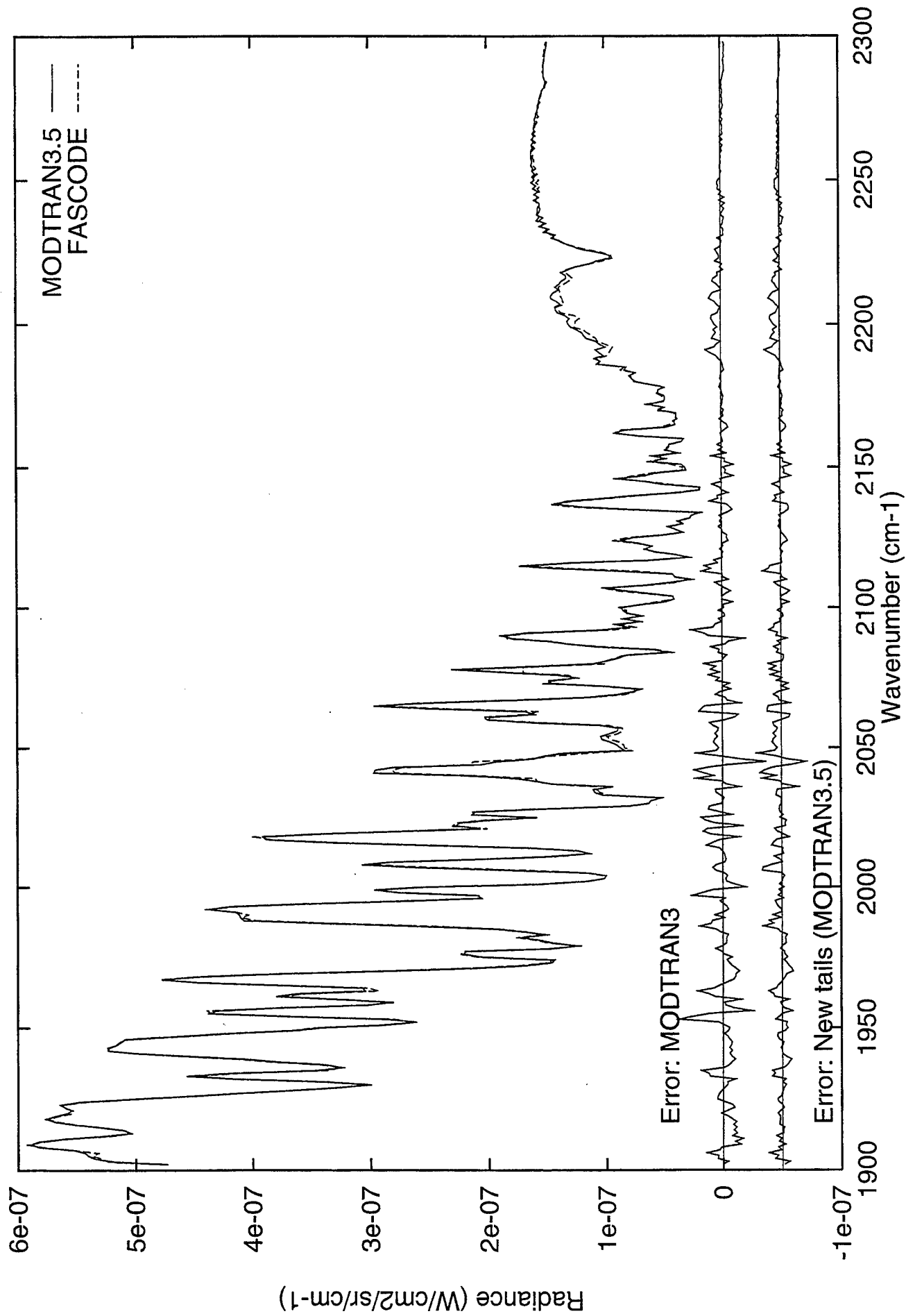
LINE CORRELATION INVESTIGATION

Developed procedure to adjust for line position correlation

- Effective no. of lines per bin is decreased or increased depending on whether line ovelap is more or less than chance

- Procedure implemented in test code only

160

CORRELATION CORRECTION RESULTS

Correction method substantially reduces line correlation errors, but they are typically small to begin with
Exception: NO_2
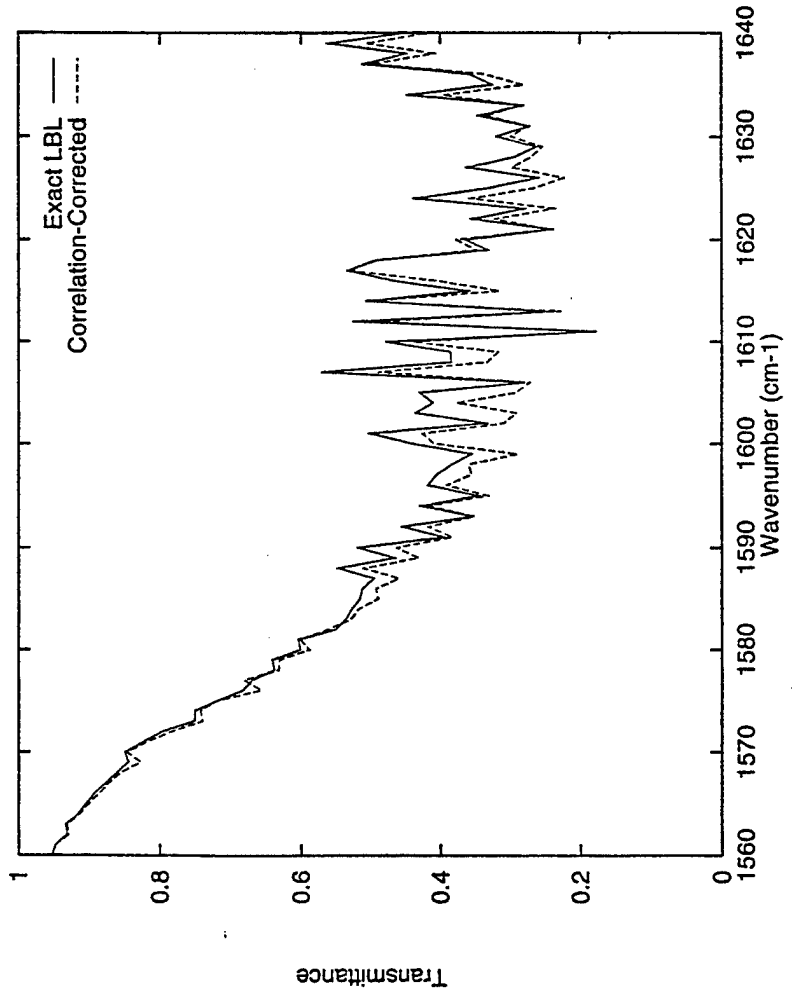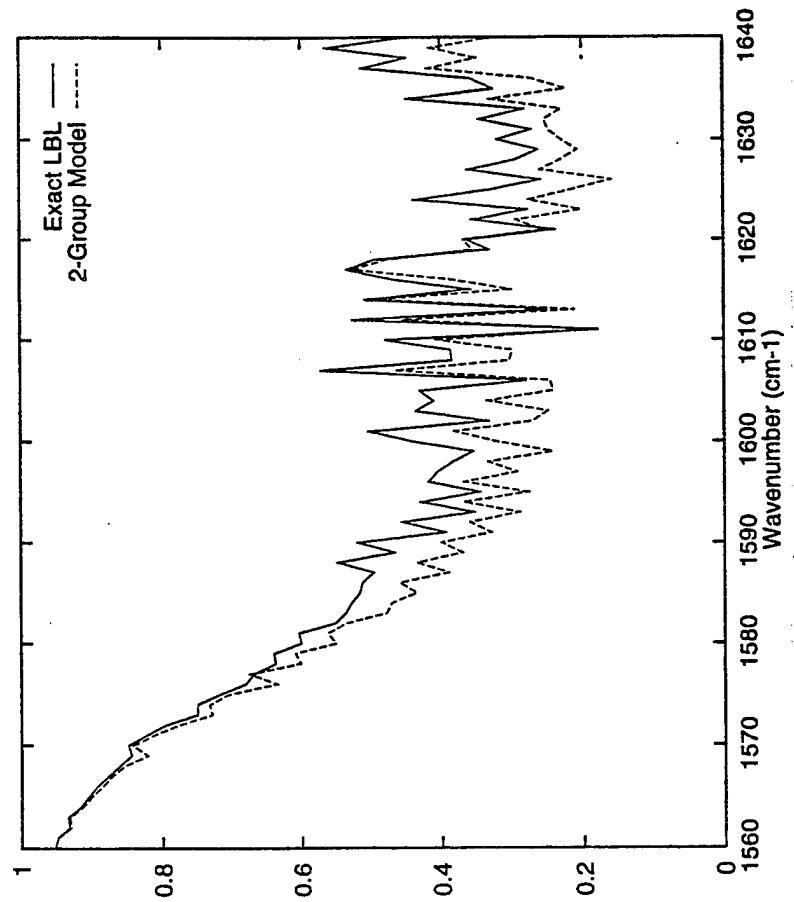
CORRELATION EFFECTS: EXAMPLE

300 atm-cm CO$_2$
0.9 atm
No smoothing
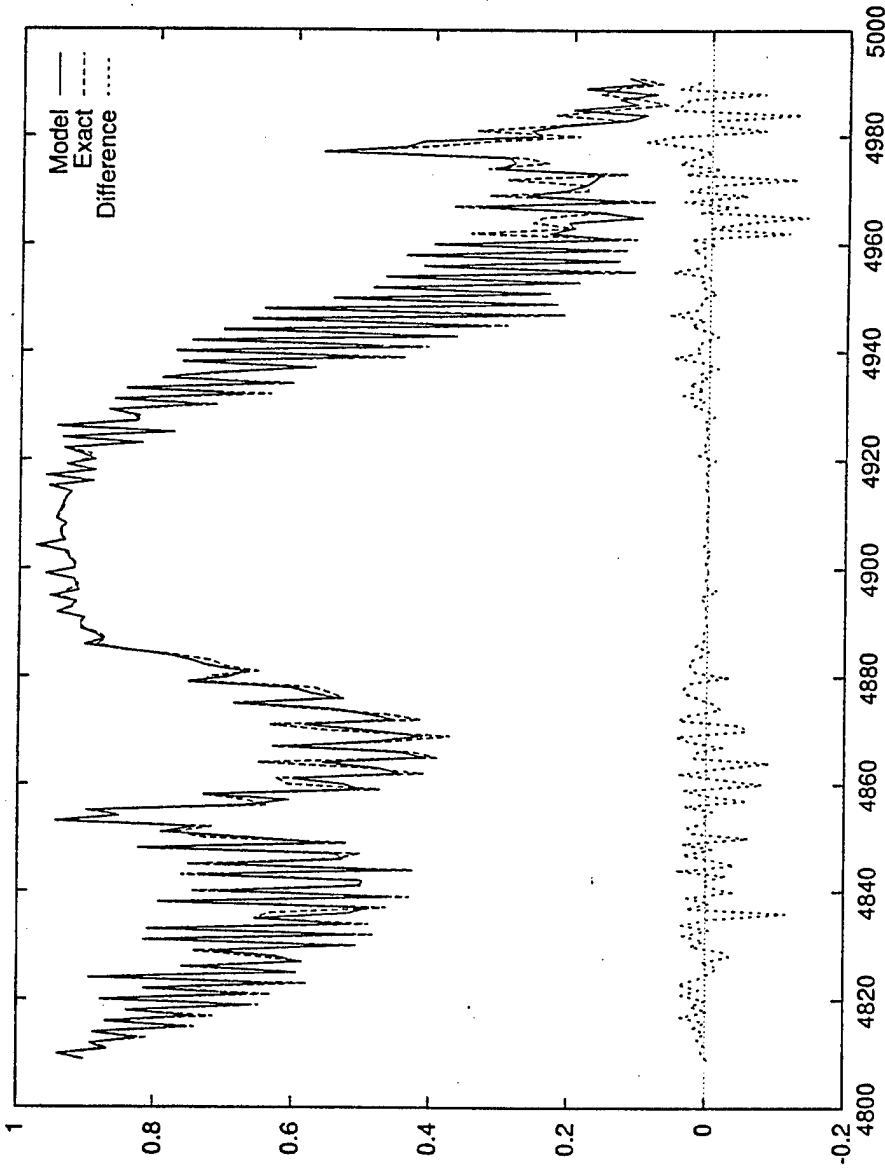
Without Correction

With Correction

Model ———
Exact - - - -
Difference ......
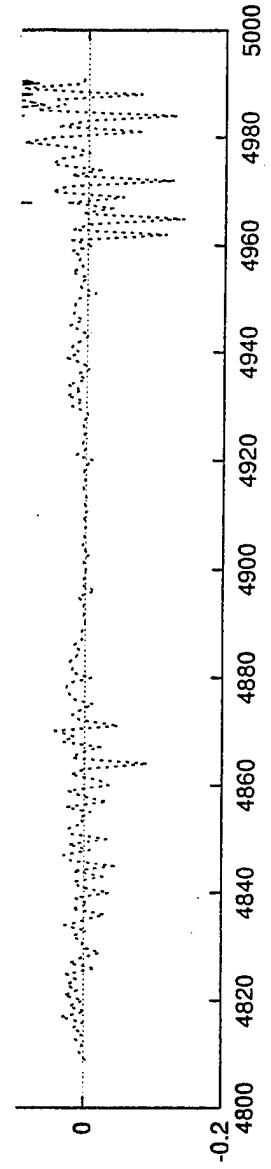
MODTRAN'S EQUAL LINE STRENGTH ASSUMPTION

- n = lines/bin is chosen for correct curve of growth in thick Lorentzian limit

- Accurate transmittances for most molecular bands

  $T \sim 1/e$ when all lines are thick

- Too much absorption for $> \sim 5$ lines/cm^{-1} (e.g., O_3)

  $T \sim 1/e$ when some lines are thick, some are thin due to wide line strength dynamic range

Partial solution:

  n's adjusted for "compromise" curve of growth

  Compensating error in W formula

163

IMPROVED TREATMENT

- 2 line groups, 1 strong, 1 weak

- Groups defined by matching s^p sums, $p = 1/2, 1, 3/2, 2, 2$

- Implemented in beta-test MODTRAN

- Lengthens computation time less than factor of 2

Results:

No effect on water vapor spectrum

Typical 40% error reduction for CO_2

Large improvements for N_2O (2100 cm^{-1}), O_3

164

HORIZONTAL PATH, 40 KM ALT.

2-Group Error

MODTRAN3 Error

MODTRAN3
FASCOD3

Wavenumber (cm^{-1})

Transmittance

165

ZENITH VIEW FROM GROUND

FASCODE
MODTRAN3.5
MODTRAN3
2-Group

Radiance (W/cm2/sr/cm-1)

Wavenumber (cm-1)
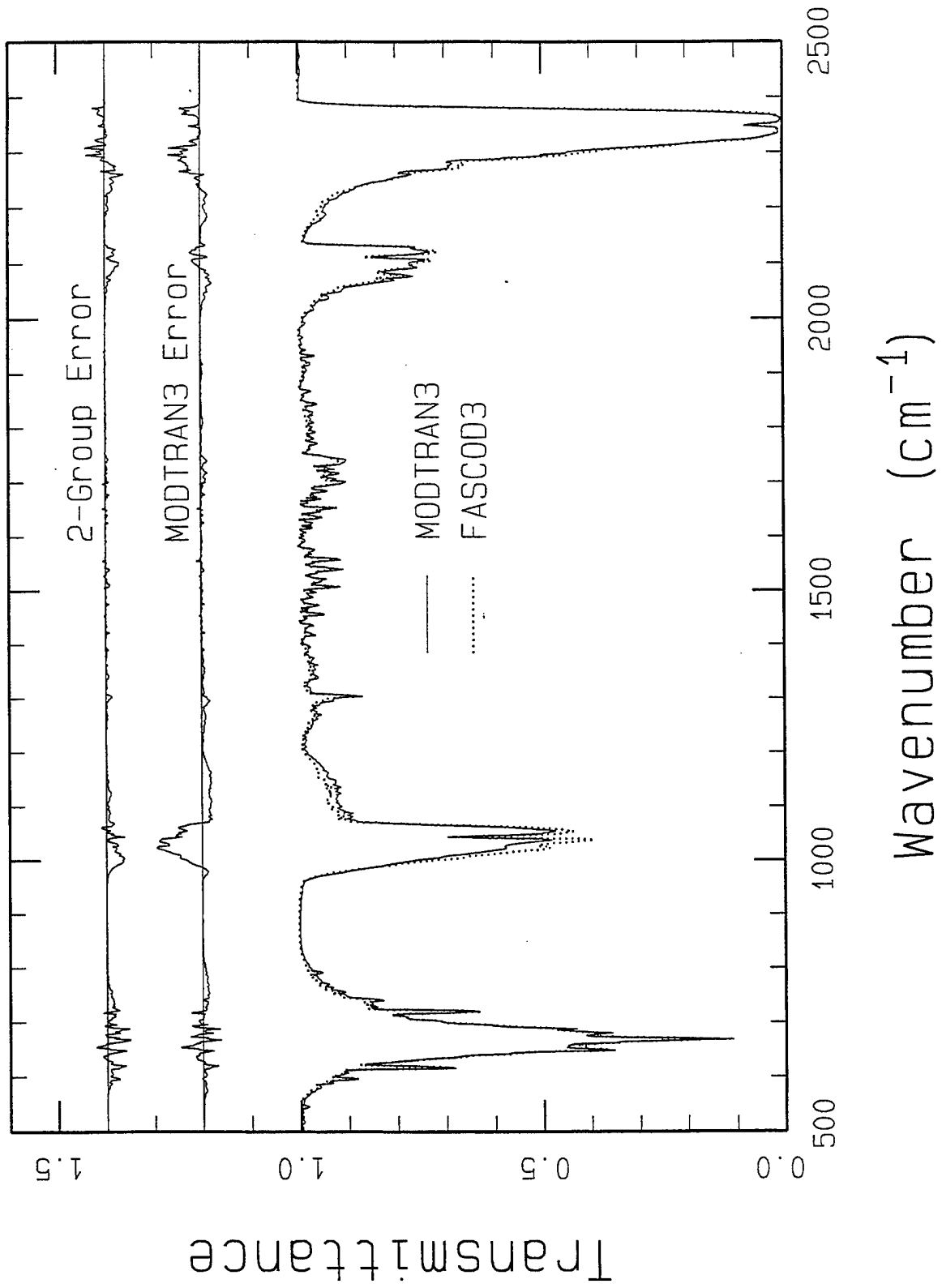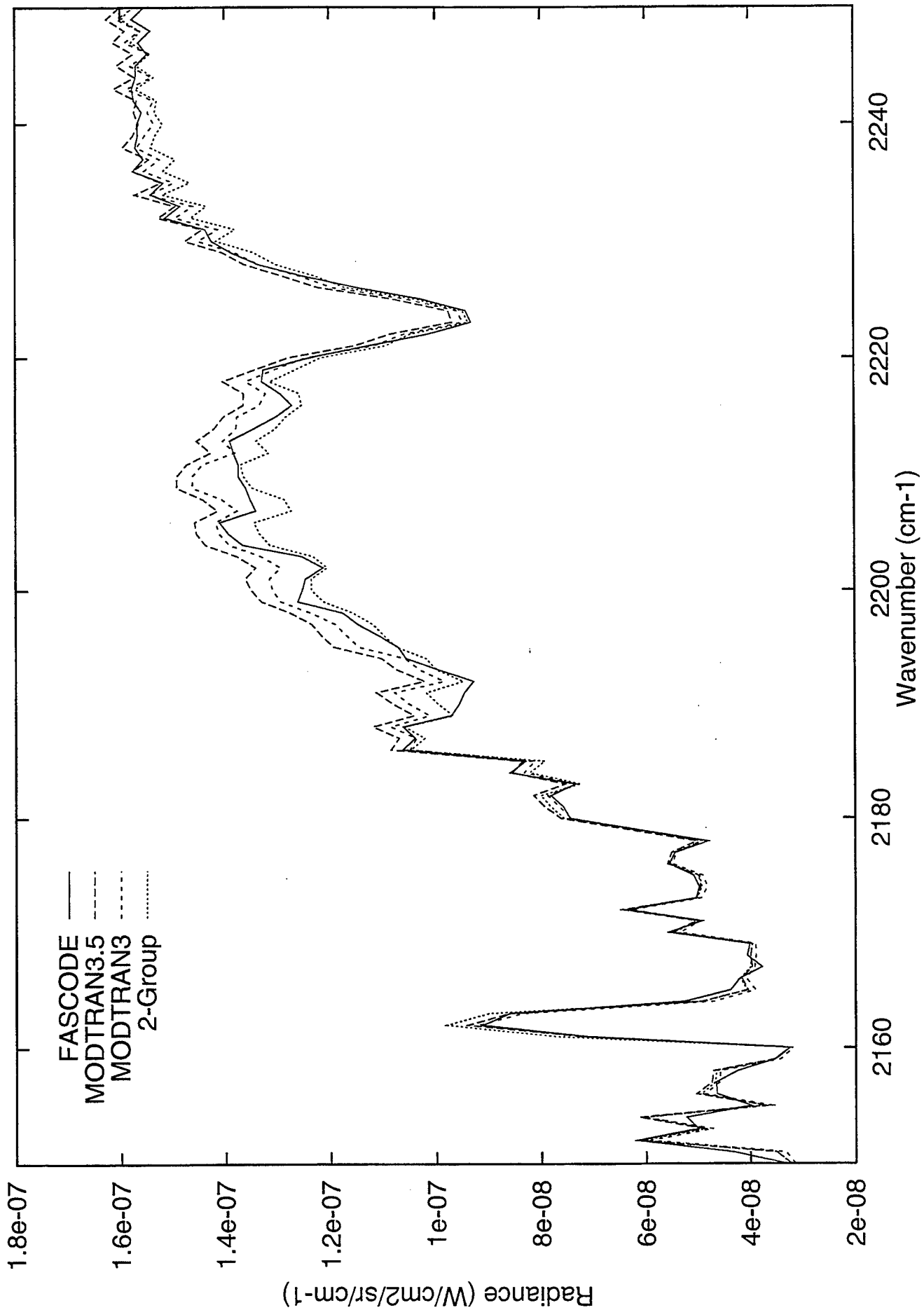
SUMMARY

- Characterized origins of MODTRAN molecular transmittance errors

- Improvements developed: some incorporated, some for future

- Line correlation effects are small except for NO_2

- Need to account for line strength dynamic range (e.g., 2-group model) for best accuracy

- MODTRAN is suitable for quantitative remote sensing

MODTRAN CLOUD AND MULTIPLE SCATTERING UPGRADES
WITH APPLICATION TO AVIRIS

A. Berk, L. S. Bernstein, D. C. Robertson, and P. K. Acharya
Spectral Sciences, Inc., 99 South Bedford St.,
Burlington, MA 01803

G. P. Anderson and J. H. Chetwynd
Phillips Laboratory, Geophysics Directorate
Hanscom AFB, MA 01731

1. INTRODUCTION

Characterization of surface properties from AVIRIS measurements is hampered by atmospheric attenuation and path radiances. MODTRAN (Berk et al., 1989), the Air Force PL/Geophysics Directorate moderate spectral resolution (2 cm^{-1}) background radiance and transmission model, is often used to account for the atmospherics in AVIRIS measurements. It rapidly predicts the molecular and aerosol/cloud emissive and scattered contributions to observed radiances along with the atmospheric attenuation. MODTRAN has been extensively validated against both measurements and the high spectral resolution FASCODE (Clough et al., 1988) model.

MODTRAN4, currently under development, contains two new features which greatly improve predictive capabilities under cloudy and/or heavy aerosol loading conditions. It allows a user to explicitly define water and ice cloud vertical profiles and spectral data either by scaling the default model clouds or by defining a new model cloud. MODTRAN4 also introduces a Correlated-k (CK) capability which significantly improves the accuracy of the multiple scattering radiance calculations. In the following sections, a discussion of the MODTRAN4 upgrades and an initial validation by comparison to airborne measurements of a solar illuminated cumulus cloud top are presented. Finally, the effect of the CK approach for two AVIRIS scenarios is demonstrated.

2. MODTRAN CLOUD/RAIN MODELS UPGRADE

The MODTRAN cloud/rain models have been upgraded (Berk, 1995) and now allow for generalized specification of layering and optical and physical properties as well as the presence of multiple properties as well as the presence of multiple overlapping and non-overlapping clouds. The cloud models affected are all of the cumulus and stratus type clouds, both with and without rain. This includes MODTRAN cloud/rain models 1 through 10. The cirrus models 17-19 only required improved layering. The cloud model upgrades include:

- adjustable cloud parameters,
  - thickness, altitude, vertical extinction, column amounts, humidity, and scattering phase functions,
- decoupling of the clouds from aerosols,
- introduction of ice particles,
- user-defined water droplet, ice particle and rain rate profiles,
- user-defined cloud spectral properties, and
- output of cloud/rain profiles and spectral data to tape6 (NOPRT − -1).

The decoupling of the cloud and aerosol models has a number of implications. Clouds and aerosols can co-exist at a single altitude, or clouds can be modeled with no aerosol profiles included. When clouds and aerosols co-exist, the cloud water droplets, cloud ice particles and aerosol particles may all have different scattering phase functions. The single scatter solar contribution of each component is properly combined. However, for multiple scattering a single effective phase function is defined based on a scattering optical depth weighted Henyey-Greenstein asymmetry factor; this is the same approach that is used to combine the aerosol and molecular scattering contributions.

Cloud profiles are merged with the other atmospheric profiles (pressure, temperature, molecular constituent and aerosol) by combining and/or adding new layer boundaries. Any cloud layer boundary within half a meter of an atmospheric boundary layer is translated to make the layer altitudes coincide; new atmospheric layer boundaries are defined to accommodate the additional cloud layer boundaries.

3. ADDITION OF A CORRELATED-*k* CAPABILITY TO MODTRAN

Addition of a CK capability to MODTRAN (Bernstein et al., 1995) provides an accurate and fast means for evaluation of the effects of clouds and heavy aerosol loading on retrievals (both surface properties and species concentration profiles) and on atmospheric radiative heating/cooling calculations. These radiative transfer computations require coupling the effects of gaseous molecular absorption due primarily to water vapor, carbon dioxide, and ozone, with particulate multiple scattering due to volcanic aerosols, ice crystals, and water droplets. The molecular absorption band model used in MODTRAN is not suitable for interfacing with standard multiple scattering algorithms. This is because the scattering models require a <u>monochromatic</u> representation of the molecular transmission (i.e., Beer's law), whereas molecular band models which represent the transmission for a <u>finite spectral interval</u> do not follow Beer's law. In order to adapt a band model approach for use in scattering calculations it is necessary to express the band model transmission function in terms of a weighted sum of Beer's law exponential terms. Thus, a method for determining the weighing factors and monochromatic absorption coefficients for the MODTRAN band model is required. An abbreviated discussion of the CK approach as tailored for integration into MODTRAN is given below; for a more complete discussion of the CK method the reader is referred to Lacis and Oinas (1991).

For simplicity, consider the problem of determining the average transmittance, as defined by Beer's law, for a homogeneous path over a finite spectral interval. The generalization to inhomogeneous paths is straightforward and is also described below. The path transmittance can be exactly determined through evaluation of

$$T(u) = \frac{1}{\omega_2 - \omega_1} \int_{\omega_1}^{\omega_2} d\omega \, \exp(-k(\omega)u) \quad , \tag{1}$$

where ω is frequency, $k(\omega)$ is the monochromatic absorption coefficient, and u is absorber column density. The basis of the CK approach is that evaluation of T(u) by integration over frequency can be replaced by an equivalent integration over the distribution of absorption coefficient values f(k) in the spectral interval

$$T(u) = \int_0^\infty dk \, f(k) \, \exp(-ku) \quad . \tag{2}$$

The difficulty in evaluation of T(u) via Equation (2) is the necessity of first determining f(k); the advantage is that k(ω) is typically a highly repetitive function of ω (i.e., there are many nearly equivalent values of a given k in a spectral interval) and thus numerical evaluation of Equation (2) requires far fewer grid points than Equation

(1). Note that $f(k) = 0$ above the maximum k_{max} and below the minimum k_{min} absorption coefficients in the spectral interval. The probability distribution $f(k)$ can be determined directly from $k(\omega)$ by binning the k's into selected Δk sub-intervals.

The distribution function $f(k)$ is not smooth or monotonic: it generally consists of a series of sharp spikes which reflects the sharp line structure of $k(\omega)$. It then becomes more computationally convenient to work with the smooth and monotonic cumulative probability distribution function

$$g(k) = \int_0^k dk' \, f(k')$$ (3)

Physically, $g(k)$ is the fraction of absorption coefficients below k within the finite spectral interval ω_1 to ω_2. It assumes the values $g = 0$ at $k = k_{min}$ and $g = 1$ at $k = k_{max}$. The transmittance is related to g by

$$T(u) = \int_0^1 dg \, \exp(-k(g)u)$$ (4)

where $k(g)$ is given by the inverse of $g(k)$, $k(g) = g^{-1}(k)$. In practice, the evaluation of Equation (4) proceeds via summation according to

$$T(u) = \sum_{i=1}^{imax} \Delta g_i \, \exp(-\overline{k}_i u)$$ (5)

where the Δg_i's and $\overline{k}_i$'s are the sub-interval weighing factors and effective absorption coefficients necessary for the MODTRAN band model. The maximum number of intervals i_{max} and the specific selection of Δg_i interval boundaries (g_i, g_{i+1}) are chosen based on consideration of a number of factors including computational speed and accuracy, and the altitude and spectral ranges of interest. For multi-layer paths it is assumed that there is perfect spectral correlation among the sub-intervals of each layer, resulting in a total path transmittance given by

$$T(u) = \sum_{i=1}^{imax} \Delta g_i \sum_{j=1}^{jmax} \exp(-\overline{k}_{ij} u)$$ (6)

where j denotes the sum over layers.

The MODTRAN band model for a single species (multiple species are discussed later) is based on four parameters: (1) the integrated line strength S in a spectral interval $\Delta \omega$ ($\Delta \omega = 1$ cm^{-1} in MODTRAN), (2) the effective number of equivalent lines n (non-integer values of n are acceptable) in the interval, (3) the average pressure broadening Lorentz line width γ_L, and (4) the Doppler line width γ_D. These parameters are determined directly from the 1992 HITRAN parameter line compilation (Rothman et al., 1992). The molecular transmittance model is given by

$$T(u) = (1 - \frac{W(S_s u, \gamma_L, \gamma_D)}{\Delta \omega})^n$$ (7)

where $S_{sl} = S/n$ is the strength for a single effective line, and W is the Voigt equivalent width of the line taking into consideration only the portion of the line shape which falls within the 1 cm^{-1} MODTRAN spectral interval. This functional form for the band model transmittance derives from the assumption that all the lines in the spectral interval are positionally uncorrelated and thus accounts for line overlap in a statistically average sense. The transmittance contribution due to the tails of lines which originate from outside the spectral interval are included as a single multiplicative Beer's law term. Detailed formulas for the equivalent width W can be found in Berk et al. (1989). As discussed elsewhere (Bernstein et al., 1995), the k-distribution g(k) for the band model can be determined from line-by-line (LBL) simulations which are physically constrained by the same assumptions used to derive Equation (7). The use of real time LBL simulation to derive g(k) during a MODTRAN run is much too slow to be of practical value; however, the approach adopted in MODTRAN4 is to use LBL simulation off-line to pre-compute a table of k-distributions which can be rapidly accessed and interpolated during a run.

4.   INITIAL VALIDATION OF MODTRAN4 MULTIPLE SCATTER SOLAR

Development of MODTRAN4 was necessary because MODTRAN3 predictions of multiple scatter solar radiances in spectral regions where non-continuum molecular absorption is important are inaccurate. Unfortunately, this scenario cannot be validated by comparisons to FASCODE because FASCODE does not calculate solar path scattered contributions. Thus, initial validation of MODTRAN4 multiple scatter solar calculations were made directly to measurements.

Figure 1 illustrates a comparison of calculated radiance predictions to airborne measurements (Malherbe et al., 1995) performed by ONERA and CELAR using SICAP, a circular variable filter cryogenic spectrometer (1500 - 5500 nm, 2% spectral resolution). The aircraft altitude was 3.0 km, the cloud top was 2.5 km, the sensor line-of-sight (LOS) zenith angle was 104°, and the solar zenith and relative azimuth angles were 48° and 137°, respectively. Three sets of calculations are shown: (1) results from NAULUM (Malherbe et al., 1995), a new radiative transport model developed at ONERA, (2) MODTRAN calculations performed without the CK approach (labeled MODTRAN3), and (3) MODTRAN calculations performed with the CK approach (labeled MODTRAN4). The MODTRAN4 cloud model upgrade enabled the cloud profile and spectral data to be explicitly entered for both the MODTRAN3 and MODTRAN4 calculations. The cumulus cloud was modeled with a homogeneous liquid water droplet density of 0.68 g/m^3 from 0.1 to 2.5 km altitude. Water droplet single scattering albedos (Hansen et al., 1970) for a mean spherical particle radius of 8μm were entered at a 0.05μm spectral resolution. Both MODTRAN calculations were performed using a simpler two-stream multiple scattering model (Isaacs et al., 1987); the discrete ordinate model in MODTRAN, DISORT (Stamnes et al., 1988), was run with 8-streams over a limited spectral sub-region and produced similar results. MODTRAN3 severely overpredicts the multiple scattering contributions; this is the expected result because the MODTRAN band model layer single scattering albedos are too large.
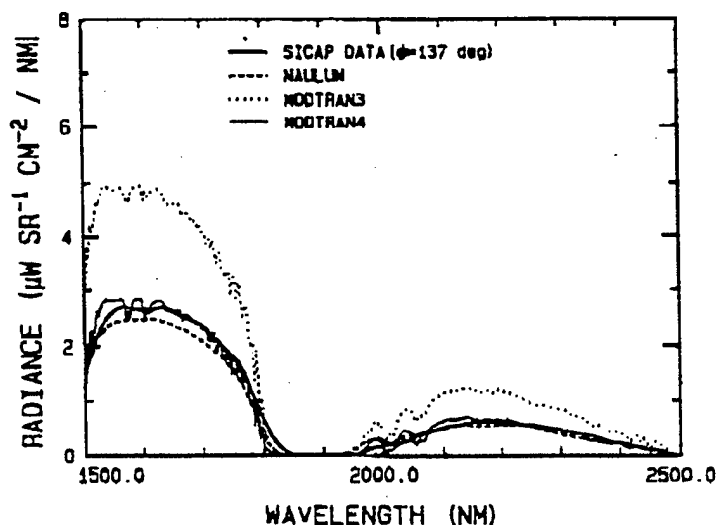
Figure 1.   A Comparison Between SICAP Measurements (Malherbe et al., 1995) and Model Predictions for a Solar Illuminated Cumulus Cloud Top with a 137° Relative Solar Azimuth Angle.

Figure 2 illustrates an additional comparison of calculated radiances to SICAP, but with a LOS zenith angle of 95° and, more importantly, with a solar relative azimuth angle of 11°. In this forward scattering case, MODTRAN4 underpredicts the measurements by a factor of 2 because the multiple scattering model averages over the azimuthal dependence (MODTRAN does properly account for the relative azimuth angle in calculation of single scatter solar but single scatter solar is less than 20% of the total radiance in this example). The better agreement of MODTRAN3 with SICAP measurements results from fortuitous cancellation of errors. The NAULUM calculation is an improvement over MODTRAN4 because it models the azimuthal distribution of radiation in its discrete ordinate multiple scattering calculation. A new version of DISORT has been developed which also models this azimuthal dependence, but this upgrade has not yet been ported to MODTRAN. For the nadir viewing geometries, such as AVIRIS, the neglect of the azimuthal dependence of the multiply scattered photons in DISORT is a reasonable approximation; similarly, the two-stream Isaac's model is also expected to yield good results.

5. APPLICATION OF MODTRAN4 TO AVIRIS

The primary focus of AVIRIS is the characterization of the Earth's terrestrial surface. For many applications, the upgrade from MODTRAN3 to MODTRAN4 will have only a minor effect on the analysis of AVIRIS data. Under clear sky or thin cirrus conditions, differences between MODTRAN3 and MODTRAN4 down-looking radiances from 20 km in the 400 to 2500 nm spectral region are generally small. This will be true whenever multiple scattering is only a small fraction of the total radiance, or whenever spectral variation of molecular absorption is small. However, these conditions are not always satisfied. Figure 3 illustrates differences between the down-looking radiances predicted by MODTRAN3 and MODTRAN4 in the center of the 1.9μm H_2O band. These calculations were performed with a 1km thick cirrus cloud at 10km altitude (0.14 vertical extinction at 550 nm), a solar zenith angle of 75°, and using the MODTRAN grass surface reflectances (Mustard, 1991). Within the 1.9μm band region, MODTRAN3 radiances are too high by 0 to 20%.

For measurements of solar illuminated optically opaque clouds, MODTRAN4 upgrades are critical. In Figure 4, MODTRAN3 and MODTRAN4 mid-IR and near-IR radiances are compared for a nadir view of the MODTRAN model altostratus cloud (ICLD = 2). The observer is at 20 km altitude and the solar zenith was again set to 75°. The MODTRAN3 radiance predictions are particularly poor in this example; in the center of the H_2O bands, the MODTRAN3 overpredicts MODTRAN4 by approximately a factor of two. Outside of the H_2O molecular bands, MODTRAN3 is still higher, but only by approximately 20%. This example demonstrates the importance of using MODTRAN4 when analyzing AVIRIS measurements of solar scatter off clouds.
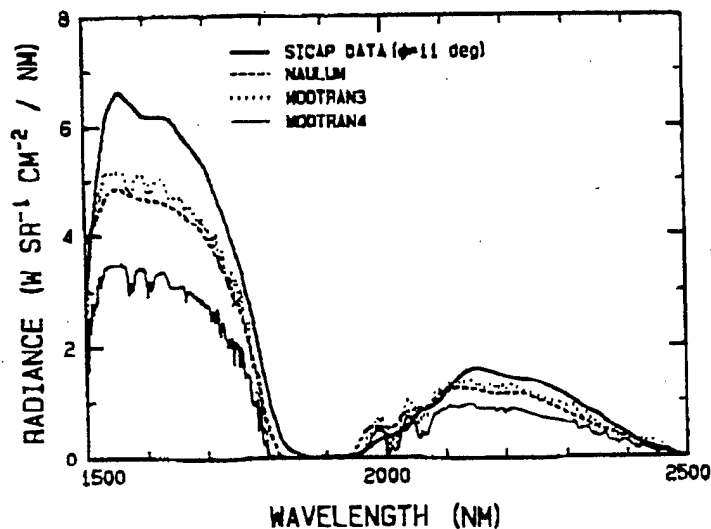
Figure 2.   A Comparison Between SICAP Measurements (Malherbe et al., 1995) and Model Predictions for a Solar Illuminated Cumulus Cloud Top with a 11° Relative Solar Azimuth Angle.
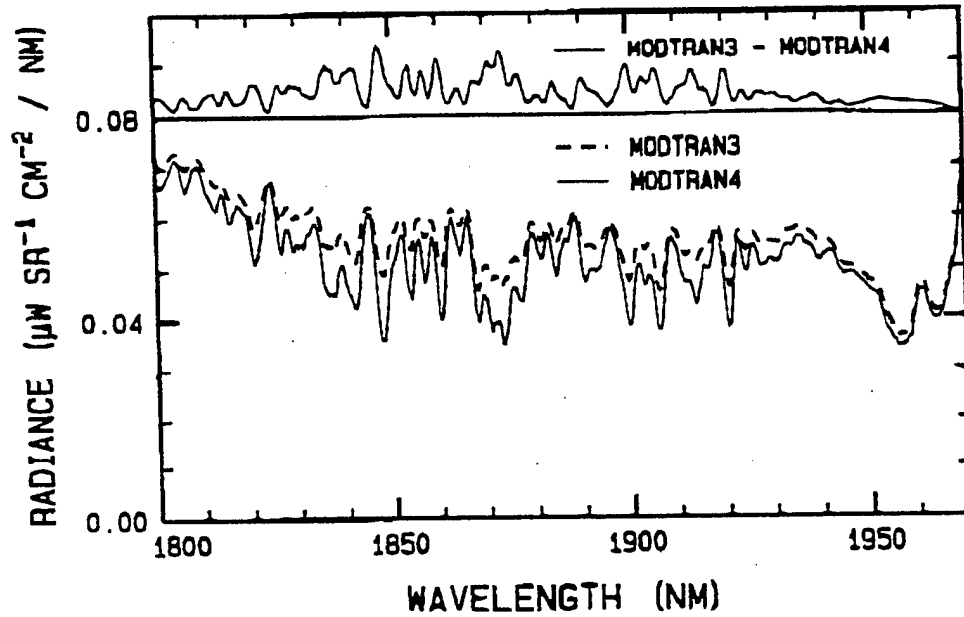
Figure 3. A Comparison Between MODTRAN3 and MODTRAN4 Radiances for Nadir Viewing of the Earth Through a Cirrus Cloud with a 75° Solar Zenith Angle. The differences Between MODTRAN3 and MODTRAN4 Are Offset by $0.08\mu w$ sr^{-1} cm^{-2} / nm.
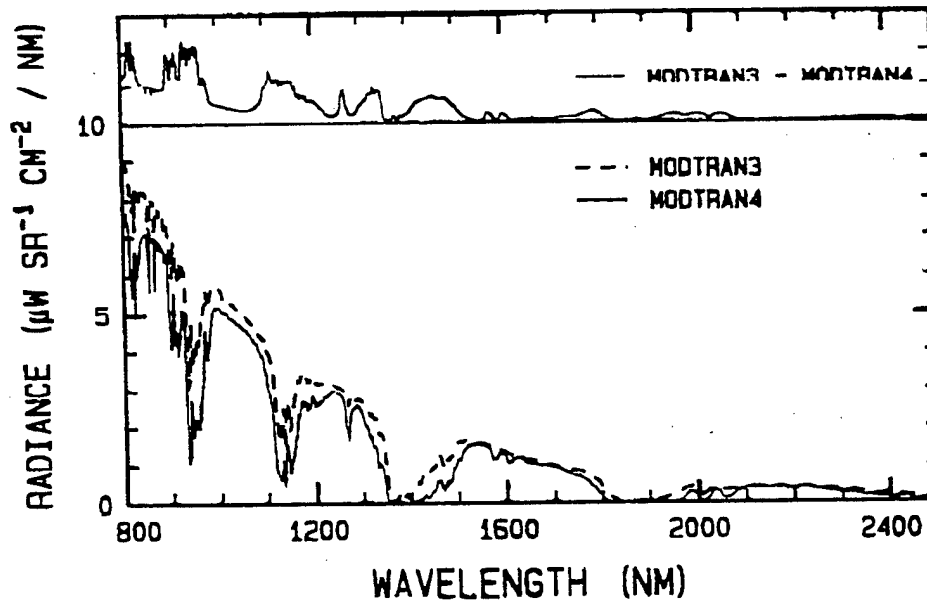
Figure 4. A Comparison Between MODTRAN3 and MODTRAN4 Radiances for Nadir Viewing of the MODTRAN Model Altostratus Cloud with a 75° Solar Zenith Angle. The differences Between MODTRAN3 and MODTRAN4 Are Offset by $10\mu w$ sr^{-1} cm^{-2} / nm.

6. SUMMARY

Major MODTRAN upgrades have been introduced which lead to significant improvements in the calculation of solar and thermal scattering from clouds and aerosols. The could/aerosol models now allow for generalized layering and specification of physical and optical properties. The new CK radiative transfer model leads to more accurate multiple scattering calculations, particularly in spectral regions containing strong molecular line absorption. It was shown that multiple scattering contributions can be important even for an optically thin solar illuminated cirrus cloud in the NIR-VIS spectral region; thus, these MODTRAN upgrades will lead to improved data analyses and atmospheric/surface property retrievals from down-looking sensors, such as AVIRIS, from whose data are often "contaminated" by sub-visual clouds.

7. ACKNOWLEDGEMENTS

REFERENCES

Berk, A., 1995, "Upgrades to the MODTRAN Layer Cloud/Rain Models," Rpt. No. SSI-SR-56, Spectral Sciences, Inc., 99 S. Bedford St., Burlington, MA.

Berk, A., L. S. Bernstein, and D. C. Robertson, 1989, "MODTRAN: A Moderate Resolution Model for LOWTRAN7," Rep. GL-TR-89-0122, Air Force Geophys. Lab., Bedford, MA.

Bernstein, L. S., A. Berk, D. C. Robertson, P. K. Acharya, G. P. Anderson, and J. H. Chetwynd, 1996, "Addition of a Correlated-k Capability to MODTRAN," Proceeding of the 1996 IRIS Targets, Backgrounds, and Discrimination Mtg.

Clough, S. A., F. X. Kneizys, G. T. Anderson, E. P. Shettle, J. H. Chetwynd, L. W. Abreu, and L. A. Hall, 1988, "FASCODE3 Spectral Simulation" Proceedings of the International Radiation Symposium, Lenoble and Geleyn, Deepak Publishing.

Hansen, J. E. and J. B. Pollack, 1970, "Near-Infrared Light Scattering by Terrestrial Clouds," J. Atmos. Sci., 27, 265 - 281.

Isaacs, R. G., W. C. Wang, R. D. Worsham, and S. Goldenberg, 1987, "Multiple Scattering LOWTRAN and FASCODE Models," Applied Optics, 26, 1272-1281.

Lacis, A. A., and V. Oinas, 1991, "A description of the Correlated K Distribution Method for Modeling Nongray Gaseous Absorption, Thermal Emission, and Multiple Scattering in Vertically in Homogeneous Atmospheres," J. Geophys. Res., 96, 9027 - 9063.

Malherbe, C., P. Simoneau, A. Boischot, G. Durand, J. Deschamps, and G. Gregoire, 1995, "Radiative Transfer Model in a Cloudy Atmosphere: A Comparison with Airborne Cumulus Measurement," Proceedings of the SPIE Conference on Passive IR Remote Sensing of Clouds and the Atmosphere III.

Mustard, J. F., 1991, "Distributions of Soil, Rock, and Grass in the Western Foothills of the Sierra Nevada," Proceedings of the Third Airborne Visible/Infrared Spectrometer (AVIRIS) Workshop, JPL Publication 91 - 28, 14 - 18.

Rothman, L. S. et al., 1992, "The HITRAN Molecular Database: Editions of 1991 and 1992," J. Quant. Spectrosc. Radiat. Transfer, 48, 469 - 507.

Stamnes, K., S. C. Tsay, W. J. Wiscombe, and K. Jayaweera, 1988, "Numerically Stable Algorithm for Discrete-Ordinate-Method Radiative Transfer in Multiple Scattering and Emitting Layered Media," Applied Optics, 27, 2502-2509.

TOTAL P.07

Terrestrial Refraction Model

Michael E. Thomas and Richard I. Joseph
Applied Physics Laboratory/Johns Hopkins University
Laurel, MD 20723
e-mail: THOMAME1@jhuapl.edu

Abstract

A model for the atmospheric ray path is constructed from a geometrical optics solution of the eikonal equation. The optical ray path is developed in the earth coordinate system for the lower atmosphere. An exact solution is obtained for a vertical refractive index profile that is quadratic in altitude. From this development, formulae for the location of the optical horizon are obtained. A general solution in the form of an integral equation is also obtained for any vertical refractive index profile.

Introduction

Precise spatial measurements within the atmosphere by remote electromagnetic techniques require equally precise knowledge of the effects of atmospheric refraction. Long path ground to ground line of sight communication links must account for the variable refractive nature of the atmosphere. Also corrections for refraction are needed to precisely locate low altitude lidar measurements. This is because the ray path is not rectilinear. Thus, atmospheric refractivity must be understood as a function of observer's position, range, frequency, and atmospheric pressure and temperature. At infrared through ultraviolet frequencies, refractivity primarily depends on the vertical temperature profile and an explicit relationship between refractivity and temperature is obtainable for a dry atmosphere. At microwave frequencies the vertical water vapor profile also contributes significantly to refraction.

The real part of the atmospheric index of refraction is a function of pressure, temperature and frequency. Many interesting low altitude refractive effects exist because of tropospheric variations in density and water vapor partial pressure as a function of position. Atmospheric refraction situations are broken down into three main categories; astronomical, terrestrial and geodesic. Astronomical refraction addresses ray bending effects of objects outside the atmosphere of the earth relative to an observer within the atmosphere. Terrestrial refraction considers the case when both object and observer are within the atmosphere of the earth. Geodesic refraction is a special case of terrestrial refraction where the object and observer are at low altitudes, as is commonly the case for surveying.

A model for the atmospheric index of refraction is constructed and a geometrical optics solution of the eikonal equation for the optical ray path is developed for the earth coordinate system in the lower atmosphere.

Index of refraction of a dry atmosphere

Because of their abundance, nitrogen and oxygen make significant contributions to the refractivity of the earth's atmosphere. These molecules have no infrared bands of importance to the refractive index thus only electronic bands need to be considered for a model valid from near dc to the ultraviolet. Based on the work of Edler [1] a simple Sellmeier type model for the dry atmospheric refractivity, N_{Dry}, can be obtained to be [2],

$$N_{Dry} \equiv (n_{dry} - 1)\times 10^6 = (237.2 + \frac{527.3\nu_1^2}{\nu_1^2 - \nu^2} + \frac{11.69\nu_2^2}{\nu_2^2 - \nu^2})P_{Dry}/T \tag{1a}$$

with the corresponding Cauchy model given by

$$N_{Dry} = (776.2 + 4.36\times 10^{-8}\nu^2)P_{Dry}/T \tag{1b}$$

where ν is wave number in cm^{-1}, $\nu_1 = 114000.0$ cm^{-1}, $\nu_2 = 62400.0$ cm^{-1}, P_{Dry} is the total dry air pressure in kiloPascal (kPa) and T is temperature in Kelvin. This model is valid up to altitudes where the mixing ratio between

O_2 and N_2 is constant and from 0.2 to 2000 μm, and compares well with other models [3,4]. Based on the hydrostatic equation for total pressure given the temperature profile, the altitude dependence can also be included in the dry air refractivity,

$$N_{Dry}(\nu, T(z)) = (776.2 + 4.36 \times 10^{-8} \nu^2) \frac{P(z_0)}{T(z)} \exp\left[-\frac{mg}{k_B} \int_{z_0}^{z} \frac{dz'}{T(z')} \right] \tag{2}$$

where z_0 is the initial altitude, m is the average molecular mass of the atmosphere, g is gravitational acceleration, and k_B is Boltzmann's constant. For altitudes up to 100 km, mg/k_B equals 34.16 [K/km].

Earth-atmosphere ray path geometry

Given that the index of refraction depends on density and the density of the atmosphere depends on altitude, then light propagating in the atmosphere will normally be bent toward lower altitudes or regions of higher density. The density of the atmosphere does not vary greatly in the horizontal direction and only vertical structure need be considered in most cases. To describe the ray path analytically, a suitable coordinate system must be used, such as illustrated in Figure 1. The surface of the earth and the structure of the atmosphere can be conveniently represented by a spherical coordinate system, as given by

$$\begin{aligned} x &= r\sin\theta\cos\phi \\ y &= r\sin\theta\sin\phi \\ z &= r\cos\theta \end{aligned} \tag{3}$$

This geometry puts the origin of the coordinate system at the center of the earth, this is not a practical location. It is more natural to locate the origin on the surface at the location of the observer. Thus translating along the r-direction by the radius of the earth, r_e, one obtains

$$r = r_e + z' = r_e\left[1 + \frac{z'}{r_e} \right] = r_e\eta. \tag{4}$$

This leads to defining a prime coordinate or earth coordinate system for small θ and ϕ angles as illustrated in Figure 1 and stated as
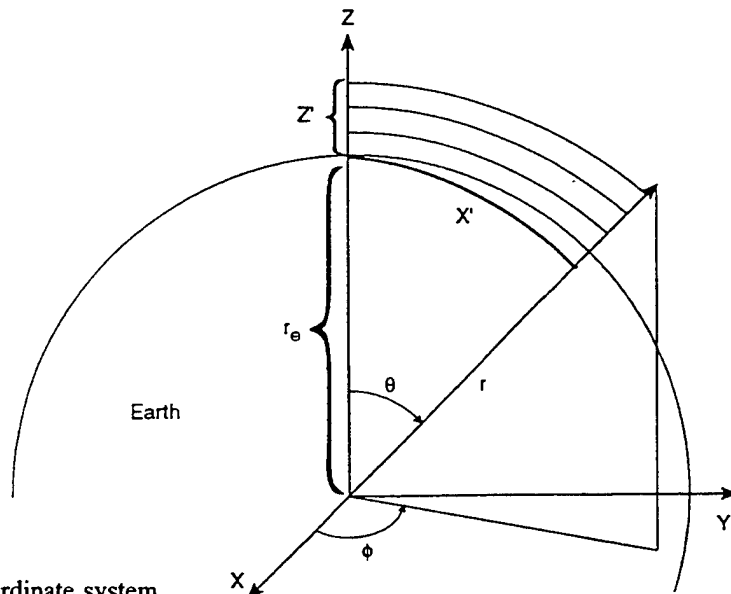
Fig. 1. Earth-atmosphere coordinate system.

$$x' = r\theta = \eta r_e \theta$$
$$y' = r\theta \phi = \eta r_e \theta \phi \tag{5}$$
$$z' = r - r_e = (\eta - 1)r_e.$$

x' and y' represent arc-lengths along the surface of the earth. The small angle approximation is valid for surface ranges up to 600 miles (i.e., θ does not exceed 10°). Although this is a logical coordinate system for describing beam propagation in the atmosphere, it has the unfortunate property that the metric in the x'- and y'-directions changes with altitude. This is described by the metric tensor, g, for this coordinate system [5],

$$g = \begin{bmatrix} \eta^2 & 0 & 0 \\ 0 & \eta^2 & 0 \\ 0 & 0 & 1 \end{bmatrix}. \tag{6}$$

This coordinate system is orthogonal because the metric tensor is diagonal. The metric tensor is useful because it allows the definition of differential operators in a curvilinear coordinate system.

Atmospheric ray path

Let us now examine geometrical optics to find the ray path within this coordinate system given a refractive index profile. Of particular interest is transforming the vector eikonal equation to the earth coordinate system. For nearly horizontal propagation, it is known that Maxwell's equations are modifiable by replacing $n(r')$ by $\eta(z')n(r')$ and treating the coordinate system as rectangular [5]. This approach is also consistent with evaluating the gradient, given the metric tensor of Eq. 6, for nearly horizontal propagation. Thus the eikonal equation becomes

$$\nabla \psi(r') = \eta(z')n(r')\hat{s} = m(r')\hat{s}. \tag{7}$$

$m(r')$ is the commonly used modified refractive index and s points in the direction of propagation. Effectively, this refractive index profile correction accounts for the curvature of a spherical earth. It is worth noting that $\eta(z')$ can be modified to include deviations from a spherical surface (e.g., mountains, etc.). Since, n is close to one, then

$$m(r') = n(r') + \frac{z'}{r_e}. \tag{8}$$

For $r_e = 6378.4$ km, then $1/r_e = 1.568 \times 10^{-4}$ km^{-1}.

Geometrical optics equations in two dimensions ($x'z'$-plane) describing the ray path in the earth coordinate system assuming a vertically varying atmosphere (i.e., $m(r') = m(z')$), are given by the following form of the eikonal equation

$$\frac{d}{ds}\left[m(z'(s))\frac{dx'(s)}{ds} \right] = 0$$
$$\frac{d}{ds}\left[m(z'(s))\frac{dz'(s)}{ds} \right] = \frac{dm(z')}{dz'}. \tag{9}$$

Given the vertical atmospheric refractivity, these equations can be used to describe the optical ray path. Note that the gradient of the refractivity determines the ray path. The following boundary conditions are applied at $x' = 0$ for a ray initially launched at z_0' with slope $\tan\delta$,

$$\text{at} \quad z' = z_0', \quad \frac{dx'}{ds} = \cos\delta \quad \text{and} \quad \frac{dz'}{dx'} = \tan\delta \tag{10}$$

177

where $(dx')^2 + (dz')^2 = (ds)^2$ is satisfied. To be consistent with the approximations leading to Eq. 7, δ must be kept small. The differential, ds, is the incremental path length. It can be expressed in terms of the vertical incremental path by solving the first equation in Eq. 9 with the boundary conditions of Eq. 10 and requiring the equation for arc-length to be satisfied. This process leads to the following useful relationship for the differential arc-length

$$ds = \frac{dz'}{\sqrt{1 - \frac{m^2(z_0')}{m^2(z')}\cos^2\delta}}. \tag{11}$$

Again applying the above boundary conditions, to the second equation in Eq. 9 reduces the two equations to a single differential equation, as given by

$$\frac{d^2z'(x')}{dx'^2} = \frac{m(z')}{m^2(z_0')}\sec^2\delta\frac{dm(z')}{dz'} = \frac{\sec^2\delta}{2m^2(z_0')}\frac{dm^2(z')}{dz'} \tag{12}$$

By inverting the above differential equation to solve for $x'(z')$, an integral equation can be obtained for $\delta \geq 0$, as follows

$$x'(z',\delta) = r_e\theta(z') = \int_{z_0'}^{z'} \frac{dz''}{\sqrt{\frac{m^2(z'')}{m^2(z_0')}\sec^2\delta - 1}}. \tag{13}$$

The quantity in the square root must be positive for a real path, thus $m(z')\sec(\delta)$ must be greater than $m(z_0')$ for all $z' \geq z_0'$. This is the case for a standard atmosphere and other conditions, but will not be satisfied for trapping ($m(z') = m(z_0')$ for all z', $\delta = 0$) or ducting. For $z' < z_0'$ and $\delta < 0$, the solution for $x'(z')$ require the limits of integration to be interchanged in Eq. 13. When $z' = 0$ the ray grazes the surface of the earth or terminates there. This locates the optical horizon when δ is minimum. These integral equations are the basis for terrestrial refraction for any m-profile that satisfies $m(z')\sec(\delta) > m(z_0')$.

Although Eqs. 13 are useful for most cases, a numerical solution is required. Possible exact solutions of Eq. 12 for $z'(x')$ also should be examined. Eq. 12 can be simplified by assuming $m(z')$ can be represented by a polynomial in a piecewise continuous fashion. Let us examine Eq. 12 when the modified index is expressible in the general quadratic form,

$$m(z) = 1 + A + Bz + Cz^2. \tag{14}$$

The coefficients, A, B, and C are functions of temperature, total atmospheric pressure (dry), water vapor partial pressure and frequency. Using the above form for $m(z')$, Eq. 12 simplifies to

$$\frac{d^2z'(x')}{dx'^2} = \frac{1 + A + Bz' + Cz'^2}{(1 + A + Bz_0' + Cz_0'^2)^2}(B + 2Cz')\sec^2\delta \tag{15}$$

with the initial boundary conditions that

$$z'(x'=0) = z_0' \quad \text{and} \quad \frac{dz'}{dx'}(x'=0) = \tan\delta. \tag{16}$$

Also, it is of interest at infrared, visible and ultraviolet frequencies to establish the relationship between the ray path and the vertical temperature profile. This can be done in a straightforward manner by assuming that

$m(z') \approx 1$ (e.g., $A + Bz' + Cz'^2 << 1$ or $z' < 20$ km). For low altitude propagation modeling, this is an excellent approximation and the resulting differential equation then becomes,

$$\frac{d^2z'(x')}{dx^2} = (B + 2Cz')\sec^2\delta, \tag{17a}$$

where the B and C coefficients are frequency dependent as

$$B(\nu) = [156.8 - \eta(\nu)\frac{P(0)}{T_0}\left[\frac{34.16}{T_0} + \frac{a}{T_0}\right]]\times10^{-6}, \tag{17b}$$

$$C(\nu) = \eta(\nu)\frac{P(0)}{T_0^2}17.08(3a + 34.16)\times10^{-6} \tag{17c}$$

a is the thermal lapse rate and based on Eq. 1b the dispersion factor is defined to be

$$\eta(\nu) = 776.2 + 4.36\times10^{-8}\nu^2 \tag{17d}$$

where ν has units of wave numbers.

Terrestrial and geodesic refraction

The solution of Eq. 17, using the boundary conditions of Eq. 15, for the ray path is obtained in a straightforward manner to be

$$z'(x',\delta) = \left[z_0' + \frac{B}{2C}\right]\cosh(\sec\delta\sqrt{2C}x') + \frac{\sin(\delta)}{\sqrt{2C}}\sinh(\sec\delta\sqrt{2C}x') - \frac{B}{2C}. \tag{18}$$

This result describes the path an optical ray takes as it propagates through the lower atmosphere ($z' < 20$ km). The B coefficient represents the reciprocal radius of curvature of the ray to the zeroth order or in regions of constant refractivity gradient. It is this term that is used in many ray-tracing procedures. The quantity $1/Br_e$ is called the refraction coefficient and can be used to correct the geometric horizon to the optical horizon. For a typical standard atmosphere ($dN/dz' = -40$), the value of $1/Br_e$ is approximately 1.33 or 4/3. (This procedure is often referred to as the 4/3 earth correction).

The function, $z'(x')$, is in terms of a rectangular coordinate system. To plot results in a curved earth or spherical coordinate system, the following transformation is used to obtain z_e',

$$\theta(x',z') = \sin^{-1}\left[\frac{x'}{r_e + z'}\right]$$
$$z_e' = (r_e + z')\cos(\theta(x',z')) - r_e$$

For near horizon observations within the lower troposphere (i.e. when $\sqrt{2C}x' << 1$ and $\delta \approx 0$), Eq. 18 reduces to a quadratic form as given by

$$z'(x') = z_0' + \delta x' + \frac{B + 2Cz_0'}{2}x'^2. \tag{19}$$

This formula can be used to compute the location of the optical horizon, x_{oh}', when $B + 2Cz_0' > 0$. This occurs when $z'(x') = 0$ for the smallest downward looking angle, δ_{oh}. Solving Eq. 19, for an observer located at $x' = 0$ and altitude $z' = z_0'$, leads to

$$x_{oh}' = \sqrt{\frac{2}{B + 2Cz_0'}}\sqrt{z_0'} = 10^3 \sqrt{\frac{2z_0'}{\left[\dfrac{dM(z')}{dz'}\right]_{z'=z_0'}}}$$

(20a)

where the units are in km. The optical horizon angle, δ_{oh}, is

$$\delta_{oh} = -\sqrt{(4Cz_0' + 2B)z_0'} = -10^{-3}\sqrt{2\left[\frac{dM(z')}{dz'}\right]_{z'=z_0'} z_0'} \; .$$

(20b)

For low altitudes $z_0' < 1$ km, $B >> 2Cz_0'$ and the 1976 U.S. standard atmosphere ($B = 130 \times 10^{-6}$), a simple formula for x_{oh}' is obtained to be

$$x_{oh}' = 124\sqrt{z_0'} \; .$$

Summary

The above approaches are fundamentally different from past ray-trace methods [6]. One common approach is to apply Snell's law to a vertically stratified medium with layers of constant refractivity. A better approach is based on the eikonal equation applied to a vertically stratified atmosphere with layers of constant refractive gradient [1]. The layer thickness must be thin enough so that the refractivity is accurately modeled. The ray path is then determined by integrating along the layers. These past models are numerically intensive because many layers are needed, which is not an issue for past applications. However, Raman and DIAL lidar require considerable signal processing to achieve the final results especially when high spatial resolution is required and efficient ray-path models are needed. The approaches given above provide this efficiency by using at least a quadratic representation of the refractivity and can be plotted in a flat or spherical earth geometry. Ray tracing is not always necessary at low altitude since a closed form solution to the eikonal equation is obtainable if the vertical refractive profile is quadratic in altitude.

References

1.   B. Edlen, "The Refractive Index of Air," *Metrologia* 2, pp. 71-80 (1966).
2.   R.W. Fenn et. al., "Optical and Infrared Properties of the Atmosphere," Chapter 18 in Air Force Handbook Of Geophysics and Space Science, (ed.) (1985).
3.   L.D. Lorah and E. Rubin, "Aerodynamic Influences on Infrared System Design," Chapter 24, The Infrared Handbook, 2nd Edition, W.L. Wolfe and C.J. Zissis (eds.), ERIM (1985).
4.   H. Barrell and J.E. Sears, "The Refraction and Dispersion of Air for the Visible Spectrum," *Phil. Trans. Roy. Soc. London* A 238, pp. 1-64 (1939).
5.   D.E. Kerr (ed.), Propagation of Short Radio Waves, Radiation Laboratory Series, McGraw-Hill, New York (1951).
6.   F.K. Brunner (ed.), Geodetic Refraction, Springer-Verlag (1984).

COMPUTING ON THE WEB

Dave Sowle, Mission Research Corp. Santa Barbara, 5 June, 1996

Abstract

Under auspices of the ARM-UAV program, MRC, in cooperation with Gautier's group at UCSB, is making available climate research community standard algorithms for use over the Web. The idea is that the user brings up our Web page at: http://arm.mrcsb.com , and choses from available algorithms. Using a GUI, the user can submit a calculation and get results, all via the Web. Advantages are hardware independence and no knowledge of code details required for operation. Two algorithms are now available: the SBDART code (Stamnes' DISORT transfer code plus LOWTRAN added by UCSB), and a Nakajima/King cloud properties algorithm.

The Problem

In almost every field of research there are a few complex computer programs that embody algorithms regarded as standard by that community. These programs span the gamut from modern, well organized, and easy to use programs all the way to programs that have been under development so long they contain fossilized IBM cards overlain by magnetic tape strata, with logic and input formats so tangled that the program can't be run confidently unless someone is employed near full time learning how to do it.

This situation is natural and not likely to change soon, for any field. However, it slows the rate of progress and is costly; an algorithm has to be continuously critical to an effort before it is worth committing resources necessary to support a person to learn and run a code.

The Idea

We are trying an experiment to alleviate this bottleneck. We have created a GUI (Graphical User Interface) for one of the atmospheric radiation transfer algorithms so that almost anyone can set up a problem and run it. Further, we are making it available over the Web, so nobody has to get it operational on their

own computer, avoiding issues of installation time, software system compatibility, and hardware compatibility.

If you can get on the Web, you can set up, run, and retrieve results of your calculation in minutes.

SBDART

SBDART (Santa Barbara DISORT Atmospheric Radiative Transfer) has been discussed by Ricchiazzi et al. 1996, and consists of Knute Stamnes' et al,, 1988, DISORT (DIScrete Ordinate Ratiative Transfer) code as modified by Gautier's UCSB group, who added standard atmospheres and gaseous radiative band models taken from LOWTRAN-7, as well as LOWTRAN-7 and 5s aerosol models, and cloud properties calculated with Mie codes by Gautier's group. Mission Research contributed the GUI, the Web interface, and maintains it on the Web. In addition to standard atmospheres and a set of ARM CART atmospheres derived from Rawinsondes on specific days, there are a set of standard instrument filter functions from which the user may chose.

Nakajima-King Cloud Properties Algorithm

Our second code is an application of the Nakajima-King, 1990, cloud properties retrieval scheme. In this algorithm, images of a cloud field are obtained in two channels, one in which radiation transfer is dominated by scattering (visible) and one dominated by absorption (infrared). Cloud top heights are estimated, preferably by far IR brightness temperatures, cloud bottoms are estimated, and a surface albedo chosen. Then with the known solar angle a table of SBDART calculations is built up for the ratio of the two channel irradiances versus cloud optical depth and equivalent cloud drop radius. Over a large range of conditions, it is then possible to determine both cloud optical depth and mean particle size from the ratio of visible and IR channel irradiances averaged over a few pixels.

We have created a GUI that allows a user to carry out such calculations for all or portions of cloud fields, which can be chosen from those stored in our computer. These are presently MAS (MODIS Airborne Simulator) images. We will add to our library all MPIR (Multispectral Pushbroom Imaging System) images generated by the ARM-UAV (Atmospheric Radiation Measurements-

Unpiloted Airborne Vehicle) program as they become available. We are interested hearing suggestions for other data that someone would find useful.

Near Term Intentions

SBDART

In the next few months we intend to upgrade SBDART by:
1. Adding the capability of the user specifying a square instrument filter,
2. Upgrade the band model to correlated-k, or maybe MODTRAN.

Nakajuma-King

We intend to develop an option allowing user supplied data to be analyzed.

Long Term Future

Visible funding will dry up within the year. That should be long enough to find out whether the idea is useful or not. If so, it will take a little funding to keep a Web site active.

References

Nakajima, T. and M. D. King ,1990: *Determination of the optical thickness and effective particle radius of clouds from reflected solar radiation measurements. Part I: Theory,* J. Atmos. Sci., **47**, 1878-1893.

Ricchiazzi, P., S. Yang, and C. Gautier, 1996: *SBDART: A Practical Tool for Plane-Parallel Radiative Transfer in the Earth's Atmosphere,* Computers and Geosciences, submitted May, 1996

Stamnes, K., S. Tsay, W. Wiscombe and K. Jayaweera, 1988: *Numerically stable algorithm for discrete-ordinate-method radiative transfer in multiple scattering and emitting layered media,* Appl. Opt., **27**, pp2502-2509

Computing on the Web

Dave Sowle, Sean Moore, Mark Frolli, Ed Savage
Mission Research Corporation
and
Catherine Gautier, Paul Ricchiazzi
U. Calif. Santa Barbara

Two community standard algorithms are available to all at

http://arm.mrcsb.com

SBDART
A plane parallel radiation transfer code with
gaseous, cloud, and aerosol effects included

and

Nakajima and King Cloud Properties
A two frequency cloud field analysis algorithm that determines
cloud optical depth
mean cloud droplet radius

Mission Research Corporation
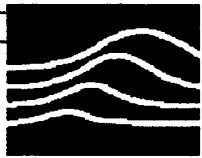
Rationale

Most technical fields have a few standard algorithms embodied in complex computer programs.

The Problem

To apply these algorithms requires serious amounts of dedicated manpower

Candidate Alleviant

Create a version that can do most applications.

Build a Graphical User Interface the makes setting up a run very easy.

Put it on the Web.

SBDART

Mission Research Corporation

Difference scheme

Stamnes, K., S. Tsay, W. Wiscombe and K. Jayaweera, 1988:*Numerically stable algorithm for discrete-ordinate-method radiative transfer in multiple scattering and emitting layered media*, Appl. Opt., 27

Atmospheres

U. S. Standard, Tropical, Mid-latitude Summer, Arctic Winter
modified per ARM-CART Rawindsondes

Band Models

LOWTRAN7

Aerosol Models

LOWTRAN7

5s

Cloud Scattering Model

Mie by UCSB Group

Ricchiazzi, P., S. Yang, and C. Gautier, 1996: SBDART: *A Practical Tool for Plane-Parallel Radiative Transfer in the Earth's Atmosphere*, Computers and Geosciences, submitted May, 1996

Instrument Filter Function

Select from several

File Edit View Go Bookmarks Options Directory Window   Help

Back   Forward   Home   Reload   Images   Open   Print   Find   Stop   N

Location: http://arm.mrcsb.com/sbdart/

SBDART

Tool for Computing Radiative Transfer in the Earth's Atmosphere

You must have an HTML+ browser to view and process this form. Netscape 2.0 or newer recommended

---

Month: Oct   **Day** 26   **GMT Hour:** 18   **Minutes** 30   **Year:** 1995

Latitude (degs N) 36.6   **Longitude (degs E)** -97.5

When checked, use 40 degs for Solar Zenith Angle and ignore Date, Time, and Location

---

Instrument Filter: Solar (0.25–4.0 um) Flat

Atmospheric Profile: C1.951026.1733

When checked, use 4.2 g/cm2 for integrated water vapor with selected profile.

Aerosol Model: Rural   **Visibility:** 23.0 km (at 0.55 microns)

Surface Albedo Model: Vegetation

When checked, use 0.15 for albedo and ignore selected albedo model.

File   Edit   View   Go   Bookmarks   Options   Directory   Window   Help

Back   Forward   Home   Reload   Images   Open   Print   Find   Stop

Location: http://arm.mrcsb.com/sbdart/cgi/plot-flux.cgi

SBDART flux plot (Case 825623849)

Questions and Comments welcome. Email to Sean Moore at Mission Research Corporation: moore@mrcsb.com

File   Edit   View   Go   Bookmarks   Options   Directory   Window   Help

Back   Forward   Home   Reload   Images   Open   Print   Find   Stop

Location: http://arm.mrcsb.com/nk/

currently under development:

Extraction of Optical Thickness and Particle Size from Measured Cloud Reflectances

Nakajima–King on the Web

Dave Sowle, Ed Savage, Sean Moore
Mission Research Corporation
Work Supported by DOE grant DE-FG03-94ER61820

Approach:

Use the Nakajima–King procedure to find optical thickness (tc) and particle size (re) values that match measured reflectance values, as calculated by SBDART.

Inputs:

Cloud reflectance field at two wavelengths, uploaded from the user (or from our pre-stored sampling of data).

Outputs:

- Nakajima–King diagram
- Optical thickness and particle size fields

Start Process:

- Nakajima–King diagram.
- Extract tc and re (includes Nakajima–King diagram).

E–mail Comments to savage@mrcsb.com

189

File   Edit   View   Go   Bookmarks   Options   Directory   Window   Help

Location: http://arm.mrcsb.com/nk/select.html

Submit Data

Select (click on) on of the pictures below to simulate submittal of user data.

Note: We don't yet accept user data. Send e-mail to us (savage@mrcsb.com) to suggest forms of data we should plan to accept. Data consists of two channels of solar reflectance values.

MAS June 6, 1992, Line 1 (252x036 pixels)

MAS June 17, 1992, Line 4 (980920 pixels)
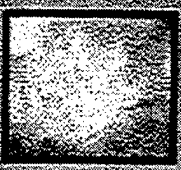
MAS June 17, 1992, Line 5 (768932 pixels)

MAS June 19, 1992, Line 15 (1140886 pixels)
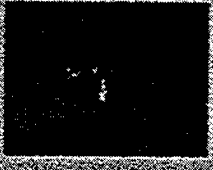
Home Page   **E-mail Comments to savage@mrcsb.com**

Nakajima–King Diagram for MAS June 8, 1992, Line 1

Position: 37:40N, 25:32W
Time: day 160, 10:48 GMT
Observer azimuthal: 126.12°
MAS Data Shift: R^N+16.0, R^A−0.1

Absorbing (2.142μ) radiance, W/m²/μ/sr

Nonabsorbing (0.664μ) radiance, W/m²/μ/sr

$r_e(\mu)$

τ_c

MAS DATA
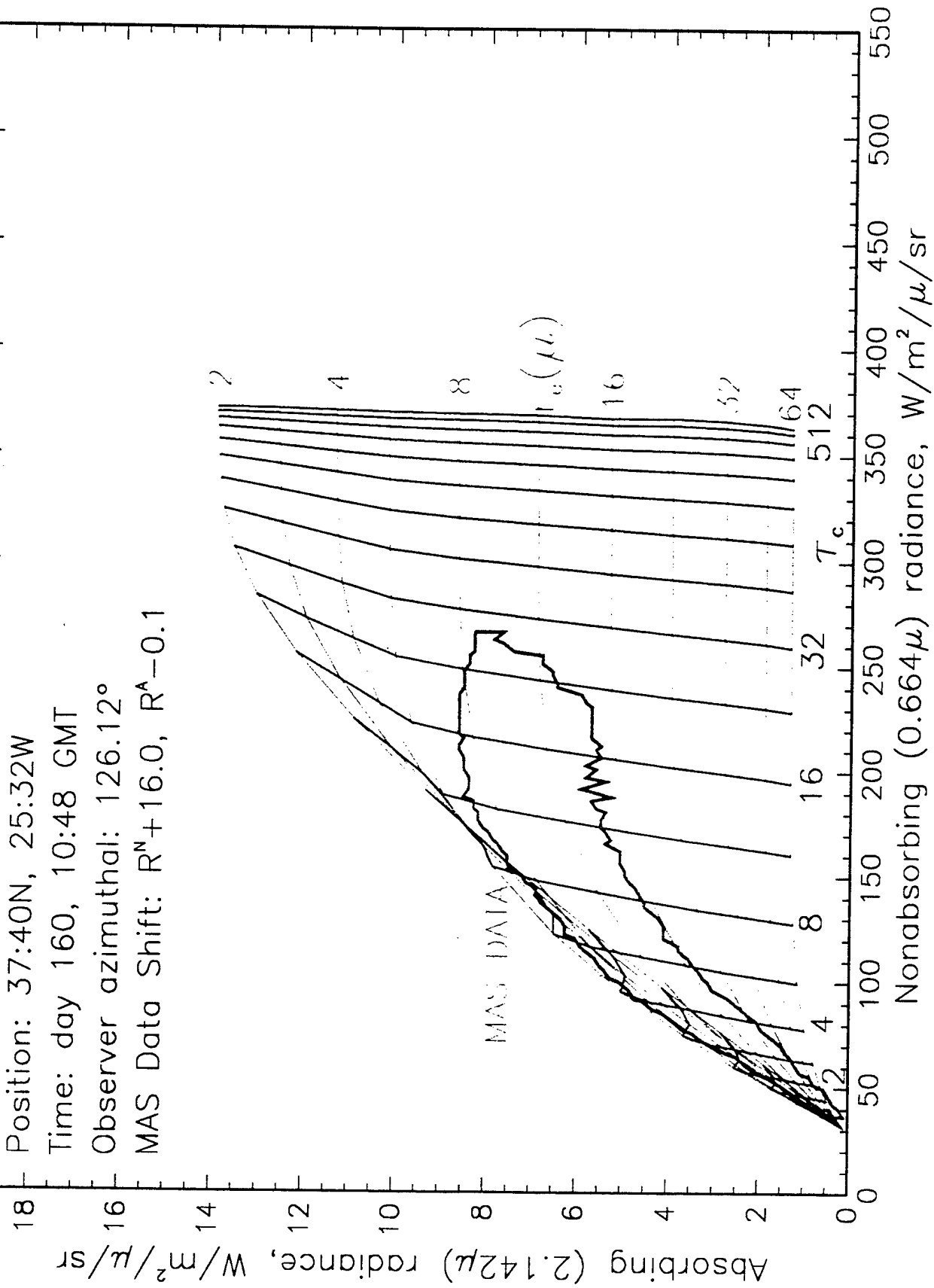
MAS June 17, 1992, Line 5 Radiances

Nonabsorbing (0.664µ) Radiance (W/m²/µ/sr):

Absorbing (2.142µ) Radiances (W/m²/µ/sr):

Location: http://arm.mrcsb.com/nk/tcre_17_05.html   N

Optical Thickness and Particle Radius

Optical Thickness:
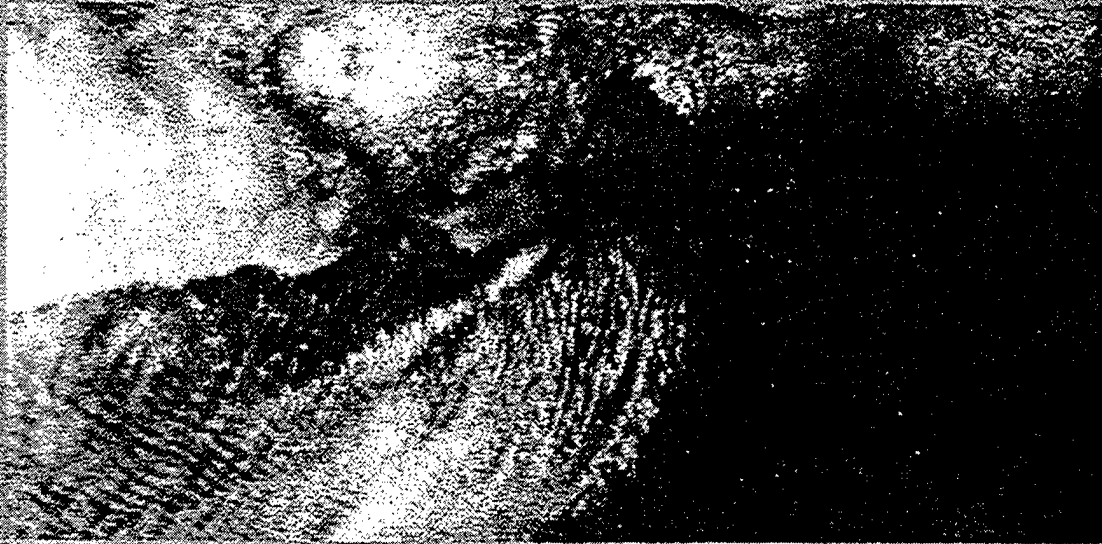
Optical Thickness (at 0.55u)

2   3   4   6   8   10   12   15   24
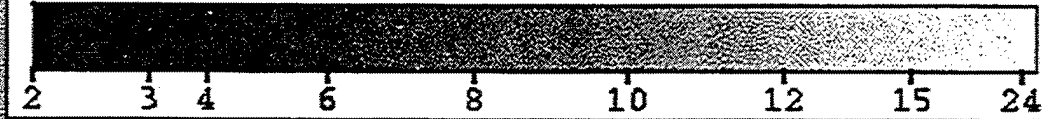
Effective Particle Radius (microns):

Particle Size (microns)

2   4   5   5.5   6   7   8   9   15
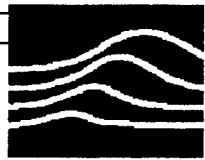
Overall

Uncertain

Known funding evaporates within a year

But a year ought to be enough to see if the idea is useful

SBDART

We plan to add a few features:

(1) User supplied instrument filter function

(2) Correlated-k or MODTRAN band scheme

Nakajima-King

(1) We will get it working well with MRC-supplied data

(2) We plan to add the capability of user supplied data

Additional Algorithms

We solicit suggestions

Architecture

Dr. Frank O. Clark & Mr. Dale Sinclair

Geophysics Directorate

Phillips Laboratory

Hanscom Air Force Base, MA

- Computer Software Architecture

- Suggested general design standards for government work (these are not "official")

- Maximize long term utility

Architecture

- Platform independent

- Dual Use: non-non-interactive & interactive

- Modular

- Distributed computing compliant

- Multi-threaded

- Single Language (C, C++, or FORTRAN)

- MODTRAN compatible vertical profiles

Platform Independent

- Platform independent

  - minimum: UNIX & MS Windows

    - UNIX > Sun, SGI, HP, Alpha

    - MS Win: Win 3.1, Win 95, Win NT

- Core code ANSI compliant

- GUI, best not!

  - (use alpha numeric text interface: ANTEBI)

  - or separate MS Windows & UNIX GUI code

Dual Use

- non-interactive
  - "batch" mode (object, subroutine, file in/out)
- interactive
  - two way communication
    - interactive batch
    - primitive text user interface (PTUI)
    - graphical user interface (GUI)
    - (maybe a Modern User Interface, MUI?)

Modular

- Modular functional units
  - each module stands alone, processes input provides output.
- API for modules *required*
- Directories specified externally
- Data flow only through API
- Robust upgrades & troubleshooting

Modular

Interactive GUI

GUI in C++

file-call

DP Call

3.0 NI core

DPI

Expert System

SAG Atmospheres
SAG in FORTRAN

Knowledge Bases

Expert System in C

DPI

CODES

codes in FORTRAN

Each code treated as a module resides in a directory of that name & uses unchanged I/O

200
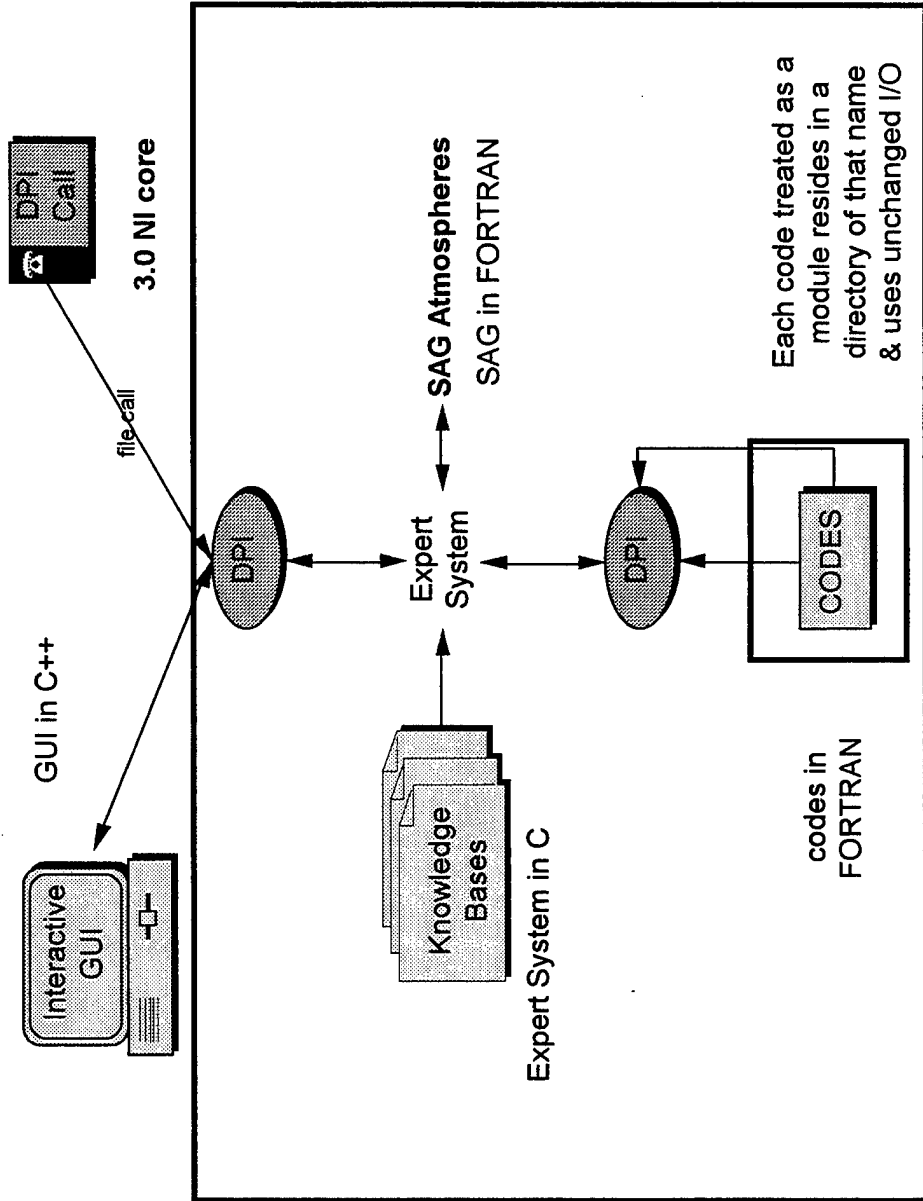
Distributed Computing Compliant

- Means:
  - distribute task across networked computers

- Directories specified externally

- VERY well defined input/output

- All timing under external control

- Can get **enormous** speed increases

- (this is not what is meant by "DIS")

Multi-threaded

- Modules execute non-sequentially
- Looped routines execute in parallel
- Means:
  - run CPU while file I/O delayed
  - compile to optimize fpu or array processors
  - design new task while old one executes
  - distribute task across several CPUs

Multi-threaded

(continued)

- Interactive & non-interactive gains

- Significant gains with single CPU

- Only industry standard methods:
  - PTHREAD
  - DCE

- Never EVER recode for specific hardware!

Language

- Only use a single language
  - e.g. C, C++, or FORTRAN
- Mixed languages increase compile & link problems for end users
  - Users need precise multiple compilers
- If new coding, use C++ (if you "C")
  - compilers far ahead of FORTRAN
- Do not recode legacy models

Versatile Inputs

- MODTRAN like vertical profile input
  - simplifies user set up
- Work towards industry standard modules
  - gas
  - aerosols
  - clouds
  - precipitation (rain, snow)

Summary

Code:

- Platform independent
- Dual Use
- Modular
- Distributed & Multi-threaded compliant
- Single Language
- Universal vertical profile input

SIG: The SHARC Image Generator - Overview of a new non-stationary stochastic scene generator for SHARC

19th Annual Transmission Meeting
4-6 June 1996

James H. Brown, PL/GPOS
Neil Grossbard, BC

SIG: The SHARC IMAGE Generator

- A New Model(s)
  - Interactive Menu Driven FORTRAN Code
  - Interfaces with SHARC 4.0
- Produces 2-D Synthetic IR Structure Images
  - User Specified Sensor and Geometry
  - Multiple Rendering Options
  - Renders Non-Stationary Structure
  - Renders Stochastic Structure
- Physics and Measurement Based
  - Depends on SHARC Chemistry & Radiance Transfer
  - Invokes Gravity Wave Understanding
  - Uses NSS Measurement Based Parameters

The Structure Problem

- Spatial Radiance Fluctuations Depend on 3-D Atmospheric Density and Temperature Structure

- The Statistics of Atmospheric Structure are Non-Stationary

- Limited Knowledge of High Altitude Structure Statistics (Covariance, PSD, and PDF functions, Variances, Correlation Lengths)

Atmospheric Structure Approach

- Treat Limb Structure as Stochastic

- Assume Atmospheric Horizontal Structure is Isotropic and Stationary

- Assume Gaussian PDF

- Assume Wittwer-Kilb-type PSD

- Adopt NSS Estimates for Temperature Variance and Correlation Lengths

- Vertical Structure is Non-Stationary

SHARC Structure Approach
Approach A - (Brute Force Approach)

- SHARC 4 Computes Path Integrated "Apparent" Radiance Fluctuation Amplitudes (FA) As Function of Segment Distance Along Given Lines-Of-Sight (LOS).

- SIG Computes Large 3-D Non-Stationary Temperature Fluctuation (DT) Database

- SIG Integrates FA*DT over each LOS.

SHARC Structure Approach
Approach B - (Faster Approach, Less Robust)

- SHARC 4 Computes Radiance Covariance Functions From NSS Specified Atmospheric Covariance Functions and SHARC Radiance Computations.

- SIG Constructs Non-Stationary Radiance Scene From Derived Radiance Covariance Functions.

SHARC Image Generator (SHARC 4 / SIG) Methods
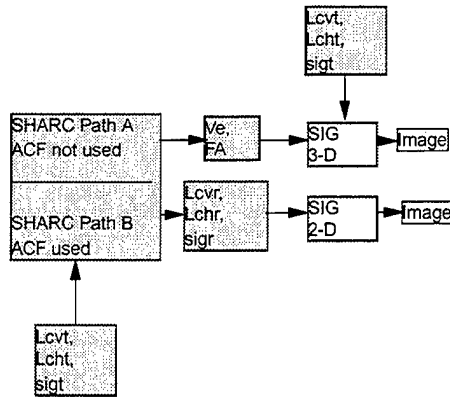
SIG Capabilities

<u>LIMB VIEW</u> - Vert. Non-Stationary

H/V Separable

Hor. Isotropic

(1) 3-D "Brute Force Integrations"

(2) 2-D AR/FFT, AR/AR

(3) 2-D Stretched Space, AR/AR, AR/FFT, FFT/AR, FFT/FFT

PSD and ACF Models

$$PSD(k) = \frac{\sigma^2 a^{2\nu}\Gamma\left(\nu + \frac{1}{2}\right)}{\sqrt{\pi}\,\Gamma(\nu)\left(a^2 + k^2\right)^{\nu+\frac{1}{2}}}$$

$$ACF(x) = \frac{\sigma^2 2^{(1-\nu)}(2\pi a x)^\nu K_\nu(2\pi a x)}{\Gamma(\nu)}$$

LIMB View: 2-D "Robust" Approach

- Use SHARC 4 computations of radiance correlation lengths, variances, and estimates of PSD slopes

- Use dynamic AR filter for vertical and AR or FFT filter for horizontal

LIMB View:

A <u>Stretched Space</u> Transformation of a Non-Stationary PSD to a Stationary PSD

- KEY
  - Transform a Non-Stationary Auto-Covariance Function to a Stationary Auto-Covariance Function by Change of Lag and Space Variables

  - Use the Resulting "Stretched Space" Stationary PSD to generate synthetic <u>Stationary Structure</u> in "Stretched Space"

  - Transform Structure in "Stretched Space" Back to "Normal Space" to Obtain <u>Non-Stationary Structure</u>

MSTI MWIR Fil 0 Daytime
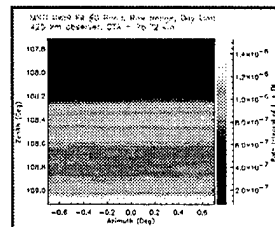
Deterministic Plus
Stochastic Structure
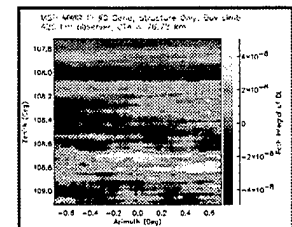
Stochastic Structure

Structure Comparison, MWIR, Fil 0, Day
3-D, 2-D dynamic AR, 2-D Stretched Space

3-D
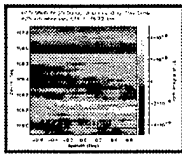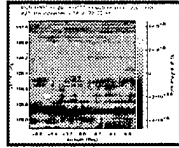
2-D Dynamic AR
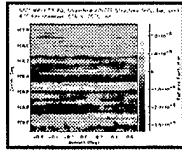
2-D Stretched Space

MSX Scenes (Structure only)
Day - B1
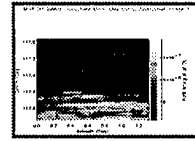
Sub-Image 1
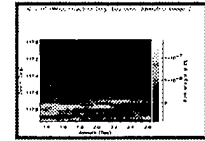
Sub-Image 2
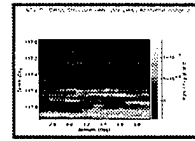
Sub-Image 3
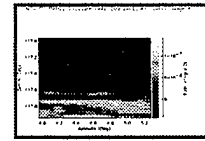
Sub-Image 4

NADIR View:
2-D FFT Approach

- Employ non-separable isotropic 2-D PSD model

- Simplest approach

Off-NADIR View:
3-D "Slicing" Approach

- Construct a 3-D Radiance Structure "Field" from SHARC 2-D Image parameters.
- Transformation requires projection of image parameters and pixel spacings to a 3-D earth centered vertical field
- Employ dynamic AR filter for vertical and 2-D FFT for horizontal
- Slice the 3-D radiance field along original image plane to produce the 2-D radiance image.

MSTI Downlooking Scenes
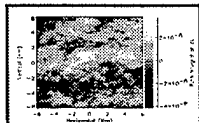
Nadir (Isotropic)

20 deg. Off-Nadir
Non-Separable 3-D Slicing
Method
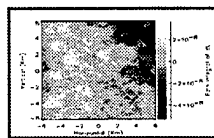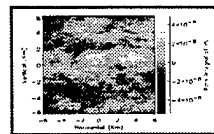
30 deg. Off-Nadir
Non-Separable 3-D Slicing
Method

Variable Limb Path Geometry

CTA = 76.72 km
CTA = 86.36 km
CTA = 96. km
96 km
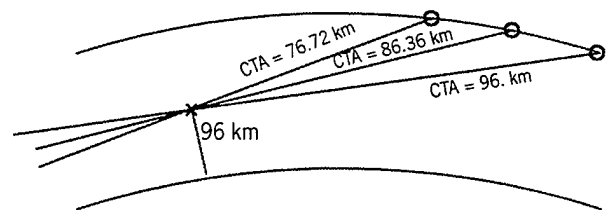
Variable Path ATH MSTI Scenes
Structure Only, MW - 0, Day
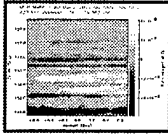
BTA = 60 km
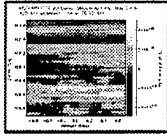
BTA = 50 km
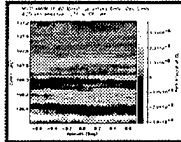
BTA = 70 km

	MSTI Timings
3-D Temp. dbase	2.5 hr
Brute Integrations	16 min
2-D AR/FFT	~ 1 sec
2-D FFT - Stretched Space	< 1 sec
2-D FFT - Nadir	< 1 sec
3-D Off-Nadir	19.5 min

15 Micron non-LTE Cooling Rates from CIRRIS-1A

P.P. Wintersteiner, ARCON Corporation, Waltham, MA, 02154
J.O. Wise, R.H. Picard, and J.R. Winick,
Phillips Laboratory/GPO, Hanscom AFB, MA, 01731-3010
R.G. Roble, National Center for Atmospheric Research, Boulder, CO, 80303

Abstract: Using the ARC non-LTE radiation code, the NCAR TIME-GCM general circulation model, and the CIRRIS-1A earthlimb data, we are able to explore the variability of 15 μm cooling rates in the mesosphere and lower thermosphere. Starting with the atmospheric conditions predicted by the NCAR TIME-GCM, we calculate the long-wave infrared radiance and the associated atmospheric cooling using the ARC line-by-line radiative transfer codes. By comparing the modeled limb radiance with the CIRRIS radiometer and interferometer data for different conditions, we show that the peak cooling rates in the lower thermosphere vary by more than a factor of two and in some cases may exceed 200 K/day. We also compare the derived cooling rates with those used in the TIME-GCM.

The subject of this talk is cooling due to 15 μm emission from CO_2, and we concentrate on the mesosphere and lower thermosphere (MLT) where this process is the among the most important of many that contribute to the thermal balance of the atmosphere. The work was done by me and my colleagues here at Phillips Laboratory, and made use of results from the TIME-GCM that Ray Roble has developed at NCAR. I would also like to acknowledge the assistance of Sam Makhlouf and Ed Richards, who retrieved data from the TIME-GCM and CIRRIS databases, respectively.

The objectives of the work were twofold (Figure 1). The first purpose was to estimate, from experimental data, the actual cooling in the MLT due to CO_2 15 μm emission, and also the variability of the cooling, and to do this for different geophysical conditions. Since the cooling rate is not directly measured, it is necessary to resort to models to get the desired information. In addition to the TIME-GCM, we used the Phillips Laboratory Atmospheric Radiance Code (ARC), which does the non-LTE calculations. The second objective was to compare the inferred cooling with the parameterization used in the TIME-GCM, in order to evaluate the latter.

The approach we used is outlined in Figure 2. We selected six subsets of the CIRRIS data, differing primarily according to magnetic latitude and local time. We ran the TIME-GCM for the dates of the CIRRIS experiment, and extracted profiles of N_2, O_2, atomic oxygen, CO_2, and kinetic temperature corresponding to the locations and times of the selected limb views. Using these, we then ran ARC to determine the non-LTE populations of the CO_2 vibrational states and the limb radiance that one would expect to see, and compared this predicted limb radiance with the CIRRIS data.

The cooling rate is a by-product of the vibrational population calculation. The latter is performed using line-by-line radiative transfer and appropriate collision processes, notably V-T excitation of the $CO_2(\nu_2)$ states by collisions with atomic oxygen, and has been validated with several previous studies.

The premise behind this work is that if we get the limb radiance right, we also get the cooling correctly. That is, since the cooling rate is a direct reflection of the emission rates of the ν_2 states, or equivalently the vibrational temperatures, and since the limb radiance can be calculated directly from the latter with confidence, then the cooling is quite close to being correct if the radiance predictions are correct, despite the fact that two or more of the profiles that go into the non-LTE calculation could be somewhat in error. Conversely, if we don't get the limb radiance right, we ask what we have to do to correct it, and we modify the input profiles in such a manner as to achieve an acceptable agreement with the experimental data.

The last step in this process is to compare the TIME-GCM cooling rates with those of the ARC calculations, in order to assess the algorithm it uses and also to see how well its results agree with the cooling that is inferred from the CIRRIS data.

To illustrate the quality of the data we are using, Figure 3 shows a sample of limb radiance data obtained from the CIRRIS radiometer, plus several points obtained by integrating (co-located) interferometer spectra over the 15 μm bands. The integrated spectral data are consistent with the wide-band data, except for a discrepancy of ~30% at the higher altitudes.

Figure 4 is a table distinguishing the six subsets of the database that we used. Four of the cases correspond to night-time blocks, including one with intense auroral activity, and the other two looked at the sunlit atmosphere. Although intrinsic day/night differences are not particularly important for the non-LTE calculations of these CO_2 states, the day and night data were taken at greatly different locations (in the northern and southern hemispheres, respectively), so differences may be expected on that account.

In fact, there are significant differences in the radiance profiles extracted from these data subsets, and among the CIRRIS 15 μm data generally. The single profile shown in Figure 3 does not begin to suggest the great variability of the experimental limb radiance. Figure 5, which was provided by Don Smith here at Phillips Lab, displays sample profiles acquired over a period of several minutes in the southern hemisphere. The radiant intensity in the 100-115 km tangent-height region varies by as much as a factor of two. In addition, the visible structure ranges from very prominent single and double discrete layers to quite smoothly-varying and unremarkable radiance profiles that simply decrease with increasing altitude.

The degree of variability in the radiance profiles strongly suggests the existence of great variability in the atmospheric cooling in the MLT, as well.

The following figures show sample limb radiance data, and model calculations based directly on the TIME-GCM/ARC results. The first example, the "mid-latitude night" case shown in Figure 6 shows good to excellent agreement throughout the range of tangent altitudes from 75 to 160 km. The discrepancies that do appear, namely underpredictions

near 100 km and at the highest altitudes, are smaller than for the other cases, but are otherwise typical. Figure 7 shows a prominent knee at a tangent height of approximately 105 km and much higher radiance in the thermosphere than the model predicts. Figure 8 illustrates a case for which the model completely underestimates the expimental data over the full range of accessible data. The difference in the radiance levels between this case and that shown in Figure 6 is between 65% and 280% everywhere above 105 km.

We believe that most of the high altitude underprediction is due to the CO_2 profiles. CIRRIS data have consistently revealed high CO_2 in the thermosphere, compared to models.

Figure 9 shows the cooling rates from ARC and the TIME-GCM for the mid-latitude night case, where the best agreement was obtained. The two calculations are in reasonably good agreement. The results are typical in several respects: the peak cooling comes at approximately 120 km; the peak cooling is greater than 100 K/day there; the TIME-GCM rates are 10-15% lower at the peak than the ARC results, and they are biased toward higher altitudes so that above 130 km or so they are actually higher than the ARC results.

Figure 10 shows the TIME-GCM cooling rates for each of the six scenarios we considered. Except for the "mid-latitude day" case, there is a uniformity in the profiles that contrasts with the lack of uniformity in the experimental radiance profiles.

We asked ourselves how we might resolve the discrepancies between the experimental and modeled limb radiance. We made numerous adjustments to the input profiles that go into the non-LTE calculation, in particular the kinetic temperature, atomic oxygen, and CO_2 profiles, and tested their effects. We found that in many cases we could reproduce the experimental limb radiance by adjusting $[CO_2]$ at high altitudes and kinetic temperature in the mesopause region. Figure 11 shows the effects of such an adjustment in the case of the "low-latitude night" example, and Figure 12 shows the change in the kinetic temperature that was required to achieve this particular result. The modified temperature profile is in fact considerably different from the original one, being as much as 25 K warmer at some altitudes. Figure 13 shows the resulting effect on the cooling profile. There is greatly enhanced cooling in the region below 110 km, where the changes are as much as 38 K/day (which is well over 100% at some altitudes), and somewhat elevated cooling higher in the thermosphere. It is worth noting that this is the only one of the six cases for which the TIME-GCM algorithm gives higher cooling at the peak than the ARC calculation does.

The last example we show is the "high-latitude day" case, for which the model underpredicted the radiance data at all altitudes. Figures 14 and 15 compare the original and modified limb radiance and cooling rates, respectively. The most remarkable feature here is the magnitude of the cooling rate everywhere above 95 km. In particular, the peak cooling is 210 K/day at about 122 km, and the elevated cooling extends well into the E region, dropping below 100 K/day only near 150 km where NO infrared emission is normally considered to be the principal cooling mechanism.

Figure 16 shows the cooling rates that we infer from the CIRRIS data for the different cases we considered. These results were achieved by adjusting profiles that comprise input to the ARC codes, and demonstrate that the cooling in the lower thermosphere is indeed quite variable. It is notable that the example cited above that produces a peak cooling of 200 K/day is not a completely anomalous case. It is also notable that among the cases showing a peak cooling of roughly 100 K/day, there is great variability in the breadth and shape of the profiles.

The conclusions that can be drawn from this study are as follows. First of all, it has demonstrated the possibility of determining cooling rates in the MLT region from experimental limb radiance data. Secondly, it has shown that the cooling is not only quite large, compared to rates that have been commonly used in recent years, but is also quite variable. Based on the examples we used, the maximum cooling is typically in the range of 120 K/day near 120 km, but it may range from ~85 K/day to more than 200 K/day, and CO_2 cooling may compete with NO cooling well into the E region. We also found that the TIME-GCM cooling algorithm agrees reasonably well with the ARC calculations for comparable calculations, although it typically produces a somewhat lower maximum and somewhat higher cooling above 125 km. However, the TIME-GCM does not reproduce the variability in the CO_2 infrared cooling that we infer from the CIRRIS data, and in fact normally underpredicts this "actual" cooling by amounts that range from modest to substantial.

List of viewgraphs:

1) Objectives

2) Approach

3) Sample CIRRIS radiometer/interferometer profile

4) Cases considered

5) Overlay of CIRRIS radiometer profiles extracted from several minutes of data in a night-time block, to demonstrate the structure and variability of the limb radiance.

6) Experimental & model band radiances, mid-latitude night, using original TIME-GCM profiles(best agreement of the six cases considered)

7) Experimental & model band radiances, high-latitude night, using original TIME-GCM profiles (typical discrepancies: ~100% underprediction near 105 km, underprediction for higher tangent heights)

8) Experimental & model band radiances, high-latitude day, using original TIME-GCM profiles (underprediction at all altitudes considered)

9) Cooling rates calculated by ARC starting with original TIME-GCM profiles, compared with cooling used by TIME-GCM for the mid-latitude night case. Discrepancies are typical of 5 of the 6 cases: ARC results are a little higher below and at the peak, lower above ~130 km.

10) Cooling rates calculated by the TIME-GCM for the six cases considered.

11) Experimental & model band radiances, low-latitude night, using original TIME-GCM profiles and also a modified model atmosphere. (Kinetic temperature was modified near the mesopause and [CO_2] was modified above 130 km.)

12) Kinetic temperature profiles used to produce 11).

13) Cooling rates calculated by ARC starting with the original TIME-GCM profiles, by ARC using modified profiles, and by the TIME-GCM itself, for the low-latitude night case. El-evated cooling appears below the peak and above 140 km as a result of the modifications

14) Same as 8), but including band radiances calculated with a modified model atmosphere. (The kinetic temperature and CO_2 profiles were modified.) "A100A" is the modified profile.

15) Cooling corresponding to the comparison in 14), showing greatly enhanced cooling.

16) Atmospheric cooling rates, inferred by ARC after matching limb radiance profiles.

17) Conclusions

Objectives:

Estimate CO_2 15 µm cooling in the lower thermosphere

 CIRRIS-1A limb radiance data

 Models: NCAR TIME-GCM
 PL Atmospheric Radiance Code (ARC)

Compare estimated cooling with that used in TIME-GCM

Figure 1

Approach:

 Select six subsets of CIRRIS data
 Magnetic Latitude
 Local Time

 Run TIME-GCM for CIRRIS dates
 Extract N_2, O_2, O, CO_2, temperature

 Run ARC, predict:
 15 µm limb radiance
 Infrared cooling (K/day)

 Compare limb radiance with data
 Correct radiance $\longrightarrow$ Correct cooling

 What's needed to get correct radiance?

 Compare cooling rates
 TIME-GCM & ARC algorithms
 TIME-GCM & cooling inferred from C-1A data

Figure 2

216

Figure 3

MET: 1:14:26:55
Block: PC12B
Mode: 34-1
Calibration: post02
Focal Plane: pst
Decimation: 8
Sec: 0.03 - 101.90
Phot. Cal.: new
Detector(s):
1-1 ,1-2 ,1-3 ,
1-4 ,1-5 ,1-6

Min, Max, Avg
Phot 1 (5577A)
25, 69, 42
Phot 2 (3914A)
11, 62, 31
Latitude (Tan. Pt.)
-45.3, -43.0, -44.0
Solar Zenith Angle
149.4, 150.2, 149.9
Local Time
23.08, 23.89

filter 0 at 0 sec

filter 0 = 8.37 - 18.0
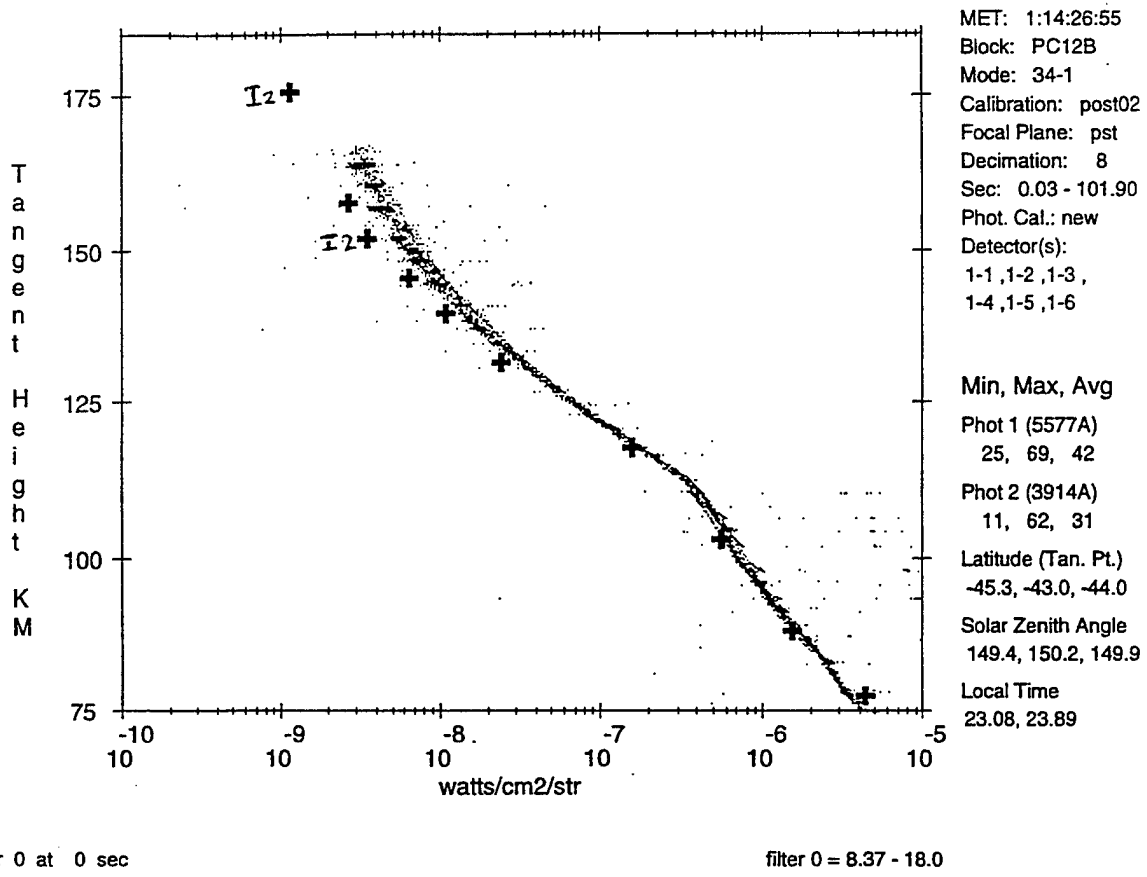
Cases considered:

		Latitude	Mag Lat	LT
a)	"auroral"	-65	-68	0
b)	low-latitude night	-12	-23	4
c)	mid/high latitude night	-45	-48	19
d)	mid-latitude night	-44	-32	23
e)	high-latitude day	+66	+61	9
f)	mid-latitude day	+49	+47	6

Figure 4

MET: 2:12:31:36
BLOCK: PC11A
MODE: 24-1
CALIBRATION: post01
DECIMATION: 64
SEC: 0.12 - 709.77
DETECTORS
1-1, 1-2, 1-3,
1-4, 1-5, 1-6,
1-8

MIN.MAX.AVG

PHOTOMETER 1
10, 60, 15

PHOTOMETER 2
1, 538, 51

LATITUDE (TAN. PT.)
-42.2, -13.2, -29.3

SOLAR ZENITH ANGLE
85.8, 125.7, 105.2

DAY/NIGHT

COURTESY of DON SMITH

Figure 5

Band Radiance

Case d: mid-latitude night

○ ARC simulation, A95
▼ CIRRIS-1A data (sample)

Band Radiance (watt/cm²-sr)

Figure 6

218

Band Radiance

Case c: high-latitude night

○ ARC simulation, A97
▼ CIRRIS-1A data (sample)

Band Radiance (watt/cm²-sr)

Figure 7

Band Radiance

Case e: high-latitude day

○ ARC simulation, A100
▼ CIRRIS-1A data (sample)

Band Radiance (watt/cm²-sr)

Figure 8

15 Micron Cooling

Case d: mid-latitude night

ARC simulation, A95
TIME-GCM cooling
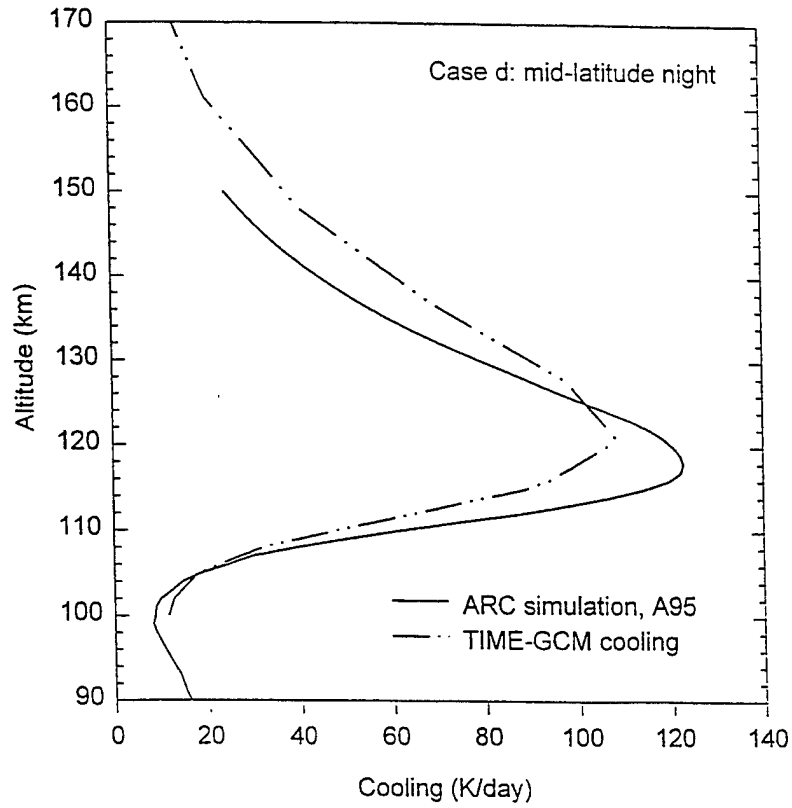
Figure 9

15 Micron Cooling, TIME-GCM

Case A, "auroral"
Case B, low-lat night
Case C, high-lat night
Case D, mid-lat night
Case E, high-lat day
Case F, mid-lat day

Figure 10

Band Radiance

Case b: low-latitude night

□ ARC Simulation, A99a_co2b
○ ARC Simulation, A99
▼ CIRRIS-1A data (sample)

Tangent Height (km)

Band Radiance (watt/cm²-sr)

Figure 11

Kinetic Temperature

Case B, low-latitude night

—— TIME-GCM temperature, A99
– – Modified temperature, A99a

Altitude (km)

Temperature (K)

Figure 12

221
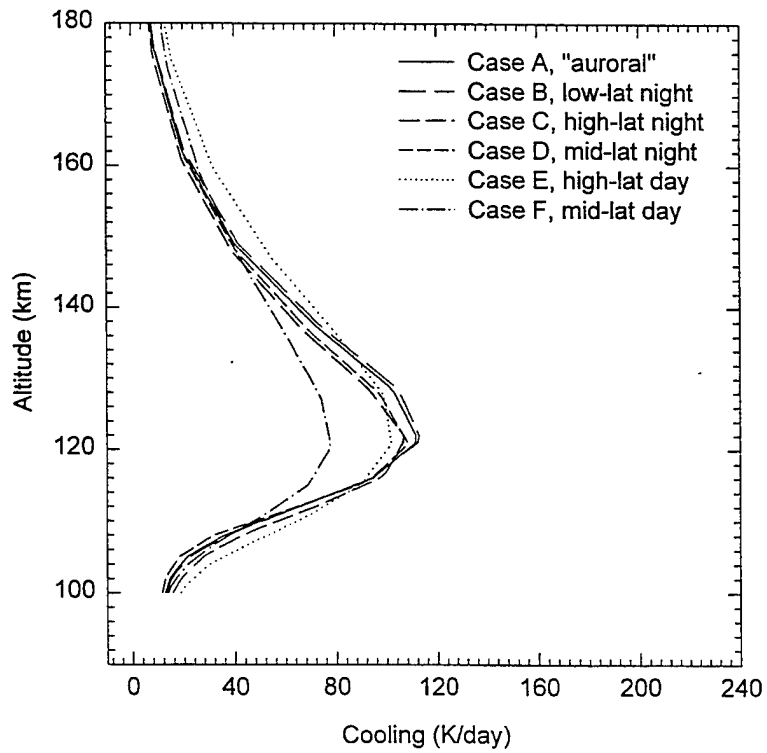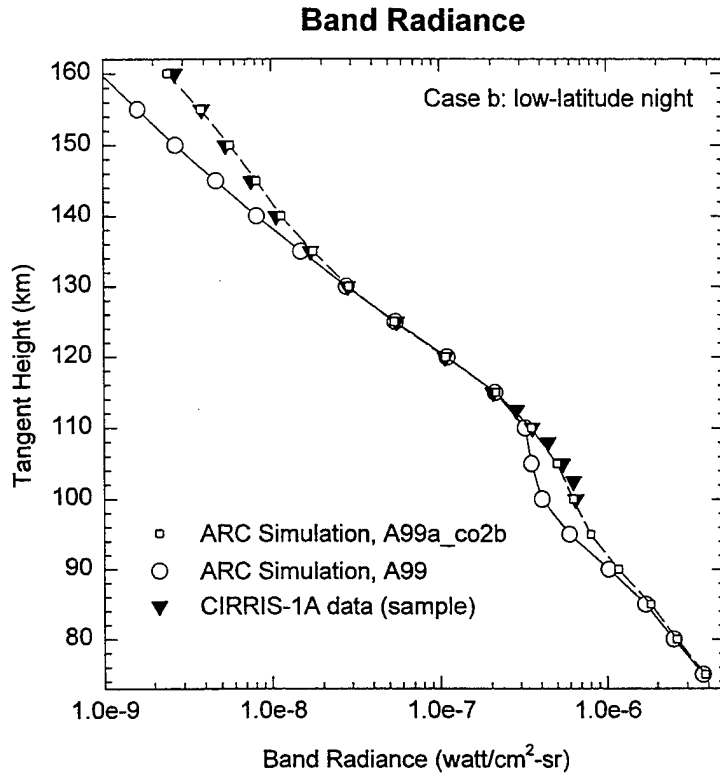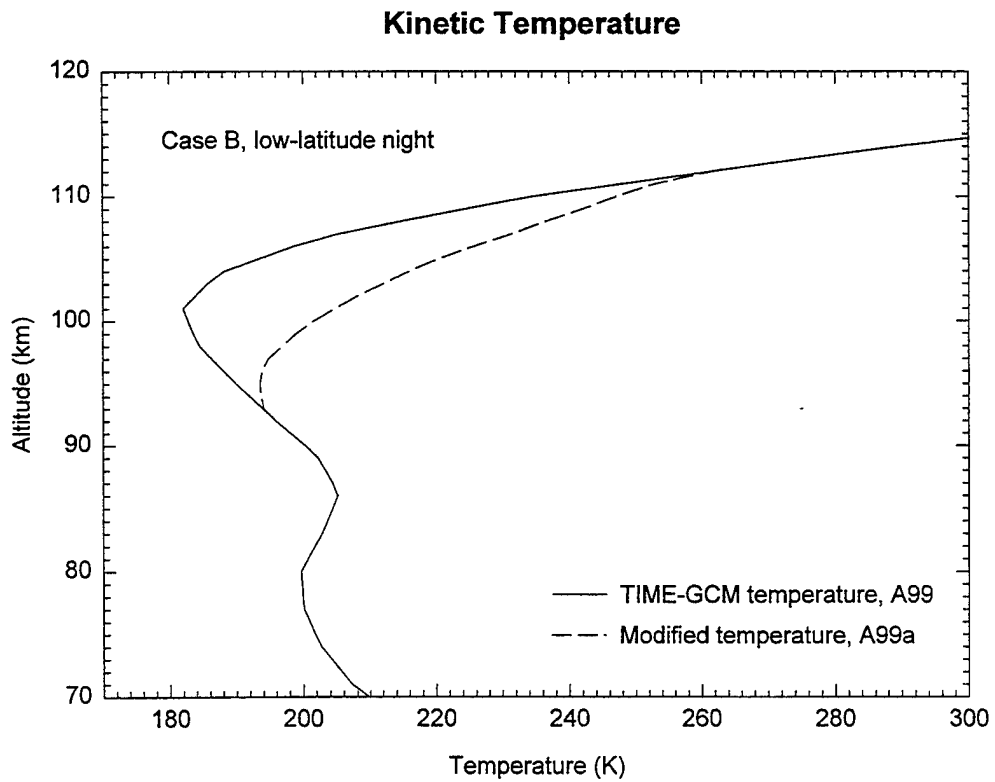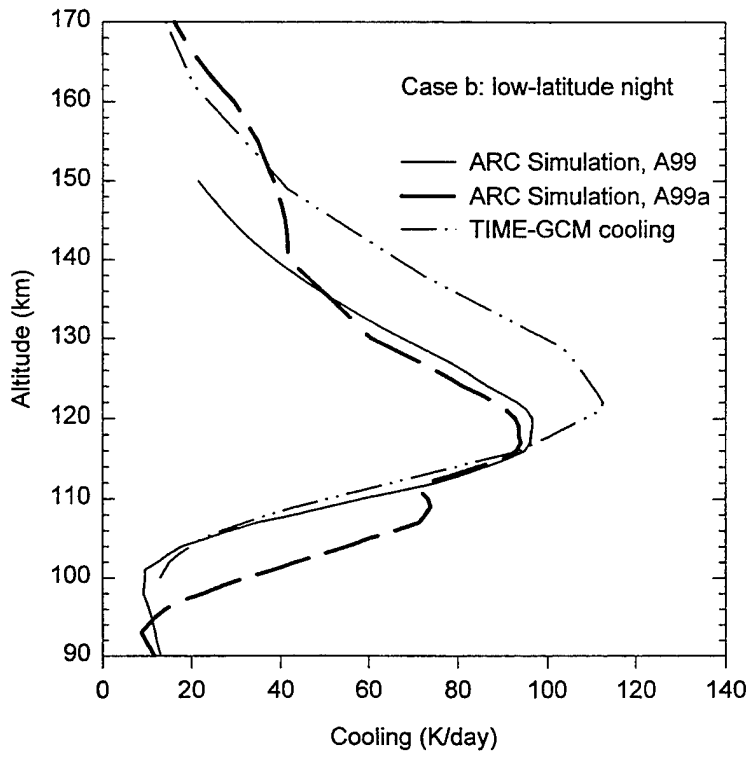
15 Micron Cooling

Figure 13

Band Radiance
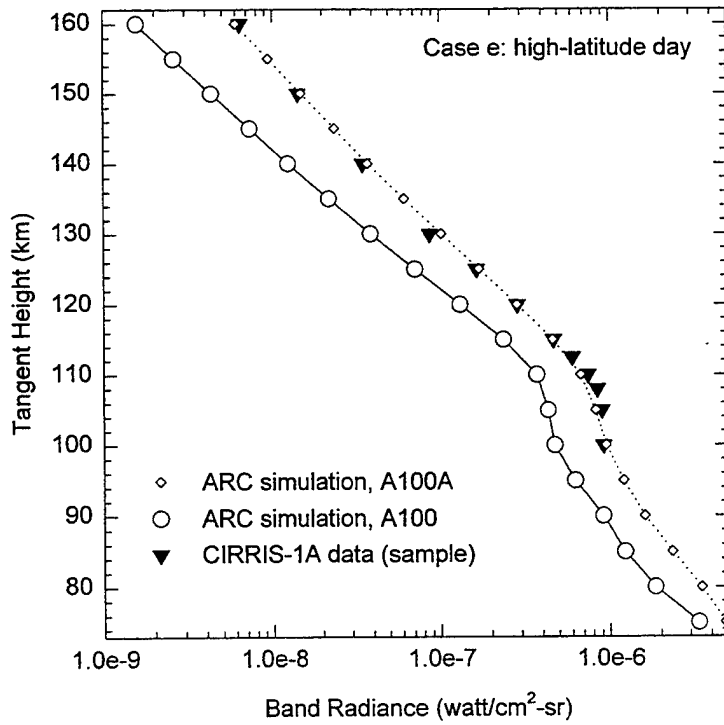
Figure 14

15 Micron Cooling
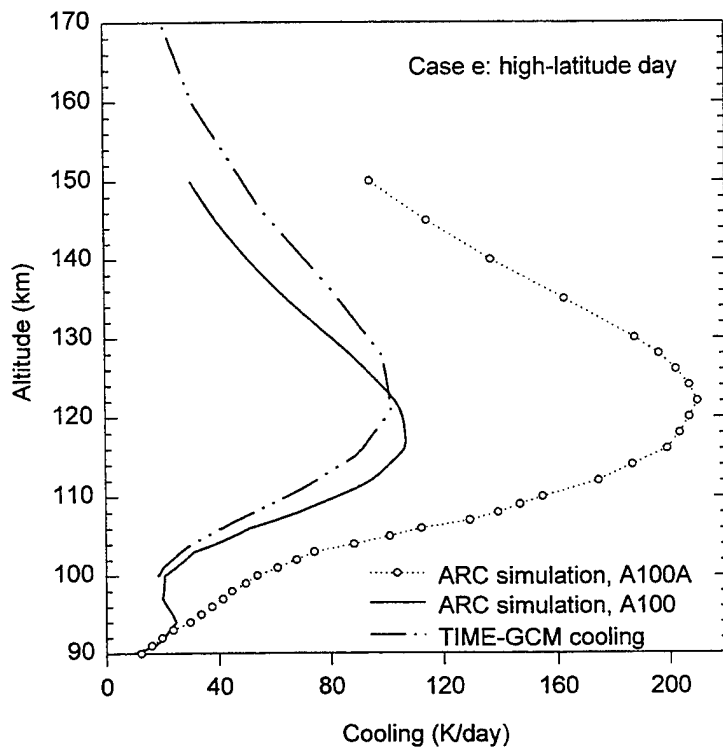
Figure 15

15 Micron Cooling Rates, ARC
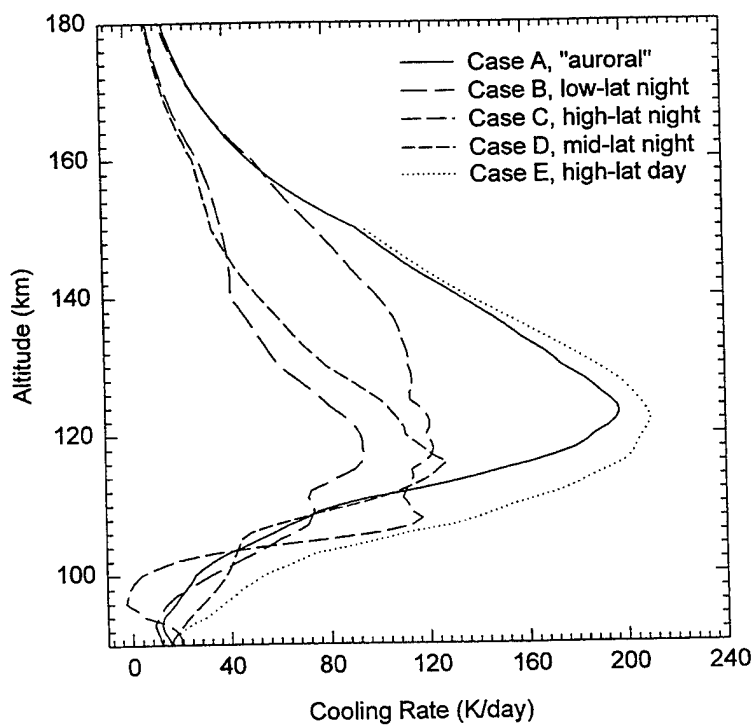
Figure 16

CONCLUSIONS

Cooling rates can be determined from 15 μm limb radiance data in the lower thermosphere

Cooling is large and quite variable

Maximum cooling occurs consistently at ~120 ± 3 km

Typical maximum cooling is ~120 K/day, BUT...

Cooling at the peak may range from ~85 K/day to > 200 K/day

TIME-GCM cooling rate algorithm agrees quite well with ARC calculations

TIME-GCM rates typically 15% lower at ~120 km

TIME-GCM rates typically higher above 125 km

TIME-GCM calculations often lead to underprediction of CIRRIS 15 μm limb radiance

Cooling rates are typically too low, compared to rates inferred from CIRRIS data

WSA

Sensitivity of Lasers in Maritime Environment

Larrene Harada
5 June 1996

19th Annual Review Conference on Atmospheric Radiation

WSA

W.J. Schafer Associates
1901 N Fort Myer Dr. #800
Arlington, VA 22209
(703) 841-3401

Concept Description

5-10 km
Near Horizontal Propagation

2-10 m
Off Ocean Surface

24741
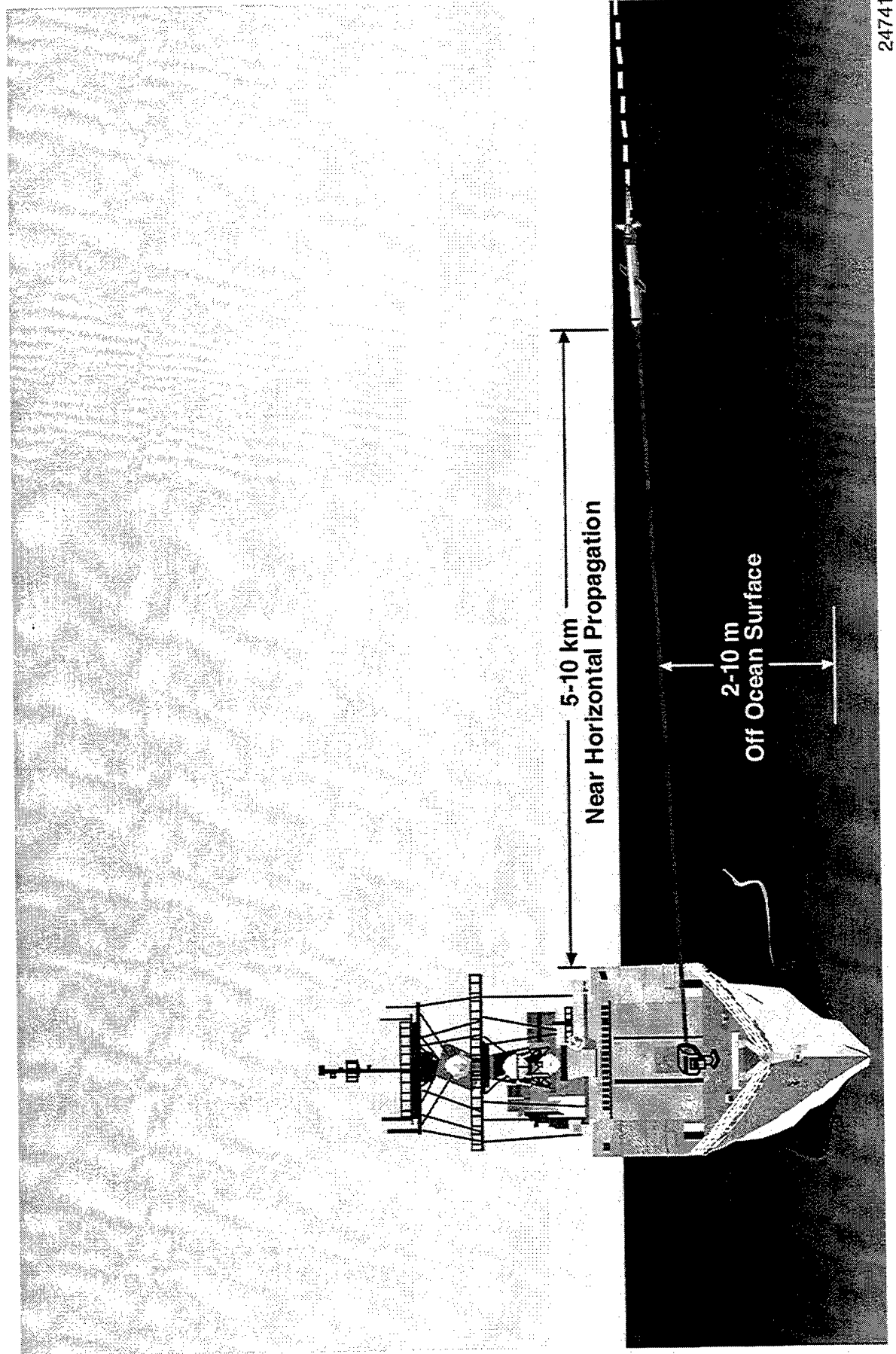
Objective of Study

Determine which wavelength region provides the greatest power on target under varying meteorological conditions for near surface maritime environments.

WSA

Atmospheric Effects

Meteorological Conditions
- Temperature
- Pressure
- Humidity
- Wind Speed
  - 24 hr Average
  - Current

Air Mass
- Open Ocean
- Coastal

H2O

CO2

Molecules

Aerosols

Sea Spray

Wind

Wind

Wind

Laser Propagating
Thermal Blooming
Absorption
Scattering
Turbulence
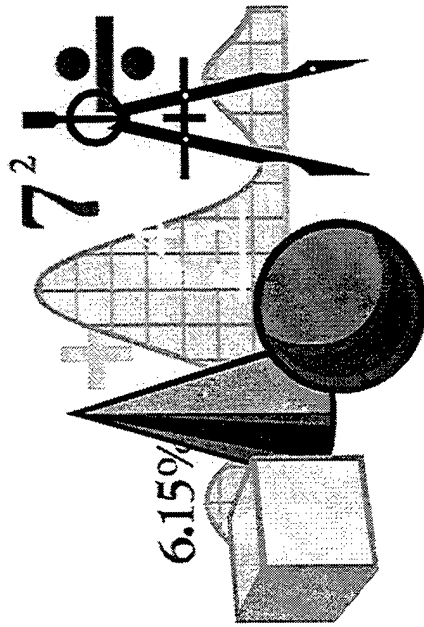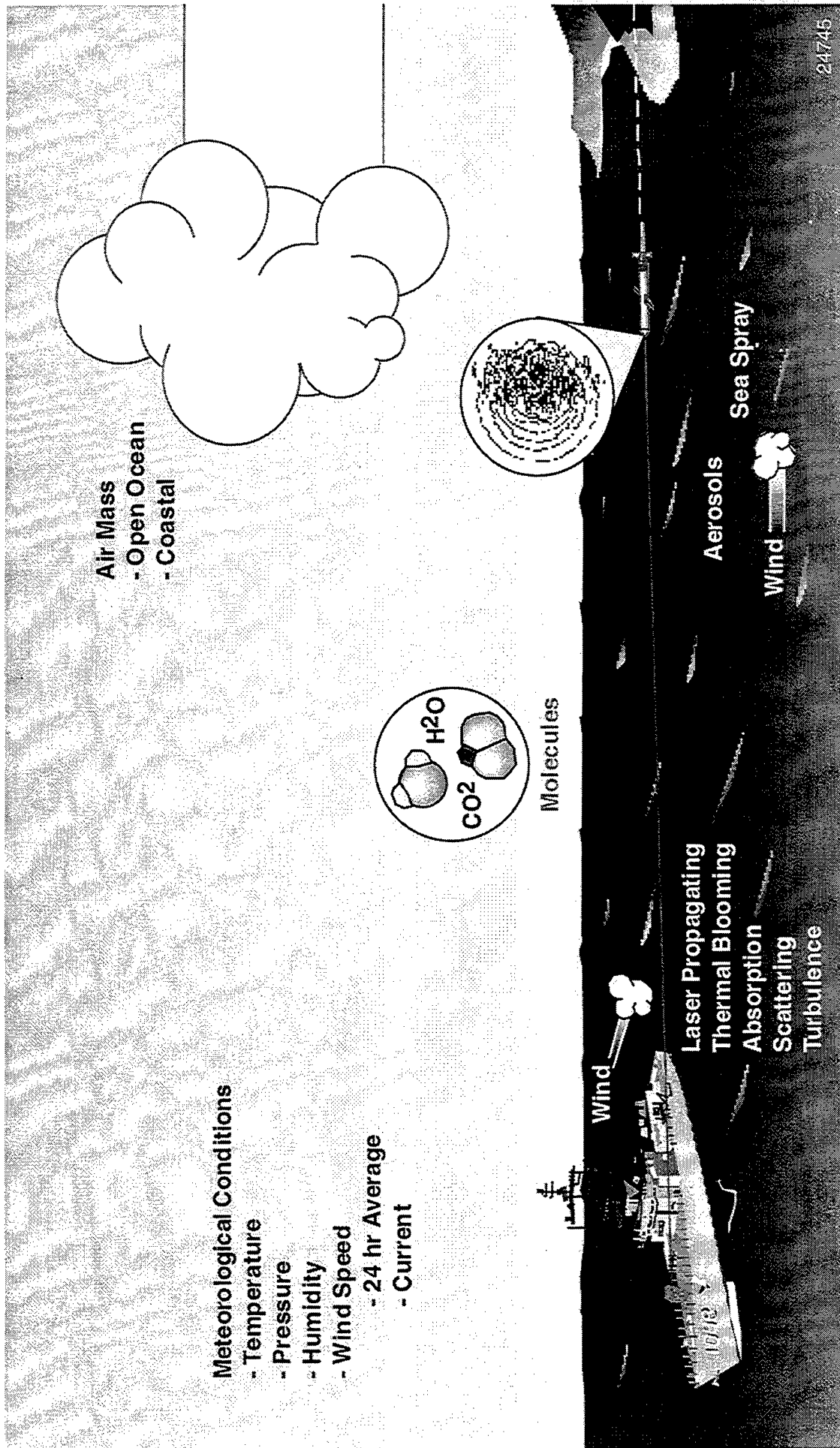
24745

Thermal Blooming in a Nutshell

early part of laser pulse heats atm.

later part sees negative lens, defocuses

> temp diff
> spreading

As beam focusses air becomes hotter relative to ambient air.

Heated Air

Light Refracts toward denser media.

molecular absorption

aerosol vaporization

Cooler/Denser Air

VSA

06/02/96

Maritime Environments for HEL Propagation

5

Balancing Act

Scattering

Absorption

thermal blooming

Limits the device power.

turbulence
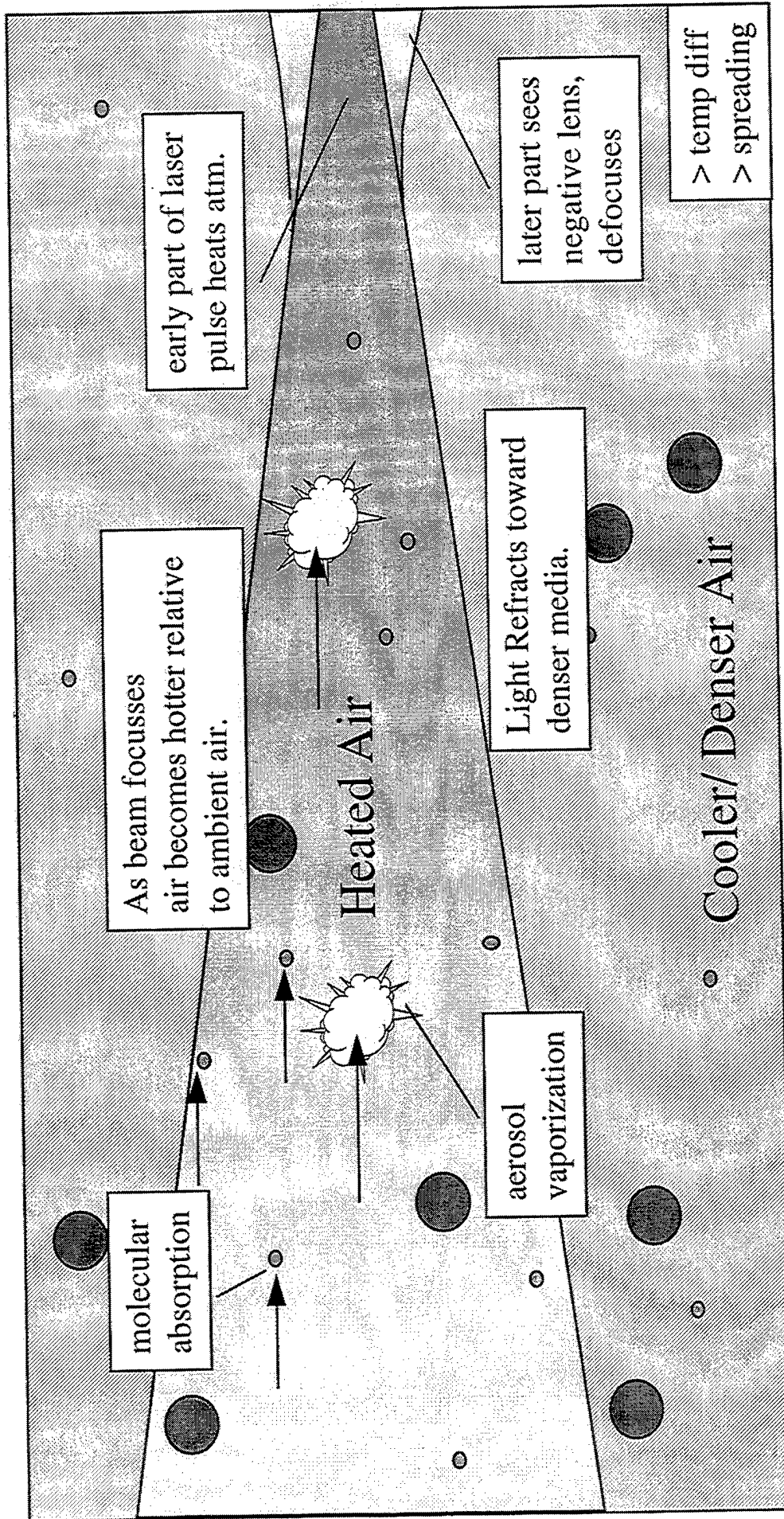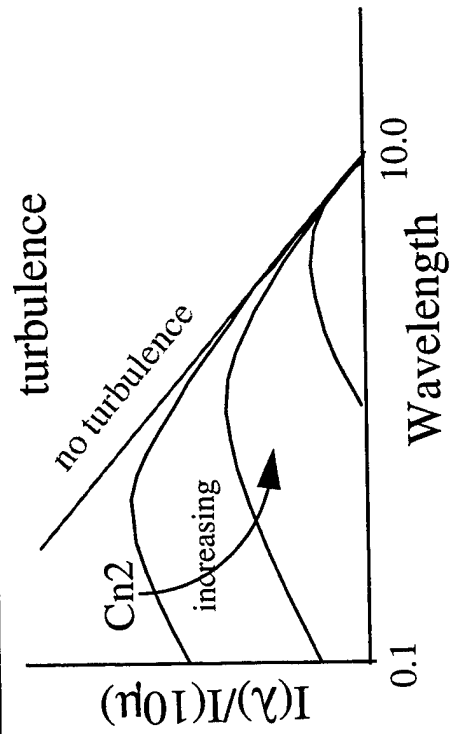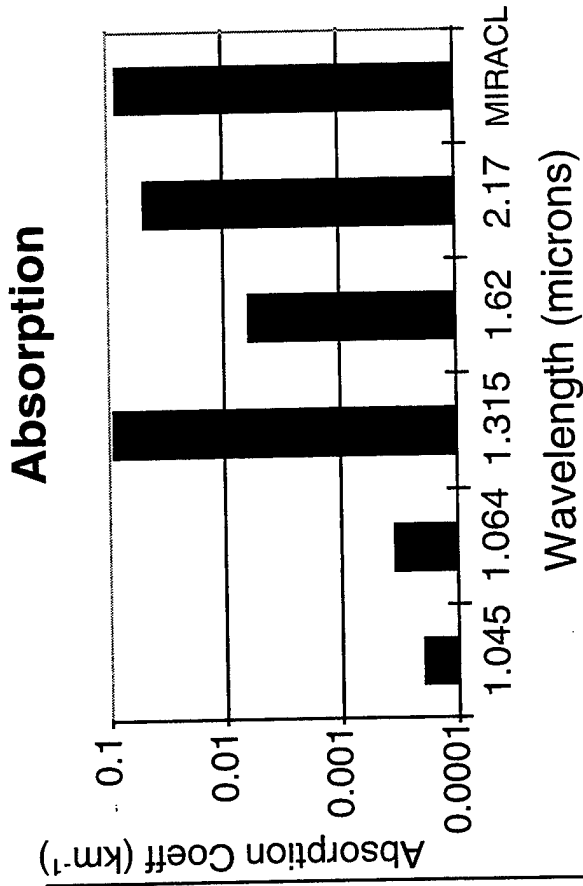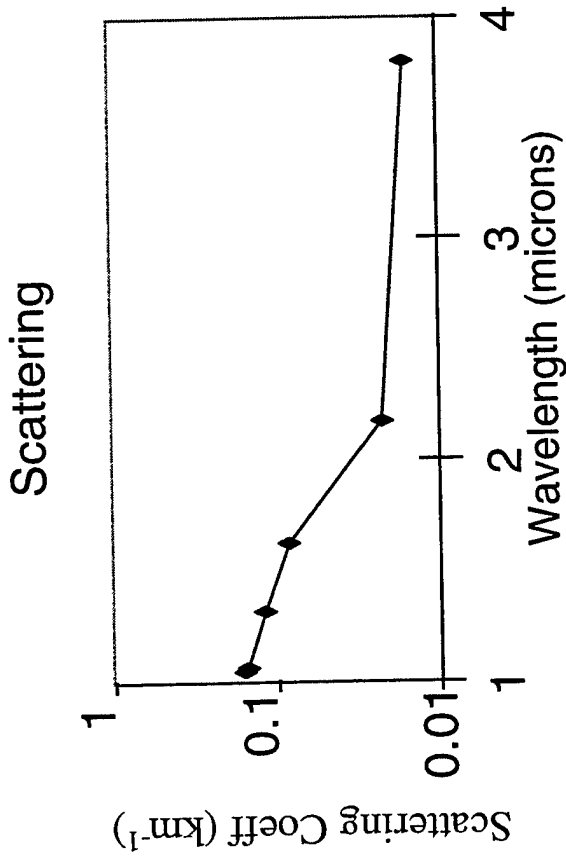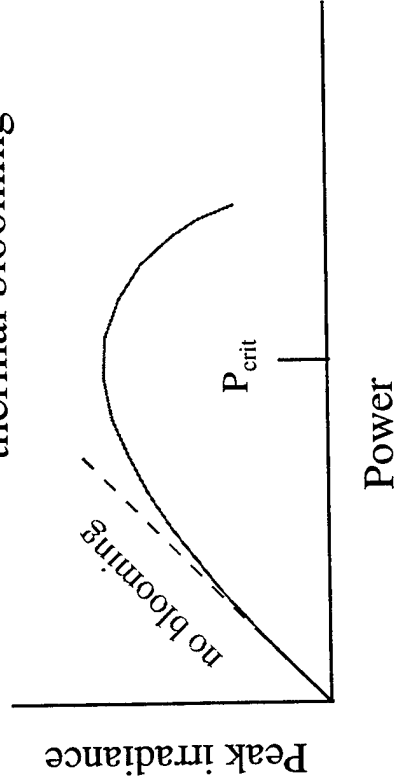
Optimum λ with Cn2, range and aperture.

WSA

Maritime Environments for HEL Propagation

Maritime Environments for HEL Propagation

06/02/96

231
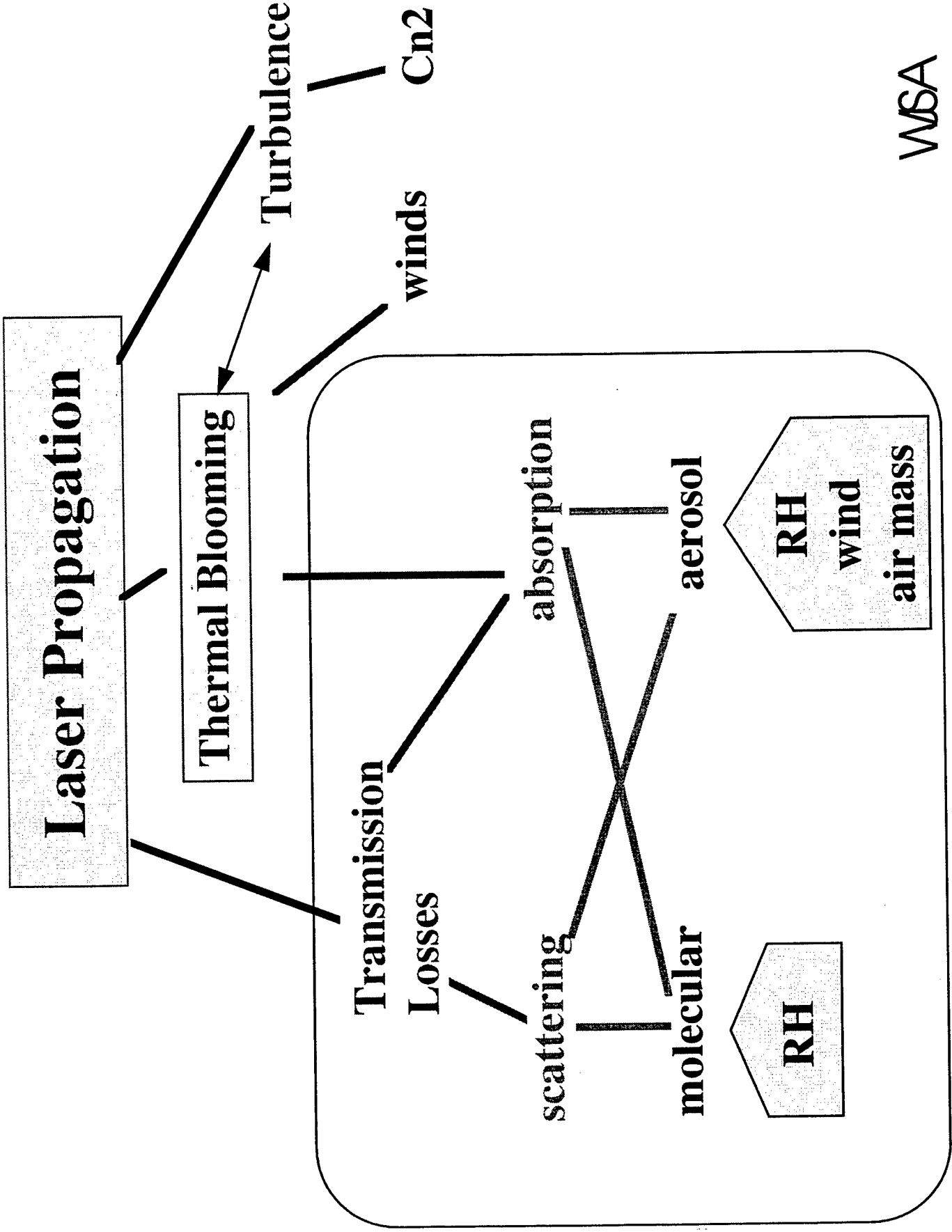
NAM
Navy Maritime Aerosol Model

- Marine Aerosol composed of three distinct populations with log-normal size distributions

  – continental component (smallest)

  = Depends on time elapsed for the air mass to travel from the continent to the point of observation.

  – stationary component

  = Depends on wind speeds. Produced by high wind and whitewater phenomena but do not fall out rapidly.

  – fresh component

  = Depends on current wind speed. Production of drops by whitewater as a result of wave action.

WSA

Attenuation Coefficients

RH=85%, Coastal, Wind= 6 m/s
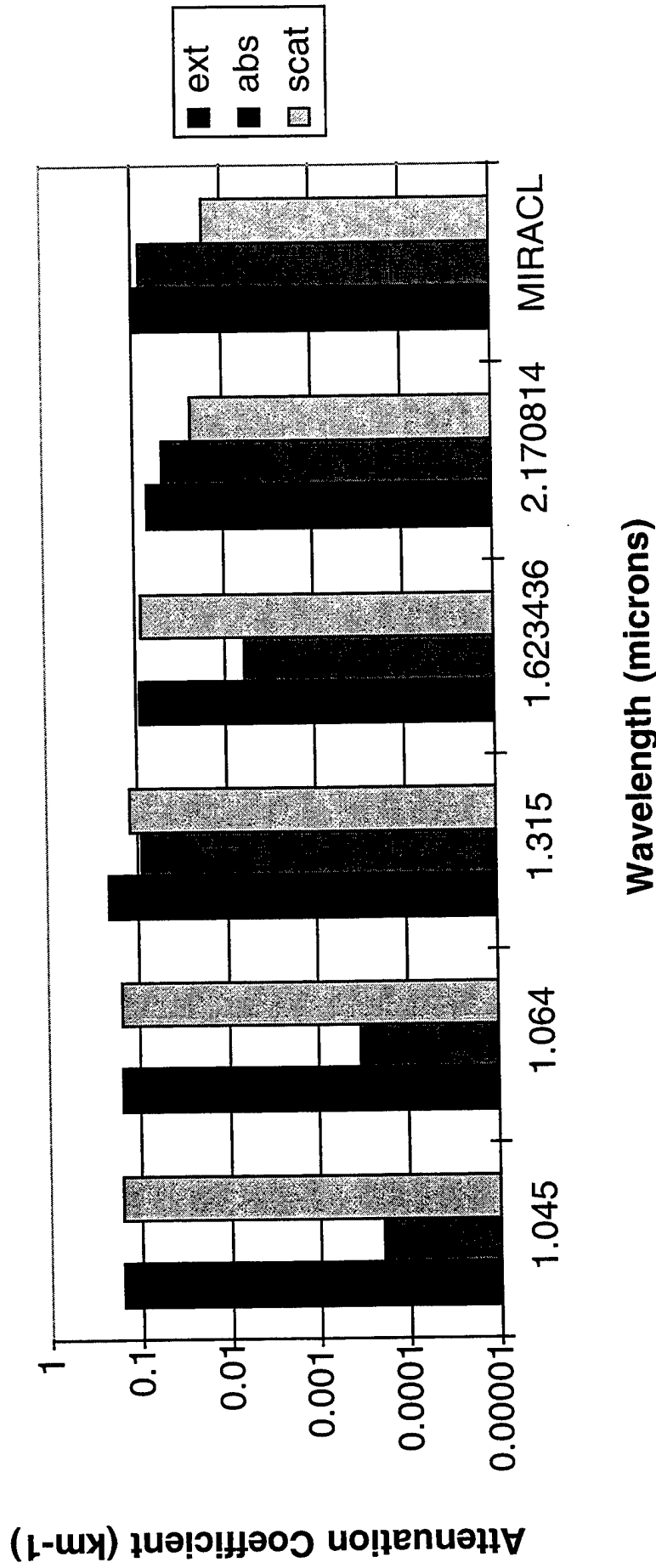
Total absorption coefficients at 1.045 or 1.064 are at least an order of magnitude less than other wavelengths.

Maritime Environments for HEL Propagation

06/02/96

9

Wind Sensitivity at 1.045 microns

RH=85%, Coastal
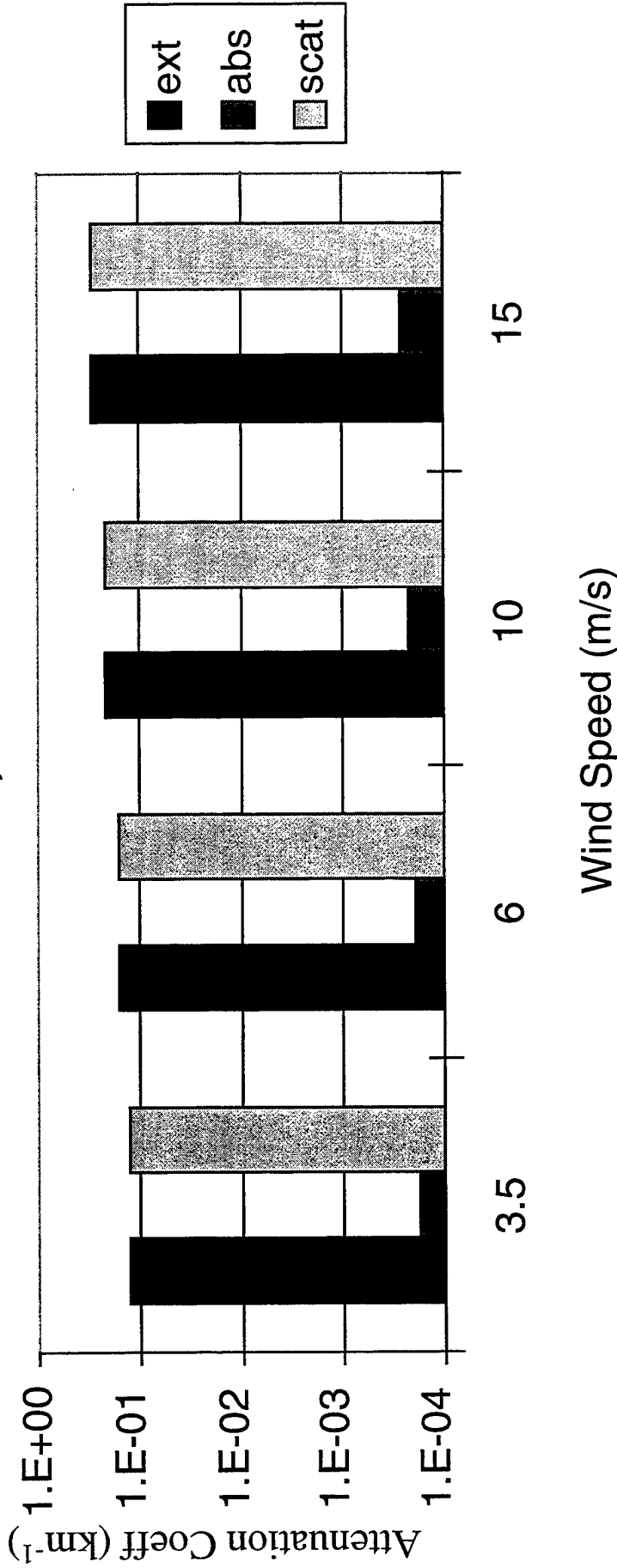
Aerosol Absorption and Scattering change by at least a factor of 2 between 3.5 and 15 m/s in wind.

For an air mass of 1, open ocean, they vary by about an order of magnitude.

WSA

Relative Humidity at 1.045 microns

Coastal, Wind= 6 m/s

Legend:
- ext
- abs
- scat

Y-axis: Attenuation Coeff (km^{-1})

Y-axis values: 1.E+00, 1.E-01, 1.E-02, 1.E-03, 1.E-04

X-axis: Relative Humidity (%)

X-axis values: 75, 85, 95

WSA

235

Maritime Environments for HEL Propagation

11
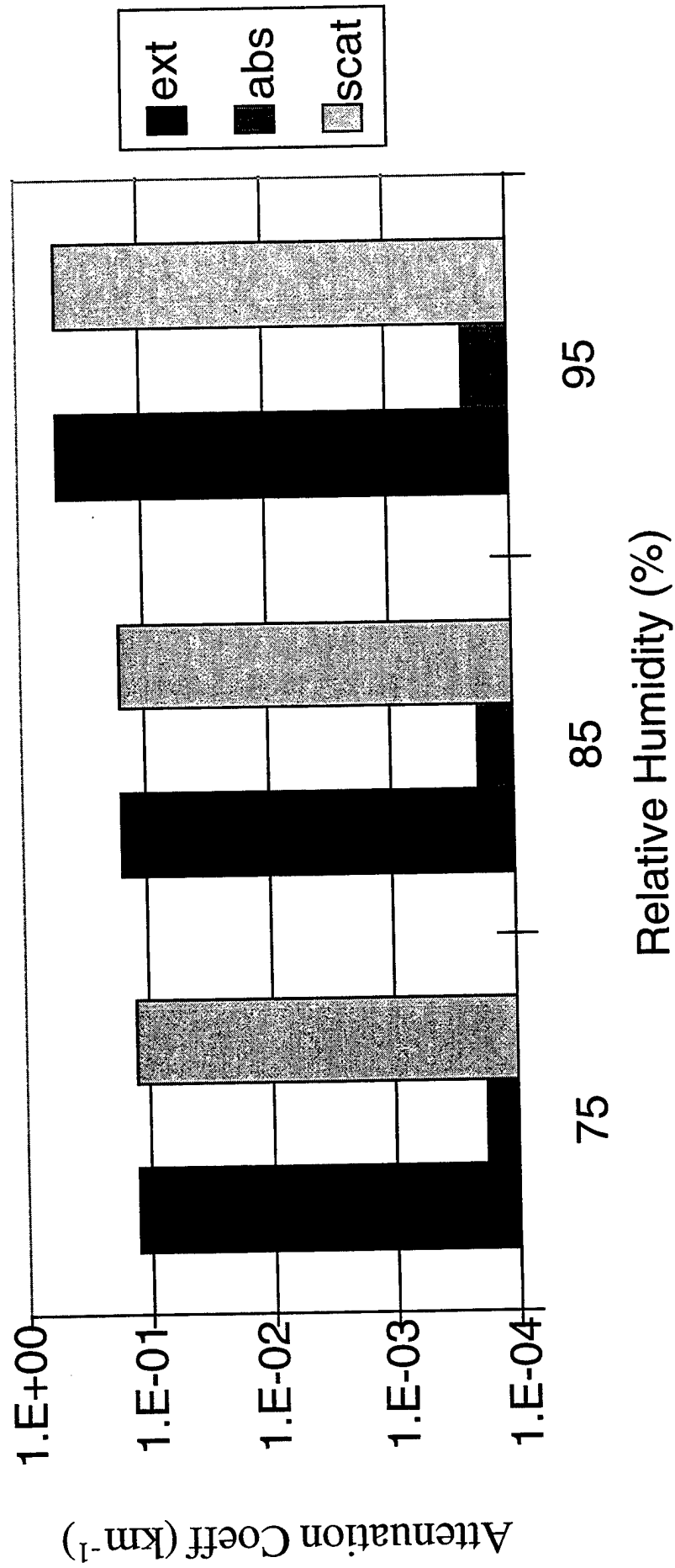
Conclusions

- **FEL tunability**
  - region of lowest absorption $\sim 1.045~\mu m$
    = Window of minimal absorption $>70~cm^{-1}$
  - $1.6~\mu m$ backup in eyesafe region.
- **Non-FEL devices**
  - $1.06~\mu m$ ND:YAG yields the lowest absorption.
  - COIL and MIRACL have absorption coefficients more than two orders of magnitude greater than $1.045~\mu m$.

WSA

06/02/96

Maritime Environments for HEL Propagation

12

LARC(Laser Radar Code)
and
Atmospheric Transmission Look-Up Table

Dima Seliverstov

MITRE Corporation

dimas@mitre.org

617-377-5314

M.John Yoder

MITRE Corporation

myoder@mitre.org

617-377-6907

Overview:

In this paper we describe a simple method for coupling FASCODE3P results to other practical applied codes. This enables these applied codes to run faster and use less powerful computers. In particular our application is the MITRE LAser Radar Code (LARC). LARC calculates the probability of detection for arbitrary sensor locations and target trajectories and includes the relevant physical effects. The laser radar range equation is solved for a real curved-earth geometry and includes free air induced turbulent beam spreading effects. LARC includes target fading and atmospheric scintillation. LARC computes the detection statistics for both pulsed and Continuous Wave (CW) laser systems.

The LARC code is decoupled from the FASCODE3P program by use of an atmospheric extinction coefficient lookup table. This method uses FASCODE3P to compute the extinction coefficients as a function of laser wavelength, altitude and atmospheric model. Using the extinction coefficients, a curved earth ray tracing routine computes the corresponding atmospheric transmission much faster then using the directly coupled FASCODE3P code. This paper describes the calculations involved and compares the results to directly calculated FASCODE3P transmission.

Laser Radar Code Description:

LARC includes the relevant physical effects needed to evaluate the probability of detection for various targets of interest. The laser radar range equation is solved for a real curved-earth geometry and includes free air induced turbulent beam spreading effects. LARC also includes target fading and atmospheric scintillation. LARC computes the detection statistics for pulsed and Continuous Wave (CW) laser systems. Combining all of these statistical effects, the code determines the probability of detection of the missile as a function of time.

A significant feature of this effort is that it combines the relevant effects into a single calculation (radar range equation, turbulent beam spreading, high spectral resolution optical transmission in curved earth geometry, target reflection/speckle effects, target fading

statistics, free air atmospheric turbulence statistics and detector statistics). This calculation results in probability-of-detection curves vs. trajectory parameters for the modeled target. Since all relevant wavelength, propagation, target and statistics effects are included in a single model, it is possible to derive laser energy and wavelength tradeoffs efficiently, consistently and reliably.

The relevant physical quantities required for LARC calculation are shown in Figure 1 for any laser radar system and detection scenario. The input parameters that must be provided by the user are shown on the left-hand side of the figure. The desired results are shown on the bottom right-hand side namely, the probability of detection, P_d, for a single measurement with the user specified probability of false alarm, P_{fa}. The calculations are signified by shaded areas.
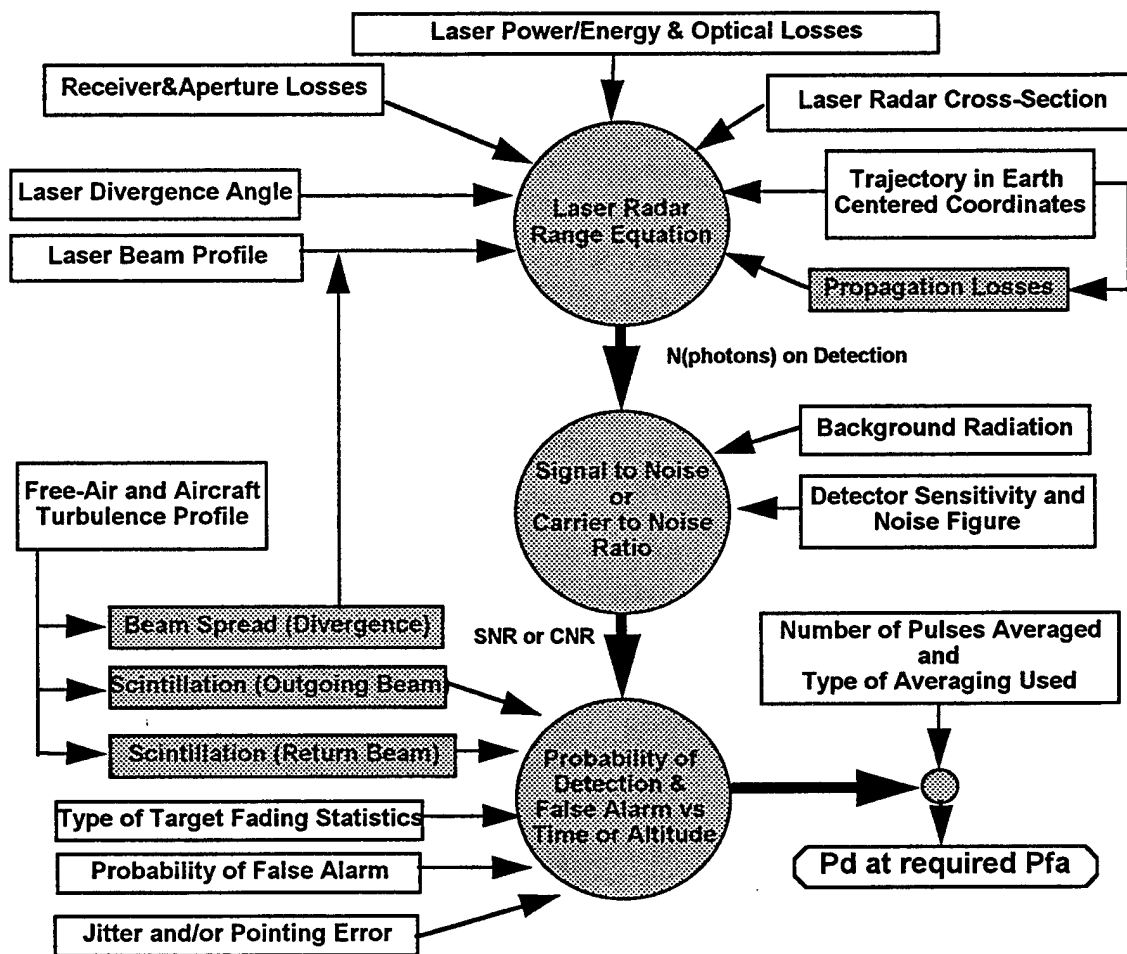
Figure 1: LARC Calculation

The LARC code is written in C and compiled for the Macintosh and SGI computer systems. Graphical output can be plotted on the shareware plotting package (GNUPLOT). The data can be saved in a Postscript format for a graphical printout. A current set of parameters can be saved to a file for later use. Previously saved inputs can be read-in from a file.

Geometry Specification:
For the following calculations, we assumed a medium range ballistic missile target trajectory profile shown in figure 2. The stationary observer was located at 29 Kft at ranges of 200,400 and 600 kilometers away from the missile threat. The missile threat flew a trajectory perpendicular to the observer.
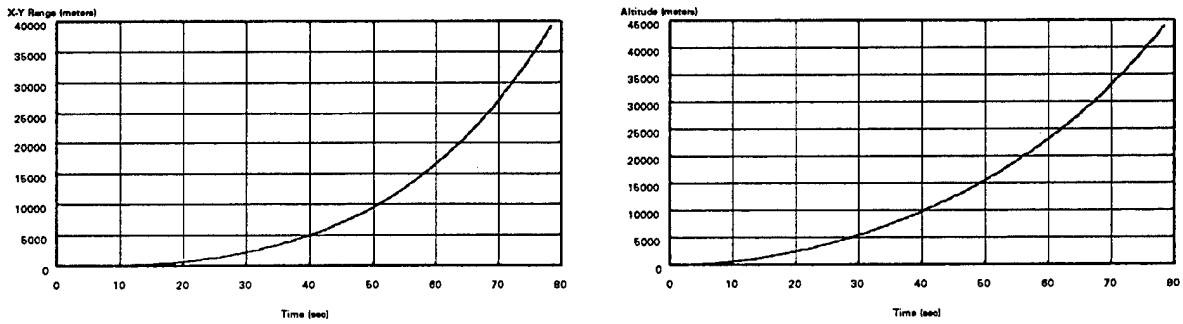
Figure 2. Target down-range and altitude profiles
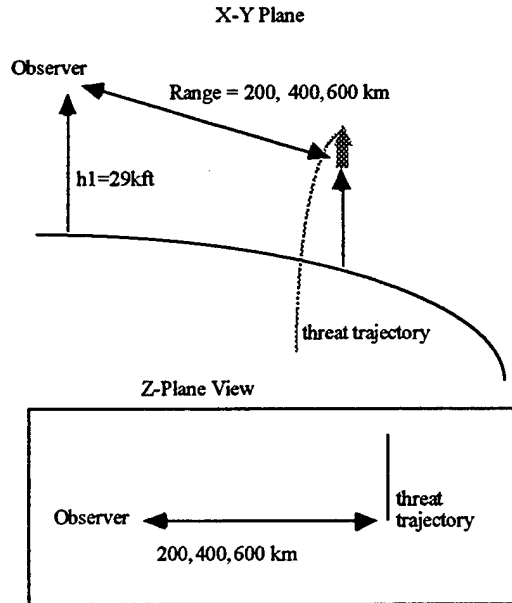
Figure 3. Geometry Parameters

The laser wavelength and atmospheric parameters used in this paper are listed in Table 1.

TABLE 1. Laser and Atmospheric Parameters

Laser wavelength µm	1.064
	1.542
	1.571
	2.096
	9.114
	11.149
Model	Midlatitude Summer
Visibility	Rural Extinction (23 km VIS)
Season	Model based default
Stratosphere	Aged/Moderate Volcanic Extinction
Cloud	No clouds or rain

Atmospheric Transmission Calculation:

The atmospheric transmission is calculated for a variable target and observer geometries using FASCODE3P generated extinction coefficients and a curved earth ray-trace model. FASCODE3P extinction coefficients are generated as a function of altitude, wavelength, and atmospheric parameters. The curved earth ray tracing routine is used to calculate transmission using these extinction coefficients. The ray tracing method is illustrated in Figure 4.
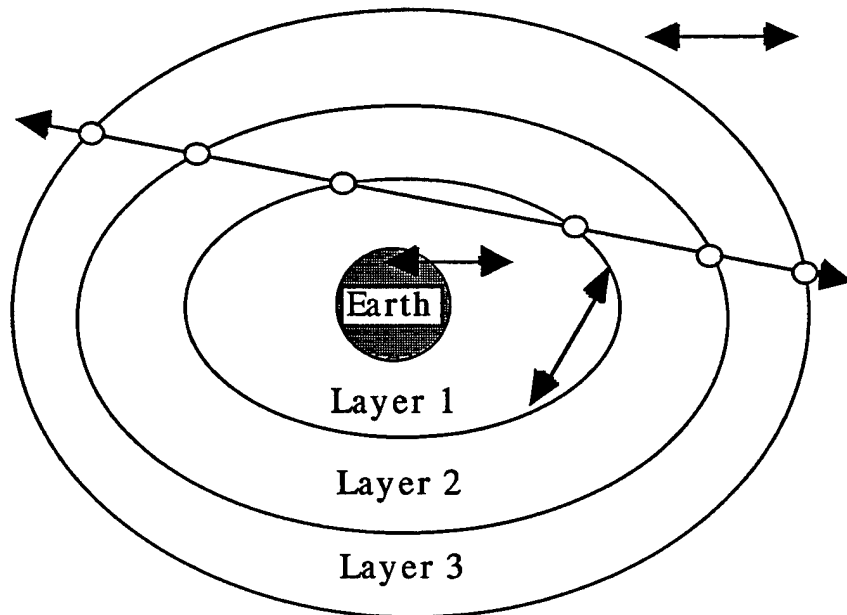
Figure 4. Curved Earth Ray Tracing Diagram

The intersections between the path and each layer is calculated. Constant extinction coefficients are assumed in each layer. The transmission outside of the upper layer is assumed to be 1 (extinction coefficients are 0). In this paper, layers below 20 kilometers altitude are separated by 1 km, layers above 20 kilometers are separated by 5 kilometers, and the upper layer is 100 kilometers.

Using a standalone program that calls FASCODE3P, a lookup table can be generated for a user defined layering, laser wavelength and atmospheric parameters. New extinction coefficients can be calculated using FASCODE3P for any atmospheric conditions supported by FASCODE3P and used with the LARC ray-trace model.

The relationship between the extinction coefficients and transmissions is:

$$T = e^{-\alpha R}$$

where

Symbol	Value
T	Atmospheric transmission
α	Extinction coefficient (1/km)
R	Range in km

Transmission Comparison to FASCODE3P:
In this section the transmission is calculated using an extinction coefficient curved earth ray tracing method and compared to transmission calculated directly using FASCODE3P. The ray tracing method is at least a factor of 10 faster than running FASCODE3P directly from LARC. The ray-tracing method can run in real time. It is also easier to distribute and support LARC version with the ray-trace method only

Figures 5-10 compare the FASCODE3P(dots) and look-up table(solid line) implementation for various laser wavelengths.

Transmittance
1.064 microns : Range 200km: Midlat. Summer
Time (sec)
FASCODE3P ●
Lookup

Transmittance
1.064 microns : Range 400km: Midlat. Summer
Time (sec)
FASCODE3P ●
Lookup

Transmittance
1.064 microns : Range 600km: Midlat. Summer
Time (sec)
FASCODE3P ●
Lookup
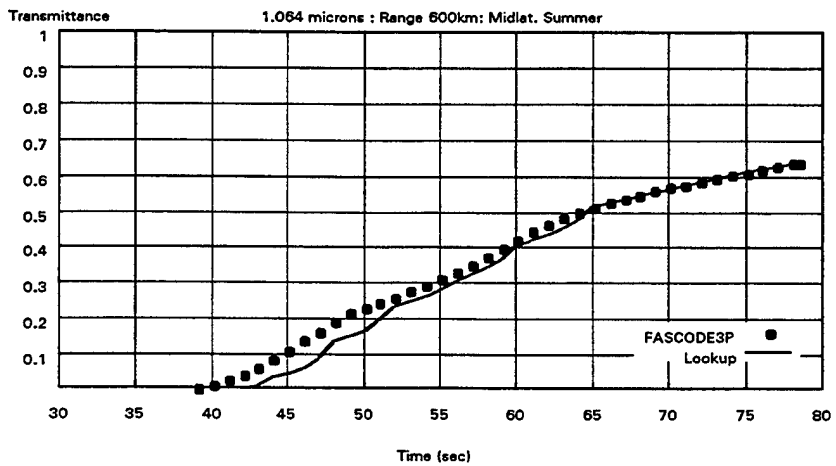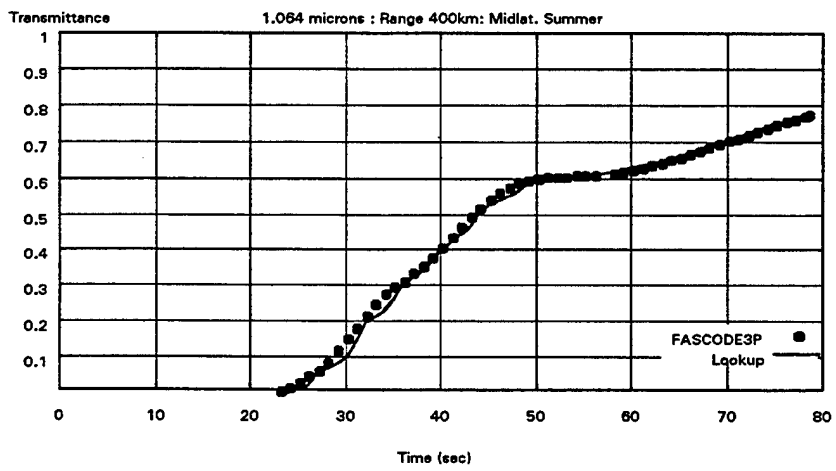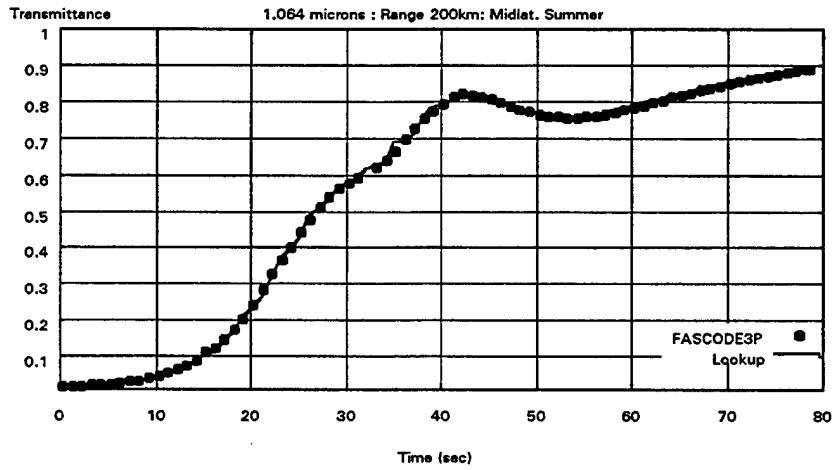
Figure 5. Transmission Comparison for 1.064 µm Laser Line

Transmittance — 1.542 microns : Range 200km: Midlat. Summer

Time (sec)

FASCODE3P ●
Lookup ——

Transmittance — 1.542 microns : Range 400km: Midlat. Summer

Time (sec)

FASCODE3P ●
Lookup ——

Transmittance — 1.542 microns : Range 600km: Midlat. Summer

Time (sec)

FASCODE3P ●
Lookup ——

244
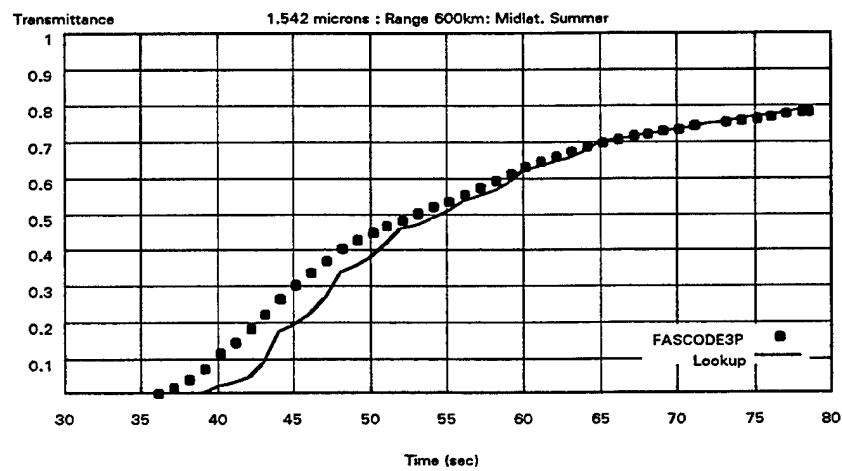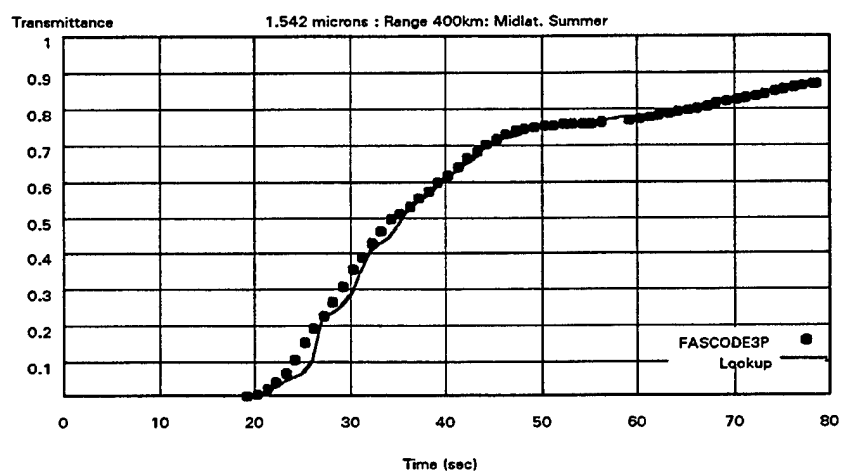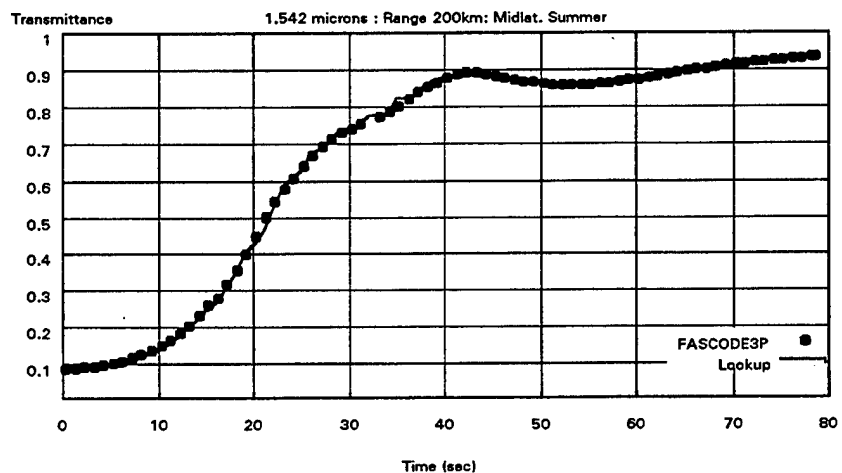
Figure 6. Transmission Comparison for 1.542 µm Laser Line

Transmittance

1.571 microns : Range 200km: Midlat. Summer

FASCODE3P

Lookup

Time (sec)

Transmittance

1.571 microns : Range 400km: Midlat. Summer

FASCODE3P

Lookup

Time (sec)

Transmittance

1.571 microns : Range 600km: Midlat. Summer

FASCODE3P

Lookup

Time (sec)
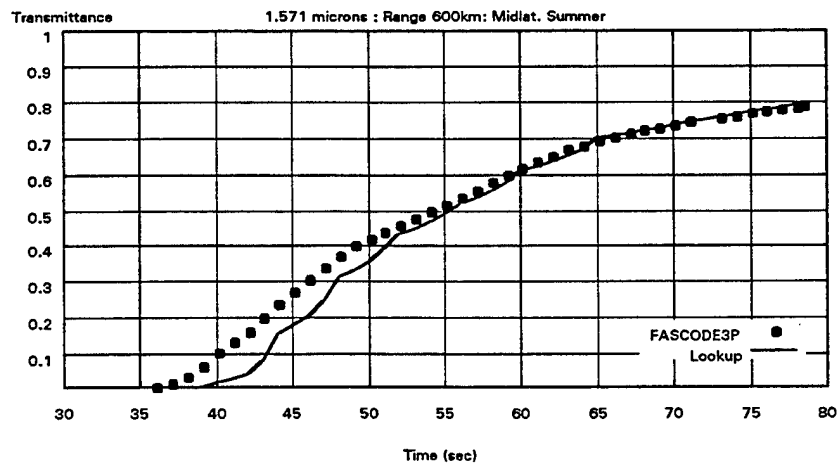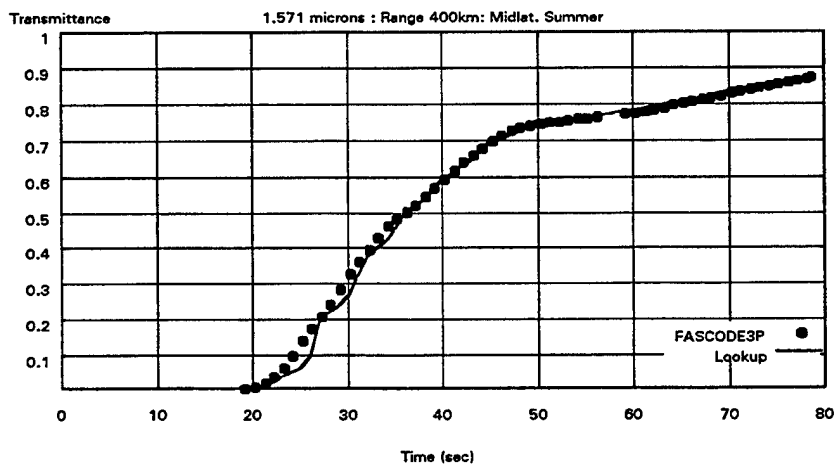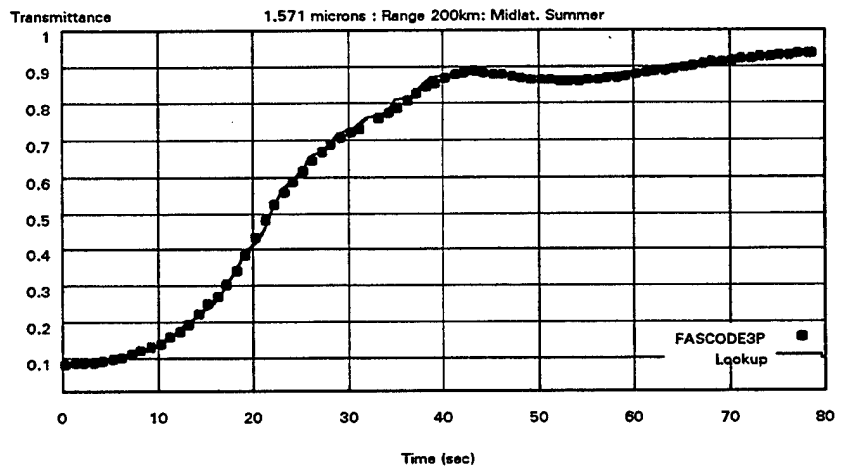
Figure 7. Transmission Comparison for 1.571 μm Laser Line

Transmittance — 2.096 microns : Range 200km: Midlat. Summer

FASCODE3P
Lookup

Time (sec)

Transmittance — 2.096 microns : Range 400km: Midlat. Summer

FASCODE3P
Lookup

Time (sec)

Transmittance — 2.096 microns : Range 600km: Midlat. Summer

FASCODE3P
Lookup

Time (sec)

246
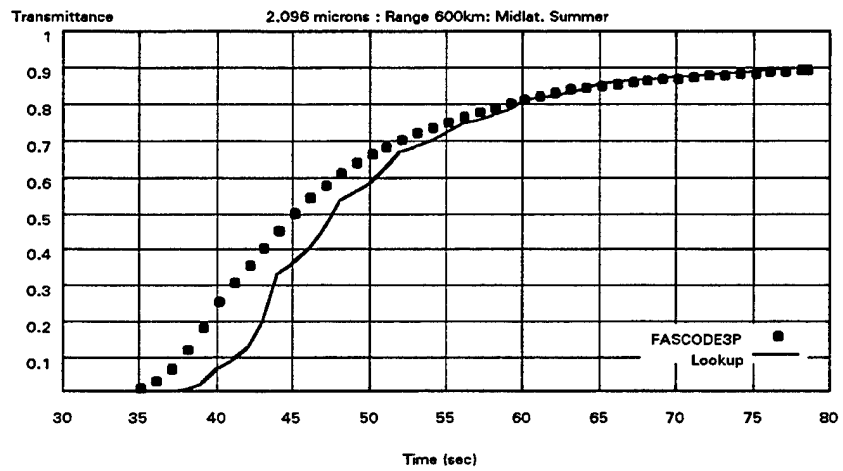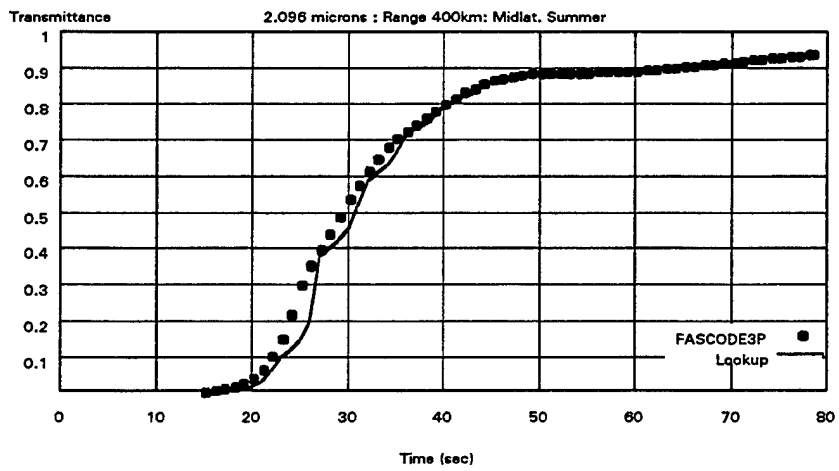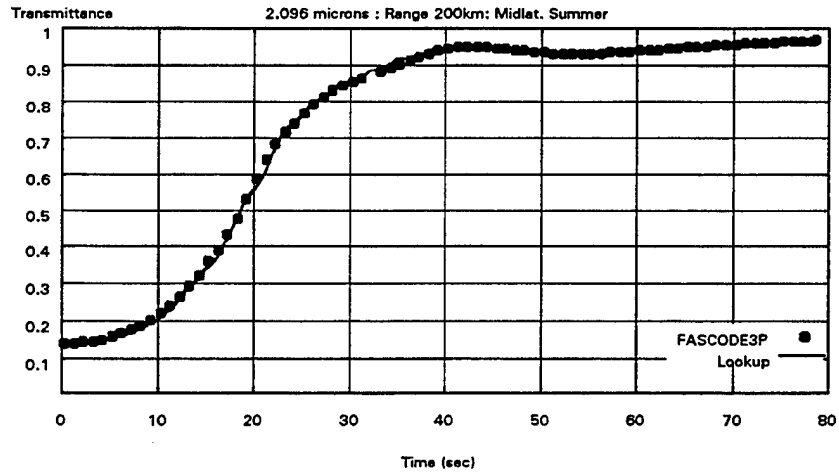
Figure 8. Transmission Comparison for 2.096 µm Laser Line

Transmittance   9.1145182 microns : Range 200km: Midlat. Summer

Time (sec)

Transmittance   9.1145182 microns : Range 400km: Midlat. Summer

Time (sec)

Transmittance   9.1145182 microns : Range 600km: Midlat. Summer

Time (sec)

247
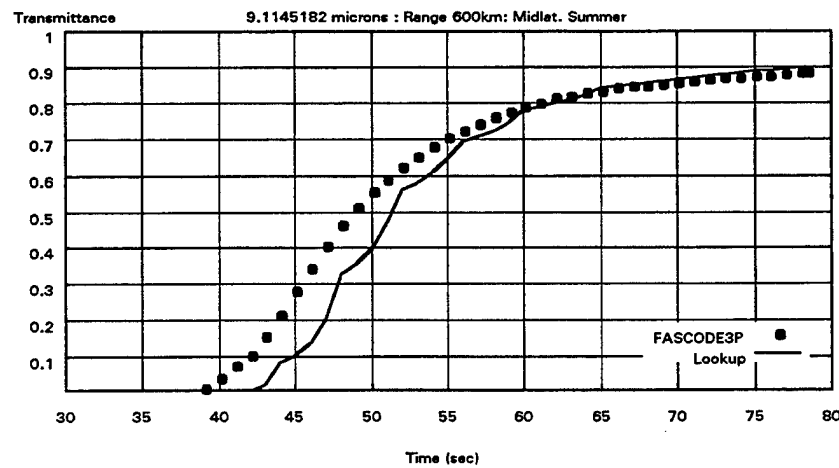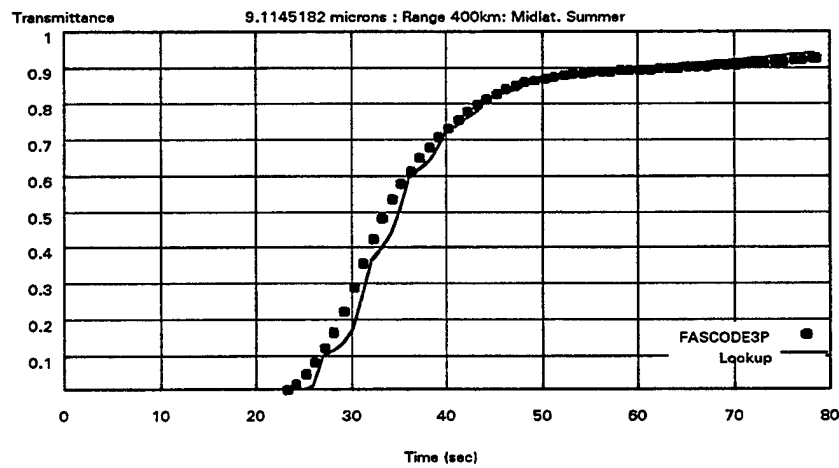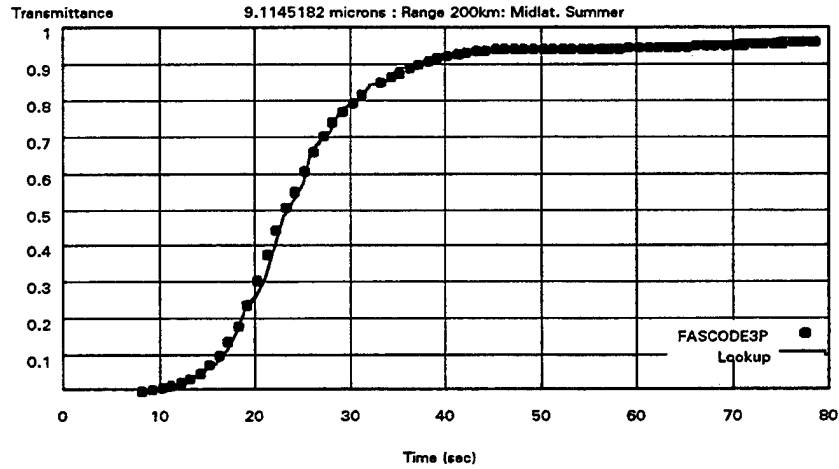
Figure 9. Transmission Comparison for 9.114 μm Laser Line

Time (sec)

Time (sec)
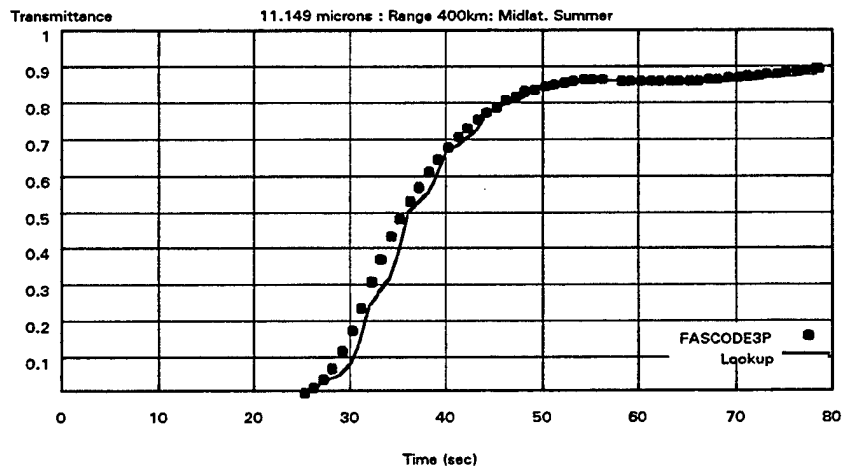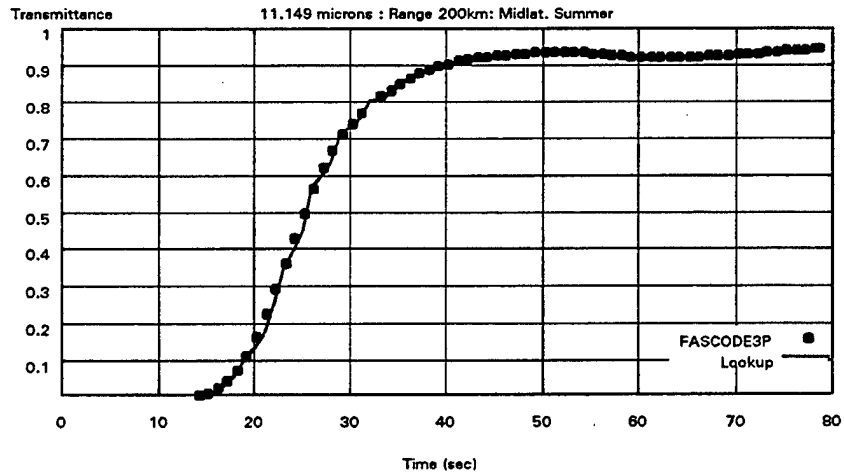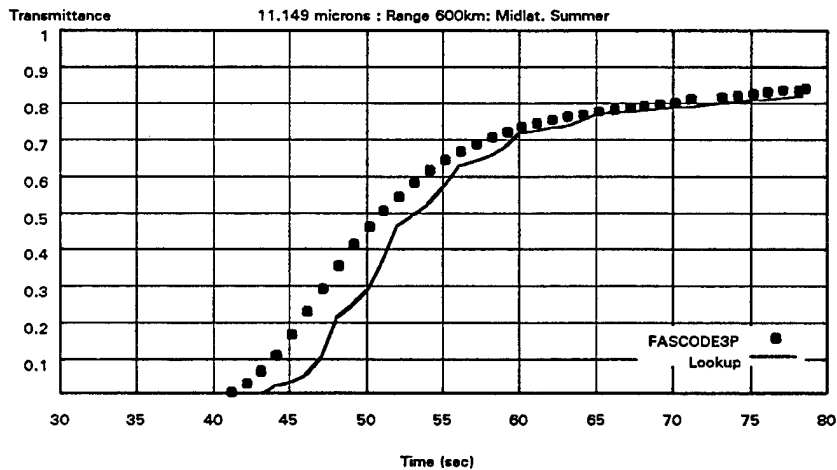
Figure 10. Transmission Comparison for 11.149 μm Laser Line

Summary and Conclusions:

A ray-trace extinction coefficient curved earth model is incorporated into LARC. This model can be implemented to solve real-time atmospheric transmission problems. The ray-trace model compares favorable to the FASCODE3P for the various laser lines. The extinction coefficient table method provides a fast method to analyze the atmospheric transmittance for large number of conditions. When more detailed analysis for a specific interesting situation is required, the use of the full execution of FASCODE3P should be used.

For the laser lines and geometry chosen for this analysis, the use of the extinction tables tended to underestimate the transmittance. This will result in a conservative estimate of the detection probability for a laser radar system. We are examining ways to improve the accuracy of the transmittance calculations for all of the laser lines of interest. Agreement can be improved by increasing the size of the table (corresponding to more atmospheric layers for each model atmosphere) or by using linear or exponential interpolation algorithms rather than the assumption of constant extinction coefficient per atmospheric layer. In addition a simplified approach to atmospheric refractivity can be incorporated.

249

High Accuracy Measurements of Small Variations in Atmospheric Transmittance Using a Laser Beam

Simon Kälin

1. Introduction

In a field experiment at Zurich airport, Switzerland, the Department of Geography at the Swiss Federal Institute of Technology Zurich is investigating the influence of aerosol particles on the atmospheric transmittance under various meteorological conditions within the boundary layer. The aim is to measure small variations of the horizontal atmospheric transmittance using a laser beam.

2. Design of a Laser Transmissometer

A He-Ne - laser, wavelength 543.5 nm, single order mode and an output power of 1.5 mW is used as radiation source. Measuring the aerosol extinction at a specific wavelength requires a careful consideration of overlapping absorption lines of other atmospheric constituents. The HITRAN database confirms that there is no important absorption line close to the laser wavelength used. Experiments with LOWTRAN have been done to estimate the influence of different aerosol models on the atmospheric transmittance at the laser wavelength used. Further calculations will be done using FASCODE.

The laser output power shows temporal fluctuations typically on the order of about 5 % during some hours of use. To allow precise transmittance measurements these fluctuations have to be controlled. The laser beam is therefore split up in two partial beams in a beam splitter. The first beam is used to measure atmospheric transmittance, the second beam is the reference beam to monitor laser amplitude fluctuations. Calculating the ratio of the two beams allows to calibrate the signal.

Using a single detector to measure both partial beams requires a little trick that allows to separate the signals in the instrument electronics. Two beam choppers are therefore used to modulate each of the beams with different frequencies. The lock - in amplifier uses the chopper frequencies to separate the signals.

Figure 1 shows the present state of the transmissometer.

Figure 1. Components of the laser transmissometer (not to scale). 1: Breadboard, 2: Power Supply, 3: He-Ne Laser, 4: High Frequency Chopper, 5: Mirror, 6: Polarizer, 7: Wave Plate, 8: Beam Splitter, 9: Low Frequency Chopper, 10: Lens, 11: Attenuator, 12: Beam Expander, 13: Transmitter resp. Reflector, 14: Probe Path, 15: Reflector, 16: Detector Housing, 17: Filter, 18: Scattering Disk, 19: Integration Chamber, 20: Si - Detector, 21: Chopper Unit, 22: Lock - In Amplifier, 23: Digitizing Unit, 24: Combiscope (Fluke), 25: IEEE - Network, 26: Controller, 27: Keyboard, 28: Screen, 29: Printer.
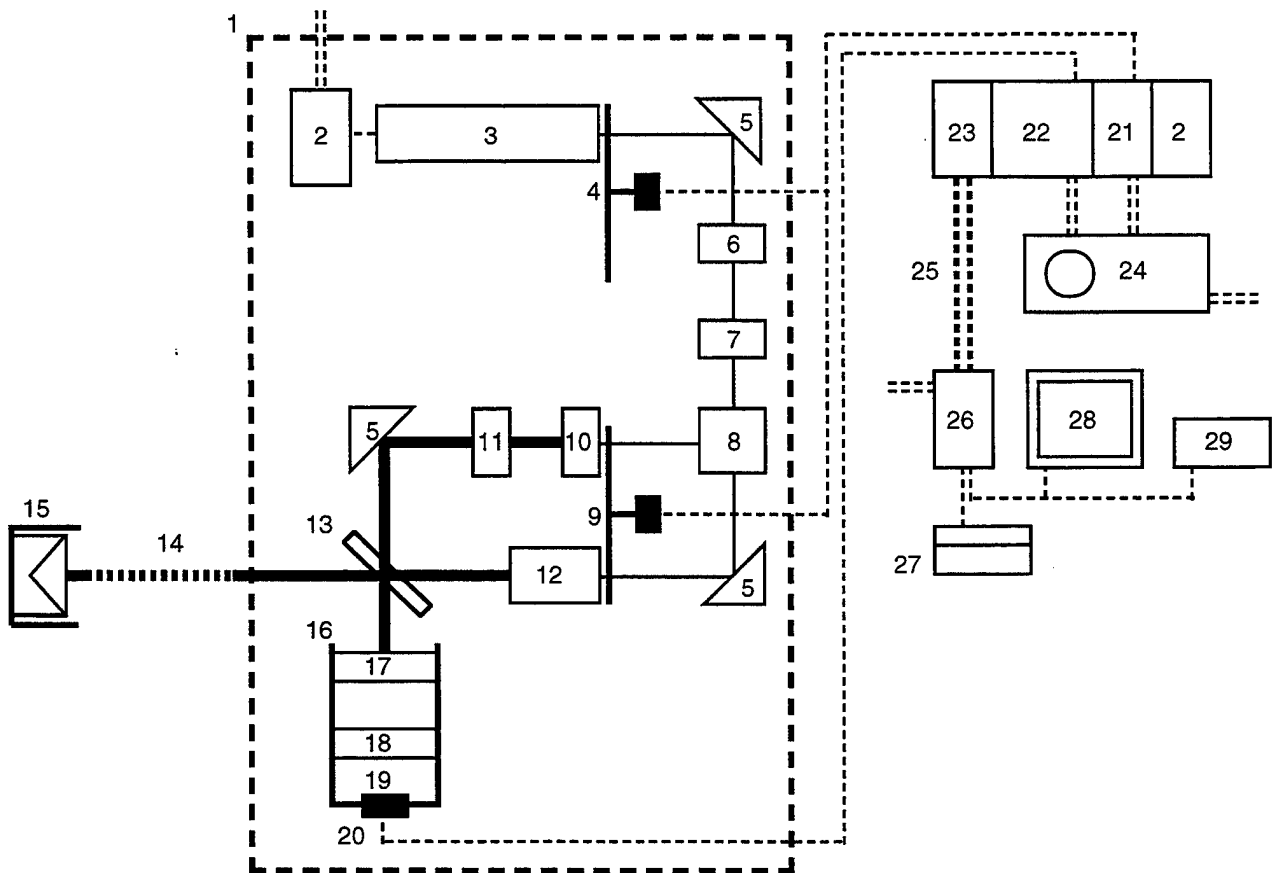
A reflector is used to minimize beam deflection and deformation due to atmospheric turbulence. The typical time constant of turbulence is much larger than the travelling time of the laser beam to the reflector and back. This allows to minimize beam disturbance.

The atmosphere destroys the laser coherence. The reference beam on the other hand conserves the coherence properties. A scattering disk destroys the remaining beam coherence and avoids interference effects on the detector surface that could lead to errors in the measurement. The scattered beams show a much broader intensitiy distribution. Measuring scattered radiation also reduces the

effects of small lateral beam displacements on the signal. Table 1 contains some basic information about the detector used. Figure 2 shows the detector responsivity as a function of the wavelength.

The response of a silicon detector is temperature dependent. During field measurements, the instrument optics and the detector are exposed to the daily temperature changes. Because the ratio of the two beams is used, temperature effects do not affect the measurements.

Table 1. Specifications of the silicon detector (Newport Instruments).

Model	818-SL, Newport Instruments
Material	Silicon
Active Area	1 cm ^{2}
Spectral Range	0.4 - 1.1 μm
Accuracy (const. Temp.)	0.4 - 1.0 μm: $\pm$ 2 %
Saturation Current	2 mA cm $^{-2}$
Responsivity	0.4 - 1.0 μm: $\geq$ 0.1 A W $^{-1}$
Peak Responsivity	0.88 μm: > 0.5 A W $^{-1}$
Risetime	$\leq$ 2 μsec
NEP	3 x 10 $^{-13}$ W ($\sqrt{\text{Hz}}$) $^{-1}$

Figure 2. Detector responsivity as a function of wavelength, for a temperature of 25 $\pm$ 0.5 $^\circ$ C (Newport Instruments).
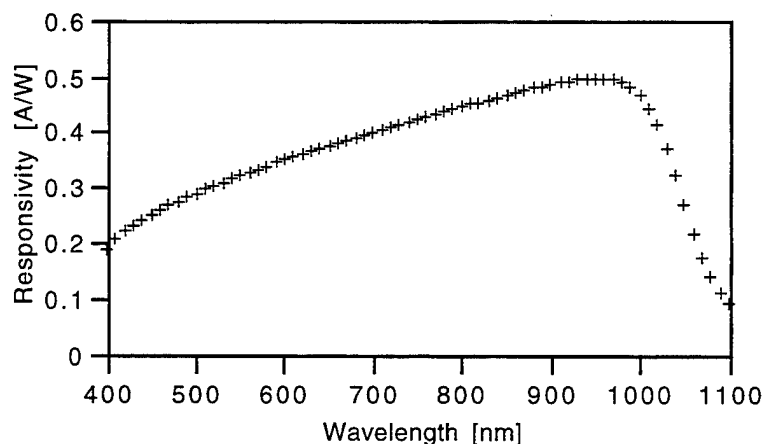
3. Field Measurements

The laser transmissometer is presently tested in the laboratory. Field measurements will be executed at Zurich airport. A large container will serve as a shelter for the electronic equipment and base for the experiment supervision. Several instruments will be used to measure optical properties, aerosol particles and meteorological parameters. Table 2 presents a list of these instruments.

Table 2. Instruments used during the field campaign at Zurich airport. Contributors: FWS (Flight Weather Service), SFIT (Swiss Federal Institute of Technology Zurich).

Parameter	Method	Instrument	Specifications	Contributor
Visual range and precipitation	Forward scattering	FD12P, Vaisala.	Visual range up to 50 km. Precipitation type, intensity and amount.	FWS
Precipitation and weather type	IR scattering	LEDWI (Light Emitting Diode Weather Identifier), OWI 240, ScTI.	Precipitation type, intensity and amount.	FWS
Spectral transmittance	Laser beam extinction	Developed at SFIT.	λ= 543.5 nm, P= 1.5 mW, TEM00.	SFIT
Aerosol number concentration distribution	Optical particle counter, Laser beam scattering.	LAS-X-CRT, PMS.	Size interval 0.1 - 7.5 μm diameter, 3 ranges with 15 channels each.	SFIT
Aerosol mass concentration distribution	Low - pressure cascade impactor	Berner impactor type LPI.	Size interval 0.06 - 16 μm, 8 size classes.	SFIT
Temperature	Sensor	YA-100, rotronic.	- 30 -> 70 °C	SFIT
Relative humidity	Sensor	YA-100, rotronic.	0 -> 100 % RH	SFIT

4. Outlook

Field experiments to test the laser transmissometer will be done until the end of the year. Using the different instruments involved in the field campaign will allow to build up an experimental database.

Model experiments will be performed to test the reliabilty and quality of the transmissometer measurements. Accurate description of aerosol forward scattering will play a keyrole in the numerical simulation of the experimental setup.

5. Acknowledgments

Analysis of Long Term Temperature Trends at the South Pole using MODTRAN3

W. G. Egan, Natural Sciences Department,

York College/City University of New York

Jamaica, NY 11451, E-Mail: EGAN@YCVAX.YORK.CUNY.EDU

and

A. W. Hogan, U. S. Army Cold Regions Research and Engineering

Laboratory, Hanover, NH 03755-1290

ABSTRACT

In published long term mean surface temperature trends at the South Pole 1958-1983, there is no annual variation; however, the Austral summer shows a temperature increase and the winter shows a decrease up to 1976. The variations are analyzed in terms of effects resulting from annual changes in aerosols, water vapor, carbon dioxide, methane and ozone with atmospheric profiles in MODTRAN3. Latent heat involved in cloud formation and dissipation is a vital input to the atmospheric temperature profiles particularly when clouds are modeled. Latent heat is not explicitly included in MODTRAN3, and must be added to accurately characterize atmospheric radiance.

INTRODUCTION

Figure 1 (Ref.1) shows the long term summer and winter mean surface temperatures at the South Pole from 1958 to 1983. Up to 1976, the Austral summers show an increasing temperature trend to 1976 and the winter temperatures show a decrease. Can these trends be caused by annual changes in water vapor, carbon dioxide, methane, or

ozone, or are they the result of natural circulation and air mass exchange over the polar plateau? We invoke the MODTRAN3 atmospheric modeling program to investigate the sensitivity of radiation to space as a function of water vapor and trace gases.

The input card to MODTRAN3 is card 5, which allows the use of selected atmospheric profiles (i.e. tropical, midlatitude summer and winter,subarctic summer and winter, and the 1976 US standard, as well as a new model atmosphere). There is no antarctic or arctic profile, and one would have to be read into the program. As a first approximation to investigate the model sensitivity to water vapor and carbon dioxide, we use the subarctic model;this model allows the variation of carbon dioxide from 330 ppm and the selection of water vapor profiles from the summer and winter subarctic to midlatitude winter into each to determine water vapor sensitivity. It is to be noted that atmospheric profiles are different between the arctic and antarctic, and further, the South Pole altitude is at 3 km.The South Pole is fundamentally warmed in the Austral spring by advection of warm air from lower latitudes.Fig.2 (Ref. 2)is a map of Antartica showing various monitoring stations;SPO is the South Pole, the ice shelves are shown stippled, and the transantarctic mountains are shown as circles. The advection of warm air enters the Polar Plateau from Elsworth land west of Mt.Howe. A warming event is shown in Fig. 3 (Ref. 1) along with aerosol concentration increase. The temperature increase is caused by the release of latent heat in precipitation; 5 to 15 cm of precipitation occur per year. One cm of precipitation causes a temperature increase of 17.4 degrees Centigrade in the lowest

kilometer above the pole.

RESULTS

The radiance to space may be computed for various models using MODTRAN3. Typical inputs to tape 5 and tape 6 are shown in Tables 1 and 2. The tape 6 outputs are summarized in Table 3.It is seen that a variation of 10 ppm has negligible effect on the Subarctic Summer and Subarctic Winter models; it is presumed that the other trace gases will correspondingly have negligible effect. However, water vapor has a significant effect.Thus, in the 3 spring months (Nov/Dec/Jan), the differential summer warming between the normal subarctic summer water vapor and an increase to midlatitude water vapor will cause a 0.46 degree Centigrade warming for a 10 km height.(refer to Table 3). The differential cooling in the winter is about the same as that of summer. We infer that the long term trend is caused by a change in water vapor: a slight increase in summer. The reverse trend in temperatures following 1976 is suggested as the result of satation move.

In this preliminary report, we have not considered the details of an Antarctic profile, nor the result of latent heat on the surface atmospheric layer above the South Pole;nor have we considered refractive effects (mirages) caused by th warm surface layer.

REFERENCES

1. A. Hogan, D. Riley, B. B. Murphey, S. C. Barnard, & J. A. Samson,"Variation in Aersol Concentration Associated with a Polar Climatic Iteration", Antartic Res. Ser. 61,175-199,1993.

2. A. W. Hogan, "A Synthesis of Warm Air Advection to the South Polar Plateau", unpublished manuscript.
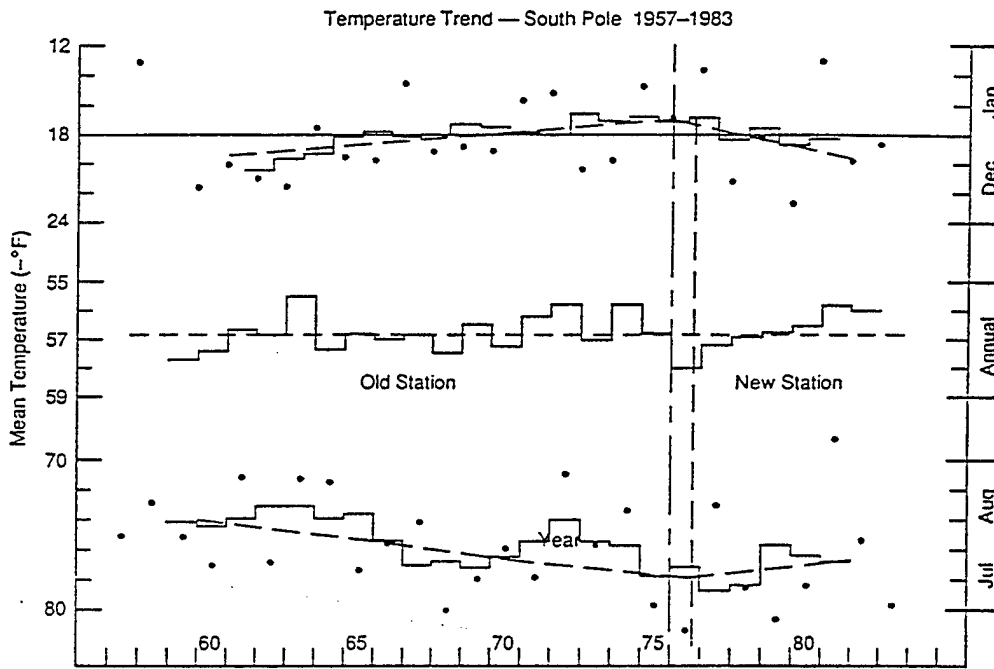
Fig. 1 Surface temperatures measured at the south pole, 1957–1983, in negative degrees Fahrenheit. Summer (December–January) and midwinter (July–August) temperatures are plotted with large dots, with plotted lines indicating the middle-year value of the 5-year running mean temperature. Mean calendar year temperatures are plotted in the center, with a dashed line indicating the 1958–1983 mean temperature. The dashed vertical lines indicate the relocation of the station in December 1974 and the observer change (NWS to New Zealand Meteorological Service) in 1976.
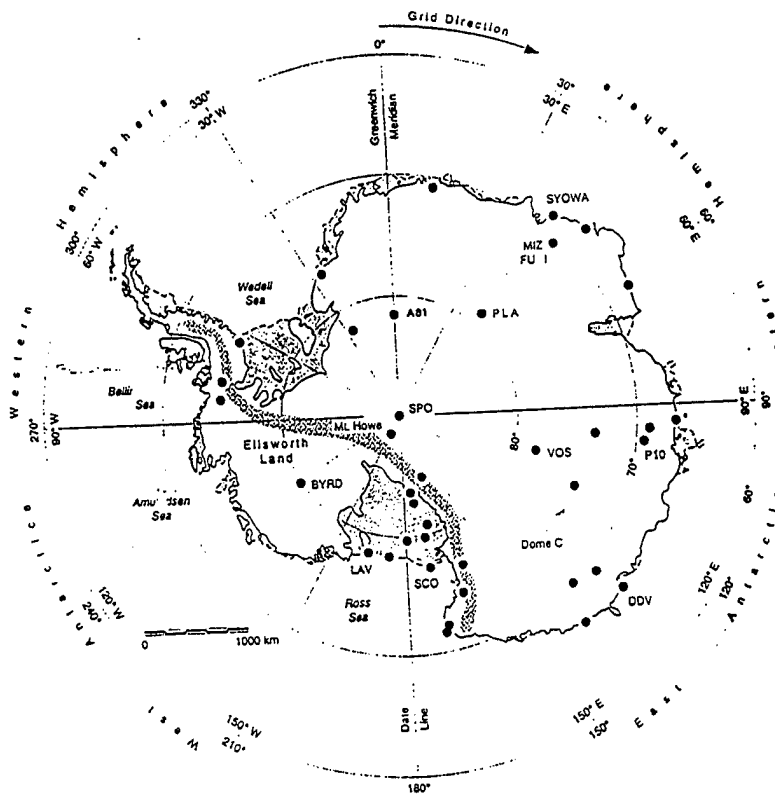
Fig.2 Map of Antarctica; Transantarctic Mountain Range shown symbolically; the ice shelves are shown stippled

258
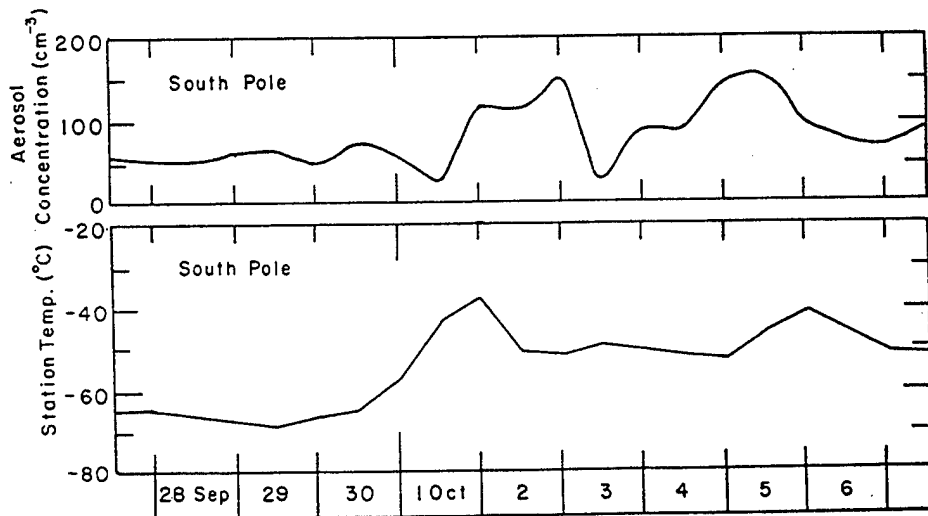
Fig. 3 Air temperatures and aerosol concentration observed on the Antarctic plateau September 27 through October 6, 1987.

```
                                              ; TAPE5
°T   4    3    1    0    0    3    0    0    0    0    0    0    0    .00    .0
°F   0F   0    0.                                                         —
°    0    0    0    0    0    0    0.000    0.000    0.000    0.000        —
°      0.0         0.0         0.                                         —
°        500        1250         5                                        —
°      0                                                                  —
°                                                                         —
°                                                                         —
°                                                                         —
```

Table 1

```
                                        . TAPE6
°1                    *****   MODTRAN   *****
°0  CARD 1  *****T   4    3    1    0    0    3    0    0    0    0    0    0    —
°0  CARD 2  *****    0    0    0    0    0    0    0.000    0.000    0.000      —
°0  CARD 3  *****    0.000      0.000      0.000    0.000    0.000    0.000    —
°0  CARD 4  *****      500       1250         5       0                       —
°0  PROGRAM WILL COMPUTE RADIANCE                                             —
°0  ATMOSPHERIC MODEL                                                         —
°          TEMPERATURE =    4    SUBARCTIC   SUMMER                           —
°          WATER VAPOR =    3    MIDLATITUDE WINTER                           —
°          OZONE       =    4    SUBARCTIC   SUMMER                           —
°                    M4 =    4  M5 =    4  M6 =    4  MDEF =    1              —
°0  SLANT PATH TO SPACE                                                       —
°          H1    =    0.000 KM                                                —
°          HMIN  =    0.000 KM                                                —
°          ANGLE =    0.000 DEG                                               —
°0  FREQUENCY RANGE                                                           —
°          IV1  =       500 CM-1  (    20.00 MICROMETERS)                     —
°          IV2  =      1250 CM-1  (     8.00 MICROMETERS)                      —
°          IDV  =         5 CM-1                                              —
°          IFWHM =        2 CM-1
°1
```

Table 2

259

TABLE 3
Summary of Tape 6 Output

Season	CO_2 ppm	Integrated Radiance W/cm/sr	Integrated Absorption cm^{-1}	Average Transmittance	Sea Level H_2O Atm.cm	$T_{surface}$
Subarctic Summer	330	4.212E-3	417.85	0.4429	2.587E+3	287.2
Subarctic Summer	340	4.236E-3	418.12	0.4425	2.587E+3	287.2
Subarctic Winter	330	2.071E-3	287.69	0.6138	5.173E+2	257.2
Subarctic Winter	340	2.075E-3	290.18	0.6131	5.173E+2	257.2
Subarctic Winter) Midlatitude) Winter H_2O)	330	2.386E-3	333.19	0.5557	1.085E+3	257.2
Subarctic Summer) Midlatitude .) Winter H_2O)	330	3.449E-3	337.54	0.5500	1.017E+3	287.2

HIGH RESOLUTION CROSS SECTION MEASUREMENTS OF NO$_2$

W.H. Parkinson, J.R. Esmond, and K. Yoshino

Harvard Smithsonian Center for Astrophysics, Cambridge, MA 02138, U.S.A.

Cross section measurements of NO$_2$ at 295 K have been obtained in the wavelength region 360 nm to 470 nm. We used the 6.65-m vacuum spectrometer with a 1200 l/mm grating, which gives 1.24 Å/mm dispersion. A tungsten lamp, operating at 12 V ac, was used as the background source. Data were taken every 0.118 sec for every 15 mÅ (0.074 cm^{-1}). In each scan range, we ran an Fe hollow cathode spectrum for wavelength calibration. The accuracy of wavelength position was 0.02 Å. The pressures of NO$_2$ were selected as 0.5, 1.0, 1.5, 2.0, 2.5, and 3.0 Torr. The cross section measurements at the beginning wavelengths show a slight but definite negative pressure dependency, because of dimer formation. As a result, we could estimate the range of dimer density of 0.5% at 0.5 Torr to 2.5% at 3 Torr. After the column density of NO$_2$ was calibrated, we obtained cross sections of NO$_2$ for all runs at all pressures. We will present the cross section values of NO$_2$, and compare them with previous results.

Experimental Conditions

Spectrometer: 6.65-m McPherson Spectrometer

Spectrometer Bandwidths: 0.0050 nm and 0.0025 nm (H)

Interval between datum points: 0.0015 nm and 0.0003 nm (H)

Period for accumulating counts: 0.118 s and 0.141 s (H)

Wavelength region: 359 nm to 470 nm

Optical Path Length: 42.3 cm

Pressure: 0.5, 1.0, 1.5, 2.0, 2.5 and 3.0 Torr

Temperature: 295K
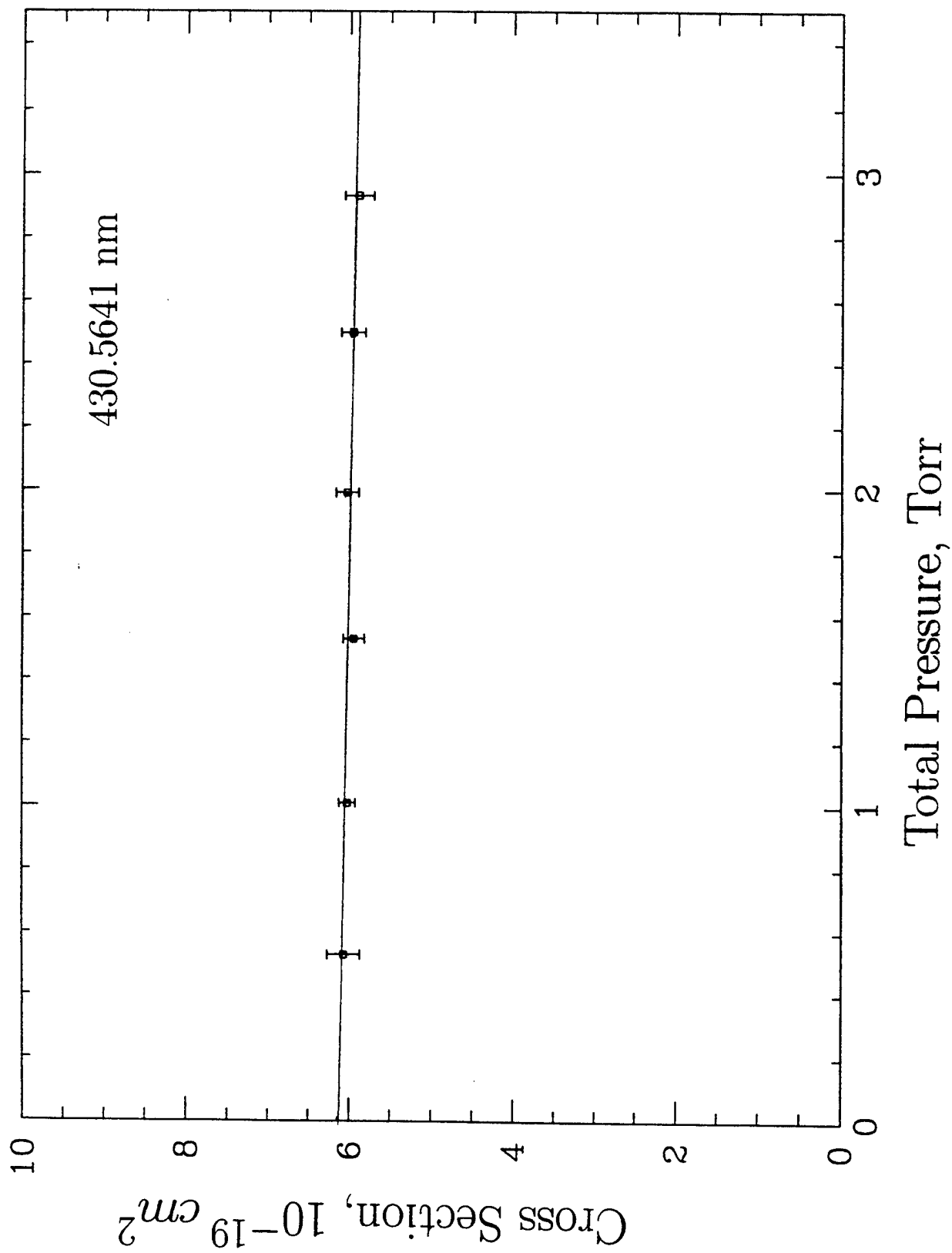
Cross Section, $10^{-19} cm^2$ vs Total Pressure, Torr
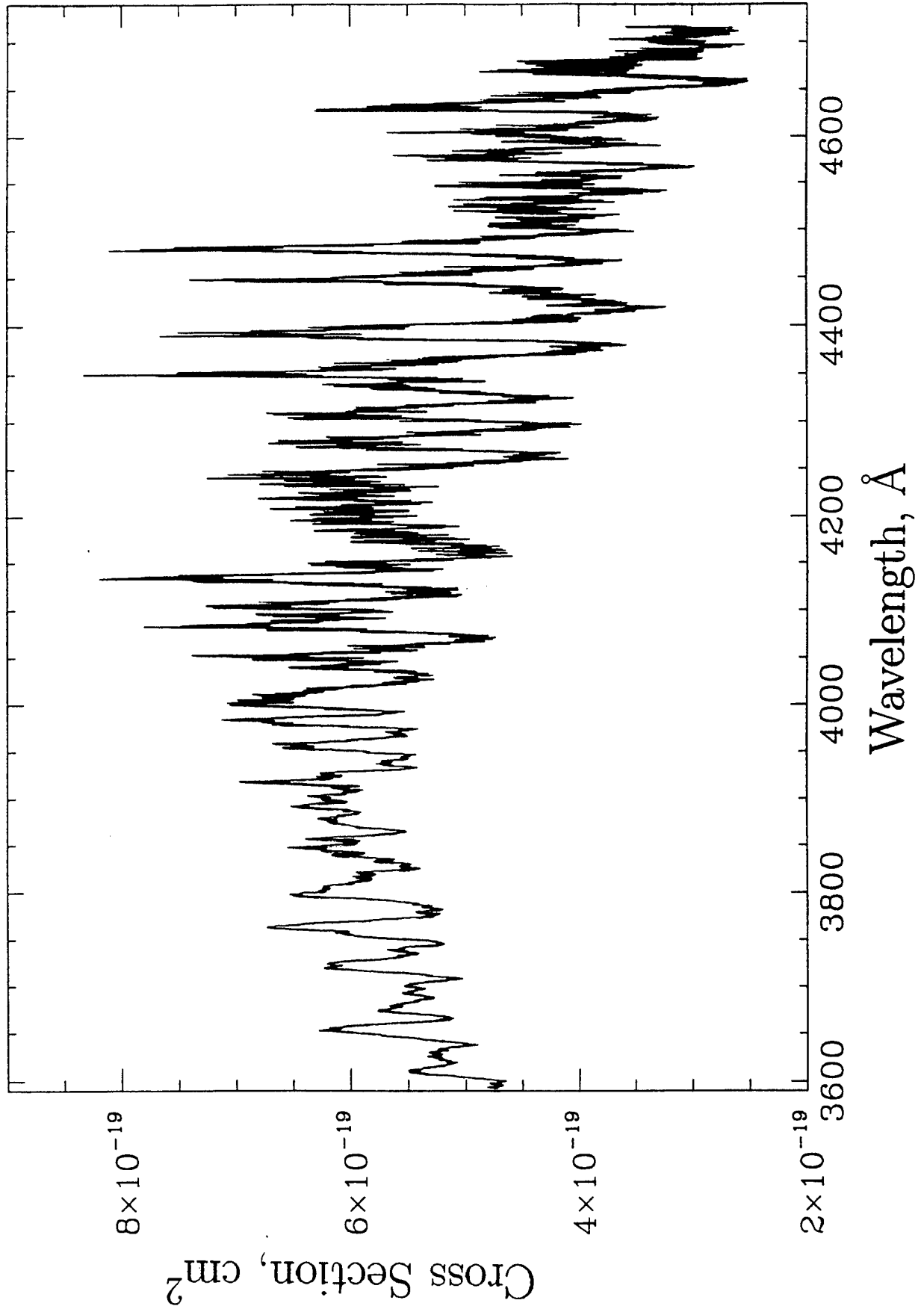
430.5641 nm

Cross Sections of NO$_2$, CfA

Wavelength, Å

Cross Section, cm^2

Radiative Forcing Calculations for CH_3Cl and CH_3Br

Allen S. Grossman
Keith E. Grant
Global Climate Research Division, L-262
Lawrence Livermore National Laboratory
P.O. 808, Livermore, CA 94551

William E. Blass
Dept. of Physics and Astronomy
University of Tennessee
Knoxville, TN 37996-1200

Donald J. Wuebbles
Dept. of Atmospheric Sciences
University of Illinois
Urbana, Il 61801

June 1996

Abstract

Methyl chloride, CH_3Cl, and methyl bromide, CH_3Br, are particularly important in the global atmosphere as major natural sources of chlorine and bromine to the stratosphere. The production of of these gases is dominated by natural sources, but smaller anthropogenic sources, such as agricultural fumigation and/or biomass burning also exist. Production has a seasonal cycle which couples with the short lifetime of tropospheric CH_3Cl and CH_3Br to produce nonuniform global mixing. As an absorber of infrared radiation, these gases are of interest for their potential effect on the tropospheric energy balance as well as for chemical interactions. In this study, we estimate the radiative forcing and Global Warming Potentials (GWPs) of CH_3Cl and CH_3Br. Our calculations use an infrared radiative transfer model based on the correlated k-distribution algorithm for band absorption. Using realistic altitude distributions, radiative forcing values of 0.0047 W/m^2 per ppbv for CH_3Cl in the troposphere and 0.0049 W/m^2 per ppbv for CH_3Br in the troposphere were obtained. These values are approximately linearly dependent on the background abundance. The radiative forcing values are about 2 percent of the forcing of CFC-11 and about 270 times the forcing of CO_2, on a per molecule basis. The Global Warming Potentials of CH_3Cl and CH_3Br were determined giving GWPs of about 8 for CH_3Cl and about 4 for CH_3Br for a time

integration of 100 years ($CO_2 = 1$). These results indicate that while CH_3Cl and CH_3Br have direct GWPs similar to that of CH_4, the current emission rates are too low to meaningfully contribute to atmospheric greenhouse heating effects.

I. Introduction

Methyl chloride (CH_3Cl) and methyl bromide (CH_3Br) are important gases in the Earth's atmosphere as major sources of stratospheric chlorine and bromine, respectively. Both are also greenhouse gases. However, there are no published attempts to determine their radiative forcing on climate relative to other gases.

Methyl chloride is the major natural source of stratospheric chlorine (WMO, 1985, 1991). CH_3Cl accounts for roughly 15 percent of the total chlorine content in the current stratosphere, with the rest coming from chlorofluorocarbons (such as $CFCl_3$ and CF_2Cl_2) and other human produced halocarbons. Atmospheric mixing ratios of CH_3Cl in the troposphere are approximately 600 pptv (parts per trillion by volume). Observations (Rasmussen et al., 1980; Singh et al., 1983; WMO, 1985, 1991; Kaye et al., 1994) do not show obvious temporal trends, with the exception of an annual cycle that is presumably related to the primary removal process by reaction of CH_3Cl with hydroxyl radicals (OH) (WMO, 1991). The atmospheric lifetime of CH_3Cl is about 1.5 years based on its reaction with hydroxyl (Prather and Spivakovsky, 1990; WMO, 1991, 1994). Primary sources of CH_3Cl are biological production and biomass burning; these sources seem to far outweigh industrial and other human related sources although quantification of the major sources is highly uncertain (Logan et al., 1981; Crutzen et al., 1983; WMO, 1985, 1991). CH_3Cl has strong infrared absorption bands at 732, 1015, 1355, 1455, 2879 and 3042 cm^{-1} (Elkins et al., 1984). As a result of these strong absorption bands the potential exists (if concentrations were to increase) for possible, anthropogenically based, greenhouse heating of the atmosphere that could result in climate changes. The line by line data in the HITRAN 91 database (Rothman et al., 1991) and the spectroscopic line data of Brown (1994) are used in this study.

Methyl bromide is the major source of bromine in the current stratosphere and the primary organabromine species in the lower atmosphere (Kaye et al., 1994; WMO, 1994). Tropospheric concentrations of CH_3Br are 11-12 pptv in the

Northern Hemisphere and 8-10 pptv in the Southern Hemisphere (Blake et al., 1993; Khalil et al., 1993; WMO, 1994). While the hemispheric differences are real, a large part of the other variations [as well as differences from earlier measurements with even larger concentrations (e.g., from Singh et al., 1983 and Penkett et al., 1985)] are presumably due to uncertainties in calibration standards (WMO, 1994). The higher Northern Hemisphere concentrations appear to correspond to the importance of human related sources in that hemisphere. The measurements of Khalil et al. (1993) show a positive trend in CH_3Br concentrations of 0.3 ($\pm$ 0.1) pptv/year. The oceans are a major natural source of CH_3Br (Singh et al., 1983; Singh and Kanakidou, 1993; Khalil et al., 1993; WMO, 1994). As discussed below, the oceans are also a sink for CH_3Br. Whether the oceans are a net source or sink of CH_3Br is yet uncertain, but the best available estimates for the gross production rate is about 90 Gg/yr with an uncertainty range of 60-160 (WMO, 1994). Biomass burning is both a natural and an anthropogenic source of CH_3Br contributing about 30 (10-50) Gg/yr, with about 5 Gg/yr due to natural production (WMO, 1994). The use of CH_3Br for agricultural purposes as a fumigant is well recognized, with about 50 percent of the CH_3Br used for these purposes escaping into the atmosphere (WMO, 1994). Total emission from this human related source is about 35 Gg/yr (in 1991-1992 according to WMO, 1994) with a range of 20-60 Gg/yr. Other more minor uses and sources of atmospheric CH_3Br result from gasoline additives, from industrial processes, and from structural purposes. Current estimates of the budget (WMO, 1994) indicate that at least 40 percent of the atmospheric emission of CH_3Br is due to human related sources. As with CH_3Cl, the major removal process for CH_3Br from the atmosphere is reaction with hydroxyl. However, the oceans are also an important sink of CH_3Br (Butler, 1994; WMO, 1994). There is also some indication (Oremland et al., 1994) of CH_3Br degradation in salt marsh sediments. The resulting net atmospheric lifetime of CH_3Br is about 1.3 years (range: 0.8 - 1.7 years), while the identified atmospheric removal processes alone would have given a lifetime of approximately 2 years (WMO, 1994). CH_3Br, like CH_3Cl, has strong absorption bands in the infrared located at 2972, 1305, 611, 3056, 1445, and 952 cm^{-1} (Graner, 1982), thus raising the possibility of its importance for greenhouse heating of the atmosphere.

The mechanism usually used for comparison of the greenhouse potential of trace gases is the Global Warming Potential or GWP as defined by IPCC (1990, 1994). The GWP is the ratio of the time integrated radiative flux change at the tropopause caused by the introduction of a unit mass impulse of a trace gas into the atmosphere relative to the time integrated radiative flux change at the tropopause caused by the introduction of a unit mass impulse of CO_2. An essential part of the GWP determination is the calculation of the radiative forcing, which is defined as the radiative flux change at the tropopause produced by a unit change in the number of molecules of a particular gas with all other abundances held constant. Usually the amount of abundance change used in a radiative forcing calculation is chosen such that the change is just enough to produce a numerically significant flux change value at the tropopause. Parameterized experiments for radiative forcing have been published, for example, in IPCC (1990, 1992, 1994), and by Ramanathan et. al. (1987). A detailed radiative transfer model is required in order to calculate the radiative forcing for the GWP determination. In this study, we used a correlated k-distribution model for the absorption by the major atmospheric molecular absorption species (H_2O, CO_2, O_3, CH_4, and N_2O) to calculate the fluxes in the 0–2500 cm^{-1} wavenumber range [Grant et al. (1992, "GGFP") and Grossman and Grant (1994a,b)]. The main purpose of this paper is to calculate the tropospheric radiative forcing of CH_3Br and CH_3Cl using the correlated k-distribution radiative transfer model in conjunction with the spectroscopic line data in the HITRAN91 data base (Rothman et al., 1991) and the spectroscopic line data of Brown (1994) for CH_3Cl, and a set of line data for CH_3Br, to be discussed below, developed for this paper. The calculation will be done for a globally and annually averaged model atmosphere with a representative cloud distribution. GWP calculations for CH_3Cl and CH_3Br will be made and compared to other trace gas GWPs given in IPCC (1992, 1994).

II. Correlated K-Distribution Radiative Transfer Model

The correlated k-distribution method utilizes a mapping of the absorption coefficient vs. wavenumber relation into an absorption coefficient vs. probability relation within a particular wavenumber interval. The probability variable g(k), the cumulative distribution function, is defined as

$$g(k) = \int_0^k f(k') \, dk' \quad , \qquad (1)$$

where f(k')dk' is the fraction of the frequency interval occupied by absorption coefficients between k' and k'+dk'(Goody and Jung, 1989, "G1"; Goody et al., 1989, "G2"; and West et al., 1990, "W1"). The limits of g(k) range between 0 and 1 within the frequency interval. The inverse of Equation 1, k(g), the k-distribution, has been shown by G2, and W1 to be a monotonic function across the frequency interval for a particular atmospheric layer. The correlated k-distribution method can mathematically provide an exact procedure for calculating the transmission, fluxes, and heating rates in a homogeneous atmosphere. For the case of inhomogeneous atmospheric paths the method is, in practice, inherently inexact since somewhat different sets of frequencies will associate with a given ordering of the k terms as the pressure and temperature vary over the path. Numerous tests of the model for various atmospheric trace gases and atmospheric temperature-pressure profiles, Lacis and Oinas (1991), Grossman and Grant (1992, 1994a,b), and Grossman et al. (1993), show that the method produces fluxes that are accurate to well within ten percent when compared to line by line calculations.

The calculation of the transmission can be expressed in the three physically equivalent forms:

$$T(u) = 1 \, / \, \Delta v \int_{\Delta v} \exp\left(-k_v u\right) dv \quad ,$$

$$= \int_0^\infty f(k') \exp(-k' u) dk' \quad , \qquad (2)$$

$$= \int_0^1 \exp\left(-k(g) u\right) dg \quad ,$$

where u is the absorber column density. Using the k-distribution form, the calculation can be performed with far fewer k-g points than the same calculation using k-wn (wavenumber) points.

The direct calculation of the molecular k-distributions contains the following steps (GGFP). First the HITRAN database (Rothman et. al., 1991) is utilized to determine the line transitions and physical properties of the selected lines (H_2O, CO_2, O_3, CH_4, N_2O and CH_3Cl). These line properties are merged with the line properties of

CH3Cl provided in the database of Brown (1994, private communication) to give a complete set of CH_3Cl lines. For CH_3Br a set of line data, discussed below, has been prepared for this paper. This line data is also merged with the HITRAN line data for the other species. Second, a modified version of the FASCODE2 code (Clough et. al., 1986) is used to calculate a finely gridded set of monochromatic absorption coefficients, with full allowance for the overlap of neighboring lines, for each layer in the atmosphere. Third, a sorting code, ABSORT, is used to calculate the f(k), g(k), and k(g) functions for each homogeneous layer. The modified FASCODE program takes the line data and fits an absorption line profile (Voigt profile) to each line and calculates the absorption coefficient k (cm^2/air mol) as a function of wavenumber. The normal cutoff point in the line profile is set at 25 cm^{-1} from line center. This is done for reasons of economy (beyond 25 cm^{-1} a given line contributes little absorption). The ABSORT code takes the absorption coefficient files generated by the FASCODE program and sorts the absorption coefficients into bins of equal logarithmic width, $\Delta \log k$, to produce a distribution function, f(k), based on the relative probability of occurence within the wave number interval (proportional to the number of entries in each bin). The cumulative distribution function, g(k) (c.f. Equation 1), is obtained by numerical integration of the f(k) function. The k-distribution, k(g), is obtained by a reverse interpolation of the g(k) relation using a spline function. For the calculations in this paper a 401 bin model was used to insure an adequate number of points at g values between 0.9 and 1.0. This g value region is important for heating rate calculations at high altitudes. The output from ABSORT is the 401 point k(g) relation for each layer. At low pressures the k(g) curves can show opacity variations of up to five orders of magnitude at g values greater than ~0.9. This kind of behavior at low pressures is thought to be due to the absence of pressure broadening on the absorption lines in the wave number band; i.e. the lines are dominated by doppler broadening near line center. These variations in the k-distributions require a careful numerical integration strategy in the transmission expression, Equation 2, in order to accurately reproduce the k(g) functions. The integration strategy which was adopted after test calculations was an 85 point variable spaced trapezoidal model with g spacings of 0.0025 for g values between 0.9 and 1.0 and larger g spacings at lower g values.

III. CH3Cl Data

Inspection of the HITRAN91 database reveals that only the lines of the ν_1, ν_4, and $3\nu_6$ bands of CH3Cl between 2907 and 3173 cm^{-1} have been included in the compilation. According to Elkins et al. (1984) the strength of these bands represent approximately 40 percent of the total line strength of all CH3Cl bands. Furthermore the contributions from the lines in this spectral region to the total radiative forcing should be small due to consideration of the small values of the upward IR fluxes compared to those in the other important spectral regions. A database for the properties of the CH3Cl lines in the ν_2, ν_3, and ν_5 bands has been developed by Brown (1994, private communication) and Brown et al. (1987) in the wavenumber regions 661 to 772 cm^{-1} (ν_3,) and 1261 to 1646 cm^{-1} (ν_2, ν_5). This is an IR window region and thus these bands should contribute the majority of the CH3Cl radiative forcing. According to Elkins et al. (1984) the ν_2, ν_3, and ν_5 bands represent approximately 55 percent of the total line strength of the CH3Cl bands. The ν_6 band at 1015 cm^{-1} is not presently tabulated on any database and cannot be included in the radiative forcing calculation. The effect of the ν_6 band omission would be on the order of 5 percent. The combined strength of the ν_2, ν_3, and ν_5 bands should be approximately 1.34 times the combined strength of the ν_1, ν_4, and $3\nu_6$ bands, Elkins et al. (1984). The ratio of the combined line strength of the ν_2, ν_3, and ν_5 bands Brown (1994) to the combined line strength of the ν_1, ν_4, and $3\nu_6$ bands in the HITRAN91 data base is 3.92, indicating that the HITRAN line strengths may be too low by a factor of 2.92. Both the Brown (1994) and the HITRAN91 batabases were numerically merged in the calculation of the k-distributions outlined in GGFP (1992) in order to calculate the complete radiative forcing of CH3Cl.

IV. CH3Br DATA

Methyl bromide has six fundamental vibration-rotation bands, ν_1 through ν_6 found at 2972, 1305, 611, 3056, 1445, and 952 cm^{-1} respectively (Graner, 1982). Graner (1982) summarizes and interprets all of the significant laboratory studies and analysis in a comprehensive review. Antilla et al. (1983) extended and improved upon the Graner (1982) and Graner and Blass (1975) analyses of ν_2 and ν_5 in a comprehensive laboratory study. The molecular parameters of Antilla et al. were used to model the ν_2 and ν_5 spectra in this work. For ν_3, and ν_6, the molecular parameters given by Graner (1982) as the best available parameters reduced from existing laboratory data were used in modeling the spectra. No attempt was made to model and use data from the ν_1 and ν_4 bands near 3000 cm^{-1}. The ν_4 band contributes only 7 percent of the fundamental intensity according to van Straten and Smit (1977), while the ν_1 and $2\nu_5$ bands are highly perturbed and not readily amenable to accurate modeling. These two bands contribute 28 percent of the fundamental intensity but were considered less consequential due to the position of the bands in the 3000 cm^{-1} region.

The methyl bromide rotation-vibration line spectra were modeled using a well tested Coriolis resonance and l-doubling (and l-resonance) computational system called PERTCOR. A discussion of PERTCOR modeling can be found in the literature (Daunt, et al., 1984). The model Hamiltonian is consistent with that of Antilla et al. (1983) and is discussed at length in Daunt et al., (1984) as well as by Blass (1987). The ν_2 and ν_5 bands were constructed using the molecular parameters of Antilla et al. (1983) including the effects of the Coriolis resonance, l-doubling and l-resonance. The PERTCOR program carries out a straight forward computational quantum mechanics calculation. The vibration-rotation Hamiltonian in the rigid rotor, harmonic oscillator basis set can be ordered so as to be block diagonal so that only order 3 subblocks of the entire Hamiltonian need to be diagonalized. The parameter set and Hamiltonian matrix elements of Antilla et al. (1983) are used in the calculation of the Hamiltonian. Further references regarding details of the Hamiltonian and its development are referenced in Blass (1987). The calculation includes the effects due to accidental and essential resonances for the first order Coriolis resonance, l-resonance, and l-doubling (Graner, (1982), Blass, (1987)). The calculated rotation-vibration energy is accurate through fourth order in the twice transformed Hamiltonian (approximately ±0.001 cm^{-1} or better). The computational system generates relative intensities taking the resonances into account. The dipole moment derivative ratio was retrieved from van Straten and Smit (1977). The calculated transitions were compared to the observed transitions of Antilla et al. (1983). Agreement was on the order of ± 1.0 mcm^{-1} (milli wavenumber) which was considered satisfactory for this work. That is to say, that the modeled line spectrum agreed with the published

observations of Antilla et al. (1983) for all samples inspected. The modeled spectrum included all allowed transitions of consequent intensity whereas the laboratory data, while extensive, was not complete in this sense. The calculations were carried out for maximum J (total angular momentum quantum number) and K (angular momentum quantum number of projection on the principal symmetry axis) values of 50 insuring inclusion of transitions with intensities greater than 10^{-25} cm^{-1}/(mol · cm^2). Separate calculations were carried out for the two isotopic modifications of methyl bromide. Integrated absolute intensities were normalized to the isotopically apportioned absolute band intensities of van Straten and Smit (1977). Measured band strengths (van Straten and Smit, 1977) were apportioned 0.505 to ^{79}Br and 0.485 to ^{81}Br. A similar set of calculations produced the ν_3 and ν_6 transition frequencies and intensities. The molecular parameters used for ν_3 and ν_6 are those collected in the review paper by Graner (1982). In this case no resonance parameters were included since none are available. As in the case of ν_2 and ν_5 both isotopic variations of methyl bromide were treated separately and the intensity normalization was carried out in the same way. For comparison purposes, the integrated fundamental band intensity for CH$_3$Br is approximately 1.19 x 10^{-17} cm^{-1}/(mol · cm^2) compared to approximately 1.35 x 10^{-17} cm^{-1}/(mol · cm^2) for CH$_3$Cl (Smith et al., 1985). Figure 1 displays the intensity distribution of the 31,155 methyl bromide rotation vibration transitions used in this study. The transition's absolute intensity was binned in 1 cm^{-1} bins and plotted. The intensity scale is in cm^{-1}/(mol · cm^2).

V. Parameters of The Calculations

Flux and radiative forcing calculations were made for a globally and seasonally averaged model atmosphere (Wuebbles et al., 1994), corresponding to roughly 1990. The mixing ratio vs. altitude profiles for H$_2$O, O$_3$ and CH$_4$ are shown in Figure 2. CO$_2$ was assumed to have a mixing ratio of 350 ppmv, constant with altitude. N$_2$O was assumed to have a mixing ratio of ~0.3 ppmv in the troposphere and then decrease to a mixing ratio of ~1.2 ppbv at 60 km altitude, bases on atmospheric observations at midlatitudes. The temperature-pressure profile for model atmosphere is shown in Figure 3. The tropopause in the globally-averaged atmosphere is specified as the altitude at which the temperature gradient in the troposphere decreases to

less than 2K/km. This occurs at a pressure of 166 mb (~13.2 km). Altitude resolution in the model atmosphere was 1 km at altitudes between 0 and 20 km, and 2 km at altitudes between 20 and 60 km. The ground temperature was 291 K. The clear sky radiative transfer model outlined in GGFP was modified to accept a cloud distribution model using an algorithm based on Harshvardhan et al. (1987). In this algorithm the transmission between atmospheric layers is multiplied by the probability of a clear line of sight between the layers. The clouds are considered to be radiatively black at the thermal wavelengths. For the case of random overlap of the cloud layers, which is the case adopted in this paper, the probability of a clear line of sight between two layers i and j is given as,

$$C_{ij} = (1-N_{j-1})(1-N_{j-2}).....(1-N_i) \quad , \qquad (3)$$

where the N's represent the fractional cloud cover of the particular layers. The transmission is then given as,

$$T_{ij} = T_{clr}C_{ij} \qquad , \qquad (4)$$

where T_{clr} is the clear sky transmission. The cloud distribution in the globally averaged atmosphere consists of three layers, each 1km thick, with bases at 2 km (low), 4 km (middle), and 10 km (high). Fractional cloud cover amounts are 0.31 (low), 0.09 (middle), and 0.17 (high). The radiative transfer calculations to determine the tropospheric radiative forcing were carried out over the wavenumber range of 500 - 3000 cm^{-1}, in 25 cm^{-1} subintervals. In addition to CH$_3$Cl and CH$_3$Br absorption, absorption due to H$_2$O, CO$_2$, O$_3$, CH$_4$, and N$_2$O were included in the calculations. CH$_3$Cl and CH$_3$Br mixing ratios of 0.0 , 1 ppbv , and 100 ppbv, scaled with altitude were used. Altitude variations used are based on available atmospheric measurements and the distributions calculated with the LLNL zonally-averaged chemical-transport model (Wuebbles et al., 1994, Kinnison et al., 1994).

Ambient concentrations of CH$_3$Br and CH$_3$Cl are on the order of 8-12 pptv and 600 pptv, respectively, in the troposphere. We will assume a background atmosphere mixing ratio of 0.0, since a forcing of 1 and/or 100 ppbv constitutes a significant increase over the background and the forcing will be linear over the small amount of background CH$_3$Br and CH$_3$Cl. Radiative forcing calculations were made for tropospheric mixing ratios of 0.0 (ambient), 1 ppbv (forced), and 100

ppbv (forced), with scaled variation with altitude in the stratosphere, in order to produce a radiative forcing which is numerically significant. Observations indicate that while the mixing ratio of CH_3Cl and CH_3Br and are essentially constant in the troposphere, it rapidly declines with altitude in the stratosphere (WMO, 1994). This will cause a decrease in the radiative forcing at the tropopause over that calculated using a constant forcing perturbation at all altitudes. The radiative forcing perturbation applied at each stratospheric altitude in this study was appropiately decreased from the 1 ppbv to 100 ppbv value used at tropospheric altitudes to reflect the decrease in mixing ratio of CH_3Br and CH_3Cl above the tropopause .

VI. Results and Discussion

The tropospheric radiative forcing calculations for CH_3Cl are shown in Table 1.

Table 1. Tropospheric radiative forcing calculations for CH_3Cl *.

INCLUDED BANDS	RADIATIVE FORCING $(W/m^2/ppbv)$
v_1, v_2, v_3, v_4, v_5, $3v_6$ (100 ppbv forcing)	4.73e-03
v_1, v_2, v_3, v_4 v_5, $3v_6$ (1 ppbv forcing)	5.28e-03
v_1, v_4, $3v_6$ (HITRAN91) (CH_3Cl only, 1ppbv forcing)	1.22e-05
v_2, v_3, v_5, (CH_3Cl only, 1ppbv forcing)	2.29e-02

*Radiative forcing perturbations are scaled with altitude above the troposphere.

The results of Table 1 show that the tropospheric radiative forcing of CH_3Cl is due entirely to the v_2, v_3, and v_5 bands. The contribution of the v_1, v_4, and $3v_6$ bands, even with a factor of 3 increase in the line strengths, will be diminished due to the Plank function reduction at ~3000 cm^{-1} compared to ~1500 cm^{-1}. Calculations were performed using both 1 ppbv and 100 ppbv forcing to insure that the 1 ppbv forcing result was numerically significant and to determine the

linearity effects in the forcing as a result of increased CH_3Cl abundance. It appears that the radiative forcing is linear to within approximately 11 percent in the abundance of CH_3Cl between 1 and 100 ppbv. The tropospheric radiative forcing calculations for CH_3Br are shown in Table 2.

Table 2. Tropospheric radiative forcing calculations for CH_3Br.*

INCLUDED BANDS	RADIATIVE FORCING $(W/m^2/ppbv)$
v_2, v_3, v_4, v_5, v_6 (100 ppbv forcing)	4.93e-03
v_2, v_3, v_4, v_5, v_6 (1 ppbv forcing)	5.33e-03

*Radiative forcing perturbations are scaled with altitude above the troposphere.

The tropospheric radiative forcing of CH_3Br is due primarily to the v_2, v_3, v_5, and v_6 bands. Although the contribution of the omitted v_1 and v_4 bands can amount to approximately 35 percent of the total line intensity, their contribution to the radiative forcing is in the 3000 cm^{-1} spectral range and will therefore be diminished due to the Plank function reduction at ~3000 cm^{-1} compared to ~1500 cm^{-1}. Calculations were performed using both 1 ppbv and 100 ppbv forcing to insure that the 1 ppbv forcing result was numerically significant and to determine the linearity effects in the forcing as a result of increased CH_3B r abundance. It appears that the radiative forcing is linear to within approximately 11 percent in the abundance of CH_3Br between 1 and 100 ppbv. The radiative forcing due to CH_3Br is about the same as that of CH_3Cl. Table 3 shows the radiative forcing of CH_3Br and CH_3Cl obtained in this study relative to other major greenhouse gases (IPCC, 1994).

270

Table 3. Radiative forcing relative to CO_2 per unit molecule change in the 1990 atmosphere (IPCC, 1994).

GAS	RADIATIVE FORCING PER UNIT MOLECULE RELATIVE TO CO_2
CO_2	1
CH_4	21
N_2O	206
CH_3Cl	267
CH_3Br	278
HCFC22	10664
CFC-11	12400
CFC12	15800

VII. GLOBAL WARMING POTENTIALS

Although a trace gas can have a strong radiative forcing per molecule, its greenhouse heating potential of the atmosphere depends also on the lifetime of an impulse of the trace gas to the atmosphere as well as its time dependent anthropogenic emission into the atmosphere. The Global Warming Potentials (GWPs) for the trace gas addresses the net effect of the combination of the radiative forcing and the lifetime of the gas by calculating the time integrated radiative forcing of a unit mass impulse to the atmosphere.

The GWP of a gas, for a given integration time, is defined as,

$$GWP(c_i) = \frac{\int_o^t \Delta F(c_i, t)dt}{\int_o^t \Delta F(c_{co_2}, t)dt} \quad , (5)$$

where ΔF is the change in radiative forcing with time as a function of the species concentration (c_i). An approximate form of Equation 5 was published in IPCC (1990) and is given by the expression;

$$GWP(c_i) = \frac{_o\int^t a_i c_i dt}{_o\int^t a_{co_2} c_{co_2} dt}, \quad (6)$$

where a_i is the instantaneous radiative forcing (per unit mass) due to a unit increase in the concentration of trace gas i, and c_i is the concentration of the trace gas i remaining at time t after its release. The corresponding values for carbon dioxide are in the denominator. Under the assumption that the quantity c_i can be approximated by the relation,

$$c_i = c_{o_i} \exp\left(-t / \tau_i\right) \quad , \quad (7)$$

the direct GWP for any greenhouse gas relative to the GWP for $CFCl_3$ (CFC-11) becomes

$$GWP(C_i) = \frac{m_{CFC-11}}{m_i} \cdot \frac{a_i}{a_{CFC-11}} \cdot \frac{\tau_i}{\tau_{CFC-1}}$$

$$\frac{(1 - \exp(-t/\tau_i))}{(1 - \exp(-t/\tau_{CFC-11}))} GWP(CFC-11) \quad (8)$$

where the a's are the radiative forcing values at the tropopause in W/m^2 per ppbv, the m's are the molecular mass, and the τ's are the atmospheric lifetimes.

Table 4 shows the results of a calculation of the GWP for CH_3Cl and CH_3Br at times of 20, 100, and 500 years, based on CFC-11 GWPs as determined in IPCC (1994) (c.f. Equation 8). The lifetime of CH_3Cl used in the calculation was 1.5 years. The lifetime of CH_3Br used in the calculation was 1.3 years.

Table 4. Global Warming Potentials for CH_3Cl and CH_3Br .

	20 YEARS	100 YEARS	500 YEARS
CH_3Cl	26.6	8.1	2.5
CH_3Br	12.8	3.9	1.2

For CFC-11, with a lifetime of 50 years, the GWP at 20, 100, and 500 year integration periods are 5000, 4000, and 1400 respectively IPCC (1994). The GWPs of CH_3Cl given in Table 4 are approximately 33 to 43 percent of GWPs of CH_4, on a per kilogram basis (IPCC, 1994). Kaye et al. (1994) gives the abundance of CH_3Cl as approximately 600 parts per trillion in the troposphere, decreasing to approximately 20 parts per trillion at altitudes around 30 km, with an annual emission of approximately 3.5 million tons per year. Kay et al. (1994) estimates an anthropogenic CH_3Cl emission rate of between 15 and 30 percent of the total emission rate, principally due to biomass burning. Given a methane emission rate of approximately 500 Tg/year (WMO, 1991), with approximately 50 percent of the total due to anthropogenic sources (IPCC,1990), the global warming effects of CH_3Cl are about 0.09 to 0.13 percent of the methane contribution contribution using IPCC (1994) methane GWP values. The GWPs of CH_3Br given in Table 4 are approximately 16 to 21 percent of GWPs of CH_4, on a per kilogram basis (IPCC, 1994). WMO (1994) gives the abundance of CH_3Br as approximately 10 parts per trillion in the troposphere with an annual emission of approximately 120 thousand tons per year. WMO (1994) estimates an anthropogenic CH_3Br emission rate of between 33 and 63 percent of the total emission rate, principally due to biomass burning and fumigant emission. The global warming effects of CH_3Br are about 0.004 to 0.005 percent of the methane contribution contribution using IPCC (1994) methane GWP values. When one considers that CH_3Cl has no human-related sources of significance and that roughly half of the CH_3Br is due to natural sources, the above results imply that these compounds have had a negligible direct impact on the warming influence from changing concentrations of greenhouse gases. Indirect effects from human-related sources of CH_3Br on lower stratospheric ozone do need to be considered, however (Daniel et al., 1995). Thus CH_3Cl and CH_3Br have not been significant contributors as greenhouse gases, at least for their direct contribution, and will not become a problem unless very large anthropogenic releases of these gases occur.

Acknowledgments

References

Antilla, R., C. Betrencourt-Stirnemann, and J. Dupre, 1983: The infrared bands v_2 and v_5 of CH_3Br with Coriolis interaction. *J. Molec. Spectrosc.*, 100, 54–74.

Blake, D. R., B. Sive, M. Zondlo, and F. S. Rowland, 1993: Estimated methyl bromide emissions from biomass burning., EOS, Transactions of the American Geophusical Union, Vol. 74, No. 43, 134.

Blass, W. E., 1987: Systematic approach to the analysis of aerturbed spectra, Part I. *Applied Spectroscopy Reviews*, 23, 1–58 .

Brown, L. R., 1994, private communication.

Brown, L. R., C. B. Farmer, C. P. Rinsland, and R. A. Toth, 1987: Molecular line parameters for the atmospheric trace molecule spectroscopy experiment. *Applied Opttics*, 26, 5154 - 5182.

Butler, J. H., 1994: The potential role of the ocean in regulating atmospheric Ch_3Br., *Geophys. Res. Lett.*, in press.

Clough, S.A., F.X. Kneizys, E.P. Shettle, and G.P. Anderson, 1986: Atmospheric radiance and transmittance: FASCODE2. *Proceedings of the Sixth Conference on Atmospheric Radiation*, 141–144, Williamsburg, VA.

Crutzen, P. J., L. E. Heidt, J. P. Krasnec, W. H. Pollack, and W. Seiler, 1979: Biomass burning as a source of atmospheric gases CO, H_2, N_2O, NO, CH_3Cl, and COS. *Nature*, 282, 253 - 256.

Crutzen, P. J., W. Seiler, A. C. Delany, J. Greenberg, P.Haagensen, L. Heidt, R. Leub, W. Pollock, A. Wartburg, and P. Zimmerman, 1983: Tropospheric chemical composition measurements in Brazil during the dry seasons., *J. Atmos. Chem.*, 2, 233 - 256.

Daniel, J. S., S. Solomon, and D. L. Albritton, 1995: On the evaluation of halocarbon radiative forcing and global warming potentials., *J. Geophys. Res.*, 100, D1, 1271–1285.

Daunt, S. J., A. K. Atakan, W. E. Blass, G.W. Halsey, D. E. Jennings, D. C. Reuter, J. Susskind, and J. W. Brault, 1984: The 12 μm band of ethane: High resolution laboratory analysis, *Astrophysical Journal*, 280, pp. 921–935.

Elkins, J. W., R. H. Kagann, and R. L. Sams, 1984: Infrared band strengths for methyl chloride in the regions of atmospheric interest. *J. Molec. Spect.*, 105, 480 - 490.

Goody, R. M., and Y. L. Jung, 1989: *Atmospheric Radiation, Theoretical Basis*, 2nd. Ed., 519 pp., Oxford, NY, (G1).

Goody, R. M., R. West, L. Chen, and D. Crisp, 1989: The correlated-k distribution method for radiation calculations in nonhomogeneous atmospheres. *J. Quant. Spectros. Radiat. Transfer*, 42, 539-550, (G2).

Graner, G. and W.E. Blass, 1975: The v_2 and v_5 vibration – rotation bands of methyl bromide, *Journal de Physique*, 36, 769 – 772.

Graner, G., 1982: The methyl bromide molecule: a critical consolidation of perturbations in spectra, *J. Molec. Spectrosc.,* **90**, 394–438.

Grant, K.E., A.S. Grossman, R. Freedman, and J.B. Pollack, 1992: A correlated k-distribution model of the heating rates for CH_4 and N_2O in the atmosphere between 0 and 60 km. *Proceedings of the 15th Annual Review Conference on Atmospheric Transmission Models,* Phillips Laboratory, Directorate of Geophysics, Air Force Material Command, Hanscom AFB, Mass., Report PL-TR-94-2135, 1994, LLNL Report UCRL-JC-110364 (GGFP).

Grossman, A.S., and K.E. Grant, 1992: A correlated k-distribution model of the heating rates for CO_2 and O_3 in the atmosphere between 0 and 60 km. LLNL Report UCRL-ID-111805.

Grossman, A.S., and K.E. Grant, 1994a: A correlated k-distribution model of the heating rates for H_2O and a molecular mixture in the 0–2500 cm^{-1} wavelength region in the atmosphere between 0 and 60 km. *Proceedings of the 8th Conference on Atmospheric Radiation,* Sponsored by the American Meteorological Society, Boston, Mass., Jan. 23-28, LLNL Report UCRL-ID-112296.

Grossman, A.S., and K.E. Grant, 1994b: Tropospheric radiative forcing of CH_4. LLNL Report UCRL-ID-111805.

Grossman, A.S., K.E. Grant, and D. J. Wuebbles, 1993: Tropospheric radiative forcing of O_3 for the 1994 IPCC report. LLNL Report UCRL-ID-115827.

Harshvardhan, R. Davies, D.A. Randall, and T.G. Corsetti, 1987: A fast radiation parameterization for atmospheric circulation models, *J. Geophys. Res.,* **92**, D1, 1009–1016.

Howard, C. J., and K. M. Evenson, 1976: Rate constants for the reactions of OH with CH_4 and fluorine, chlorine, and bromine substituted methanes at 296K. *J. Chem. Phys.,* **64**, 197 - 203.

Intergovernmental Panel on Climate Change (IPCC): Climate Change; The IPCC Scientific Assessment, Cambridge University Press, Cambridge, UK, 1990.

Intergovernmental Panel on Climate Change (IPCC): Climate Change 1992; The Supplementary Report to the IPCC Scientific Assessment, Cambridge University Press, Cambridge, UK, 1992.

Intergovernmental Panel on Climate Change (IPCC): Climate Change 1994; The Report to the IPCC Scientific Assessment Working Group, in press.

Kaye, J. A., S. A. Penkett, and F. M. Ormond, 1994: Report on Concentrations, lifetimes, and trends of CFC's, halons, and related species., NASA Reference Publication 1339, NASA *Office of Mission to Planet Earth, Science Division, Washington, DC.*

Kinnison, D. E., K. E. Grant, P. S. Connell, D. A. Rotman, and D. J. Wuebbles, 1994: The chemical and radiative effects of the Mount Pinatubo eruption, *J. Geophys. Res.,* **99**, 25705-25731.

Khalil, M. A. K., R. A. Rasmusses, and R. Gunawardena, 1993: Atmospheric methyl bromide: trends and global mass balance., *J. Geophys. Res.,* **98**, 2887 - 2896.

Logan, J. A., M. J. Prather, S. C. Wofsy, and M. B. McElroy, 1981: Tropospheric Chemistry: a global perspective., *J. Geophys. Res.,* **86**, 7210 - 7254.

Oremland, R. S., L. G. Miller, and F. R. Strohmaier, 1994: Degradation of methyl bromide in anaerobic sediments., *Env. Sci. and Tech.,* in press.

Penkett, S., B. Jones, B. Rycroft, and D. Simmons, 1985: An interhemispheric comparison of the concentrations of bromine compounds in the atmosphere., *Nature,* **318**, 550 - 553.

Prather, M. J., and C. M. Spivakovsky, 1990: Tropospheric OH and the lifetimes of hydrochlorfluorocarbons (HCFCs). *J. Geophys. Res.,* **95**, 18723 - 18729.

Ramanathan, V., L. Callis, R. Cess, J. Hansen, I. Isaksen, W. Kuhn, A. Lacis, F. Luther, J. Mahlman, R. Reck, and M. Schlesinger, 1987: Climate-chemical interactions and effects of changing atmospheric trace gases. *Revs. Geophys.,* **25**. 7, 1441- 1482.

Rasmussen, R. A., L. E. Rasmussen, M. A. K. Khalil, and R. W. Dalluge, 1980: Concentration distribution of methyl chloride in the atmosphere. *J. Geophys. Res.,* **85**, 7350 - 7356.

Rothman, L.S., R.R. Gamache, R.H. Tipping, C.P. Rinsland, M.A.H. Smith, D.C. Benner, V. Malathy Devi, J.M. Flaud, C. Camy-Peyret, A. Perrin, A. Goldman, S.T. Massie, L.R. Brown, and R.A. Toth, 1992: The HITRAN molecular database: Editions of 1991 and 1992. *J. Quant. Spectrosc. Radiat. Transfer.,* **48**, N5, pp 469–507.

Singh, H. B., and M. Kanikidou, 1993: An investigation of the atmospheric sources and sinks of methyl bromide., *Geophys. Res. Lett.,* **20**, 133 - 136.

Singh, H. B., L. J. Salas, and R. E. Stiles, 1983: Selected man made halogenated chemicals in the air and ocean environment. *J. Geophys. Res.,* **88**, 3684 - 3690.

van Straten, A. J., and W. M. A. Smit, 1977: Absolute infrared intensities of methyl bromide and all deuterium derivatives. *J. Chem. Phys.,* **67**, 970 - 975.

West, R., D. Crisp, and L. Chen, 1990: Mapping transformations for broad band atmospheric radiation calculations. *J. Quant. Spectros. Radiat. Transfer,* **43**, 191-199, (W1).

WMO, World Meteorological Organization, 1985: Scientific Atmospheric Ozone: 1985, Global Ozone Research and Monitoring Project Report 16, Geneva.

WMO, World Meteorological Organization, 1991: Scientific Assessment of Ozone Depletion: 1991, Global Ozone Research and Monitoring Project Report 25, Geneva.

WMO, World Meteorological Organization, 1994: Scientific Assessment of Ozone Depletion: 1994, Global Ozone Research and Monitoring Project Report 25, Geneva.

Wuebbles, D.J., D.E. Kinnison, K.E. Grant, and J. Lean, 1991: The effect of solar flux variations and trace gas emissions on recent trends in stratospheric ozone and temperature, *J. Geomag. Geoelectr.,* **43**, 709–718.

Wuebbles, D.J., A.S. Grossman, J. S. Tamaresis, K. O. Patten, A. Jain, and K. E. Grant, 1994: Indirect global warming effects of tropospheric ozone induced by surface methane emission. *Proceedings of the 17th Annual Review Conference on Atmospheric Transmission models,*Bedford, MA, in press, LLNL Report UCRL-ID-118061.

Figure Captions

Figure 1. Absolute intensity distribution of 31,155 methyl bromide rotation-vibration transitions in the four fundamental vibration rotation bands for each of the isotopmers, $CH_3{}^{79}Br$ and $CH_3{}^{81}Br$, used in this study.

Figure 2. Globally and annually averaged profiles of water vapor, ozone, and methane as a function of altitude for the ambient atmosphere.

Figure 3. Pressure-temperature profile for the ambient atmosphere. The temperatures are globally and anually averaged.
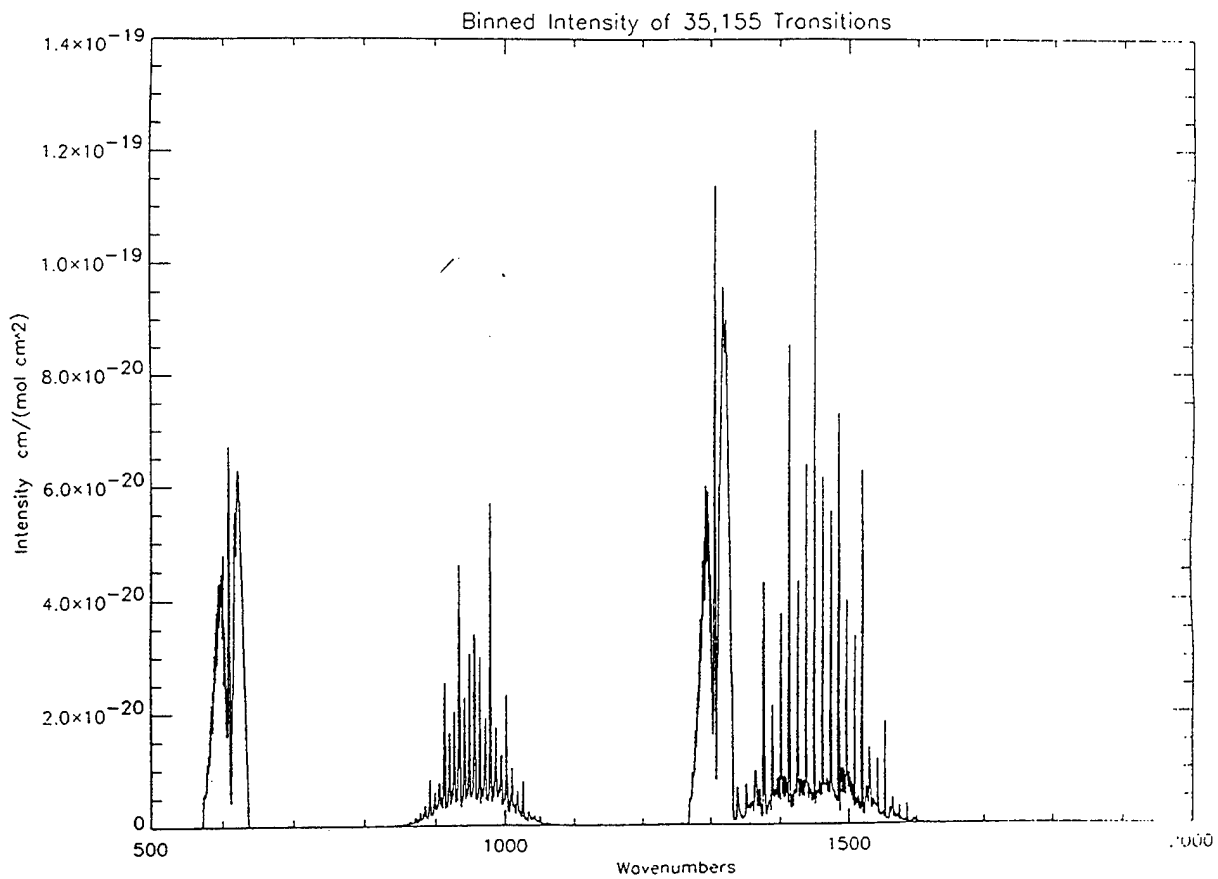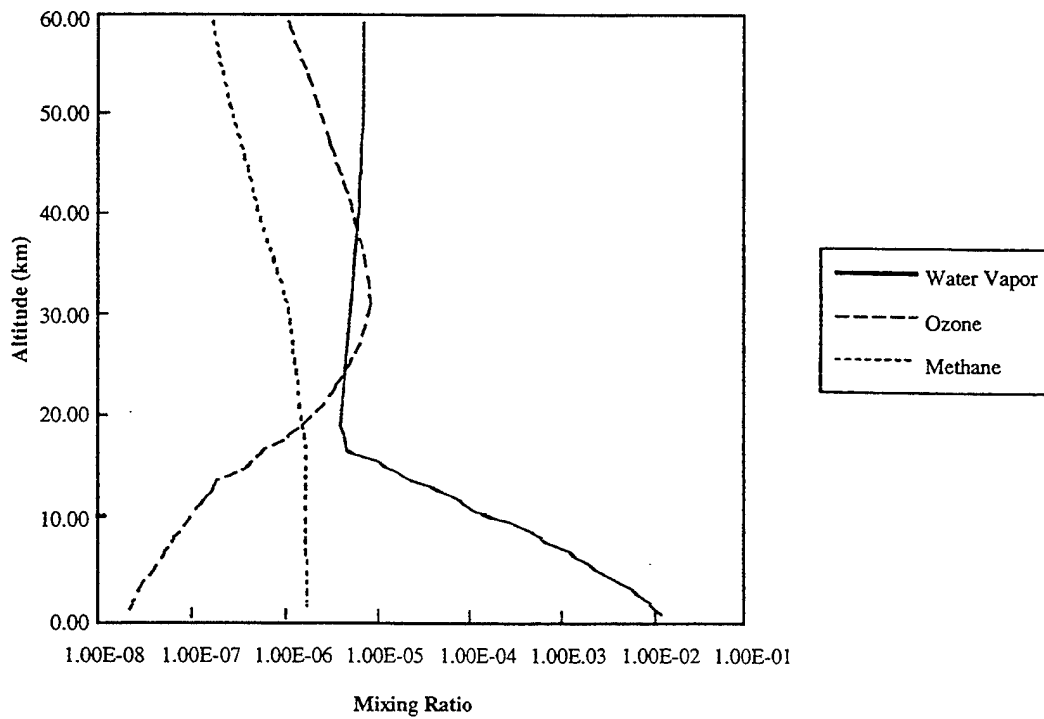
273

Figure 1

Figure 2 Globally- and annually-averaged profiles of water vapor, ozone, and methane as a function of altitude for the ambient atmosphere.
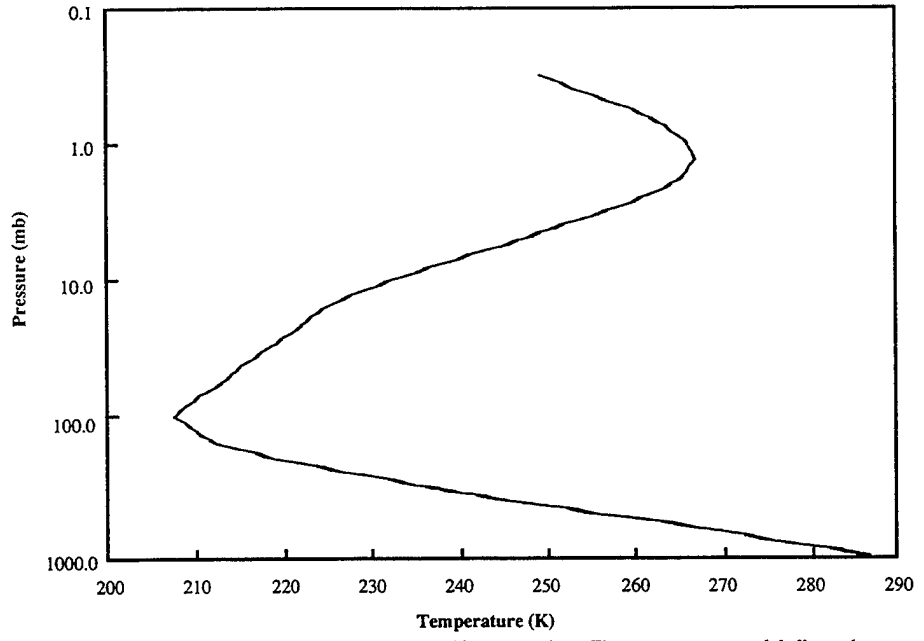
Figure 3 Pressure-temperature profile for ambient atmosphere. The temperatures are globally- and annually-averaged.

FASCODE for the Environment (FASE)

H.E. Snell
Atmospheric and Environmental Research, Inc.
840 Memorial Dr.
Cambridge, MA 02139

G.P. Anderson, J.H. Chetwynd, and S. Miller
Geophysics Directorate, Phillips Laboratory
Hanscom AFB, MA 01731

ABSTRACT

The Optical Physics Division of the Phillips Laboratory with support from the DoE Atmospheric Radiation Measurement (ARM) Program is developing a state-of-the-art line-by-line atmospheric radiative transfer model as the successor to FASCODE. The goal of this project is to create a computationally efficient model which contains the most up-to-date physics. The new model, known as FASCODE for the Environment, or "FASE", combines the best features of FASCODE and LBLRTM, the DoE's standard radiative transfer model. Upgrades to FASE include improvement of the cloud and aerosol descriptors, based on changes made to MODTRAN, and the capability of incorporating the new heavy molecule absorption cross-section data found on HITRAN96, which is of slightly different format from the previous HITRAN cross-section data. This paper addresses changes which have been made to FASCODE and LBLRTM to create FASE, and gives an overview of the new capabilities and recent model validations.

INTRODUCTION

FASCODE for the Environment (FASE) was developed by combining features from the line-by-line radiative transfer codes of the Air Force Phillips Laboratory (FASCODE)[1] and the Department of Energy (LBLRTM)[2]. Both of these models were derived from FASCOD3 which was based on FASCOD1B, a four-function line-by-line code developed by Clough and Kneizys[3,4]. The rationale for the development of FASE is to make available to the atmospheric spectroscopy community the results of on-going work sponsored by the Department of Energy (DOE) while incorporating the results of continuing research and development at the Air Force Phillips Laboratory. An initial version of FASE[5] was available for limited release and testing in the summer of 1995; beta-version 2.0 will be available in September 1996. This paper will summarize recent improvements which have been made to FASE, and describe the on-going effort to fully merge the capabilities of FASCODE and LBLRTM. The reader is referred to the paper by Snell et al.[6] for information about initial model validations against measurements.

NEW / IMPROVED FEATURES

The current version of FASE contains several new or improved features including the FASCODE option for LASER calculations (which had been dropped by LBLRTM), updated coefficients for calculations in the UV/visible spectral region, and the addition of a solar spectrum module for atmospheric transmittance and surface reflectance calculations.

LASER Option

The laser option from FASCODE allows the user to calculate only the narrow region centered at a specific wavenumber and is useful for the simulation of laser-based experiments, and as input to LIDAR analyses. Due to the nature of the algorithm employed by FASE, FASCODE, and LBLRTM to merge the optical properties of different atmospheric layers[7], use of the LASER option is recommended for accurate results at a single monochromatic frequency. Calculations show that distortions arising from fixed frequency assumptions can be significant, particularly in spectral regions where the absorption changes rapidly over a narrow spectral interval. For example, at 23.8 GHz (0.794 cm^{-1}) an error of about 5% is introduced if one does not use the LASER option.

Calculations in the UV / Visible

Two major changes were made for UV / Visible calculations. First, the coefficients for ozone absorption were updated and a temperature dependence was introduced[8]. The new values, which include both the Chappuis and Wulf absorption, cover the range from 9170 to 24565 cm^{-1} at a resolution of 5 cm^{-1}. The second change in the UV was the inclusion of the O_2 Schumann-Runge absorption cross-sections between 49000 cm^{-1} and 57000 cm^{-1}. The Schumann-Runge system is interesting because it results from a pre-dissociative electronic transition[9] which leads to natural halfwidths of order 0.5 to 1.0 cm^{-1}, about ten times larger than the assumed NTP halfwidths of the transitions on the HITRAN database. These lines are on the HITRAN96 spectral database but are incompatible with the Voigt lineshape decomposition algorithm employed by FASE, FASCODE, and LBLRTM because of their inherent halfwidth assumption. Thus FASE computes the absorption using polynomial coefficients developed from a fit devised by Minschwaner et al.[10,11]. The fit was accomplished on a 0.5 cm^{-1} spectral grid using cross-sections obtained from a line-by-line radiative transfer model and includes contributions from the temperature dependent Schumann-Runge continuum.

Figure 1 illustrates the Schumann-Runge absorption in the spectral region from 50500 - 52500 cm^{-1}. The dashed line is the FASE calculation and the solid line is the measured spectrum[12,13]. The calculation was made using only the known viewing zenith angle, balloon altitude and corresponding pressure level, and the US Standard temperature and ozone profiles. No specific attempt was made to accurately retrieve molecular amounts to obtain a better fit between model and measurement. However, this comparison

shows the good agreement between the structure of the computed spectral features and those of the measurement.

Solar Spectrum

The addition of a solar spectrum module gives FASE the capability of computing solar transmission through the atmosphere. This is particularly useful for simulations of experiments employing the technique of solar absorption spectroscopy, but is also necessary when simulating a down-looking measurement over a reflective surface. Currently the module may be used to compute the transmitted solar irradiance either as the direct component (for direct solar observations or limb-viewing cases), or the direct component reflected off a surface (for down-looking applications). Ultimately the solar model will be used with a multiple-scattering routine to include the diffuse radiation component for a better treatment of the atmospheric radiation field. The solar spectrum was calculated by Kurucz[14] for wavelengths greater than 200 nm; for wavelengths less than 200 nm, SUSIM data collected on the Space Lab 2 flight of the Space Shuttle[15] was used. Figure 2 shows the good agreement between FASE and measurements in the region 49000 - 50000 cm^{-1}. This spectral region contains many solar Fraunhofer lines and this structure is captured in the FASE solar spectrum (as with Figure 1, no attempt was made to retrieve the molecular species and obtain a better fit between the model and the measurement).

ON-GOING SCIENCE IMPROVEMENTS

New Cloud/Rain Descriptors

Changes to the cloud and rain routines are underway based on improvements that have been developed for MODTRAN[16]. This set of upgrades makes it easier to modify the cloud/rain models (by re-configuring and clarifying the coding structure) as well as providing for a more flexible prescription of realistic cloud and aerosol layers and their associated optical properties. The improved layering scheme allows for multiple overlapping and non-overlapping clouds. For cumulus and stratus type clouds, with and without rain, the upgrades include adjustable cloud parameters (thickness, altitude, vertical extinction, etc.), decoupling of the clouds from aerosols (allowing clouds and aerosols to be present at the same altitude), the introduction of ice particles, and a flexible set of user-defined cloud spectral properties, water droplet, ice particle, and rain rate profiles.

Calculations with the new cloud models illustrate (Figure 3) the change in radiance with a change in cloud thickness and base height. The cloud consisted of a cumulus cloud with overlying cirrus (the cloud top and cirrus thickness were held constant). The marked change in radiance for a cloud with a base at 0.4 km and one at 1.88 km shows the need for a versatile cloud simulation capability, even for direct radiance and transmittance (no scattering) calculations.

New Absorption Cross-Sections

Laboratory measurements of the absorption properties of heavy molecules have recently been made by Varanasi et al.[17] (subsequently referred to as "Varanasi's cross sections") and are expected to be included on the release of the HITRAN96 databases[18]. Because of the complexity of the transitions of these molecules and the fact that individual spectral lines cannot be resolved at temperatures and pressures typical of the earth's atmosphere, the measurements consist of $0.01 - 0.03$ cm^{-1} spectral information in the form of absorption cross-sections (i.e. without information about line strengths, positions, halfwidths, etc.). Many of these molecules have already been included in that form, as temperature dependent cross sections, on previous versions of the HITRAN databases. However, the Varanasi measurements are provided as a function of pressure and temperature as opposed to the previous HITRAN format, which extrapolated the temperature-dependent values to zero pressure. (This extrapolation has been done without fully correcting for the change in Voigt line shape at the lower pressures, so that the apparent spectral line features remain those of the primary instrument resolution.) To compute the optical depth for a particular (p,T) combination with the 'old' data, it was necessary to interpolate between temperatures while convolving with the appropriate Lorentz line shape for the pressure, finally combining this derived cross section with the density weighted path amounts. With the Varanasi data, one is required to interpolate and/or extrapolate between the tabulated data in order to arrive at the correct absorption coefficient. Thus in order to accommodate this new data directly it would be necessary to re-configure the FASE algorithms to bypass the convolution and perform the necessary interpolation and/or extrapolation. Further, one must develop an appropriate scheme for extrapolating the tabulated values to pressures and temperatures outside the range of the measurements, which tended to be preselected for pressure/temperature combinations encountered during limb viewing. Limb viewing is only one of many types of viewing geometry supported by FASE, and the other types of paths must also be supported for users to take full advantage of these recent measurements.

One approach through which the Varanasi cross-sections may be utilized by the FASE algorithms is to perform a least-squares fit to the data with a series of spectral lines, solving for the line strength, halfwidth, and lower state energy[19]. The pseudo-line approach incorporates all the (p,T) combinations of data into the least-squares fit and extends the applicability from a simple interpolation between two (p,T) values. The pseudo-line data is easily merged with the spectral line data taken from HITRAN when creating the spectral line file to be used by FASE, and the radiative transfer calculations are performed as usual, with the model using the spectral line routines, rather than the cross-section routines, when computing the absorption of these species. Figure 4 shows a comparison of Varanasi's data for CFC-12 with the absorption cross-section computed in this manner.

shows the good agreement between the structure of the computed spectral features and those of the measurement.

Solar Spectrum

The addition of a solar spectrum module gives FASE the capability of computing solar transmission through the atmosphere. This is particularly useful for simulations of experiments employing the technique of solar absorption spectroscopy, but is also necessary when simulating a down-looking measurement over a reflective surface. Currently the module may be used to compute the transmitted solar irradiance either as the direct component (for direct solar observations or limb-viewing cases), or the direct component reflected off a surface (for down-looking applications). Ultimately the solar model will be used with a multiple-scattering routine to include the diffuse radiation component for a better treatment of the atmospheric radiation field. The solar spectrum was calculated by Kurucz[14] for wavelengths greater than 200 nm; for wavelengths less than 200 nm, SUSIM data collected on the Space Lab 2 flight of the Space Shuttle[15] was used. Figure 2 shows the good agreement between FASE and measurements in the region 49000 - 50000 cm^{-1}. This spectral region contains many solar Fraunhofer lines and this structure is captured in the FASE solar spectrum (as with Figure 1, no attempt was made to retrieve the molecular species and obtain a better fit between the model and the measurement).

ON-GOING SCIENCE IMPROVEMENTS

New Cloud/Rain Descriptors

Changes to the cloud and rain routines are underway based on improvements that have been developed for MODTRAN[16]. This set of upgrades makes it easier to modify the cloud/rain models (by re-configuring and clarifying the coding structure) as well as providing for a more flexible prescription of realistic cloud and aerosol layers and their associated optical properties. The improved layering scheme allows for multiple overlapping and non-overlapping clouds. For cumulus and stratus type clouds, with and without rain, the upgrades include adjustable cloud parameters (thickness, altitude, vertical extinction, etc.), decoupling of the clouds from aerosols (allowing clouds and aerosols to be present at the same altitude), the introduction of ice particles, and a flexible set of user-defined cloud spectral properties, water droplet, ice particle, and rain rate profiles.

Calculations with the new cloud models illustrate (Figure 3) the change in radiance with a change in cloud thickness and base height. The cloud consisted of a cumulus cloud with overlying cirrus (the cloud top and cirrus thickness were held constant). The marked change in radiance for a cloud with a base at 0.4 km and one at 1.88 km shows the need for a versatile cloud simulation capability, even for direct radiance and transmittance (no scattering) calculations.

One drawback to the pseudo-line approach is that new sets of pseudo-lines are required as more molecules are added. In the long run it might be desirable to develop a scheme to use the cross-sections given as a function of pressure and temperature. Since the problem lies in interpolating/extrapolating the absorption coefficient data to specific values of the pressure and temperature, one might use the pseudo-line approach to fill out the full matrix of required pressures and temperatures (that is, use FASE to compute the absorption coefficients for the regions not represented by the measurements). For the time being the pseudo-line approach has been implemented in FASE and exploration continues on ways in which the actual data can be used, perhaps in conjunction with 'pseudo-data' based on calculations with the pseudo-lines.

CONCLUSIONS

Significant progress has been made in the merging of FASCODE and LBLRTM to create FASE. The result is a radiative transfer model which contains state-of-the-art atmospheric physics through validations of LBLRTM with ARM data, while also incorporating many of the features from FASCODE which are not found in LBLRTM but are required for flexible use of the code under airborne, ground- and space-based conditions. Continued validation is planned as a means of ensuring that the code meets or exceeds the requirements of the atmospheric modeling community. Current updates planned for FASE include the re-introduction of the FASCODE multiple-scattering routines[20] and the complete implementation of Varanasi's data as a set of pseudo-line parameters.

ACKNOWLEDGMENTS
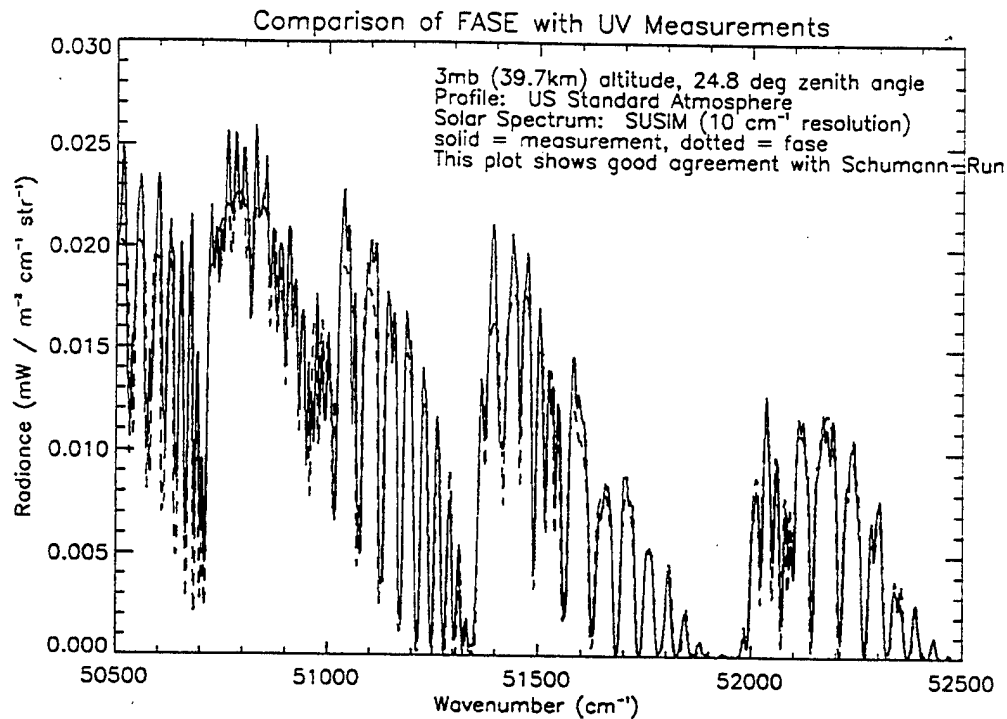
Figure 1: FASE calculation in the UV showing excellent agreement between the modeled Schumann-Runge bands and a measured spectrum.
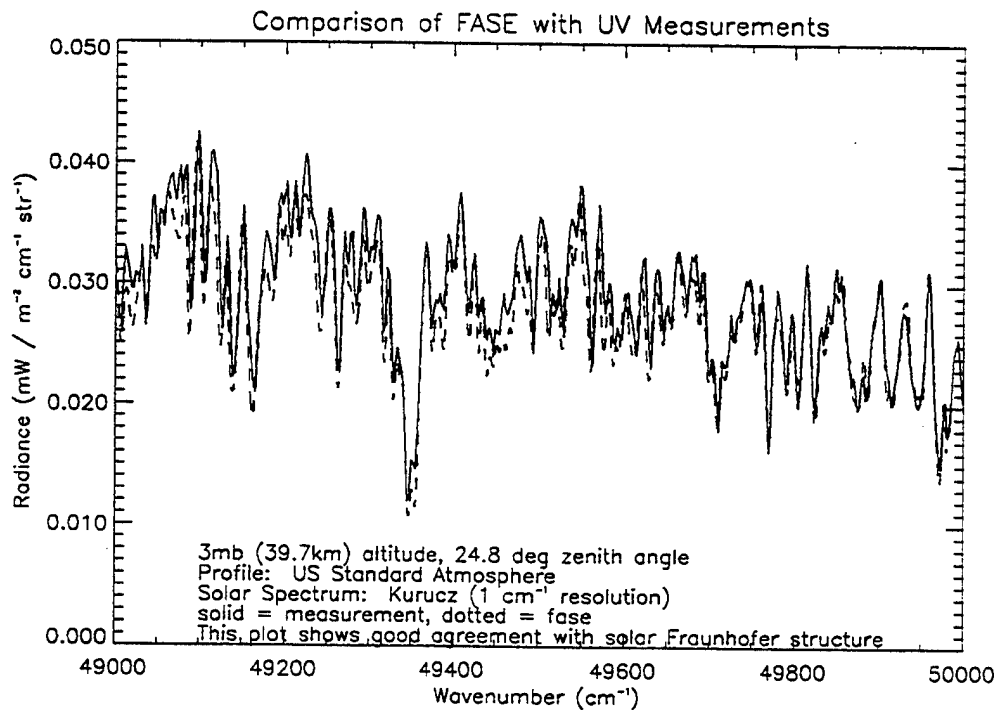
Figure 2: FASE calculation in the UV showing excellent agreement between the model and a measured spectrum. Note that most of the structure in this region is due to solar Fraunhofer lines, which are accurately reproduced with the Kurucz solar spectrum.

Varying Cloud Base and Thickness
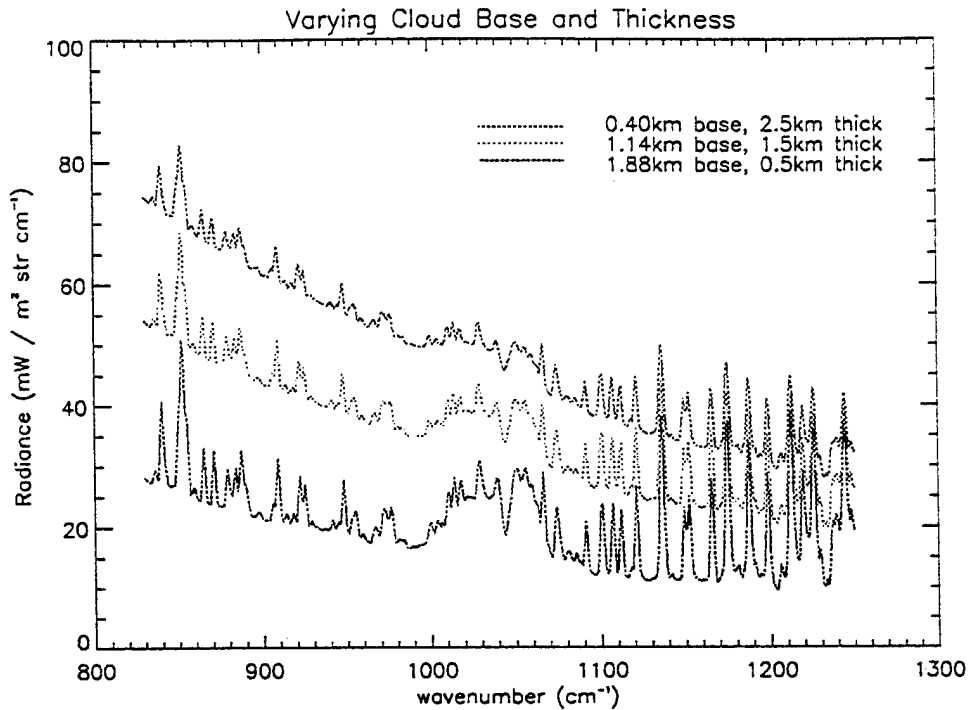
Figure 3: Example of the one of the new FASE cloud options: the user now has the ability to easily change cloud base altitude and cloud thickness.
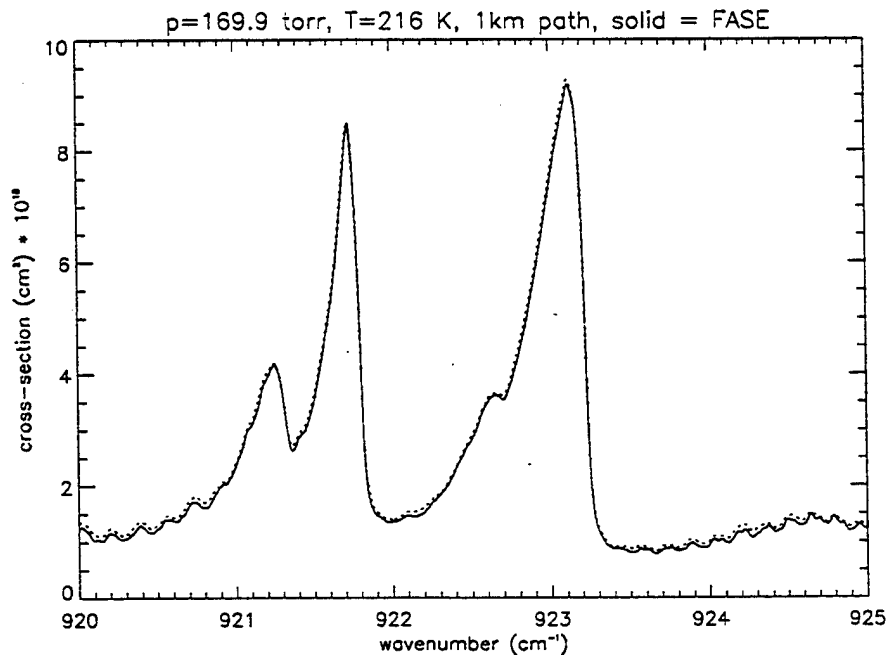
Figure 4: Comparison of the computed CFC-12 cross-section (solid line) with the measured cross-section (dotted line) at 169.9 torr and 216 K.

[1]Anderson, G.P., et al., History of One Family of Atmospheric Radiative Transfer Codes, The European Symposium on Satellite Remote Sensing, Conference on Passive Infrared Remote Sensing of Clouds and Atmosphere II, 26-30 September 1994, Rome, Italy.

[2]Clough, S.A., et al., Radiative Transfer Model Development in Support of the Atmospheric Radiation Measurement (ARM) Program, Proceedings of the Second ARM Science Team Meeting, DOE Conf. 9303112, Norman, OK, 1-4 March 1993.

[3]Clough, S.A., F.X. Kneizys, L.S. Rothman, and W.O. Gallery, Atmospheric Spectral Transmittance and Radiance: FASCODE 1B, *Proc. SPIE, 277, Atm. Transmission*, 1981.

[4]Clough, S.A. and F.X. Kneizys, Convolution Algorithm for the Lorentz Function, *Applied Optics, 18*, 2329, 1979.

[5]Snell, H.E., J.-L. Moncet, G.P. Anderson, J.H. Chetwynd, S. Miller, and J. Wang, FASCODE for the Environment (FASE), Proceedings of the Fifth ARM Science Team Meeting, San Diego, CA, 19-23 March 1995.

[6]Snell, H.E., G.P. Anderson, J. Wang, J.-L. Moncet, J.H. Chetwynd, and S.J. English, Validation of FASE (FASCODE for the Environment) and MODTRAN3: updates and comparisons with clear-sky measurements, in Proceedings of Conf. on Passive Infrared Remote Sensing of Clouds and the Atmosphere III, SPIE Vol. 2578, Paris, France, 25-27 September 1995.

[7]Snell, H.E., J.-L. Moncet, G.P. Anderson, J.H. Chetwynd, S. Miller, and J. Wang, FASCODE for the Environment (FASE), Proceedings of Conf. on Atmospheric Propagation and Remote Sensing IV, SPIE Vol. 2471, Orlando, FL, 17-19 April 1995.

[8]Shettle, E.P., and S.M. Anderson, Ozone Cross-Sections for the Chappuis and Wulf Absorption Bands, submitted to *Geophys. Res. Letters*, 1995.

[9]Yoshino, K., D.E. Freeman, and W.H. Parkinson, High Resolution Absorption Cross Section Measurements and Band Oscillator Strengths of the (1-0)-(12-0) Schumann-Runge Bands of O_2, *Planet. Space Sci., 31*, 339-353, 1983.

[10]Minschwaner, K., G.P. Anderson, L.A. Hall, and K. Yoshino, Polynomial Coefficients for Calculating O_2 Schumann-Runge Cross-Sections at 0.5 cm^{-1} Resolution, *J. Geophys. Res., 97*, 10103-10108, 20 June 1992.

[11]Minschwaner, K., G.P. Anderson, L.A. Hall, R.J. Thomas, D. Rusch, A. Berk, and J. Conant, Scattered Ultraviolet Radiation in the Upper Stratosphere 3: Modeling and Analysis, *J. Geophys. Res.*, in press 1995.

[12]Anderson, G.P., and L.A. Hall, Stratospheric determination of O_2 cross sections and photodissociation rate coefficients: 191 - 215 nm, *J. Geophys. Res., 91*, 14509-14515, 1986.

[13]Anderson, G.P., and L.A. Hall, Attenuation of solar irradiance in the Stratosphere: Spectrometer Measurements between 191 and 207 nm, *J. Geophys. Res., 88*, 6801-6806, 1983.

[14]Kurucz, R.L., The Solar Irradiance by Computation, in Proc. of the 17th Annual Review Conference on Atmospheric Transmission Models, 7 June 1994, Geophysics Directorate/Phillips Laboratory, Hanscom AFB, MA, 1994.

[15]Hall, L.A., and G.P. Anderson, High-Resolution Solar Spectrum between 2000 and 3100 Å, *J. Geophys. Res., 96*, 12927-12931, 1991.

[16]Berk, A., Upgrades to the MODTRAN Layer Cloud/Rain Models, *Rpt. No. SSI-SR-56*, Spectral Sciences Inc., 99 S. Bedford St., Burlington, MA, 01803, 1995.

[17]Varanasi, P., and V. Nemtchinov, Thermal Infrared Absorption Coefficients of CFC-12 at Atmospheric Conditions, J. Quant. Spectro. Radiat. Transfer, 51, 679-687, 1994.

[18]Rothman, L.S., R.R. Gamache, A. Goldman, L.R. Brown, R.A. Toth, H.M. Pickett, R. Poynter, J.-M. Flaud, C. Camy-Peyret, A. Barbe, N. Husson, C.P. Rinsland, and M.A.H. Smith, the HITRAN Database 1986 Edition, *Applied Optics*, 26, 1987.

[19] Geoff Toon, Jet Propulsion Laboratory, Private Communication, November 1995.

[20]Isaacs, R.G., W.-C. Wang, R.D. Worsham, and S. Goldenberg, Multiple scattering LOWTRAN and FASCODE models, *Applied Optics*, 26, 1272-1281, 1987.

AUTHORS

ABRAMS, M.C.	54
ACHARYA, P.	23,24,25,152,168
ADLER-GOLDEN, S.	23,152
ANDERSON, G.P.	11,23,24,25,152,168,276
BALSIGER, F.	41
BARBE, A.	53,58
BATTALINO, T.E.	18
BELL, R.A.	15
BERK, A.	23,24,25,152,168
BERNSTEIN, L.S.	23,24,25,152,168
BEVILAQUA, R.M.	10,95
BLASS, W.E.	49,265
BONNER, B.	58
BROWN, J.H.	35,207
BROWN, L.R.	46,58,59,60
BROWN, P.D.	8
BURRIEZ, J.C.	13,106
CAMY-PEYRET, C.	63
CAUDIL, T.	20,132
CHACKERIAN, C.	54
CHAMPION, J.P.	58
CHANCE, K.	1
CHEDIN, A.	58
CHETWYND, J.H.	11,23,24,25,152,168,276
CHRIEN, T.G.	2
CHURNSIDE, J.H.	4
CHURSIN, A.	58
CLARK, F.O.	31,32,195
CLOUGH, S.A.	4,8,12
COHEN, E.A.	57
CORNETTE, W.M.	22,138,147
CRISP, D.	59,60
CRISP, J.A.	59,60
DALGARNO, A.	37
DANA, V.	53
DELITSKY, M.L.	57
DEWAN, E.M.	33,34
DOTHE, H.	54
DROR, I.	17,118
DUBUISSON, P.	13,106
DUFF, J.W.	37

ESMOND, J.R.	48,261
EGAN, W.G.	16,43,112,255
FLAUD, J.M.	45,63
FOUQUART, Y.	13,106
FOX, J.L.	37
FROMM, M.D.	10, 95
GAMACHE, R.R.	52,58,63
GOLDMAN, A.	52,54,56,63
GOLOVKO, V.	58
GOORVITCH, D.	54
GRANT, K.E.	49,265
GREEN, R.O.	2
GROSSBARD, N.	35,207
GROSSMAN, A.S.	49,265
HAN, Y.	4
HARADA, L.K.	39,225
HARTMAN, J.M.	50
HAWKINS, R.L.	62
HESTAND, P.D.	27
HIGGINS, G.J.	27
HILICO, J.C.	46
HOGAN, A.W.	43,255
HOKE, M.L.	51
HOPPEL, K.W.	10,95
HUANG, T.Y.	33
JACQUINET-HUSSON, N.	58
JOSEPH, J.Jr.	16,112
JOSEPH, R.I.	28,175
KADOKURA, S.	14
KAELIN, S.	250
KLEINER, I.	59
KNUTESON, R.O.	3,64
KOBAYASHI, H.	14
KOPEIKA, N.S.	17,118
KWON, T.Y.	5
LEE, S.C.	3,64
LILJEGREN, J.C.	8
LOETE, M.	46
LUMPE, J.D.	10,95

MANDIN, J.Y.	53
MAKHLOUF, U.B.	34
MARGOLIS, J.S.	59
MASSIE, S.	10,56,95
MELEN, F.	54
MILLER, S.M.	11,276
MLAWER, E.J.	12
MOREAU, D.	61
MULLER, C.	61
MULLER, H.S.P.	57
NAUMENKO, O.V.	60
OUARDI, O.	46
PARKINSON, W.H.	48,261
PEARSON, J.C.	57
PERRIN, A.	53,60
PHILBRICK, C.R.	21,41
PICARD, R.H.	33,34,36,211
PICKETT, H.M.	57
POYNTER, R.L.	57
PRACNA, P.	59
RAFFENSBERGER, M.	20,132
REGALIA, L.	53
REVERCOMB, H.E.	3,64
ROBLE, R.G.	36,211
RODIN, A.V.	61
ROBERTSON, D.C.	24,25,168
RODRIGUES, R.	50
ROTHMAN, L.S.	44,52,62,63
RYU, K.S.	5
SCALDIFERRI, K.	15
SCHMIDT, E.	20, 132
SCHOENFELD, W.G.	54
SCOTT, N.A.	58
SELBY, J.E.A.	63
SELIVERSTOV, D.	40,237
SHARMA, R.D.	37
SHAW, J.A.	4
SHETTLE, E.P.	10, 95
SHIMOTA, A.	14
SHIPPERT, T.R.	8
SINITSA, L.N.	60
SMIRNOV, M.A.	60
SNELL, H.E.	11,276
SINCLAIR, D.	31,32,195
SMITH, W.L.	3,63
SOWLE, D.	30,181
STEVENS, T.D.	21,41

TARRAGO, G.	59
TELFORD, J.W.	19,126
THOMAS, M.E.	28,175
TIPPING, R.H.	63
TUAN, T.F.	33
TURNER, D.D.	8
TYUTEREV, V.G.	58
URBAN, S.	59
VARANASI, P.	47
WAN, Z.	7,85
WATTSON, R.B.	62,63
WEUBLES, D.J.	49,265
WINNEWISSER, M.	58
WINNICK, J.R.	34,36,211
WINTERSTEINER, P.P.	34,36,211
WISE, J.O.	36,211
YODER, M.J.	40,237
YOSHINO, K.	48,261